Faculty of Engineering and Science

Durability of Northern Sarawak Shale against Short-Term Weathering Based on Geochemistry, Mineralogy, and Textural Properties

Fianita Anthony

0000-0002-6726-5244

**This thesis is presented for the Degree of
Master of Philosophy
of
Curtin University Malaysia**

August 2022

Declaration

I hereby declare that the work presented in this thesis has not been submitted for any other degree or professional qualification, and that it is the result of my own independent work.

Fianita Anthony

08/08/2022

Date

Abstract

Shales are often associated with numerous geotechnical issues involving slope stability, landslides, and structural failures in engineering projects. They typically have low durability and are very susceptible to weathering upon exposure to atmospheric conditions. The rate at which they weather in a tropical climate such as in Northern Sarawak depends primarily on the temperature, humidity, and precipitation. The knowledge of shale durability in this region and its controlling parameters becomes essential due to the increased demand for engineering and construction works. Landslides and road damages associated with shale formations have been reported along the Pan Borneo Highway. Thus, stabilisation works are required to protect the area from further erosion and degradation. Therefore, this research aims to characterise the durability of shales in Northern Sarawak against short-term weathering in relation to its intrinsic properties.

Five shales from five different geological formations in the study area between Miri and Batu Niah were cored and assessed for durability. The durability was evaluated, and the physical, mineralogy, geochemistry, and textural properties were determined. Based on the results, shale from all studied formations has low to very low durability. The Sibuti shale is the most durable, while the Lambir shale is the least durable. The physical properties were presented according to the following parameters: particle size distribution, initial moisture content, specific gravity, Atterberg's limit, porosity, and permeability. The shales studied were composed of quartz, clay minerals (illite, kaolinite, chlorite, smectite), feldspars (k-feldspar and plagioclase), pyrite, and amorphous. Microtextural characteristics were mainly studied through petrography and scanning electron microscopy (SEM). The samples were described based on the following features: fabric, grain size, matrix and composition, fossils content, and porosity.

It was found that shale properties such as amount and types of clay, moisture content, porosity, permeability, and the presence of reactive iron oxyhydroxides

(pyrite) have significant control over its durability. Natural slake tests were carried out to investigate shale behaviour and changes to its properties under physical and chemical weathering. It was found that the slaking behaviour during weathering was related to the shale plasticity and clay activity. The main chemical processes involved during weathering were the dissolution of clays and pyrite oxidation. The mobile elements show a preferential removal sequence.

The magnitude of element leaching was escalated by the acidic condition developed during pyrite oxidation. The Fe (II) was further oxidised into Fe (III). However, it was found that for shale containing carbonate such as calcite, pyrite oxidation was halted due to the buffering condition. As a result, gypsum and Fe (III) oxyhydroxides were precipitated. It is with the hope that the findings will contribute to understanding the weathering mechanisms and shale behaviour in this region. The transitional nature from rock to the soil-like may give insights to future research on the remediation methods for preventing erosion. However, more research needs to be done for a successful and cost-effective remedial approach.

Acknowledgements

Table of Contents

List of Figures

List of Tables

Chapter 1: Introduction

1.1. Background

Shale is a type of fine-grained sedimentary rock that is extensively exposed throughout the world. It is composed of mostly compacted silt and clay-sized mineral particles. The main field characteristic that distinguished it from other fine-grained sedimentary rock is its lamination and fissility. Shale is one of the most common rocks encountered in engineering projects and is frequently found interbedded with other rock units.

A common problem experienced with shale during and after the construction of civil engineering works is its rapid degradation in response to environmental changes. These changes may occur as a result of physical weathering, chemical weathering, or both simultaneously. Problems may arise even when shale constituent is only a minor part of the geological formation. This is because, as it weathered, it breakdowns into fine-grained 'soil-like' materials that in turn modifies its deformability, strength, and permeability (Gemici, 2001; Marques et al., 2005).

However, not all shales are weathered equally. Some are highly susceptible to weathering, in which they slake almost immediately when exposed to air and water while others are very little affected (Wood, 1984; Bell, 2005). The ease at which a rock weathers or its resistance to weathering process is called durability. In geotechnical investigations, the time factor considered in the assessment of shale durability is in the engineering time scale. The term 'engineering time scale' referred to the period of degradation of this material ranging from few years to a few decades and is used to differentiate the weathering process on geological scale (Miscevic, 2001).

1.2. Problem Statement and Research Gap

One of the major challenges faced in the study of shale weathering is the under or overestimation in predicting its durability. This is mostly due to the limitations of the current laboratory methods in measuring the durability value. Hence, most recent studies are focussing on modifications to the durability tests (Bell, 1978; Taylor, 1988; Gokceoglu et al., 2000; Erguler et al., 2009; Nandi et al., 2009a; Bryson et al., 2012; Gautam et al., 2013; Heidari et al., 2015; Heidari et al., 2018a; Revia Oktaviani et al., 2018; Liu et al., 2020; Selen et al., 2020). Efforts have also been made by various researchers to investigate the factors affecting durability. These include mineralogy, clay content, moisture content, fabric and texture, fissility, microfabric, cementing agents, carbonate content, and chemical composition. However, due to the wide range of shale intrinsic properties, conclusive correlations remained debatable.

The mechanisms of weathering are often studied separately. In many instances, the physical weathering of shale is usually associated with its slaking behaviour and reduction in strength (Nesbitt et al., 1984; Alonso et al., 2006; Alatas et al., 2015; Berisavljevic et al., 2018; Shen et al., 2020). On the other hand, the chemical weathering of shale is typically studied through mineralogy changes to model soil and rock weathering profile (Chigira, 1990; Jin et al., 2013; Lerouge et al., 2018; Gu et al., 2020). Limited research has been done in studying the changes in the shale properties that influence its durability during these weathering processes. Weathering is typically accelerated by temperature variation over the year and/or by the considerable amount of rain. Therefore, the behaviour of shales in the tropical regions like Malaysia may differ from shales in other regions. Hence, there is still a gap in understanding the nature of rocks in the study area, and their rate and weathering process due to short-term weathering.

Countries that have similar climate conditions with Malaysia include Indonesia, Brunei, Vietnam, Brazil, and some part of Australia. It has also been reported in the literature that Indonesia often experienced landslides that are associated with clay shale. The incidents caused catastrophe to their infrastructures

such as buildings, highways, and power plants (Alatas et al., 2015; Putera Agung et al., 2017; Revia Oktaviani et al., 2018). However, it should be noted that other parameters may also contribute to the geotechnical issues such as rainfall intensity, overburden, bedding thickness and slope angle.

Some of the previous studies carried out in this region discussed the geological profile of the formations (Kessler et al., 2015), regional tectonic events and unconformities (Kessler et al., 2017), sediment provenance, paleo-weathering, and depositional and tectonic setting based on geochemistry and mineralogy studies (Nagarajan et al., 2014; Nagarajan et al., 2015; R. Nagarajan et al., 2017; Ramasamy Nagarajan et al., 2017b). There are no published papers particularly discussing the laboratory and natural setting investigation on shale properties subjected to physical and chemical weathering. Hence, there is a gap in the literature for shale durability assessment in the Northern Sarawak and the study of changes in its properties relative to the present tropical climate weathering.

1.3. Objectives

The aim of this study is to extend the evaluation of shale weathering and its durability through integral and quantitative analysis of shale intrinsic properties during the natural short-term weathering process. The objectives of the research are outlined below:

(i)   To identify shales of highest and lowest durability in the Northern Sarawak,

(ii) To determine the physical, mineralogical, and chemical composition of shale through physical test, optical microscopy, XRD, XRF, ICP methods, SEM and EDS – spot analysis,

(iii) To investigate a relationship between durability against short-term weathering in relation to their physical properties, mineralogy, and chemical composition, and

(iv) To establish which properties would be useful in differentiating a high and low durability shale.

1.4. Significance

The increase in the demand for engineering and construction projects in the study area leads to exposure of the rock slopes through excavation and road cuttings. The recently constructed Pan Borneo Highway along the Sarawak region has been reporting several issues of landslides and road damages that are associated with shales and clay-bearing rocks. Depending on the durability and weathering grades of these weak materials, stabilisation works are required to protect the area from further erosion and degradation. In light of the issues, the option to produce low-cost engineering and bio-engineering techniques becomes more favourable as mitigation measures. Therefore, the mechanism and behaviour of the rock units towards weathering should be fully understood.

The knowledge of durability assessment and subsequent controlling parameters will be useful in understanding slope failure mechanism, evaluation of rock materials, and identifying problematic shales. Moreover, chemical analysis that leads to shale disintegration during short-term weathering would provide an understanding of its chemical composition and structure. This in turn would contribute to the development of chemical additives that could potentially stabilise, strengthen and/or minimise its weathering effects. Significant geotechnical failures and safety hazards could then be averted.

1.5. Climate and Geology of the Study Area

The tropical climate in the area such as in Northern Sarawak has a high annual rainfall of 2,750 mm for Miri (*World Weather & Climate Information*, 2021) and between 3,300 and 4,600 mm for the Sarawak region as a whole (*Sarawak Government*, 2021). The temperature is consistent throughout the year with a daily average between 23 °C and 32 °C. The relative humidity ranges from 80 and 90 %. The wet season is during Northeast Monsoon from November to December. Meanwhile the dry season is during Southwest Monsoon from August to September (Rahman et al., 2019). The most-reported rainfall is 20 days per month and the least rainfall is 10 days per month

(*World Weather Online*, 2021). This condition typically promotes slope failures, erosion, and landslides, especially in clay-bearing rocks such as shale and mudstone that are sensitive to water content variations.

The geological formations of Northern Sarawak comprise of sedimentary rocks deposited during Neogene and Recent ages (Alluvium). The shale units for this study considered as from Miri Formation, Tukau Formation, Lambir Formation, Sibuti Formation and Setap Shale Formation with their age range from Oligocene to Pliocene. The upper part of the study area is littoral to inner shelf deposits of Lambir/Miri Formation and unconformably overlain by coastal plain deposits of the Tukau Formation (Hutchison, 2005). Meanwhile, the bottom part overlies the Sibuti Member of the Setap Shale Formation with a notable unconformity (Kessler et al., 2019). The Late Miocene-Pliocene tectonic compression in this area resulted in numerous folds, such as the Riam-Buri anticline, the Liku-Badas syncline, and the Miri-Rasau anticline (Hutchison, 2005).

The Miri Formation is divided into Upper Miri and Lower Miri units based on their lithology. The Upper Miri Formation consists of an alternation of sandstone and shales while the Lower Miri consists of interbedded sandstones and mudstones. The Tukau Formation consists of sandstone, shale and alternate layers of shale and sandstone with minor conglomerates. The lithology of the Setap Shale Formation consists of thick and extensive shale with thin sandstone beds and lenses of limestone. The Sibuti Formation is a member of the Setap Shale Formation and is distinguishable by its higher fossil content, marl lenses and thin limestone beds (Peng et al., 1997). The Sibuti Formation consists of shale, locally calcareous with thin lenses of limestone and sandstone (Hutchison, 2005).
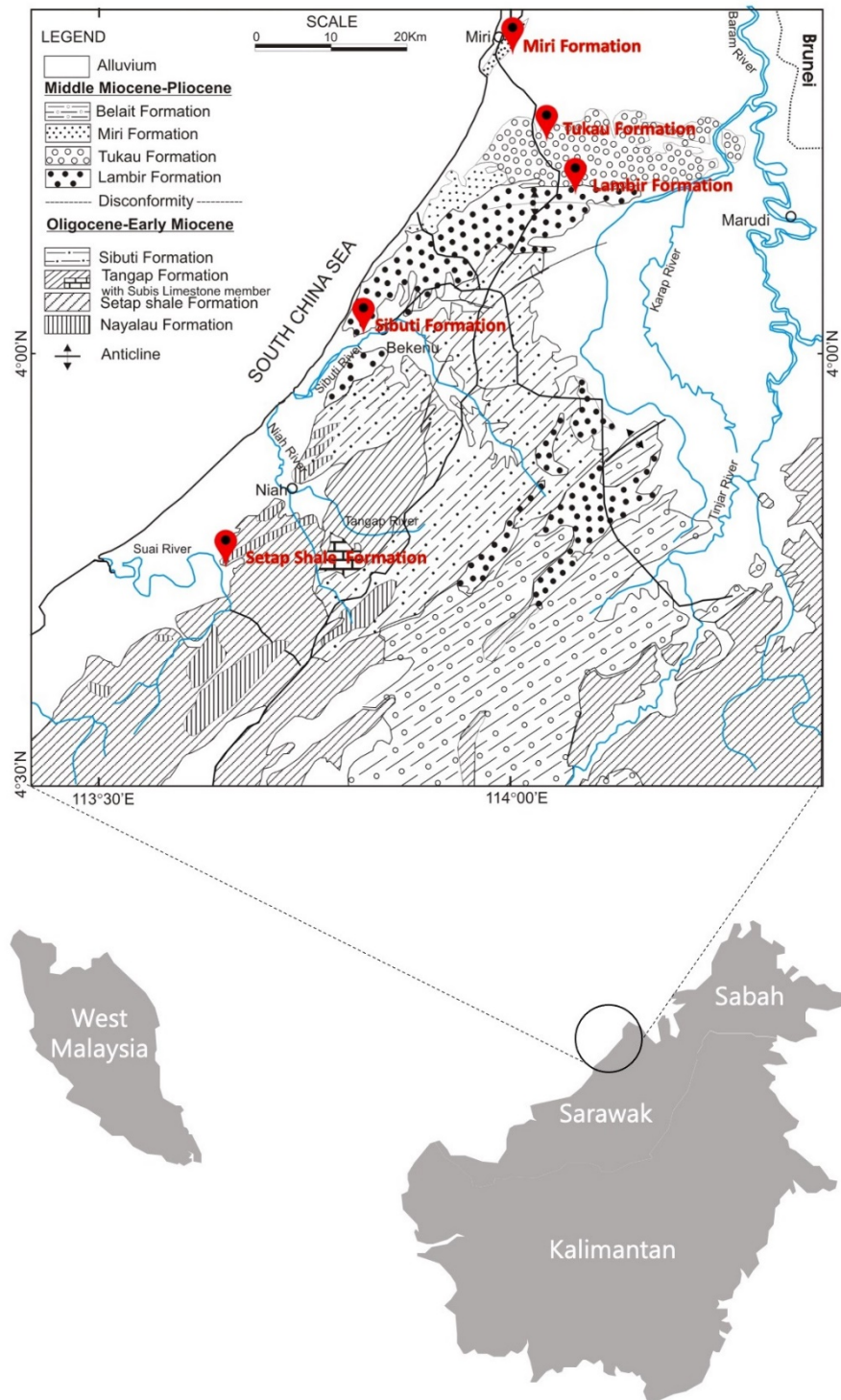
Figure 1.1: Geological map of Northern Sarawak (modified after (Ramasamy Nagarajan et al., 2017b))

1.6. Thesis Structure

Chapter 1 introduces the background of the topic, a review of the problem statement, and the knowledge gap. It also highlights the aims and significance of the research, and an overview of the study area. Chapter 2 reviews literature covering the background study of shales, weathering process and slaking behaviour, geological and geotechnical characteristic of shales, and how these properties affect their durability. A detailed methodology adopted in achieving the results for this study is outlined in Chapter 3. Chapter 4 discusses the physical properties and durability assessment of the studied shales. Bulk mineralogy, geochemistry, microtextural analysis, and the relation of these properties in contributing to durability are presented in Chapter 5. Chapter 6 presents the results of natural slake test and short-term weathering mechanisms occurred during the testing period. Lastly, Chapter 7 draws the conclusion and suggestions for possible future studies.

Chapter 2: Literature Review

2.1. Introduction

This chapter introduces an overview of the research where the background and previous findings are outlined. The chapter begins with a definition of shale and its classifications in both geological and engineering fields. Next, this chapter explains the process of weathering, the mechanisms, and how tropical climate such as in Malaysia affect the disintegration of the rocks. This is to better understand how weathering leads to the durability aspect of the rock as a geotechnical parameter. Then, durability tests and durability classifications are discussed. Finally, the extent of the rock properties contributing to durability is assessed.

2.2. Shale: Nomenclature, Characteristics, and Classifications

Shales, claystone, mudstones, and siltstones are generally classified as fine to very fine-grained siliciclastic sedimentary rocks. These rocks occupy approximately two-thirds of the stratigraphic column and one-third of the Earth's land surface area (Potter et al., 1980; Blatt, 1983; Franklin et al., 1983). Siliciclastic rocks refer to rocks composed predominantly of silica-bearing clasts such as quartz and other silicate minerals, including clay minerals. Shale is commonly interbedded and lacks well-developed sedimentary structures. Thus, making it lagged in the study as compared to sandstones, carbonates, coal, and sedimentary iron formation (i.e., Fe-concretions).

2.2.1. Nomenclature

Geologists often use various terminologies in addition to shales for the fine-grained siliciclastic rocks such as claystone, mudstone, and siltstone. On the other hand, geotechnical experts would typically refer to this material as shale, soft rock, weak rock, and argillaceous material while petroleum engineers would call them shale. The

reasons behind this are that geologists usually study the rock under thin sections and classified them by emphasising the grain size and/or chemical composition. However, geotechnical engineers often work at the ground surface or shallow depth constructions such as buildings, dams and tunnels where weathering features are obvious and significant. In the petroleum industry, shales are important as source rock, reservoir and seal rock because of their organic carbon content, low porosity and permeability, and impermeable nature. The rock is encountered at different depths from shallow to deep. Although the effect of natural weathering may not exist, its relatively weak strength and obvious discontinuities may be observed (Farrokhrouz et al., 2013).

Shales are fine-grained sedimentary rocks composed of compacted silt and clay, and typically show fissile lamination. The term shale was first explicitly established by John Farey in 1811 and Lyell in 1833 to describe any fine-grained rocks or laminated clayey rocks (Tourtelot, 1960). However, the dual usage of this term has not been critically accepted by most researchers such as Lundegard et al. (1980), Spears (1980), and Stow et al. (1984). Hence, the term shale has been continually redefined over the years. Potter et al. (2005) acknowledged the term mudstone as a group name for fine-grained sedimentary rocks as favoured by these researchers and restricted the usage of shale to rocks with a fissile characteristic.

Most clays are formed as the products of chemical weathering that occurred on igneous and metamorphic rocks. Meanwhile, most silts are formed due to mechanical abrasion between hard particles during the transportation of the sediments. These particles are deposited as aggregates in flocculated form (Jeremias et al., 2020). As sedimentation continues, the older and more buried sediments become more compacted and lithified, contributing to diagenesis. The fissility developed during compaction due to the orientation and alignment of the particles into parallel layers.

2.2.2. Characteristic of Shale

Shale is often soft enough to be scratched by a knife on the field and is commonly known to have very low porosity and permeability. Their colours may vary from black, grey, brown, or even red depending mainly on the carbon content and oxidation state of their iron minerals (Potter et al., 1980). Their depositional conditions are also contributing to the colouration. However, since the colour may change due to diagenesis, it is not a reliable indicator for depositional environments.

The main minerals constituents of shales are clay minerals, silt-sized quartz, fine size micas and feldspar (Boggs, 2009). Other minor minerals may include carbonates, iron oxides, heavy minerals, sulfates, and sulfides. The mean grained size is typically less than 0.0625 mm depending on the respective clay and silt content, and the lamination thickness is less than 10 mm (Farrokhrouz et al., 2013). They are a lot of other aspects and properties of shale contributing to its comprehensive study. Figure 2.1 shows a typical approach to the study of shales from various perspectives. However, due to the scope and length of the current research, only durability aspects relative to weathering are covered in this thesis. This includes slaking behaviour during weathering, durability parameters, texture, geochemistry, mineralogy, physical characteristics, and fossil content.

Figure 2.1: Typical approach contributing to the study of shale (modified after Potter et al. (1980))

2.2.3. Classifications

In this study, ideas expressed in geological and engineering classification of shales based on perusal literature reviews are narrowed down into (i) grain size and texture; (ii) chemical composition; and (iii) plasticity.

2.2.3.1. Grain size and texture

Wentworth (1922) established the first classification of shale based on grain size, to distinguish argillaceous material from the rest of the sedimentary rocks. He placed the upper limit of clay particles at 4 µm. Ingram (1953) further modified the classification by dividing the clayey materials into silt and clay. According to Grim et al. (1957), for the shale to develop fissility, the silt particle size should be more than 5 µm. Meanwhile, Tanner (1969) reviewed the particle size scale and found clay size of 2 µm corresponded closely to mineralogical changes. Shale is commonly classified based on its relative abundance of clay and silt, and occasionally sand-size particles

after this classification. This includes the standard group names of clayey shale, silty shale, and sandy shale.

The usage of the term clay in this study refers to both the texture and mineralogical definition. The upper boundaries of the clay particle size are classified slightly different in terms of grain size distribution scale and remained controversial depending on the state of practice in the studied area. Texturally, clay is any material finer than 2 μm (Atterberg, 1905; Tanner, 1969; BS, 1990), 4 μm (Wentworth, 1922), or 5 μm (Grim et al., 1957; ASTM, 2006). Meanwhile, the boundaries for silt are 2 – 63 μm and 5 – 75 μm for BS and ASTM respectively (Figure 2.2). The size of these fine particles is determined through sedimentation analysis (also known as hydrometer) by applying Stoke's law to calculate the settling velocity of the suspension in water. This sedimentation analysis together with the standard sieving method to determine particle size distribution based on ASTM is further described in Chapter 3.

Other classifications based on clay-size and silt-size particles are proposed by Trefethen (1950) (Figure 2.3) and Picard (1971) (Figure 2.4). Their trilinear plots raised a more detailed nomenclature for rocks and sediments aiming to provide a greater understanding of fine-grained clastic rocks, in particular, relative to transportation, deposition, and diagenesis process.
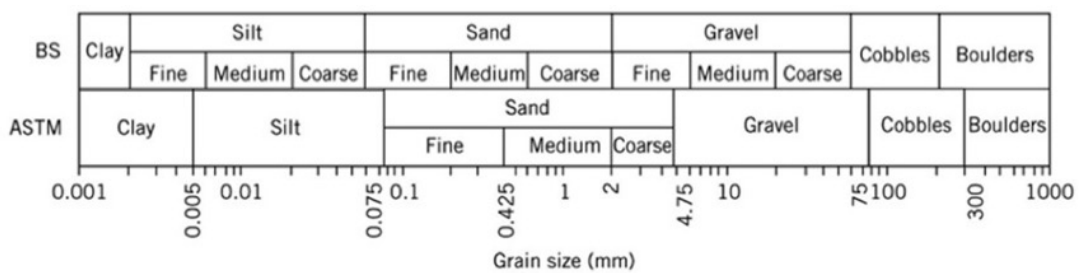
Figure 2.2: Particle size scale (in mm) used in British Standard (BS) and American Standard Test Method (ASTM)
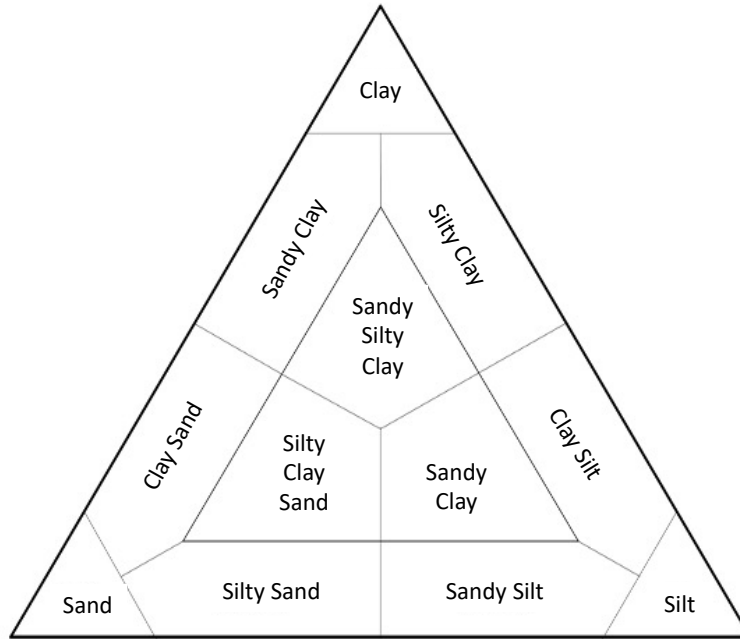
Figure 2.3: Sediment nomenclature plot (Trefethen, 1950)
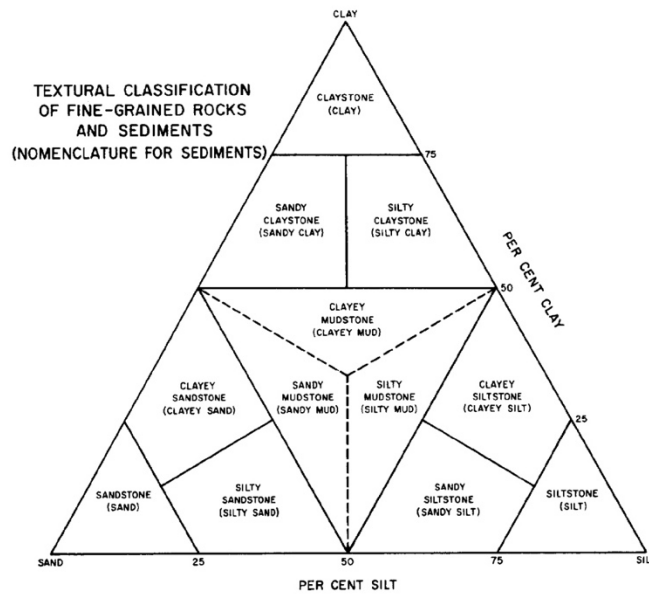
Figure 2.4: Fine-grained rocks and sediments nomenclature plot (Picard, 1971)

2.2.3.2. Chemical Composition

Since the process of quantifying particle sizes of fine-grained rocks can be quite challenging, classifications based on chemical composition are introduced. The geochemical classification of terrigenous sedimentary rocks based on the major element composition proposed by Pettijohn et al. (1972); Crook et al. (1974); Blatt

(1980); Herron (1988) are widely being used in the geological studies. Pettijohn et al. (1972) suggested a classification for terrigenous sands based on a plot of log (Na_2O/K_2O) versus log (SiO_2/Al_2O_3), based on the indices of SiO_2/Al_2O_3 and Na_2O/K_2O ratios. Herron (1988) proposed Geochemical Logging Tool (GLT^2) logs (Figure 2.5) by modifying the diagram of Pettijohn et al. (1972). The log of SiO_2/Al_2O_3 is remained on the x-axis but the y-axis is replaced by the log of Fe_2O_3/K_2O. The Fe_2O_3/K_2O ratio aids in the classification of arkoses and is a measure of mineral stability. This classification is one of the most widely used geochemical classifications.

The basis of this classification is based on the concentrations of major oxides (silica, aluminium, iron, and potassium) relative to mechanical and chemical changes at low temperature and pressure during burial diagenesis. The SiO_2/Al_2O_3 ratio provides an indicator of mineral maturity. The enrichment of SiO_2 over Al_2O_3 allows distinction of mineral maturity from low ratio shales to high ratio sandstones and clay-rich, and quartz arenites (Pettijohn, 1975; Herron, 1988). Meanwhile, the ratio of total iron (Fe_2O_3/K_2O) provides an indicator of mineral stability. Less stable minerals are located close to the sediment source. Stable minerals such as K-feldspar, muscovite mica, and quartz has high potassium and low iron content (Herron, 1988).
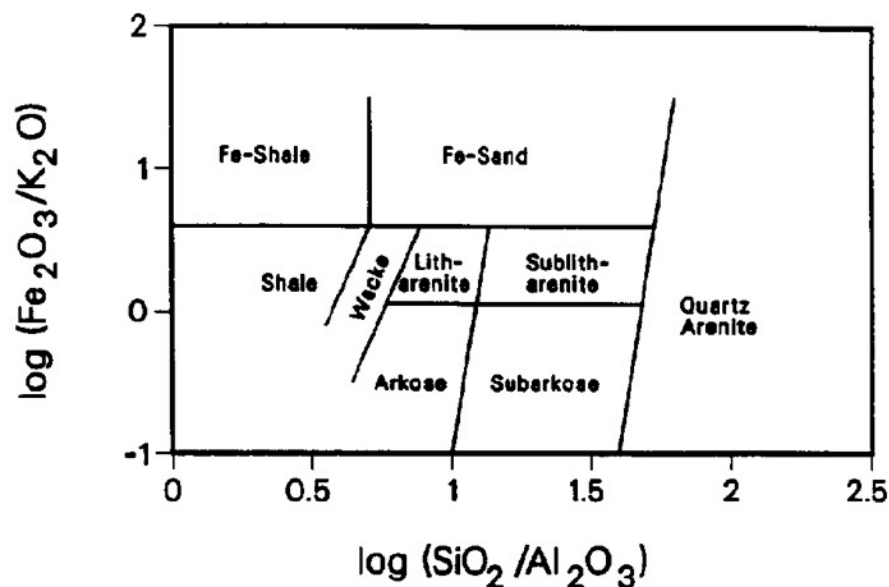
Figure 2.5: Geochemical classification of clastic sedimentary rocks (Herron, 1988)

2.3. Weathering

Weathering of rock has a long history in continent alteration since the Archean era, long before life appeared. The geologist would typically study the weathering of most terrains from the parent rocks to the large volume of ground. In this setting, weathering occurs gradually in the span of geological times. However, weathering of extremely small volumes of ground materials could happen in a very short period, which could lead to major engineering problems (Hack, 2020). Hence, in this study, the time factor used is based on the engineering time scale, ranging from a few years to a few decades.

Weathering is defined as all physical or chemical changes in a rock as a result of its interaction with the environment. Both may coexist and have complementary effects in natural conditions where changes in moisture content and temperature are significant. Such alteration affects the rock's deformability, strength, and permeability (Marques et al., 2005). Physical weathering leads to in-situ fracturing and fragment of shales into smaller pieces. On the contrary, chemical weathering results in chemical changes to its geochemistry and mineralogy. Because physical disintegration occurs faster than chemical decomposition, physical weathering is considered as the more dominant process (Taylor et al., 1987).

2.3.1. Physical Weathering

Taylor et al. (1986) defined physical weathering as any process that contributes to in situ fracturing of the rock without chemical changes. Some important causes of physical weathering include wetting and drying, thermal stress, frost action, pressure release, hydraulic action, presence of sedimentary structures and discontinuities. In tropical climates (warm and humid) such as Malaysia, wetting and drying is the foremost process that leads to shale degradation.

2.3.2. Chemical Weathering

Chemical weathering is caused by water and air interaction with the minerals. The reactions result in chemical decomposition, minerals dissolution, and new mineral formation. Since these reactions occur rapidly under high temperatures, chemical weathering is more significant in the tropical climate. Some important mechanisms of chemical weathering are dissolution, oxidation, hydrolysis, hydration, and ion exchange. The majority of minerals expected in shales are comparatively stable in normal surface conditions, with the exception of reactive iron sulfides such as pyrite, marcasite, and pyrrhotite. In this study, the occurrence of the following process will be the focus: (i) oxidation of sulfides; (ii) dissolution of calcite cement; and (iii) hydration of clay minerals (Taylor et al., 1970, 1981; Taylor et al., 1987; Taylor, 1988; Franklin et al., 1989).

A recent study by Li et al. (2019) described the geochemical characteristic and weathering behaviour of black shale. It was found through hydrochemistry and mineralogy analyses that pyrite oxidised into secondary minerals such as copiapite and rozenite and released acid water. This acidity condition promotes further dissolution of carbonate minerals and may cause damage to the rock structure. The same chemical reaction was observed by Liao et al. (2019) through their 7 days field and indoor semi-immersion experiment of black shales (Figure 2.6). They concluded that water-rock interaction under different conditions influences the oxidation of pyrite.

$$2Fe_2S_2(pyrite) + 7O_2 + 2H_2O \rightarrow 2FeSO_4(ferrous\ sulfate) + 2H_2SO_4(sulfuric\ acid)\ 2.1$$

$$FeSO_4 + 4H_2O \rightarrow FeSO_4.4H_2O(rozenite) \qquad 2.2$$

$$FeSO_4 + 7H_2O \rightarrow FeSO_4.7H_2O(melanterite) \qquad 2.3$$

$$Fe^{2+} + 4Fe^{3+} + 6SO_4^{2-} + 22H_2O \rightarrow Fe^{2+}Fe_4^{3+}.(SO_4)_6(OH)_2.20H_2O(copiapite) + 2H^+ 2.4$$
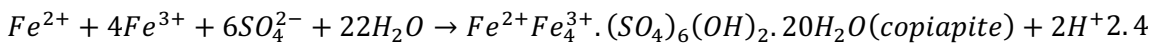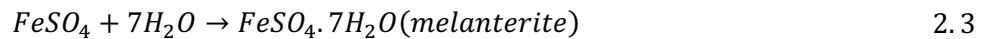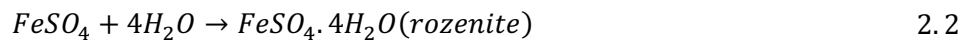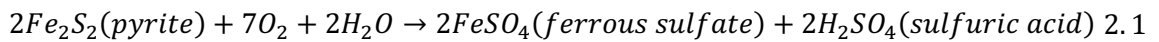
Gupta et al. (2007) in their study of the effect of pH water and mineralogy on rock durability found that rocks containing calcite and dolomite are highly susceptible to slaking at lower pH. Calcite is a soft mineral and converts to calcium bicarbonate,

Ca(HCO₃)₂ when in contact with a mildly acidic solution (Nandi et al., 2009b). Calcium bicarbonate promotes slaking as it is soluble and volumetrically larger. The presence of calcite together with sulphuric acid released from pyrite oxidation will produce gypsum, which is prone to swelling and degradation.

$$CaCO3_3(calcite) + CO_2 + H_2O \rightarrow Ca(HCO_3)_2(calcium\ bicarbonate) \qquad 2.5$$

$$2Fe_2S_2(pyrite) + 7O_2 + 2H_2O \rightarrow 2FeSO_4(ferrous\ sulfate) + 2H_2SO_4(sulfuric\ acid)\ 2.6$$

$$CaCO_3(calcite) + H_2SO_4 + 2H_2O \rightarrow CaSO_4 \cdot 2H_2O(gypsum) + CO_2 + H_2O \qquad 2.7$$
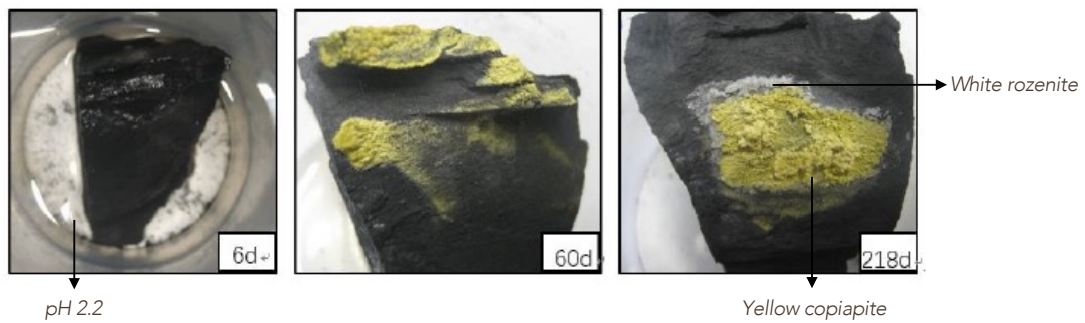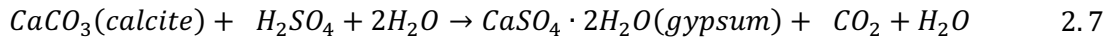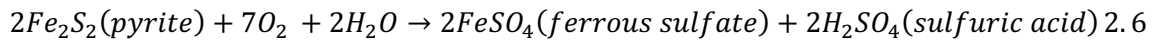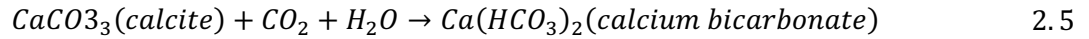
Figure 2.6: Semi-immersion experiment of black shale. No significant changes were observed after 6 days. On the 60th day, yellow copiapite formed on the surface. White rozenite gradually formed as an outer ring surrounding copiapite as observed on the 218th day (Liao et al., 2019).

2.4. Slaking Behaviour and Durability of Shale

Shales disintegrate or slake into fine-grained 'soil-like' materials as a result of weathering. However, not all shales weather equally. Some are extremely susceptible to weathering, slaking nearly instant when exposed to air, while others are little affected (Wood, 1984; Bell, 2005). This slaking behaviour is evaluated as the durability of the rock and is a vital engineering parameter in the geotechnical field.

2.4.1. Slaking

The main mechanism that induced slaking in shales where they are exposed to air and water is pore-air compression (Moriwaki, 1974; Vallejo et al., 1993; Vallejo et al.,

2001; Marques et al., 2005). The pore is assumed to resemble a small tube inside the shale. The air is trapped in the pores when water penetrated the rock by capillary suction during hydration (Moriwaki, 1974). Since the gas cannot escape during capillary imbibition, it pushes ahead and compresses. Due to the very low permeability of shale, the pore air pressure is high enough to produce significant stress on the rock fabric (Marques et al., 2005).

According to Schmitt et al. (1994) and Marques et al. (2005) the air entrapment and pressurised of pore-air may occur in three processes: (i) connected pore networks, (ii) roughness of macropores, and (iii) capillary condensation within pore throats (Figure 2.7). Air entrapment due to the configuration of the connected pore network has been studied by Bellanger et al. (1993) and Schmitt et al. (1994). The air is trapped into the macropore when a large pore is short circuit by a smaller one. In addition, when the surface of the macropore is very rough due to the clay minerals arrangement, air can be isolated by the action of extensive capillary condensation (Schmitt et al., 1994; Vallejo et al., 2001). Capillary condensation first occurs in the smallest intergranular spaces, entrapping the originally filled pore-air inside the macropores. Air is pushed between the capillary meniscus as the hydration continues. Means et al. (1963) modelled the interaction of air and water in the macropore and concluded that the smaller the diameter of the macropore, the larger the pore-air pressure. Therefore, slaking is more pronounced in shales containing a small diameter of macropores.
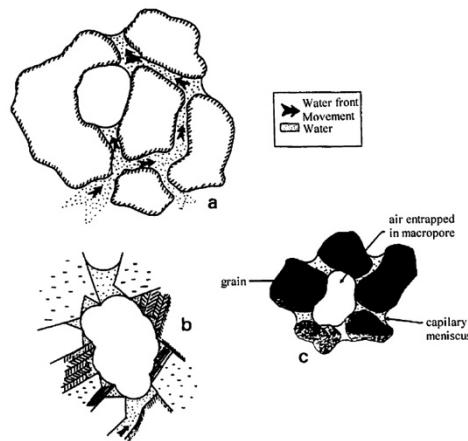
Figure 2.7: Air entrapment (a) by short circuit of macropore (b) in a rough macropore (c) by condensation of water in pore accesses (Schmitt et al., 1994; Marques et al., 2005)

Perry et al. (1982) reported that there are two modes of slaking in mudrocks. The first one is the degradation of the rock into flat fragments with a thickness of 0.6 to 2.0 mm and length and width from 25 to 150 mm. The second mode is the further breakdown into inherent fine-grained particles that leads to complete disintegration. Shen et al. (2020) elaborated more on the approach and divided it into three stages: (i) crack propagation, (ii) crack coalescence, and (iii) complete disintegration (Figure 2.8). During crack propagation, clay minerals are repeatedly swelled and shrank due to the thermal-hydro stress of water and heat. In crack coalescence, more swelling and shrinking occurs as the cracks form and grow in the weak parts. Complete disintegration occurs when the clay minerals are eroded and transported by water.
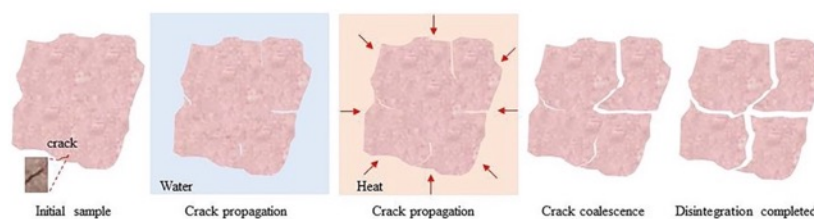
Figure 2.8: Disintegration process of mudstone fragments proposed by Shen et al. (2020)

2.4.2. Durability Test and Classifications

The resistance of rock to weathering process is called durability. The British coal mining industry initiated the first durability research in the 1950s in response to

difficulties with a high wall and mine roof failure (Taylor, 1988). Since then, several studies and methods have been developed to classify shale durability. The three common test methods are (i) jar slake test, (ii) slake index test, and (iii) slake durability test. Slake Durability Test (SDT) developed by Franklin et al. (1972) is the most widely used to describe the disintegration potential of rocks relative to climatic wetting and drying. The method has been recommended by the International Society for Rock Mechanics, (ISRM, 1981, 2007) and standardised by the American Society for Testing and Materials (ASTM, 2016).

From the use of SDT results, standard classifications recommended by Gamble (1971), Franklin et al. (1972), and Dick et al. (1994) are based on the value of slake durability index (Table 2.1). Slake durability index is defined as the proportion of dry-weight rock remaining in the drum after one or two disintegration cycles (I_{d1}, I_{d2}). Franklin et al. (1972) proposed the slake durability classification based on the values of I_d from the first cycle. Gamble (1971) further improved the classification based on the values of I_d from the second cycle and plasticity index to give a greater differentiation in behaviour. Dick et al. (1992) determined the durability of 51 mudrock samples collected for their study that consisted of 10 claystones, 18 mudstones, 6 mudshales, 6 siltshales, 5 siltstones, and 6 argillites. They classified the durability of the rocks from I_d of the second cycle with the respective lithology type.

Czerewko et al. (2012) evaluated and reviewed various tests that have been used to predict slaking potential in weak rocks and highlighted the limitations of SDT. Several researchers have proposed various modifications to address these weaknesses such as increasing the number of disintegration cycles (Bell, 1978; Taylor, 1988; Gokceoglu et al., 2000; Nandi et al., 2009a; Nandi et al., 2009b) , modification on the drum apparatus (Heidari et al., 2015), and suggestion for new indices: Disintegration Ratio, D_R (Erguler et al., 2009; Gautam et al., 2013), Loss Slake Index, LSI (Bryson et al., 2012), and Decay Index, DI (Heidari et al., 2018a).

However, the current laboratory methods do not fully reflect the slaking potential of shales relative to real ground surface exposure in engineering projects.

Gautam et al. (2013) developed a natural slake test to assess the durability of clay-bearing rocks under actual climatic conditions.

Table 2.1: Durability classifications by Gamble (1971), Franklin et al. (1972), and Dick et al. (1994)

Group Name	Gamble (1971)		Franklin & Chandra (1972)
	I_{d1} (%)	I_{d2} (%)	I_d (%)
Extremely High	-	-	95-100
Very High Durability	>99	>98	90-95
High Durability	98-99	95-98	75-90
Medium High Durability	95-98	85-95	-
Medium Durability	85-95	60-85	50-75
Low Durability	60-85	30-60	25-50
Very Low Durability	<60	<30	0-25

Dick et al. (1992)			
Lithology Class	I_{d2} (%)	Mean (%)	Standard Deviation (%)
Claystone	1-50	16.9	16.7
Mudstone	3-93	54.3	30.6
Shale	36-99	76.9	20.2
Siltstone	25-79	49.2	22.7
Argillite	99-100	99.2	0.41
Siltstone-siltshale	25-97	718	26.9

I_d=Slake durability index; I_{d1}: after the first cycle; I_{d2}: after the second cycle
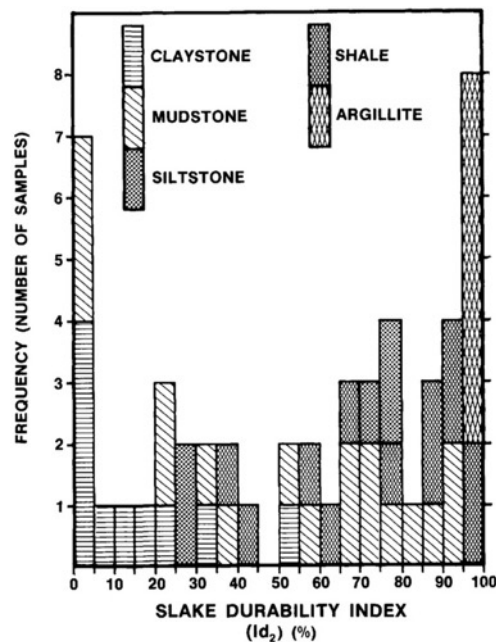
Figure 2.9: Slake durability frequency histogram of all the mudrock types used in Dick et al. (1992) Durability Classification

2.5. Factors affecting Durability

According to previous studies, clay-bearing rocks like shales break down to varying degrees depending on their properties. These include mineralogy, clay content, moisture content, fabric and texture, fissility, microfabric, cementing agents, carbonate content, and chemical composition (Taylor et al., 1970; Russell, 1982; Dick et al., 1992; Dick et al., 1994; Yagiz, 2001; Lashkaripour et al., 2002; Sadisun et al., 2004; Sadisun et al., 2005; Nandi et al., 2009a; Nandi et al., 2009b; Jin et al., 2010; Bryson et al., 2012; Gautam et al., 2013; Koralegedara et al., 2017; Heidari et al., 2018a; Ling et al., 2018; Li et al., 2019; Liao et al., 2019). These are discussed one by one, here below.

2.5.1. Mineralogy

Shale is composed of at least more than 50% of siliciclastic debris such as clay minerals, quartz, and feldspar and some non-detrital minerals such as carbonates, iron oxides, pyrite, and organic matter (Jeremias, 2000). There is, however, limited study reporting bulk mineralogy of shales due to the difficulty in generalising their composition. This is because the composition may vary due to several factors such as the variation in grain size, degree of cementation and compaction, tectonic setting and/or depositional environment (Blatt et al., 1981; Bhatia, 1985; O'Brien et al., 1990; Boggs, 2009). For example, coarse-grained shales have higher quartz content while fine-grained shales have higher clay minerals content. Marine shales deposited near the shoreline have higher quartz content compared to deep marine shales.

On average, the relative abundance of the minerals are: (i) clay minerals (17 – 57 %), (ii) quartz (15 – 54 %), and (iii) feldspar (<1 – 15 %) (Boggs, 2009). Secondary minerals such as calcite, dolomite, and pyrite are relatively low in most shales. Table 2.2 summarises the range and average mineral composition of argillaceous rocks reported by O'Brien et al. (1990). It is noted however in their study that the distribution and depositional environments of the rocks are not uniform. Several rocks from one geological period may come from a single formation or related

formations. General trends of K-feldspar decreases with age are observed (Figure 2.10) (O'Brien et al., 1990). Apart from that, illite-smectite and kaolinite decrease with age while illite and chlorite increase with age.
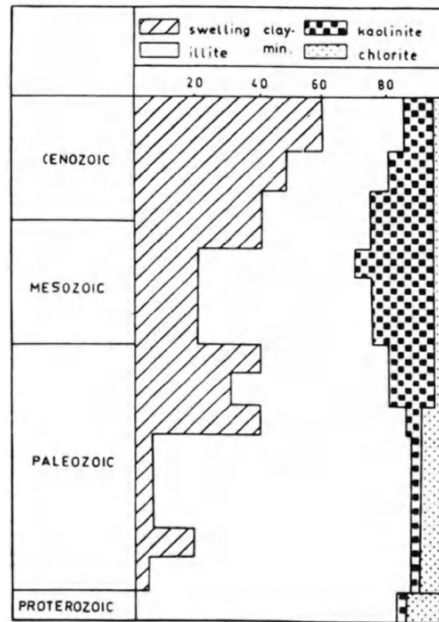
Figure 2.10: Summary of key clay minerals in argillaceous rock's composition as a function of age (O'Brien et al., 1990)

Table 2.2: The average mineralogical composition (in %) of shales of different geological ages (O'Brien et al., 1990)

	Age	Number of analyses	Clay minerals	Quartz	Potassium feldspar	Plagioclase feldspar	Calcite	Dolomite	Siderite	Pyrite	Other minerals	Organic carbon
Youngest	Quaternary	5	29.9	42.3	12.4	-	6.6	2.4	-	5.6	-	0.9
	Pliocene	4	56.5	14.6	5.7	11.9	3.2	-	2.9	1.8	<1	2.6
	Miocene	9	25.3	34.1	7.4	11.7	14.6	1.2	-	1.9	2.4	1.4
	Oligocene	4	33.7	53.5	3.0	-	5.5	-	-	-	4.0	0.4
	Eocene	11	40.2	34.6	2.0	8.1	3.8	4.6	1.7	1.6	-	3.5
	Cretaceous	9	27.4	52.9	3.6	1.6	2.9	7.9	0.1	1.6	-	2.0
	Jurassic	10	34.7	21.9	0.6	4.4	14.6	1.6	0.4	10.9	-	10.9
	Triassic	9	29.4	45.9	10.7	0.7	3.7	4.1	5.1	-	-	0.3
	Permian	1	17.0	28.0	4.0	8.0	-	1.0	-	-	42.0	0.2
	Pennsylvanian	7	48.9	32.6	0.8	6.2	1.4	2.1	3.4	3.5	-	1.0
	Mississippian	3	57.2	29.1	0.4	2.9	-	-	0.6	5.1	-	4.7
Oldest	Devonian	22	41.8	47.1	0.6	-	2.0	1.3	0.3	3.3	-	3.7
	Ordovician	2	44.9	32.2	<1	6.3	9.8	0.5	0.5	3.4	-	1.5
	Misc. ages	29	47.8	33.1	<1	5.5	5.2	2.3	0.8	3.1	-	4.5
	Ranges		17.0 - 57.2	14.6 - 53.5	0.4 - 12.4	0.7 - 11.9	1.4 - 14.6	0.5 - 7.9	0.1 - 5.1	1.6 - 10.9	2.4 - 42.0	0.2 - 10.9
	Average		38.2	35.9	4.3	6.1	6.1	2.6	1.6	3.8	16.1	2.7

2.5.1.1. Clay minerals

Clay minerals are hydrous aluminosilicates. Some common examples are kaolinite, smectite, illite, chlorite, and vermiculite. These minerals are derived mainly from the weathering of the parent rock and soil formation.

Kaolinite forms under strongly leaching conditions such as abundant rainfall, good drainage and acid waters (Potter et al., 1980; Boggs, 2009). It is the product of alumino-silicate minerals alteration such as plagioclase and muscovite (Farrokhrouz et al., 2013). Smectite is hydrated, expandable clay that alters to illite during burial. Illite is a non-expandable clay and is the most abundant clay mineral in shales. The product of illite diagenesis is muscovite. Chlorite is very sensitive to weathering and

forms diagenetically with burial. It is generally more abundant in Paleozoic and older shales. Vermiculite typically converts into corrensite and finally into chlorite during diagenesis (Potter et al., 1980; Boggs, 2009). Jin et al. (2010) and Ling et al. (2018) reported a potential sequence of clay minerals weathering in black shales under acidic conditions wherein the parent minerals illite and chlorite weather to vermiculite, hydroxy-interlayered vermiculite (HIV), smectite, kaolinite and gibbsite.

$$Mica/Illite {\nearrow M-S \,/\, I-S\ mixed-layer\ mineral \searrow \atop \searrow M-V\,/\,I-V \rightarrow chlorite\ (V,HIV) \qquad \nearrow} Smectite \rightarrow Kaolinite \rightarrow Gibbsite$$
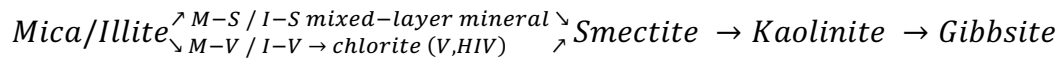
2.5.1.2. Quartz

Quartz is a silicate mineral with the chemical formula of SiO_2. It is commonly existing in angular silt-sized particles in shales and it is the main constituent of many detrital rocks due to its high resistance to chemical weathering (Potter et al., 1980).

2.5.1.3. Feldspar

Feldspar is generally found in less quantity compared to quartz in sedimentary rocks, as feldspars are of igneous origin and significantly less resistant to weathering than quartz. There are two types of common feldspars: (i) K/Alkali feldspar and (ii) plagioclase feldspar. Feldspar compositional end members are K-feldspar ($KAlSi_3O_8$), albite ($NaAlSi_3O_8$) and anorthite ($CaAl_2Si_2O_8$) (Figure 2.11). Alkali feldspars range from orthoclase, microcline to albite while plagioclase feldspars range from albite to anorthite (A Solid Solution Series). There are no feldspars between K and Ca due to the differences in ionic size and charges (Young, 1983).

Goldich (1938), proposed the chemical weathering stability series (Figure 2.12) based on the mineralogical changes in granitoid rocks during weathering. He concluded that the composition of sedimentary rocks depends on the mineralogy of the parent rock. Minerals like quartz and muscovite weathered less and are more stable. Igneous minerals that are high in magnesium and iron weather quickly to form

clays. Therefore, in sedimentary rocks, less resistant minerals (olivine, Ca-rich plagioclase feldspar) will be less common, and quartz and clay minerals are more abundant. According to the series, the increasing order of feldspars stability is anorthite < bytownite < labradorite < andesine < oligoclase < albite < K-feldspars. Microcline is more stable than orthoclase in the K-feldspar group due to the difference in the volume occupied by the O-atoms in mineral structure (Huang et al., 2005).
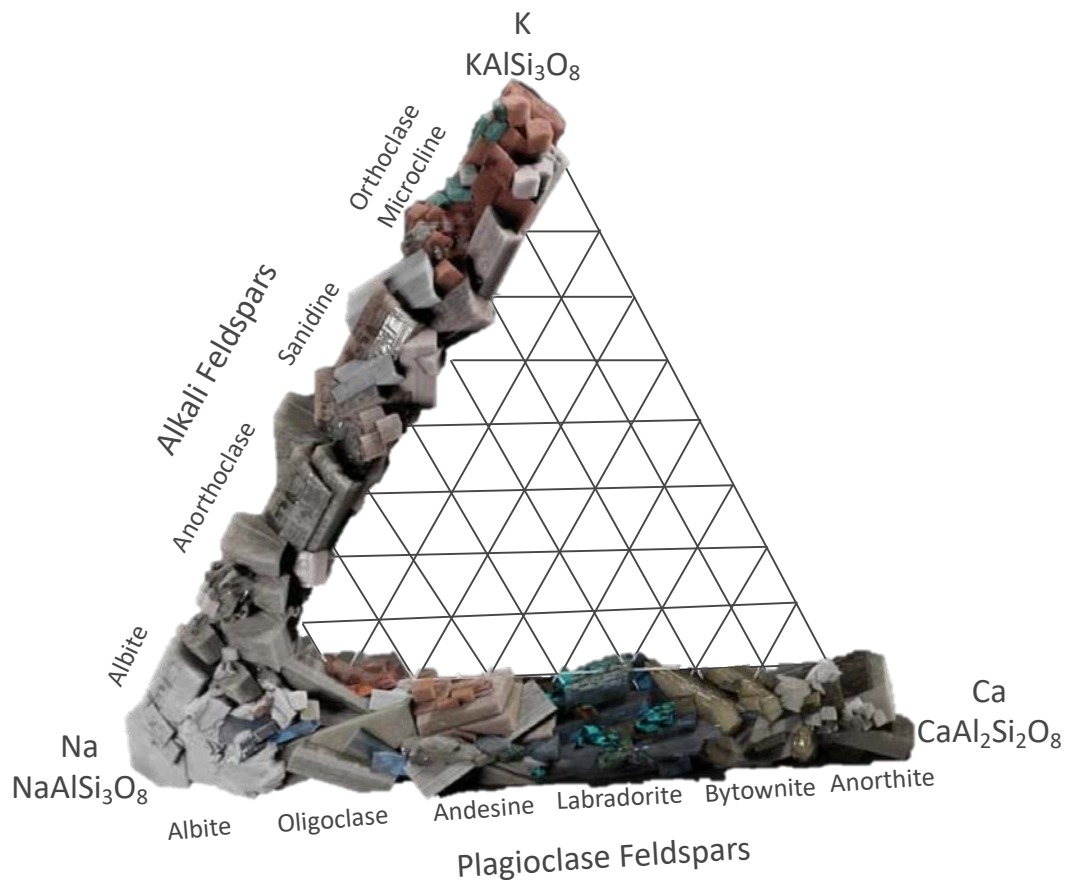
Figure 2.11: Feldspar classification, based on chemical composition. Adapted from (Jakaitė, 2019)
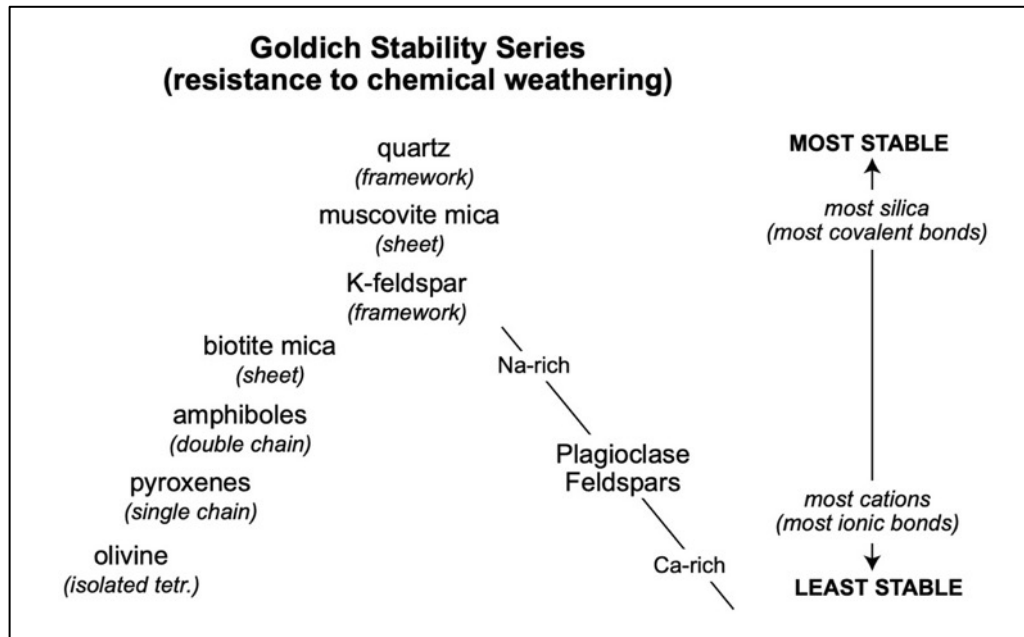
Figure 2.12: Sequence of minerals stability in chemical weathering according to Goldich Stability Series (Goldich, 1938)

2.5.1.4. Secondary minerals

Other secondary minerals that constituent in shale composition are carbonates (calcite, dolomite, and siderite), iron oxides and hydroxides (hematite and geothite), and sulfur minerals (pyrite and marcasite). Carbonates typically occur as cementing minerals, inorganic precipitation of microcrystals through the rock, or concentration in nodules formed during the diagenetic process (Tucker, 1994). Iron oxides and hydroxides exist as pigmentation agents and provide coatings on clay minerals. Sulfides such as pyrite and marcasite are the most abundant in marine shales and an indicator of reducing conditions during deposition or diagenesis (Potter et al., 1980; Boggs, 2009).

2.5.1.5. Mineralogy and durability

Rocks with expandable smectite and weak minerals like pyrite are known to be less durable (Taylor et al., 1970; Sadisun et al., 2005). Pyrite has been known to be the culprit for foundation heave, concrete degradation, environmental damage, acid drainage, accelerated rock weathering, and loss of strength and stability of

geomaterials (Soga et al., 2005). Materials containing as little as 0.1 % pyritic sulfur have been associated with sulfide-induced heave (Belgeri et al., 1998). The increase in size and diameter of the pores caused by the oxidation and dissolution of these minerals promotes rock cracking (Sadisun et al., 2005; Liao et al., 2019). Soluble calcareous minerals like calcite and siderite also influence rock durability (Taylor et al., 1970; Russell, 1982; Gupta et al., 2007; Nandi et al., 2009b; Sadisun et al., 2010). Russell (1982) suggested that the amount of calcite in shales and the presence of hard bands that are usually richer in calcite have significant control over slake durability. Slake durability value decreases for shale with higher calcite content.

The presence of more stable minerals such as quartz and orthoclase increased the durability of shale, but the presence of montmorillonite, gypsum, and calcite decrease the durability (Nandi et al., 2009a). The log of the total quantity of expandable minerals such as montmorillonite and illite-smectite has a significant linear relationship with slake durability (Dick et al., 1992). Bryson et al. (2012) found that quartz is abundant in harder and more durable shale. However, they also found that soft and medium-hard shales with low durability have a similar quantity of quartz. The correlation between durability and quartz content is therefore not clear.

2.5.2. Clay Content

The usage of clay in this research refers to both textural and mineralogical definition. In texture context, Gupta et al. (2007) observed that fine-grained rocks have higher slake potential in comparison to coarse-grained rocks. Shale with higher clay content has higher water absorption and adsorption values (Gokceoglu et al., 2000; Gautam et al., 2013). These values increase when the number of microcracks and porosity increases. Hence, the inter-granular bond between the particles weakens and promotes slaking. Durability in clay-bearing rocks also depends on the type of clays and their percentage (Yagiz, 2001; Heidari et al., 2018b). Since shales are composed of different types of clay minerals, their silicate structures carried ranges of hydroaffinity degree and volume changes. Hence, when exposed to wetting and

drying cycles, the clay swells during the rainy season and shrinks during the dry season (Tse, 2016).

2.5.2.1. Texture

The Texture of a rock refers to the size, shape, and arrangement of the grains. The size of clay particles for the purpose of this study is stipulated as finer than 0.005 mm based on the ASTM particle size scale. Kuenen (1959, 1960) in his study found that during sediment transport, very small quartz particles of less than 0.1 mm do not become rounded. The shape of clay- and silt-size particles are unaffected by transport abrasion and reflect the original shapes of the detrital particles or minerals during diagenesis. It is reckoned that very fine particles are very angular and have very low sphericity. Sudo et al. (1978) in their investigation of clay minerals' shape under electron microscopy revealed that most clay minerals have platy, flaky or acicular shapes. In practice, clay-size particles can include tectosilicates (quartz and feldspar), phyllosilicates (kaolinite, smectite, Illite, etc.) and small portions of oxide-hydroxide minerals (hematite, manganese oxides, or zeolites) (Farrokhrouz et al., 2013).

2.5.2.2. Clay minerals

Clay minerals make up the most fraction of siliciclastic grains in most mudstones and shales. They are silicate minerals known as phyllosilicates, characterised by SiO_4^{4-} ionic charge. Figure 2.13 displays the classification of silicate minerals. There are many derivations of the phyllosilicates group but for the purpose of this study, the focus will only be given to the common clay minerals. Among the minerals, illite, chlorite, and kaolinite are non-expanding clays while montmorillonite and smectite are expandable clays. Because of these properties, the amount and type of clay minerals in shale are expected to have a pronounced effect on its durability.
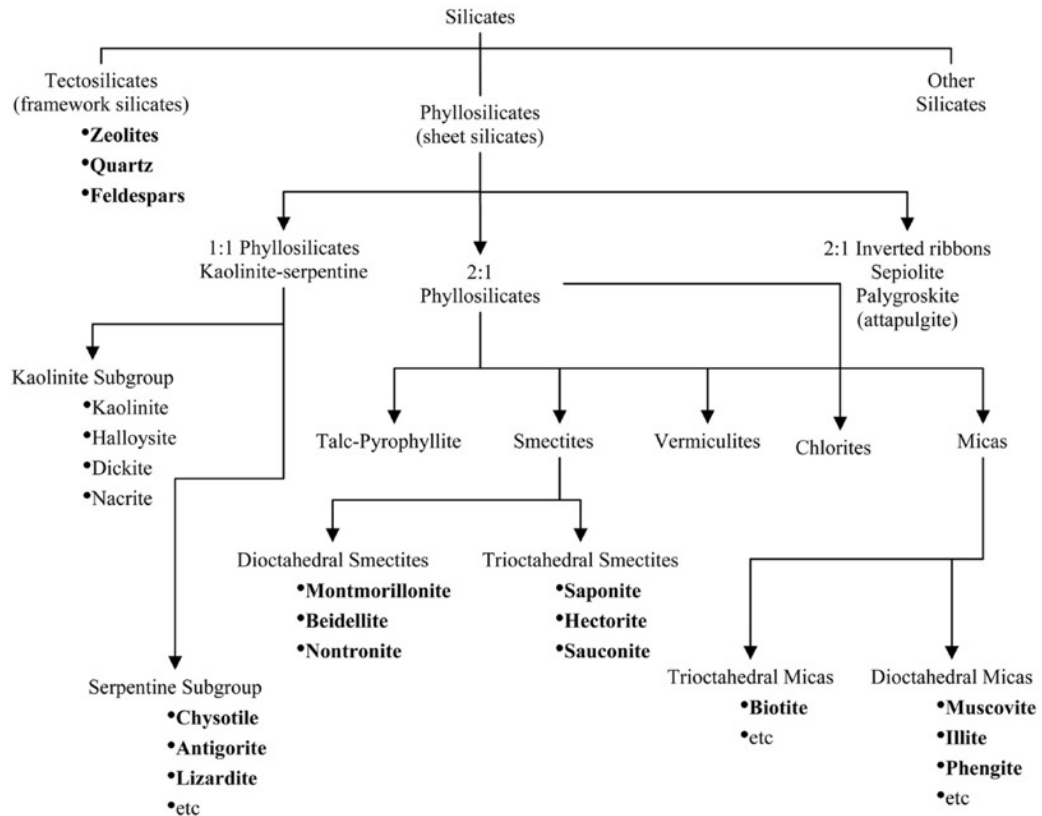
Figure 2.13: The classification of silicates. Common minerals are in bold. (Bailey, 1980; Rieder et al., 1999)

2.5.2.3. Cation Exchange Capacity

Figure 2.14 shows the sheet-like structure of clay minerals for kaolinite, illite, smectite, and chlorite. The structure is composed of a tetrahedral layer of silica (Si_2O_6), an octahedral layer of alumina ($Al_2(OH)_6$), and/or interlayer cation fixation (Czerewko et al., 2012). 1:1 mineral such as kaolinite, does not have any heterovalent and has relatively low homovalent substitutions ($Al^{3+} \Leftrightarrow F^{e3+}$ or $Mg^{2+} \Leftrightarrow Fe^{2+}$) (Velde et al., 2008). In 2:1 minerals such as illite, smectite and chlorite, the charging layer is encompassed by two tetrahedral sheets enclosing one octahedral sheet. Substitution of Al^{4+} or Fe^{3+} for Si in the silica tetrahedral layer or Mg^{2+}, K^+, or Fe^{2+} for Al in the alumina octahedral layer raised the permanent charge to the mineral (Brinkman, 1985). The exchangeable cations that neutralising the permanent charge are electrostatically bound to the clay surface and correlate to the Cation Exchange Capacity of the mineral. Due to the very small size of clay particles, the surface area

per unit volume is large, which subsequently promotes a large number of cations adsorption (Czerewko et al., 2012).

Table 2.3 presents the Cation Exchange Capacity of the common clay minerals. Expandable smectite and vermiculite have a high capacity to change volume by absorbing water molecules in their hydrated state (H_2O) or other polar ions (Ca^{2+}, Na^+) in their structure. During wetting, smectite swells as water is adsorbed and during drying, it shrinks or decreases in volume as the water is removed (Potter et al., 2005).
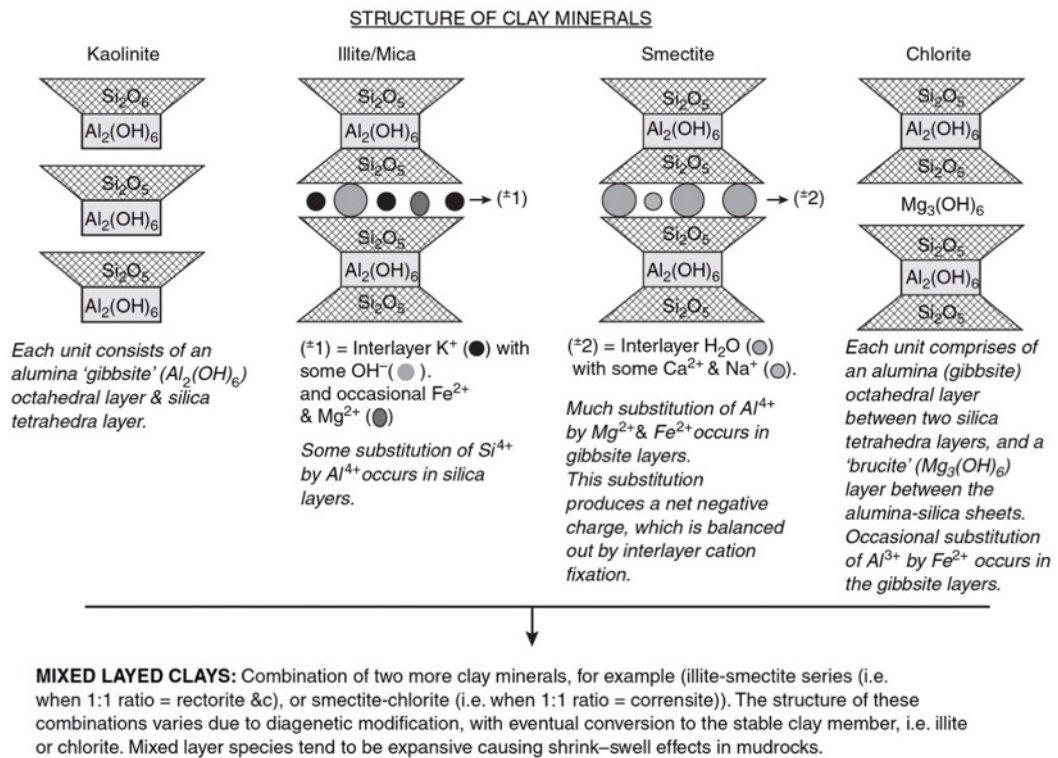
Figure 2.14: Sheet like structure of clay minerals (Czerewko et al., 2012)

Table 2.3: The CEC values of common clay minerals at pH = 7 and the at room temperature of 25°C (Velde et al., 2008)

Mineral	Cation Exchange Capacity (CEC), cmol kg^{-1}
Kaolinite	5 – 15
Illite	25 – 40
Vermiculite	100 – 150

Mineral	Cation Exchange Capacity (CEC), cmol kg^{-1}
Montmorillonite/Smectite	80 – 120
Chlorite	5 – 15

2.5.3. Fabric and Microfabric

Rock fabric is defined as the geometric arrangement of the particles, particle groups, and pore spaces (Edil, 1988). Olphen (1964) introduced the following terms in describing clay suspension particles in fabric features: (i) dispersed: No face-to-face association of clay particles, (ii) aggregated: Face-to-face association of several clay particles, (iii) flocculated: Edge-to-edge or edge-to-face association of aggregates, and (iv) deflocculated: No association between aggregates. Figure 2.15 illustrates the usage of the terminology in the fabric of clay particle suspensions.

Orientation of the clay particle is the directional parameter of the fabric analysis. It represents the angular relationship (oriented or random) between the linear and planar elements (Edil, 1988). Parallel orientation characterised oriented fabric while random fabric implies that the particles do not have a preferred orientation direction but are oriented equally in all directions. Jeremias (2000) provides a descriptive scheme for the microfabric characterisation of mudrocks (Figure 2.16). Other factors that contribute to the initial formation of fabric and its post-depositional alteration include bioturbation, silt and sand-size particles, carbonates, organic matter, and mineralogy changes. Therefore, silty clays are more likely compared to pure clays to have a random fabric (Jeremias, 2000).

Variations in fabric and grain size give rise to a different type of lamination (Lundegard et al., 1980). Fabric lamination is produced by the parallel orientation of clay mineral grains and grain size lamination is due to alternating layers of clay mineral and silt-sized quartz grain material. Koralegedara et al. (2017) found that there is a relationship between fabric and durability. Laminated mudstones with turbostratic fabric showed higher durability and lower moisture content than the non-laminated mudstones with matrix fabric (Table 2.4). Turbostratic fabric refers to

parallel packet fabric of dominant face-to-face contact between the clay flakes. Dick et al. (1992) in their study of durability and shale lithology found that well-laminated shales indicated a high degree of consolidation, which corresponds to a low mean void ratio. Results from their simple regression model showed that there is an inverse relationship between durability and void ratio.
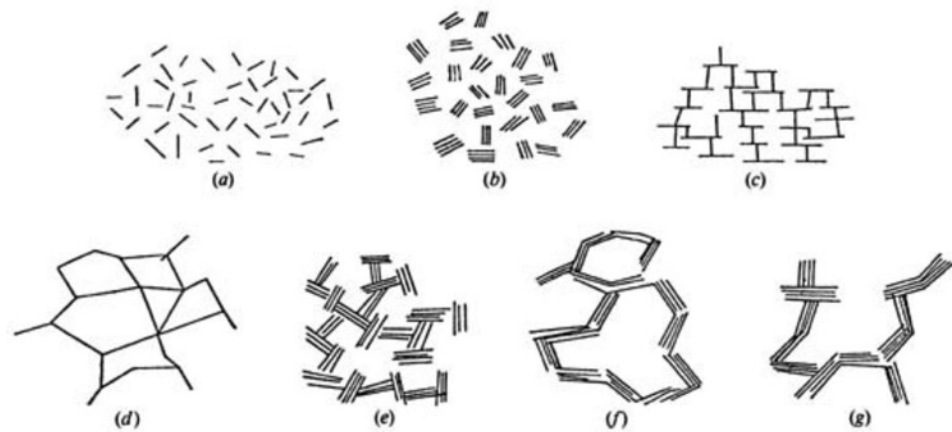
Figure 2.15 (a) Dispersed and deflocculated, (b) aggregated but deflocculated, (c) edge-to-face flocculated but dispersed, (d) edge-to-edge flocculated but dispersed, (e) edge-to-face flocculated and aggregated, (f) edge-to-edge flocculated and aggregated, (g) edge-to-face and edge-to edge flocculated and aggregated (Olphen, 1964; Edil, 1988)
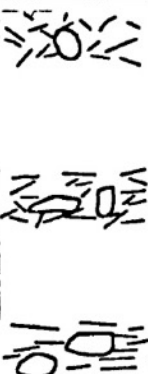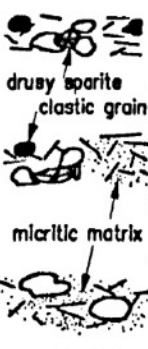
FEATURE	VISUAL DESCRIPTION	
A - Particle orientation	1 - Microlamination absent, the rock constituents have a random orientation. 2 - Microlamination absent, but the platy minerals *e.g.* micas show some preferred orientation. 3 - Well-developed lamination or microlamination.	
B - Grain-to- -grain relations	1 - Predominantly grain-to-grain relations by long or point contacts, and/or by the development of cementation bonds. 2 - Occurrence, both of grain-to-grain contacts (1), and of floating grains (3). 3 - Predominantly floating grains.	
C - Clay fabric	1 - Mostly clay particle arrangements of EE and EF types, loose structure, high porosity. 2 - Clay particle arrangements of EF, FF and low-angle EF types, denser and less porous structure than the former (1). 3 - Predominantly clay particle arrangement of the FF type, very dense structure, low porosity.	
D - Carbonate occurrence mode	1 - Carbonate minerals occur mainly as individual grains greater than 5 μm in diameter, or as sparry cement. 2 - Carbonate minerals occur in both modes described in (1) and (3). 3 - Carbonate minerals essentially occur as a fine-grained micrite matrix.	

Figure 2.16: Description of microtextural features of mudrocks. EE: Edge-to-edge association, EF: Edge-to-face association, FF: Face-to-face association (Jeremias (2000)

Table 2.4: Correlation between rock fabric and slake durability index of mudstones studied by Koralegedara et al. (2017). SEM Images showing the fabric type are shown in Figure 2.17.

Mudstone type	Fabric type	Characteristics observed by scanning electron microscope	Slake durability
Non-laminated (NLMs)	Matrix	Wide angles of edge-face contacts between clay flakes Relatively high void ratio Disturbed and irregular surface area	Low
Laminated (LMs)	Turbostratic	Good face-face contacts between clay flakes Very low void ratio Undisturbed surface area	High
Laminated (LMs)	Laminar	Both edge-face and face-face contacts between clay flakes In some areas, clusters of stacks of clay flakes with face-face contacts are oriented at an angle to the bedding plane making irregular surfaces	Moderate
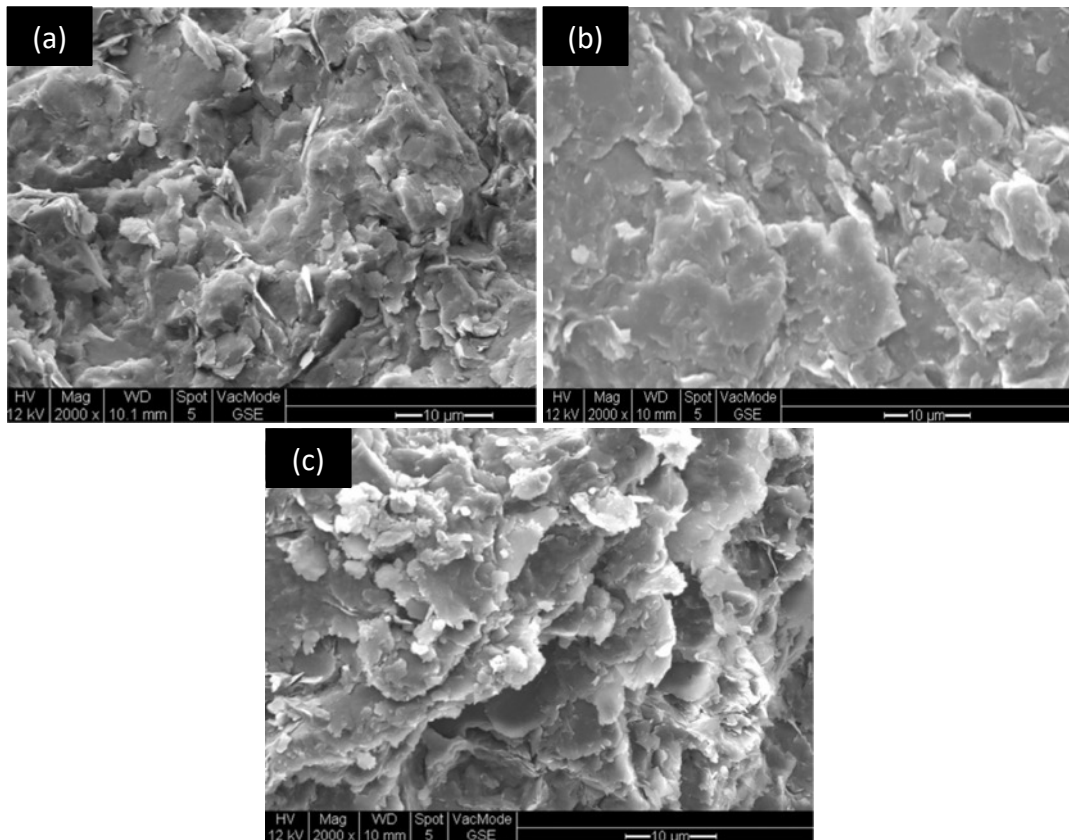
Figure 2.17: Scanning electron microscopic images of: (a) non-laminated mudstones – Matrix type; (b) Laminated mudstones – Turbostratic type; (c) Laminated mudstones – laminar type (Koralegedara et al., 2017)

2.5.4. Fissility

Fissility is defined as the ability of some rocks to easily split into thin layers along closely spaced, generally flat, and roughly parallel surfaces. The lamination and parallel orientation of minerals and organic material is discovered to be related to the shale's fissility (Ingram, 1953; Pettijohn, 1975). Hence, there is a relationship between fabric and fissility. Potter et al. (1980) define fissile as the tendency to split along lamination or bedding (degree of parting) especially due to weathering. The thickness in fissile parting is within 0.5 mm to 1.0 mm, papery parting is thinner than 0.5 mm, and parting is thicker than 1mm and is referred to as platy, flaggy, or slabby (Alling, 1945; McKee et al., 1953; Ingram, 1954; Potter et al., 1980). Parting units increase when the clay and organic contents of shales decrease whereas the sand, silt, and carbonate content increases (Potter et al., 1980).

The degree of fissility is thought to have some correlation to rock durability. The more fissile the rock is the more likely it is to slake. This is because, fissility increases the potential surface area of the rock that is exposed to air and water during weathering. It is also appearing to be related to the volume of permeable void space present in shale, and subsequently, to its percentage of absorption (Shakoor et al., 1987). Highly fissile shales have a smaller permeable void space and lower absorption percentages, while less fissile shales have a larger permeable void space and greater absorption percentages (Marques et al., 2005).

2.5.5. Moisture Content

A rock's moisture content can affect its strength and durability through five processes: reducing fracture energy, decreasing capillary tension, raising pore pressure, reducing particle friction, and chemical and mechanical deterioration (Dìaz-PÈrez et al., 2007; Koralegedara et al., 2017). When humidity is maintained close to the natural moisture content of the rock, its sensitivity to weathering is low (Marques et al., 2005)

Researchers such as ODOT (2011), Marques et al. (2005), Bryson et al. (2011), and Masada T. (2013) suggested that weight and natural moisture content influence durability. Rock unit weight less than 140 pcf (2.2 kgm^{-3}) is commonly associated with low durability. On the other hand, a rock of unit weight greater than 160 pcf (2.66 kgm^{-3}) is commonly associated with high durability (ODOT, 2011, Masada, 2013). (Marques et al., 2005) and Bryson et al. (2011) found that the natural water content is a strong indicator of durability parameter. Harder shale corresponds to low clay fraction and low natural moisture content.

2.5.6. Porosity and Microfractures

Changes in pores relative to their size distribution, geometry, connectivity, infilling, and formation of new pores led to gradual alteration to the rock porosity during weathering (Winslow et al., 1981; Tuğrul et al., 1997; Nicholson, 2001). These characteristics together with mineralogy and texture, control the durability of the rock unit (Hudec, 1998). Porosity and water absorption capacity increase with the function of rock fracturing (Heidari et al., 2018a). However, water absorption capacity is dependent on the pore networks. Microcracks and voids in the rock increase as weathering progresses. This could be due to oxidation and dissolution of the minerals (Sadisun et al., 2005; Liao et al., 2019), the extent of swelling properties of clay minerals (Jeremias, 2000), and characteristic of microfractures (Nandi et al., 2009a). Since disintegration is initiated along fracture planes during weathering, microfractures play a significant role in durability.

2.5.7. Chemical Composition

The chemical composition of shale is a direct function of its mineralogy content. Boggs (2009) summarised the average chemical composition of shales and mudstones taken from various data reported in the literature (Table 2.5). The most abundant oxide is SiO_2, reflecting the silicate mineral content, in particular quartz. Al_2O_3 is particularly related to the abundance of feldspar and clay minerals. K_2O and

MgO constituent is less than 5 % of the average shale. The magnesium is typically supplied by dolomite and potassium is from K-feldspar content. The relative abundance of Na_2O is between 1 and 3 % of average shale. The sodium content is commonly associated with smectite and sodium plagioclase. Fe_2O_3 + FeO constituent in average shales is reported in the range of 5 – 10 % and is correlated to the abundance of iron oxides and sulfide minerals. The abundance of CaO in average shale can be as low as less than 1 % to 10 %. Calcium is derived from calcium-rich plagioclase and carbonates such as calcite and dolomite. Koralegedara et al. (2017) in their study found, there is no significant relationship between the chemical composition of mudstone to its durability.

Table 2.5: The average chemical composition (in Wt.%) of shales (Boggs, 2009).

	1	2	3	4	5	6	7	8	9	10	11	12	13
SiO_2	60.65	64.80	59.75	56.78	67.78	64.09	66.90	63.04	62.13	65.47	64.21	64.10	40–73
Al_2O_3	17.53	16.90	17.79	16.89	16.59	16.65	16.67	18.63	18.11	16.11	17.02	17.70	13–32
Fe_2O_3	7.11	–	–	–	–	–	–	–	–	–	–	2.70	
FeO	–	5.66	5.59	6.56	4.11	6.03	5.87	7.66	7.33	5.85	6.71	4.05	2–20
MgO	2.04	2.86	4.02	4.56	3.38	2.54	2.59	2.60	3.57	2.50	2.70	2.65	<1–6
CaO	0.52	3.63	6.10	8.91	3.91	5.65	0.53	1.31	2.22	4.10	3.44	1.88	<1–6
Na_2O	1.47	1.14	0.72	0.77	0.98	1.27	1.50	1.02	2.68	2.80	1.44	1.91	<0.1–5
K_2O	3.28	3.97	4.82	4.38	2.44	2.73	4.97	4.57	2.92	2.37	3.58	3.60	<1–11
TiO_2	0.97	0.70	0.98	0.92	0.70	0.82	0.78	0.94	0.78	0.49	0.72	0.86	
P_2O_5	0.13	0.13	0.12	0.13	0.10	0.12	0.14	0.10	0.17	–	–	–	
MnO	0.10	0.06		0.08		0.07	0.06	0.12	1.10	0.07	0.05	–	<0.1–0.3

Chapter 3: Methodology

3.1. Introduction

This chapter describes in detail the methods adopted in this research. The research design, instruments, and procedures followed in this study are outlined.

3.2. Research Design

The research was divided into three stages. Stage 1 covered the screening of geological shale formations. In this stage, fieldwork was carried out to survey shale outcrops in the study area, followed by coring activities. A total of five shale samples from five geological formations (Miri, Tukau, Lambir, Sibuti, and Setap Shale) were cored for further analysis. Slake durability tests were carried out to determine the durability of the shale samples. The samples were classified, and shales of highest and lowest durability were identified.

Stage 2 covered the integral analysis of shale. The highest and lowest durable shale obtained from the results of the slake durability test in Stage 2 were selected for further analysis. In this stage, the geomechanical and physical properties, texture, mineralogy, and geochemistry of the selected shales were determined. The slaking behaviour, changes in the rock properties, and its durability during short-term weathering were studied in three phases: (i) Initial phase – before field test, (ii) Middle phase – midst of field test, and (iii) Final phase – post-field test.

The findings from Stage 2 were used to characterise shale durability in Stage 3. The changes in shale intrinsic properties during short-term weathering that might correlate to its durability were evaluated. The parameters in determining the high and low durability of shale were assessed. Figure 3.1 illustrates the flow chart of the research design. Table 3.1 summarises the parameters, test methods and standards adopted in the study.
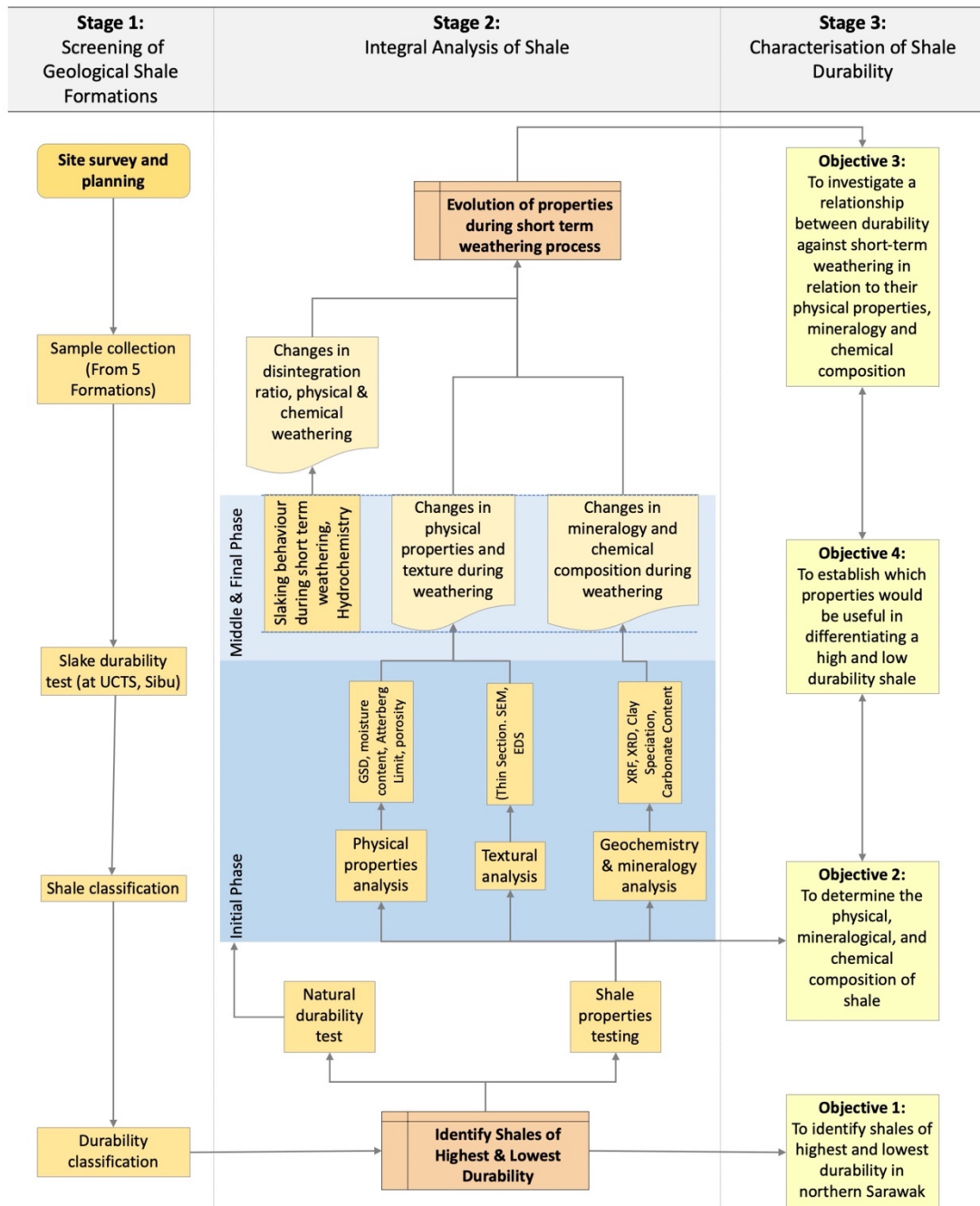
Figure 3.1: Flowchart of the research design

Table 3.1: List of parameters and test methods used in this study

Parameters	Tests	Standards
Particle size distribution	Dry sieve analysis	ASTM C136-19
	Wet sieve analysis	ASTM C117-17
	Hydrometer analysis	ASTM D7928-17
Moisture content	Laboratory determination of rock moisture content by mass	ASTM D2216-19
Specific gravity	Specific Gravity of Soil Solids by Water Pycnometer	ASTM D854-14
Atterberg Limit	Determination of the cone liquid limit of a soil	AS 1289.3.9.1:2015
	Plastic Limit, and Plasticity Index of Soils	ASTM D4318-17
Porosity	Helium porosimeter	
Permeability	Gar permeameter	
Durability index	Slake durability index of shales and other similar rocks	ASTM D4644-16
Microtextural analysis	Thin section studies, SEM, EDS mapping	
Mineralogy	XRD, Clay Speciation	
Geochemistry	XRF	
Hydrochemistry	Water analysis	APHA 3030F, 3120B, 3125B, 4500 2005/2017

3.3. Field Sampling

Shale samples used in this study were taken from varied geological formations around Miri, Sarawak. The formations are Miri, Tukau, Lambir, Sibuti and Setap Shale. Miri, Tukau and Lambir formations formed during the Middle Miocene-Pliocene period. On the other hand, Sibuti and Setap Shale formations formed during the Oligocene-Early Miocene period. The fieldworks were carried out from 17th October to 8th November 2021. The outcrops were chosen based on their lithological description, exposure, and their accessibility. The weathered materials were removed at a distance of at least 0.3 m and measured horizontally from the face of the outcrops by using a geological hammer and a hoe. This distance is typically sufficient to obtain unweathered and fresh samples (Hopkins et al., 1984; Bryson et

al., 2011; Bryson et al., 2012). The weathered surface can be distinguished from the unweathered one based on the heavy discolouration and friable fractures. Field observations such as colour, fissility, strength, lamination, weathering features, and acid test were recorded on the field. Dip and strike measurements of the bedding plane were measured by using Silva Expedition S, Model 15 Compass.

Core samples were obtained using the Shaw portable core drill (Figure 3.2), with a 41 mm outer diameter and length of 0.7 m core barrel. The core samples extracted were within 1 m depth from the surface with an inner core diameter of 36 mm. During sampling, the drill was positioned at 0° to the bedding/lamination (Figure 3.3). The total lengths of the cores collected were 4.0 - 4.5 m per formation. The core samples were wiped out using a dry cloth and thoroughly wrapped with transparent plastic seals to preserve the sample and retain the moisture. In order to prevent mechanical damage to the sample during transportation, bubble wraps and styrofoam were used as cushion materials and the cores were secured in an insulated box (Figure 3.4). The samples were then stored in coring boxes and kept at room temperature (humidity controlled) for future testing.
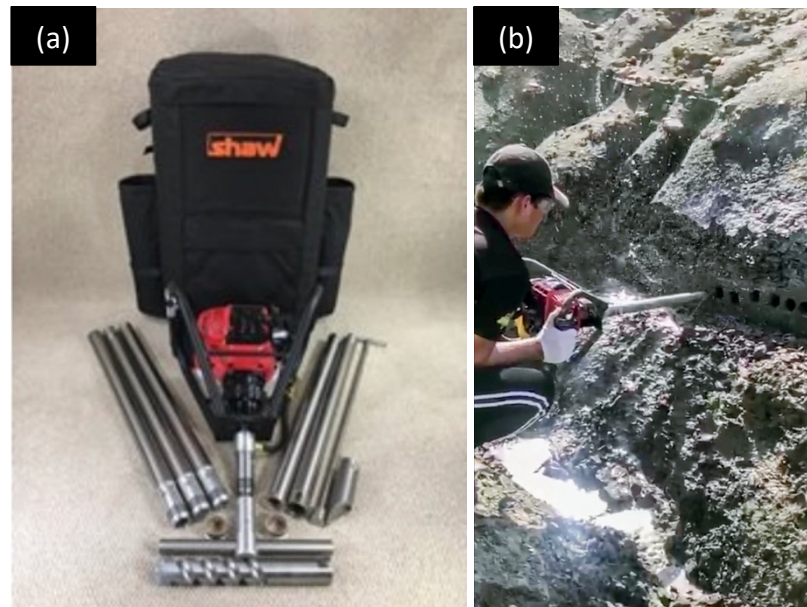
Figure 3.2: (a) Shaw portable core drill assemblages (b) Coring work during sampling
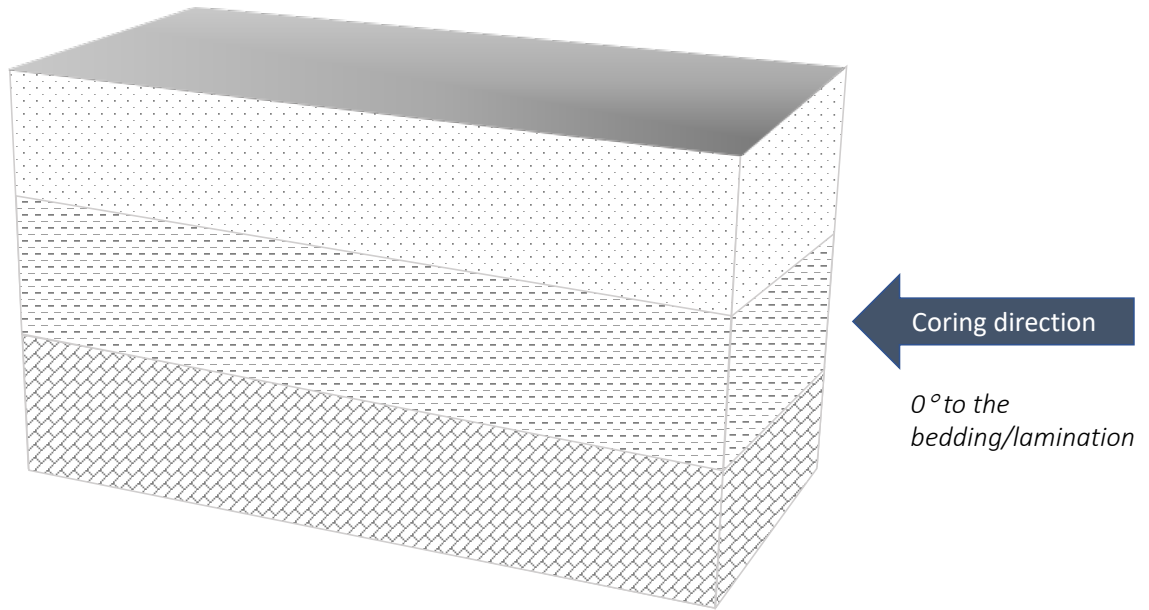
Figure 3.3: Coring direction during sampling, 0° to the bedding/lamination

Figure 3.4: (a) Wrapped core sample in cushioned insulation box; (b, c) Core samples stored in coring boxes

3.4. Particle Size Distribution

Particle size distribution was carried out to determine the size distribution of individual particles, (i.e.) sand, silt, and clay. For distribution of particles larger than 75 µm, Test Method ASTM C136-19 (Dry Sieving Analysis) and ASTM C117-17 (Wet Sieving Analysis) were followed. For distribution of particles finer than 75 µm, Test Method D7928-17 (Hydrometer Analysis) was followed. Data from these test methods were combined to plot the graph of the percentage of materials passing against the diameter of particle size.

3.4.1. Sample Preparation

Prior to sieving, the samples were oven-dried at 110 ± 5°C to a constant mass. This step was crosscut during slake durability procedure. Dried samples used for sieving were from materials passing through and retained in the 2 mm drum during the cycle rotation. Figure 3.5 displays the flowchart of the particle size distribution analysis procedure taken in this study.

Wet sieve by 2 mm sieve drum during slake durability test. Materials retained and passing through the 2mm sieve were oven-dried at 110 ± 5°C to a constant mass.

Dry sieve following ASTM C136-19. Materials passing through 0.075 mm sieve were collected for hydrometer analysis.

Wet sieve following ASTM C117-17 for a thorough separation of particles.

Hydrometer analysis following ASTM D7928-17 for particles finer than 0.075 mm.

Figure 3.5: Flowchart of particle size distribution analysis procedure

3.4.2. Dry Sieve Analysis

The total weight of the materials for each set was determined. The following British Standard (BS) 410-1, ISO 3310-1 sieves and pan were nested in the order of decreasing opening sizes from the top to the bottom: 4.75 mm, 2.36 mm, 1.18 mm, 0.6 mm, 0.425 mm, 0.3 mm, 0.015 mm, 0.075 mm, and pan. Sample materials were loaded on the top sieve and the set was agitated by a mechanical sieve shaker for 20 minutes. This duration is sufficient to allow not more than 1 % by mass of the material retained on any individual sieve passes through. The mass retained on each sieve was determined. Cumulative percentage passing was calculated. The materials retained at the bottom pan were collected for hydrometer analysis. There is a percentage of sediment loss during the process, which ranged between 0.1 % and 3 %.

3.4.3. Wet Sieve Analysis

Wet sieve analysis was carried out to ensure accurate determination of particle size distribution by separating larger particles and finer materials more thoroughly and efficiently. This method was typically carried out before dry sieve analysis. However, to collect the dry mass of materials finer than 75 µm for hydrometer analysis, this test method was instead carried out after dry sieve analysis. Sieved materials of particle size above 75 µm during dry sieving were washed using plain water and agitated with sufficient vigour. The fine suspension was then poured into the stack of sieves, from the top to the bottom: 4.75 mm, 2.36 mm, 1.18 mm, 0.6 mm, 0.425 mm, 0.3 mm, 0.015 mm, 0.075 mm, and a bucket. Meanwhile, the suspended materials were washed, agitated, and decanted as before until the wash water was clear. The washed samples were then flushed into the nested sieves and oven-dried to a constant mass at a temperature of 110 ± 5°C. The mass retained on each individual sieve was determined and cumulative percentage passing was calculated. The total weight loss due to washing was reported as the percentage of material finer than 75 µm.

3.4.4. Hydrometer Analysis

Hydrometer, also known as sedimentation analysis, is a test method to quantify the distribution of particle size finer than 75 μm (silts and clays). Hydrometer results are combined with sieve analysis to produce a complete gradation curve. This test method was adapted from Stokes' Law, where larger particles will fall through faster than smaller particles in a stationary fluid. However, there were a few assumptions applied: (i) particles are spherical and smooth; (ii) no disturbance between the particles and the current within the container; (iii) the flow is laminar; and (iv) the particles have the same density.

A standard glass hydrometer type 152H, as specified in ASTM E100-19 was used and calibrated. Sodium hexametaphosphate was used as a dispersing agent to break apart the aggregates. The first step in the hydrometer analysis procedure is dissolving 5 g of sodium hexametaphosphate, $Na_6[(PO_3)_6]$ in 100 mL of distilled water. The dispersant was then added into 50 g of the sedimentation sample and agitated using a mechanical stirrer until all aggregations were broken up. Next, all the dispersed slurry was transferred fully into the sedimentation cylinder and was topped up with distilled water until the 1000 mL mark. By using the tipping method, a rubber stopper was placed on the top of the cylinder to cover the opening. The cylinder was then vigorously shaken and turned upside down repeatedly for a period of one minute to ensure complete agitation. The timer was started soon as the completion of the last inversions. Hydrometer readings were taken at elapsed times of the following: 0, 1, 2, 5, 8, 15, 30, 60, 120, 180, 240, and 1440 minutes. After taking the hydrometer reading, a thermometer was gently inserted to record the temperature. The thermometer was then removed, and the cylinder was covered to prevent evaporation. Equations 3.1, 3.2, and 3.3 were applied to calculate the correct hydrometer reading, particle size diameter, and mass percentage finer. Finally, the particle size distribution graph of log of particle diameter vs percentage of passing was plotted using the combined results of sieving and hydrometer.

$$Corrected\ Hydrometer\ Reading, r_m = r + c_m + c_t + c_\alpha \qquad 3.1$$

$$Particle\ Size\ Diameter, D(mm) = \sqrt{\frac{30\eta}{G_s - 1}} \sqrt{\frac{L(cm)}{t(\min)}} = \kappa \sqrt{\frac{L(cm)}{t(\min)}} \qquad 3.2$$

$$Mass\ Percentage\ Finer, P = \left(\frac{r_m \alpha}{M_{<0.075mm}}\right)\left(\frac{M_{<0.075mm}}{M_{total}}\right) \qquad 3.3$$

where:

r	=	Hydrometer reading in test cylinder, g/L
c_m	=	Meniscus correction factor, g/L
c_t	=	Temperature correction at 25°C
c_α	=	Dispersing agent correction, g/L
η	=	Coefficient of viscosity
G_s	=	Specific gravity of particles
L	=	Effective depth, cm
t	=	Elapsed time, min
κ	=	Constant
α	=	Correction factor
$M_{<0.0075mm}$	=	Mass of sample less than 0.0075 mm, g
M_{Total}	=	Total mass of the sample, g

3.5. Moisture Content

Laboratory determination of moisture content was carried out according to the standard test method ASTM D2216-19. The method involved oven drying of the samples at 110 ± 5°C until a constant mass is achieved. This step has been followed through during the first oven-drying procedure of slake durability test. The weight loss due to oven drying is considered to be water. Hence, the moisture content can be calculated using the percentage of the mass of water to the dry mass of the samples.

$$w = \frac{M_{cms} - M_{cds}}{M_{cds} - M_c} \times 100 = \frac{M_w}{M_s} \times 100 \qquad\qquad 3.4$$

where:

w	=	Moisture content, %
M_{cms}	=	Mass of container and moist samples, g
M_{cds}	=	Mass of container and oven-dry samples, g
M_c	=	Mass of container, g
M_w	=	Mass of water ($M_w = M_{cms} - M_{cds}$), g
M_s	=	Mass of oven dry samples ($M_s = M_{cds} - M_c$), g

3.6. Specific Gravity

Determination of the specific gravity was carried out in accordance with ASTM D854-14, Method B (Procedure for Oven-Dry Samples). The apparatus used to carry out the test include a 500 ml volumetric flask (water pycnometer), balance, drying oven, thermometer, vacuum pump, and funnel. The test was carried out at Geochemistry Lab, Curtin University Malaysia. The oven-dried test samples were a representative unit of the shale samples, that were grinded by using mortar and pestle and sieved through the 4.75 mm sieve. 50 g samples were prepared for each test set. Prior to testing, calibration was carried out to determine the calibrated volume of the pycnometer and the formula used is shown in Equation 3.5 below. The calibration was carried out by determining the mass of the pycnometer and water at the calibration temperature and the average mass of the dry pycnometer. The calibration test was repeated 5 times to ensure accuracy of less than or equal to 0.02 standard deviation.

$$V_p = \frac{(M_{pw,t} - M_p)}{\rho_{w,t}} \qquad\qquad 3.5$$

where:

$M_{pw,c}$	=	Mass of the pycnometer and water at the calibration temperature, g
M_p	=	Average mass of the dry pycnometer, g
$\rho_{w,t}$	=	Mass density of water at the calibration temperature, g/mL

3.6.1. Test Method

First, the test samples were channelled into the pycnometer using a funnel. Any particles remaining on the funnel were washed using a squirt bottle to avoid wastage. Next, water was added to the pycnometer until the water level was between one-third or half of the height of the pycnometer. The mixture was agitated until a slurry was formed. Any particles adhering to the wall of the pycnometer were rinsed into the slurry. Entrapped air in the slurry was removed using a vacuum pump system for at least 2 hours. Silt and clay particles were ensured to be remained in suspension by agitating the slurry continually in a constant motion during de-airing using an orbital shaker. De-aired water was then added carefully below the surface of the slurry until the calibration mark. To achieve thermal equilibrium, the pycnometer was left in a closed insulated container overnight, along with the thermometer. The mass of the pycnometer, sample, and water was recorded to the nearest 0.01 g. The testing temperature was recorded nearest to the 0.1°C. The slurry was then transferred to a tared pan and oven-dried to a constant mass at 110°C. The dry mass of the sample was recorded to the nearest 0.01 g. The test was repeated twice for each formation with a standard acceptable range of 0.06 between the results.
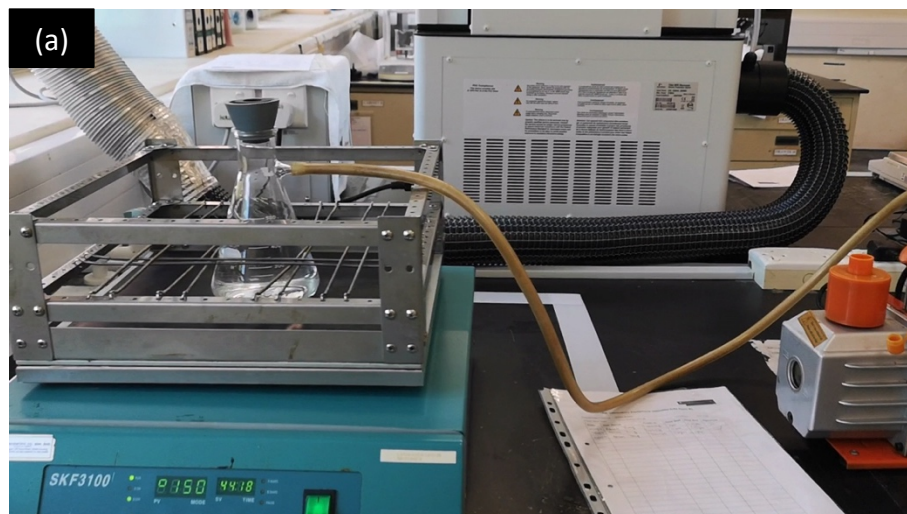
Figure 3.6: (a) Set up of the specific gravity test showing the volumetric flask (water pycnometer connected to vacuum system and agitated in constant motion by using the orbital shaker. (b) Bubbles formed during deairing process to remove entrapped air in the slurry.

3.6.2. Calculation of Specific Gravity

The results were used to calculate the specific gravity of the studied shales. The formulae used in the calculations were as follows:

$$M_{\rho w,t} = M_p + \left(V_p \times \rho_{w,t}\right) \qquad 3.6$$

where:

$M_{pw,t}$ = Mass of the pycnometer and water at the test temperature (T_t), g

M_p = Average calibrated mass of the dry pycnometer, g

V_p = Average calibrated volume of the pycnometer, mL

$\rho_{w,t}$ = Density of water at the test temperature (T_t), g/mL (from Table 3.2)

$$G_t = \frac{\rho_s}{\rho_{w,t}} = \frac{M_s}{\left[M_{\rho w,t} - \left(M_{\rho ws,t} - M_s\right)\right]} \qquad 3.7$$

where:

ρ_s = Density of the sample, g/cm^3

$\rho_{w,t}$ = Density of water at the test temperature (T_t), g/mL (from Table 3.2)

V_p = Average calibrated volume of the pycnometer, mL

$\rho_{w,t}$ = Density of water at the test temperature (T_t), g/mL

$$G_s = K \times G_t; \; where \qquad\qquad 3.8$$

$$K = {\rho_w}/{0.9982063} \qquad\qquad 3.9$$

where:

K = Temperature coefficient (from Table 3.2)

ρ_w = $1.00034038 - (7.77 \times 10^{-6}) \times T_t - (4.95 \times 10^{-6}) \times T^2$

The density of water used in this test method was based on the ASTM density of water and temperature coefficient table, attached in the standard document of ASTM D854-14. Table 3.2 shows the values relevant to this study.

Table 3.2: Density of water and temperature coefficient (K) used in this study (from ASTM D854-14).

Temperature (°C)	Density (g/mL)	Temperature Coefficient, K
24.0	0.99730	0.99909
25.0	0.99705	0.99884

3.7. Atterberg Limit Test

The Atterberg limits include the liquid limit, plastic limit, and the plasticity index of the sample. They were determined from test method procedures outlined in Australia Standard (AS) 1289.3.9.1:2015 (cone penetrometer method) for liquid limit and ASTM D4318 - 17 for plastic limit and plasticity index. The cone penetrometer method was preferred in this study compared to the Casagrande method in ASTM D4318 as it was less operator sensitive and yielded a more reproducible result. Since both test methods required the same sample preparation, the plastic limit test was performed using the material prepared for the liquid limit test. On the other hand, the plasticity index was calculated from the results of plastic and liquid limit tests. All the tests were carried out at the Geomechanics Lab, Curtin University Malaysia.

3.7.1. Sample Preparation

A representative portion from the core sample of each formation was obtained, grinded by using pastel and mortar, and sieved through a 0.425 µm sieve. A total of 250 g samples were prepared.

3.7.2. Liquid Limit

The liquid limit of the shale sample was determined using the standard procedures outlined in the American Standard (AS) 1289.3.9.1:2015 – Determination of the cone liquid limit of soil. 250 g sample passing through a 0.425 µm sieve was prepared. Water was added incrementally into the sample and mixed thoroughly until a consistent homogeneous mixture was achieved. The mixture was then transferred into an airtight container and left to cure for 12 hours at room temperature.

The cured sample was then thoroughly mixed for about 1 min. The mixture was then filled into a cylindrical cup of the cone penetrometer apparatus with caution taken to ensure that no air pockets were trapped. The excess mixture at the top of the cup was removed, leaving a smooth surface, and levelled with the rim of the cup. The mixture-filled cup was then carefully placed at the centre, underneath the cone penetrometer (Figure 3.7a), with the tip of the cone point touching the surface of the paste (Figure 3.7b). The Initial reading on the dial gauge was recorded to the nearest 0.1 mm as R1. The cone was then released, allowing it to penetrate freely into the mixture for a period of 5 seconds, and the reading on the dial gauge was recorded as R2. The penetration depth was determined by subtracting R1 from R2. The cone was then lifted and cleaned. About 10 g of the sample was scoped out from the cup, and its moisture content was determined. The procedures were repeated four (4) times by adding the water incrementally into the mixture so that the penetration depths were evenly distributed between 15 mm and 25 mm.

A semi-log graph of moisture content against penetration depth was plotted, and the best fit line was drawn. The liquid limit was measured by determining the moisture content value that corresponded to a penetration depth of 20 mm.
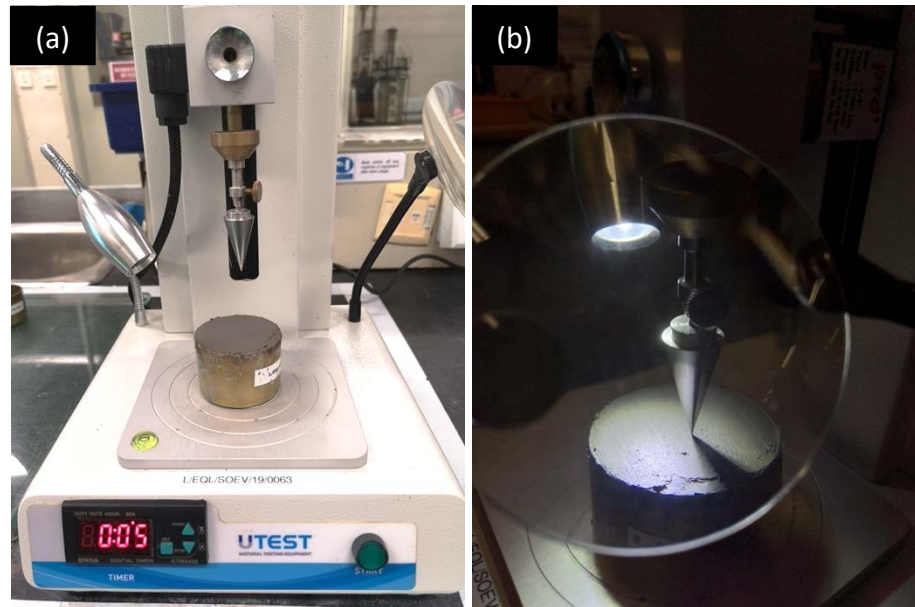
Figure 3.7: (a) Mixture-filled cup placed under the cone penetrometer. (b) Tip of the cone penetrometer touching just the surface of the mixture.

3.7.3. Plastic Limit

The plastic limit test in this study was carried out using the hand rolling method. A 1.5 to 2.0 g portion of the sample prepared for the liquid limit test was taken and formed into an ellipsoidal mass. The mass was then rolled on a ground-glass plate with sufficient pressure from the palm to form a uniform diameter thread. The rolling was continued for 2 minutes to further deformed the thread until it had reached a diameter of 3.2 mm. A steel rod of 3.2 mm diameter was used as a reference size.

After the thread had reached 3.2mm, the thread was broken into several pieces. The pieces were crumbled together, kneaded, reformed into an ellipsoidal mass, and re-rolled into a 3.2 mm diameter. The procedure was repeated until the mass could no longer be rolled into a 3.2 mm diameter thread. The crumbled threads were then gathered and placed in a container of known mass. The container was

quickly covered to prevent moisture loss. The procedures were repeated using another 1.5 to 2.0 g portion of the samples from the plastic-limit test until the container weighed 6 g of crumbled threads. The test was repeated to make another container of 6 g of crumbled threads. The containers were then dried out in the oven to determine the moisture content outlined in ASTM D2216-19 in section 3.5. The average of the two moisture content results was rounded off to the nearest whole number, referred to as the plastic limit (PL) value.
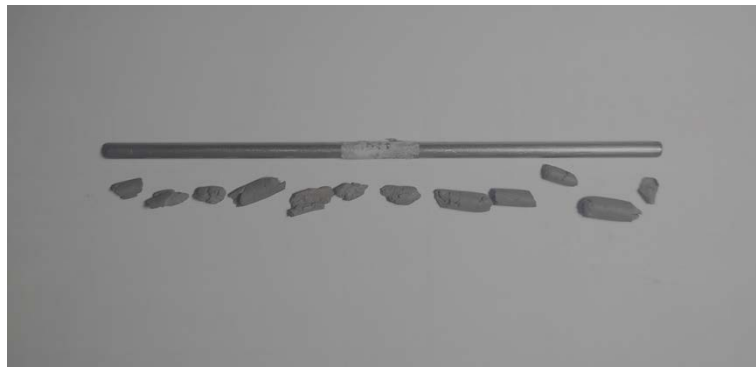
Figure 3.8: Crumbled threads at the plastic limit.

3.7.4. Plasticity Index

The plasticity index of the shale sample can be determined based on the following formula:

$$PI = LL - PL \qquad\qquad 3.10$$

where:

    LL =   Liquid limit (whole number)

    PL =   Plastic limit (whole number)

3.8. Porosity

The porosity of the samples was measured by using the Helium Porosimeter, Model TPI-219, Coretest Systems, available at the Petrophysics Lab, Curtin University Malaysia. The test was carried out based on the operator manual of the equipment

– porosity determination by grain volume measurement. Figure 3.9 shows the cores samples prepared for the porosity test. Three cylindrical core samples of height between 2.5 and 3.8 cm were prepared for each formation. The samples were air-dried at room temperature to a constant mass.
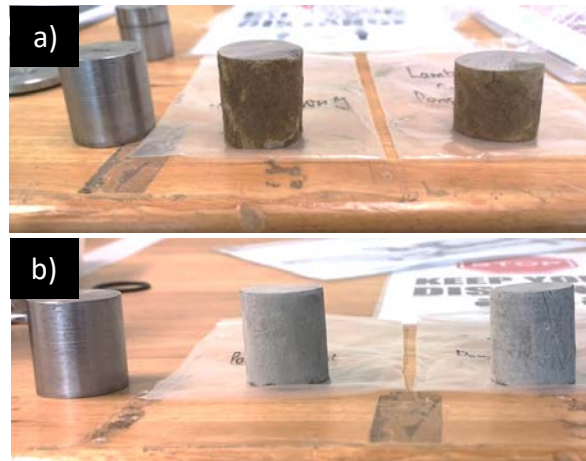
Figure 3.9: Core samples prepared for Helium Porosimeter Test. (a) Lambir Formation (b) Sibuti Formation.

The principle behind the measurement was based on the application of Boyle's Law wherein, under the conditions of constant temperature, the pressure (P) of a given quantity of gas varies inversely with its volume (V) (Equation 3.13). Any changes in the volume occupied by a gas at constant temperature and quantity will result in a change in the pressure exerted by it. Hence, the product of the initial pressure and the initial volume of a gas is equivalent to the product of its final pressure and final volume (mathematically expressed in Equation 3.14). This relationship enables the determination of the volume of grains or void spaces in the test sample using a pressure chamber, non-reactive gas (such as Helium), and an accurate pressure measuring device. Helium has the smallest atom making it best suited to measure even the smallest void spaces in the test sample.

$$P \propto \frac{1}{V} \hspace{4cm} 3.11$$

$$P_1 V_1 = P_2 V_2 \hspace{4cm} 3.12$$

In this study, the pore volume and porosity were determined from grain volume data since the bulk volume of the core sample can be measured. Prior to testing, initial calibration was carried out to determine the system reference volume (Equation 3.15). The system reference volume is a critical value in this test method, and accuracy is essential. The calibration test was carried out five times, and the mean reference volume value was used for the subsequent calculations. The pore volume was calculated by subtracting the grain volume from the bulk volume (Equation 3.16). Finally, the porosity was calculated by dividing the pore volume by the bulk volume and multiplying the fraction by 100% (Equation 3.17).

$$V_{REF} = \frac{V_{BILLETSREMOVED}}{\left(\frac{P_{REFREM}}{P_{CUPREM}}\right) - \left(\frac{P_{REFFULL}}{P_{CUPFULL}}\right)} \qquad 3.13$$

$$V_{GRAIN} = V_{BILLETSREMOVED} + \left[\left(\frac{P_{REFFULL}}{P_{CUPFULL}}\right)V_{REF}\right] - \left[\left(\frac{P_{REFSAMPLE}}{P_{CUPSAMPLE}}\right)V_{REF}\right] \qquad 3.14$$

$$Porosity\ (\%) = \left(\frac{V_{SAMPLE} - V_{GRAIN}}{V_{SAMPLE}}\right) \times 100 \qquad 3.15$$

where:

V_{REF}	=	System reference volume, cm³
$V_{BILLETSREMOVED}$	=	Volume of the removed billets, cm³
$P_{REFFULL}$	=	Reference pressure for full cup measurement, psi
$P_{CUPFULL}$	=	Cup pressure with all billets in cup, psi
P_{REFREM}	=	Reference pressure for measurement with a billet removed, psi
P_{CUPREM}	=	Cup pressure with a billet removed, psi
V_{GRAIN}	=	Grain volume, cm³
V_{REF}	=	System reference volume, cm³
$P_{REFSAMPLE}$	=	Reference system pressure prior TO CORE measurement, psi
$P_{CUPSAMPLE}$	=	Cup pressure with sample inside, psi
V_{SAMPLE}	=	Bulk volume of sample, cm³

3.9. Permeability

The permeability of the sample was measured by using a gas permeameter, Model TKA-209, Coretest Systems, available at the Petrophysics Lab, Curtin University Malaysia. The test was carried out based on the procedures outlined in the user's manual. The same core samples used in the previous porosity test were used for this test. The permeability can be measured by applying the steady-state flow technique of Darcy's Law. The law implies a constant flow rate across the sample of a given volume at ambient temperature and moderate confining pressure. Hence, gas can be injected over a range of pressures and flow rates, and the inline pressure gas flow can be recorded. The permeability was then calculated using the following formula:

$$K_a = \frac{2\mu Q_b P_b L}{A(P_1^2 - P_2^2)} \times 1000 \qquad\qquad 3.16$$

where:

K_a	=	Permeability to gas (not corrected for slip), mD
μ	=	Gas viscosity at room temperature, centipoise
Q_b	=	Flow rate of gas from meter reading at room conditions, cc/sec
P_b	=	Atmospheric pressure, atmosphere absolute
P_1	=	Inlet pressure, atmosphere absolute
		When $\Delta P < 3\ psi: Downstream\ Pressure + \Delta P + Atmospheric\ Pressure$
		When $\Delta P \geq 3\ psi: Upstream\ Pressure + Atmospheric\ Pressure$
$P_{\Delta P}$	=	Differential pressure (from meter reading), atmospheres
P_2	=	Outlet pressure, atmospheres
		$Downstream\ Pressure + Atmospheric\ Pressure, P_b$
L	=	Sample length, cm
A	=	Sample area, cm^2

3.10. Slake Durability Test

3.10.1. Sample Preparation

Slake durability tests in this study were carried out following the guideline procedure of standard test method ASTM D4644-16. For each set of tests, the core samples were cut into 10 smaller cylindrical pieces of 40 – 60 g each by using Single Trim Saw (STS-425), available at Sedimentology Lab, Curtin University Malaysia. The samples were brushed off to remove any dust before weighing. The total mass of the samples for each set was between 450 and 550 g. The samples were then carefully wrapped in transparent plastic seals to retain as much as possible their natural water content.

3.10.2. Test Method

The tests were carried out using slake durability device at Soil and Geotechnic Lab, University College of Technology Sarawak (UCTS). The test was carried out twice for each formation to obtain the average value. The test was then carried out for the third time if the discrepancy percentage between the first two results is more than 5 %. First, photographs of the initial state of the samples were taken using a phone camera. Next, the mass of the empty drums was determined as C. The samples were then placed inside the drums and were oven-dried at the temperature of 110 ± 5°C for 3 hours. The mass is obtained and recorded as W_i. The duration of the oven drying until a constant mass was achieved was determined during preliminary tests. The drums containing the samples were then cooled off for 20 minutes before being mounted on the troughs. The troughs were then filled with room temperature distilled water to 20mm below the drum axis (Figure 3.10). The drums were rotated at 20 rpm for 10 minutes. The temperature of the water at the beginning and the end of the cycle was recorded. Immediately after the rotation period, the drums were removed from the troughs and oven-dried at the temperature of 110 ± 5°C for 3 hours. The oven-dried mass of the drum with the samples, W_{f1} was obtained after 20 minutes of cooling off. The procedures were repeated to determine the final oven-dried mass of the second cycle, W_{f2}. Finally, photographs of the samples during each cycle were recorded for fragment type description.
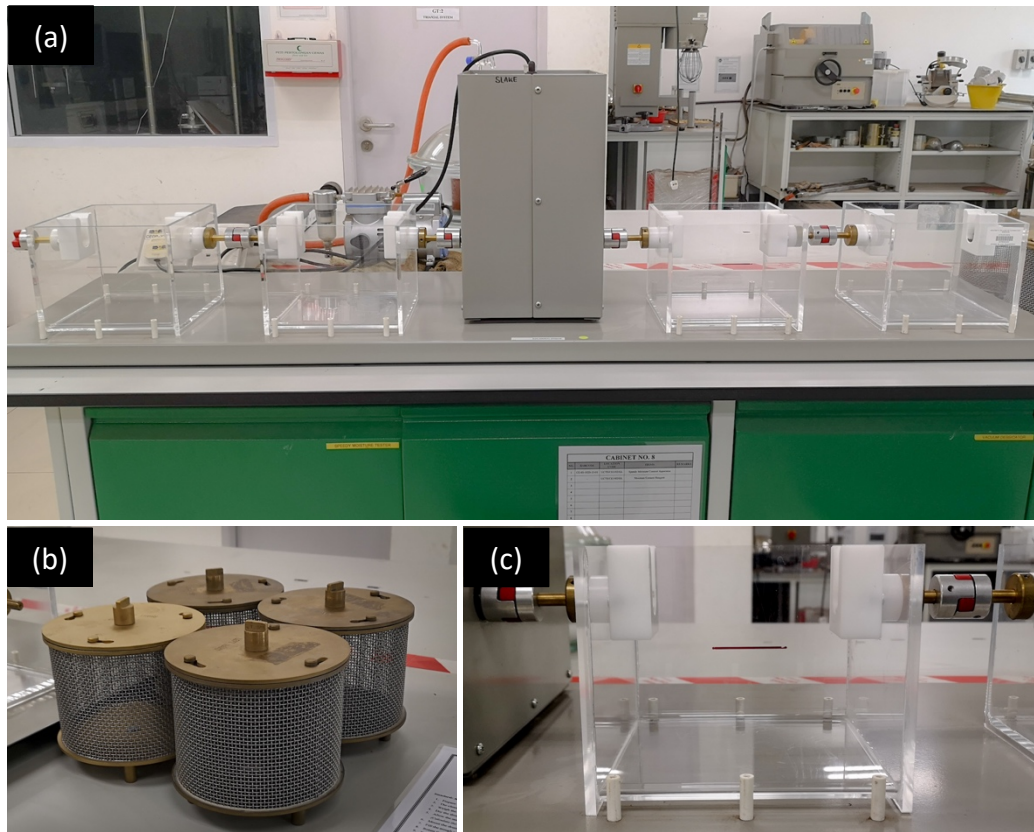
Figure 3.10: (a) Slake durability test set up (b) drums (c) trough with drum axis marked.

3.10.3. Calculation of Slake Durability Index

The slake durability index (I_d) is defined as the percentage of the dry mass retained on the drum after one or two disintegration cycles. The values of I_d were calculated using the following formula:

$$I_{d1} = \frac{W_{f1} - C}{W_i - C} \times 100 \qquad\qquad 3.17$$

$$I_{d2} = \frac{W_{f2} - C}{W_i - C} \times 100 \qquad\qquad 3.18$$

where:

I_{d1} and I_{d2}	=	Slake durability index after first and second cycles, %
W_1	=	Mass of drum plus oven-dried samples before the first cycle, g
W_{f1} and W_{f2}	=	Mass of drum plus oven-dried samples retained after the first and the second cycles, g

C = Mass of drum, g

3.10.4. Durability Classification

Based on the I_d values from slake durability tests, standard classifications recommended by Gamble (1971) and Franklin et al. (1972) were used to classify the durability of the studied shales. Franklin et al. (1972) proposed the slake durability test method and the classification in their PhD thesis in 1970. Their classification is based on the values of I_d from the first cycle. Gamble (1971) further improved the classification based on the values of I_d from the second cycle and plasticity index to give a greater differentiation in behaviour. His durability-plasticity classification has been recommended by the International Soil Rock Mechanic (ISRM) 2007. The comparison between the two classifications can be referred in Table 2.1.

3.11. Petrography

The petrographic analysis involved a microscopic study of the rock sample to identify the type of minerals present, fabric, and other microscopic features. The analysis was carried out using Nikon Eclipse LV100N Polarised Light Microscope with Nikon Camera at Mineralogy Lab, Curtin University Malaysia.

Prior to that, the samples were prepared into petrographic thin sections in Geochemistry and Sedimentology Lab, Curtin University Malaysia. The method adopted was based on modifications from Hirsch (2012). First, core samples were cut into half of a 2 cm cylinder by using a Single Trim Saw (STS-425). The samples were then dried on a hotplate at 100°C for 20 minutes. Next, the samples were then impregnated into an epoxy glue mixture of ratio 2:2:1 containing 50 ml of resin, 50 ml of hardener and 25 ml of acetone. The impregnation process was carried out by submerging the samples into the epoxy glue solution for 30 minutes in a vacuum chamber. The samples with the epoxy impregnation were then left to dry overnight.

The samples were then polished by using sandpapers of grit 600 cc, 1500 cc, and 2000 cc respectively from the coarsest to the finest until a flat, smooth surface was achieved. The polished surfaces were then glued into the glass slides by using Epoxy Loctite 0151 Hysol. To avoid trapping bubbles, the polished surface was heated up on a hotplate before spreading the epoxy and any extra epoxy during application was squeezed out by moving a finger at the centre of the glass in a circular motion. The samples were then left to dry overnight. Next, the samples were trimmed off, leaving a thin-sliced on the glass by using the INGRAM-WARD Thin Section Machine. The slides were then grinded on a glass plate by using 1000 and 2000 grit carborundum powder until an appropriate thickness was achieved. This proper thickness was determined by preliminary inspection of the mineral's birefringence (typically quartz) under the microscope.

3.12. Scanning Electron Microscopy (SEM)

The SEM used for image acquisition in this study is the Thermo Scientific Quattro ESEM, available at Curtin BioValley Malaysia. It is equipped with X-ray spectroscopy (EDS), electron backscatter diffraction (EBSD) and wavelength dispersive X-ray spectroscopy (WDS). The images were captured at desired magnification with a voltage of 10 to 20 kV, by using either a Low Vacuum Detector (LVD) and Circular Backscatter Detector (CBS). Elemental maps and EDS spot analysis, showing the intensity of the elements were produced simultaneously by using the EDS detector. The analysis aimed to study the pore spaces, microcracks and minerals cementation of the samples. The shale samples prepared for this analysis were from the remaining core samples trimmed off during thin section preparation. The sections of the sample for the analysis were polished using sandpapers of grit 600 cc, 1500 cc, and 2000 cc to obtain a flat, smooth surface.

3.13. X-Ray Diffraction (XRD)

XRD analysis is an instrumental technique used to determine the composition of crystalline minerals. Each mineral produces a unique diffraction pattern. The minerals were identified by comparing their patterns with a library of over 17,000 minerals diffraction patterns stored in the International Centre for Diffraction Data (ICDD). However, due to detection limits, minerals present in approximately less than 2 % of the overall rock composition might not be detected.

For this analysis, core samples were air-dried for three days and pulverised by using agate mortar to pass through an ASTM E11 <63 µm sieve. A total of 5 g per sample was packed and sent for analysis to Actlabs (Activation Laboratories Ltd.). Canada. A portion of each pulverised sample was mixed with corundum as an internal standard to determine the amount of X-ray amorphous material. The analysis was carried out on a Bruker D8 Endeavour diffractometer equipped with a Cu X-ray source running at 40 kV and 40 mA. The data were collected from 4 - 70° 2-theta for random specimens and 3 - 30° 2-theta for oriented specimens with a continuous scanning speed of 2.4° 2-theta/min. XRD peaks were interpreted by using X'Pert HighScore Plus software, and the minerals were identified by using the PDF-4/Minerals ICDD database. The Rietveld method based on the calculation of the full diffraction pattern from crystal structure data was used to quantify the minerals. The amounts of crystalline minerals were re-calculated based on the known percentage of corundum. The remainder to 100 % was considered X-ray amorphous material.

3.14. Clay Speciation

Clay speciation is an additional XRD analysis to identify and quantify clay minerals. An intact core sample of 100 g was packed and sent for analysis to Actlabs Activation Laboratories Ltd. Canada. For this analysis, the core samples were air-dried for three days and were dispersed in distilled water. Clay minerals of <4 µm size fraction were separated by gravity settling of particles in suspension. The suspended clay minerals of <4 µm size fraction were placed onto oriented glass slides and were analysed based

on air drying and after treatment with ethylene glycol. The relative abundances of the clay minerals were calculated using the relative ratios of the basal-peak areas.

3.15. X-Ray Fluorescence (XRF)

XRF analysis was carried out to analyse major and trace elements of the whole rock composition. Core samples were air-dried for three days, pulverised using an agate mortar and then sieved using an ASTM E11 <63 µm sieve. The resulting powder was packed into 5 g per sample and sent to Actlabs (Activation Laboratories Ltd.). Canada for 4C - Fusion XRF analysis. The heavy absorber fusion technique of Norrish and Hutton, (1969) was used for this analysis to minimise the matrix effects of the samples. Prior to fusion, loss of ignition (LOI) was determined from the weight loss of H_2O^+, CO_2, S, and other volatiles after roasting the sample at 1000°C for 2 hours. An approximate amount of 0.75 g of the roasted sample was mixed into a fusion disk with 9.75 g of a combination of lithium metaborate and lithium tetraborate with lithium bromide as a releasing agent. Samples were then fused in platinum crucibles by using an automatic crucible fluxed and were poured into platinum molds for casting. The oxides of 10 major elements (Si, Al, Ti, Fe, Ca, Mg, Na, K, Mn, and P) were analysed on a Panalytical Axios Advanced wavelength dispersive XRF. Certified Reference Materials (CRMs) used in the analysis and detection limits of the oxides are listed in Table 3.3.

Table 3.3: CRMs and detection limits used in the XRF Analysis

Analyte Symbol	SiO2	Al2O3	Fe2O3(T)	MnO	MgO	CaO	Na2O	K2O	TiO2	P2O5
Unit Symbol	%	%	%	%	%	%	%	%	%	%
Lower Limit	0.01	0.01	0.01	0.001	0.01	0.01	0.01	0.01	0.01	0.01
Method Code	FUS-XRF	FUS-XRF	FUS-XRF	FUS-XRF	FUS-XRF	FUS-XRF	FUS-XRF	FUS-XRF	FUS-XRF	FUS-XRF
FK-N Meas	64.97	18.55	0.07			0.13	2.58	12.89	0.01	0.01
FK-N Cert	65.0	18.6	0.0900			0.110	2.58	12.8	0.0200	0.0240
AC-E Meas	69.84	14.55	2.53	0.054		0.39	6.71	4.48	0.11	
AC-E Cert	70.35	14.70	2.56	0.058		0.34	6.54	4.49	0.11	
DR-N Meas	52.01	17.16	9.68	0.215	4.31	6.95	2.93	1.68	1.05	0.24
DR-N Cert	52.85	17.52	9.70	0.220	4.40	7.05	2.99	1.70	1.09	0.25
GS-N Meas	65.62	14.51	3.69	0.050	2.32	2.50	3.80	4.69	0.66	0.29
GS-N Cert	65.80	14.67	3.75	0.056	2.30	2.50	3.77	4.63	0.68	0.28
WS-E Meas	51.25	13.75	13.39	0.173	5.67	9.12	2.52	1.01	2.46	0.31
WS-E Cert	50.70	13.78	13.15	0.170	5.55	8.95	2.47	1.00	2.40	0.30
NCS DC73304 (GBW 07106) Meas	91.75	3.36	3.23		0.04	0.27	0.07	0.65		0.23
NCS DC73304 (GBW 07106) Cert	90.36	3.52	3.22		0.082	0.30	0.061	0.65		0.222

3.16. Natural Slake Test

The natural slake test was carried out to evaluate shale slaking behaviour and the changes to its properties during weathering, under natural climatic conditions. The test method adopted in this study was the modified method from Gautam et al. (2013) and Lai et al. (2022). The test was carried out for shale samples of selected formations. The Lambir and the Sibuti shales were selected as the highest and lowest durable shale based on the result from the laboratory slake durability test.

3.16.1. Sample Preparation

The samples were collected during coring and cut into smaller cylindrical samples weighing 40 – 60 g each. The samples were ensured to be equidimensional (Figure 3.11) and air-dried to a constant mass. The moisture content was recorded. Four sample sets were prepared per formation. Each set consists of ten representative units with a total mass between 450 – 550 g.
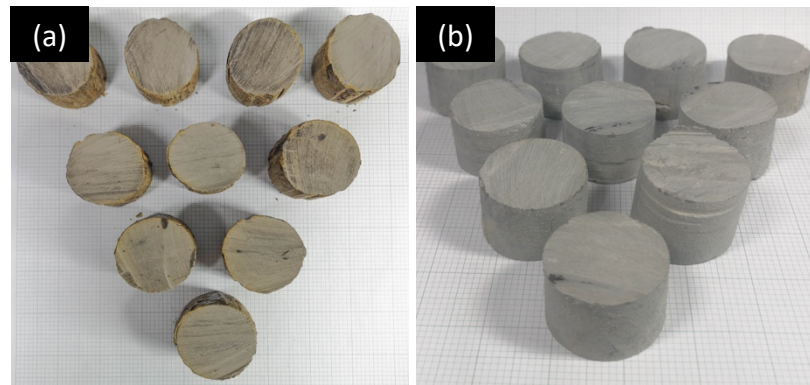
Figure 3.11: Core samples prepared for the natural slake test. (a) Lambir shale (b) Sibuti shale.

3.16.2. Test Set-Up

The test set-up was fabricated by the Advanced Metallurgy & Welding Technology Sdn. Bhd. (Figure 3.12). The materials used in the fabrication were stainless steel, coated with aluminium to prevent corrosion during weather exposure. Each set-up consisted of three sieves of 2 mm, 1 mm, 0.063 mm in sizes and a bucket, arranged in that order accordingly. The 2 mm sieve size was chosen as the top sieve following the mesh size of the drum used in the ASTM D4644 – Slake Durability Test. The 1 mm sieve size was used as the apertures were large enough to prevent clotting when small slaked fragments passed through it during the weathering process. On the other hand, the 0.063 mm sieve was used to filter between clay and silt-sized slaked materials. A bucket wrapped in heavy-duty aluminium foil was included in the set-up to collect the rainwater and slaked particles passing through the 0.063 mm sieve. The sieves and the bucket were stacked with a gap of 10 cm each to prevent water ponding.
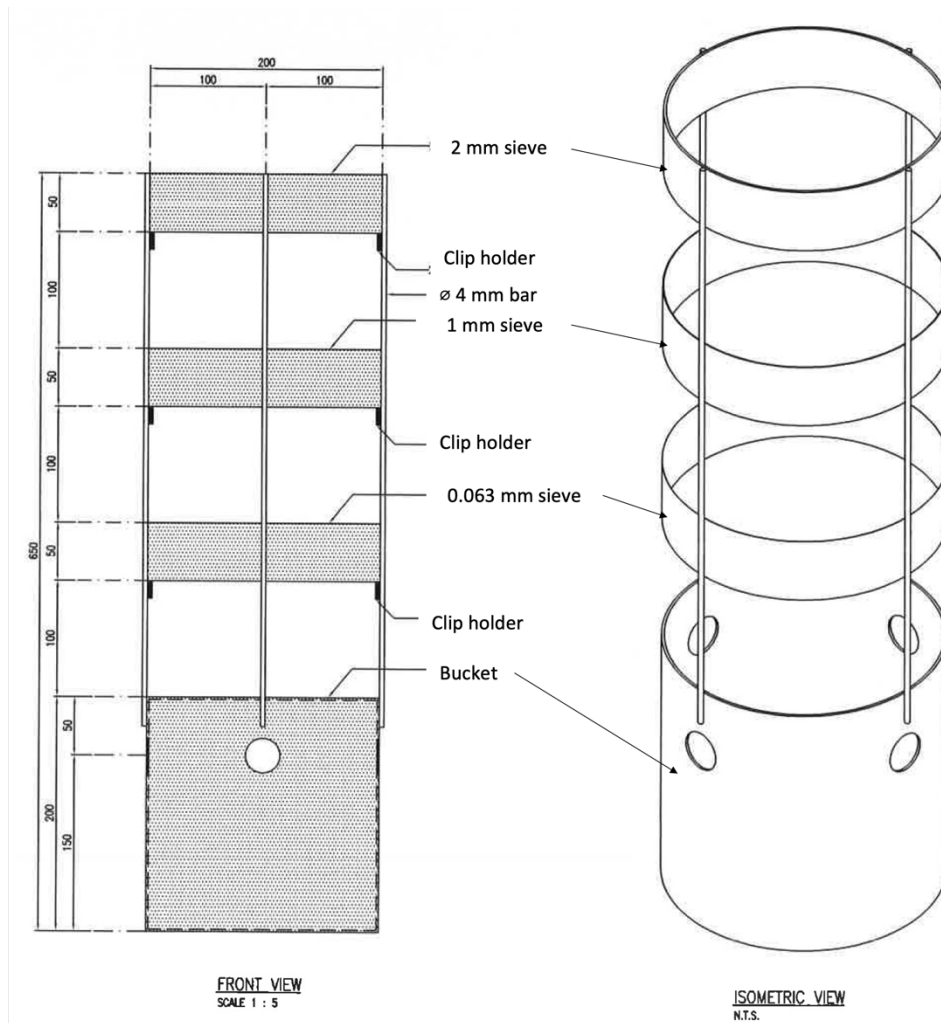
Figure 3.12: Front and isometric view of the fabricated natural slake test set-up.

3.16.3. Test Method

The sample-set were arranged and labelled as Set 1, Set 2, Set 3, and Set 4 (Table 3.4). Set 1 – 3 were placed under the sun with exposure both to the rain and sunlight, while Set 4 was placed under a shed, exposing the samples only to the humidity of the environment. The initial mass of each set was recorded, and photographs of the initial sample state were taken. The test set-up was placed on a flat surface. The test was conducted outside Curtin University Malaysia campus, within a 2.5 km radius, in a residential area. The weather variabilities throughout the experiment, such as the rainfall, temperature, and humidity, were recorded by using Vantage Pro 2 Weather Station located at the Curtin University, Malaysia campus.

Photographs and the weight change of the samples on the top sieve (2 mm sieve) were taken daily. The pH, salinity, total dissolved solids (TDS), and electrical conductivity (EC) were recorded daily when enough water was collected in the bucket after the rain events.

Table 3.4: Sample set labelling in the natural slake test and the descriptions.

Sample Label	Description
Set 1	A control test set up exposed under climatic conditions where the mode of slaking and weight changes will be recorded.
Set 2 and Set 3	A test set up exposed under climatic conditions where weight changes will be recorded. When the sample has reached the middle and final phase, slaked fragments will be collected for XRD, XRF, SEM, and grain size analysis.
Set 4	A control test set up stored under a shed where the sample will not be exposed to the sun and rain.

Figure 3.13: Natural slake test set-up exposed to the weather during the testing period.

When the samples had reached the middle and final phase of weathering, the set-up was taken indoors and air-dried to a constant mass. Grain size analysis was

carried out on the samples retained on the 2 mm sieve, and the disintegration ratio (D_R) was determined. Gautam and Shakoor (2009) proposed D_R, to quantify the degree of slaking and disintegration, and the durability classification is presented in Table x. The sieving was done manually to prevent further disintegration of the slaked material. The sizes of the sieves used were 25 mm, 19 mm, 14 mm, 10 mm, 8 mm, 6.3 mm, 4 mm, 2 mm, 1.18 mm, 0.3 mm, and 0.075 mm. The 25 mm sieve was ideally chosen as the upper limit for the slaked materials as the initial PSD analysis results showed that the maximum size of the individual particles of the sample is 5 mm.

The water sample from the bucket was collected when the samples reached the middle and final weathering phase. The water samples were then packed and sent for hydrochemistry analysis. The remaining sediment in the bucket was air-dried and prepared for geochemistry and mineralogy analysis. SEM and EDS mapping analyses were also carried out to study the microtexture changes on the sample during weathering.

3.16.4. Weathering Phase and Calculations of Disintegration Ratio

Weathering phase during the natural slake test was divided into the initial, middle, and final phases. The initial phase was defined as the initial stage and weight of the sample set on the top sieve at the beginning of the test. The middle and final phase were defined when the weight of the sample set on the top sieve has been reduced to 50% and 0% of its original weight. Weight loss percentage was calculated as shown in equation 3.19. The D_R was calculated from the grain size analysis graph, as shown in equation 3.20.

$$Weight\ loss, \% = \frac{(W_2 - W_S) - W_1}{W_1} \times 100 \qquad 3.19$$

where:

W_S =   Mass of empty sieve, g

W_1 =   Initial mass of the sample set, g

W_2 =   Mass of the exposed sample with sieve, g

$$Disintegration\ Ratio, D_R = \frac{Area\ under\ the\ graph}{Area\ of\ the\ encompassing\ curve} \qquad 3.20$$

The areas are taken from the graph of grain/fragments size distribution. The area under the graph represents the area under the curve, while the area encompassing the curve is the rectangular area enclosing the curve.

3.17. Hydrochemistry

The hydrochemistry analysis was carried out to study the mobility of the major and minor ions during weathering, specifically during rainy events. 1 litre of the water sample collected from the bucket in the natural slake test was packed and sent to Chemsain Konsultant Sdn. Bhd. The Ca^{2+}, Na^+, Mg^{2+}, and K^+ were analysed using an inductively coupled plasma – optical emission spectrometer (ICP-OES) following the standard procedures in APHA 3030F & 3120 B, 2005/2017. On the other hand, $Fe^{2+/3+}$, Rb^+, Cs^+, V^{2+}, and Al^{3+} were analysed using an inductively coupled plasma – mass spectrometer (ICP-MS) following the standard procedures in APHA 3125 B 2005/2017. Additionally, the Cl^- and SO^{4-} ions were determined following the standard procedures in APHA 4500 2005/2017.

3.18. Factor Analysis

Factor analysis was carried out to determine the degree of correlation among the shared variance that exists within the studied parameters. A large and unwieldy set of variables were converted into a smaller set of latent variables called a factor. The factors were calculated in the IBM SPSS Statistic v. 26 software package. The dataset was arranged in a matrix where the number of samples was placed in rows, and the number of independent variables (parameters) was placed in columns. The correlation matrix for the variables was examined. The data matrix was then condensed into factors that maximised the explained variance in the data on each successive factor. Eigenvalue representing the data variability and correlation

magnitude (scores) of each factor was calculated. Tabulation of the loading values representing the correlation coefficients between factors and the original variables/parameters was presented. An orthogonal rotation called the Varimax rotation was applied to rotate the factors and clarified the relationship among factors. All these steps and calculations were included in the standard settings of the software.

Chapter 4: Shale Physical Properties and Durability

4.1. Introduction

This chapter presents the findings of this research through sampling, physical properties analyses, and durability test. These include slake durability test, initial moisture content, particle size distribution analysis, Atterberg limit test, porosity, permeability, and durability. The correlation between the results is discussed at the end of the chapter.

4.2. Shale Samples

Table 4.1 summarised geological formation, geological period, location, field description, and strike and dip measurement of the shales used in this study. The field descriptions were made by subjective observations. There is a certain degree of lamination observed in shales from Miri, Tukau and Lambir formations. No lamination is observed in shales from Sibuti and Setap Shale Formation. Shales from Sibuti and Setap Shale Formations are carbonaceous as they react with acid on the field while shales from Miri, Lambir and Tukau Formation does not. Figure 4.1 shows some of the field photographs taken during sampling.

Table 4.1:List of shale samples used in this study and their description.

Geological Formation	Geological Period	Location	Field Description	Strike & Dip
Miri	Middle Miocene	The Height Residence, <u>Coordinates:</u> *4°22'16.42"N 113°59'21.12"E*	**Sample Observation:** • Colour: Brownish grey • Strength: Hard • Fissility: Fissile (Split easily with firm pressure) • Lamination: Thin lamination of coal and siltstone • Acidity: Does not react with acid (not calcareous) **Coring Observation:** • The hardest formation to core due to a thin layer of coal. Core sample tend to break easily	038/70 SE
Tukau	Middle Miocene-Pliocene	Jalan Miri-Bintulu <u>Coordinates:</u> *4°16'38.0"N 114°01'42.4"E*	**Sample Observation:** • Colour: Brownish grey • Strength: Soft (Easily moulded by hand) • Fissility: Less fissile • Lamination: Some degree of very thin sandstone layer and coal lamination • Acidity: No reaction with acid (not calcareous) • A lot of amber clasts were found at the outcrop location **Coring Observation:** • Used the least water during coring • The longest cored sample obtained: 56 cm	112/16 SE
Lambir	Middle – Late Miocene	Jalan Miri-Bintulu <u>Coordinates:</u> *4°13'5.43"N 114° 3'24.48"E*	**Sample Observation:** • Colour: Brownish grey • Strength: Firm (Can be moulded by fingers with firm pressure) • Fissility: Fissile (Split easily with firm pressure)	088/18 N

Geological Formation	Geological Period	Location	Field Description	Strike & Dip
			• Lamination: Some degree of very thin sandstone lamination • Acidity: No reaction with acid (not calcareous) **Coring Observation:** • The weathered surface shows a lot of oxidised iron minerals. Discharged of odourless reddish-brown liquid during coring	
Sibuti	Miocene	Bekenu <u>Coordinates:</u> *4° 3'24.72"N 113°48'32.55"E*	**Sample Observation:** • Colour: Light to dark grey • Strength: Very hard, stiff, and brittle • Fissility: Fissile (Split easily with firm pressure) • Lamination: No lamination observed • Acidity: React with acid (calcareous) **Coring Observation:** • Heavily weathered outcrop • Difficult in getting a good long sample as they tend to break easily	204/24 NE
Setap Shale	Oligocene-Early Miocene	Batu Niah <u>Coordinates:</u> *3°47'39.23"N 113°38'43.31"E*	**Sample Observation:** • Colour: Dark grey • Strength: Very stiff and brittle • Fissility: Very fissile • Lamination: No lamination observed • Acidity: React with acid (calcareous) **Coring Observation:** • Fresh surface cracks within half an hour of air exposure	074/18 NW
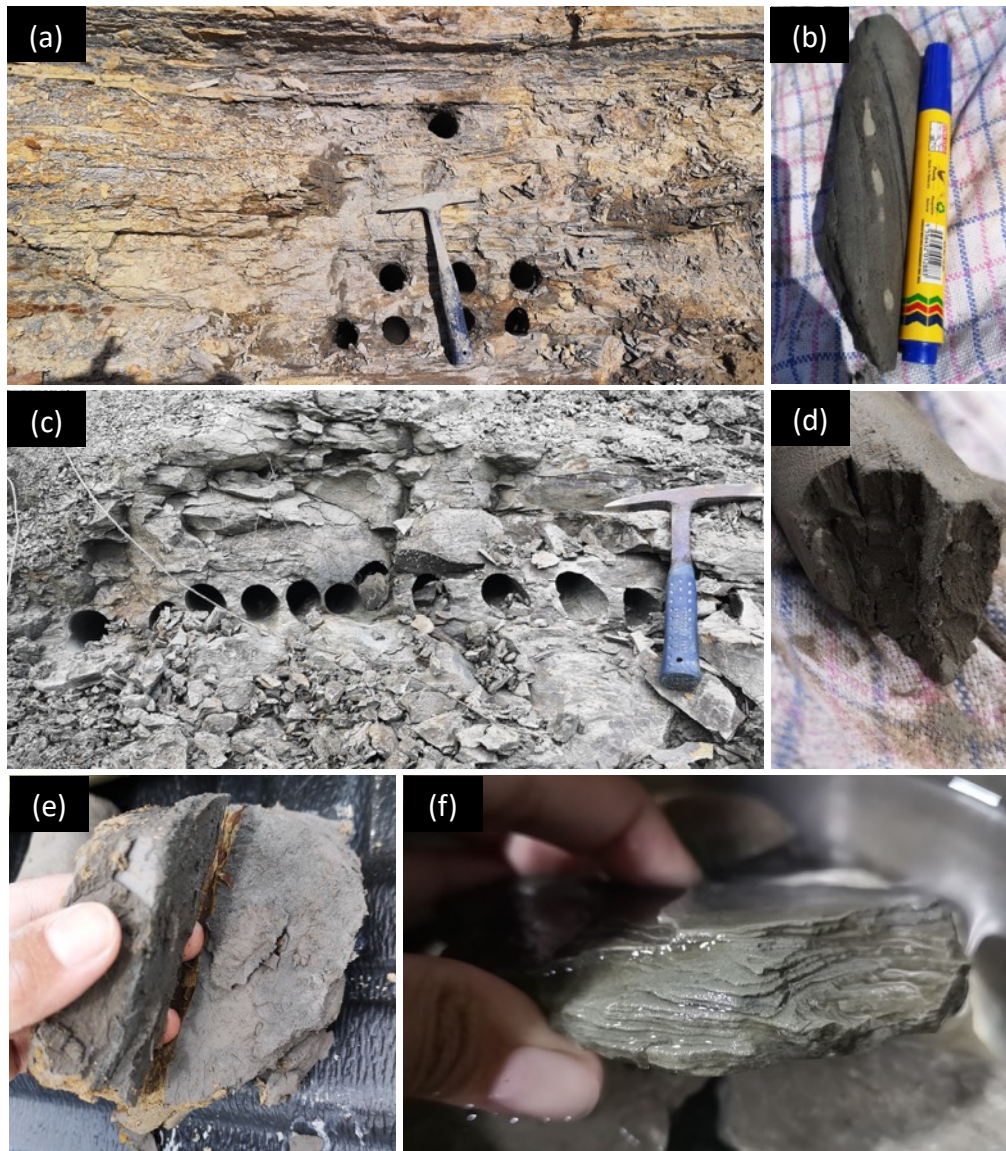
Figure 4.1: **(a)** Brownish-grey and fissile shale of Miri Formation; **(b)** Thin lamination of siltstone and coal in shale from the Miri Formation; **(c)** Heavily weathered, very hard and brittle shale from the Sibuti Formation; **(d)** Soft and less fissile shale with very thin lamination of sandstone from Tukau Formation; **(e)** Shale of the Lambir Formation show the ease of split along fissility plane with firm pressure; **(f)** Very fissile shale of the Setap Shale Formation.

4.3. Particle Size Distribution

Shales are fine-grained sedimentary rock, typically composed of compacted silts and clays. On the basis of texture, shales can be grouped into silty shale (silt dominant), clayey shale (clay dominant), and occasionally sandy shale (sand dominant). Table 4.2 and Figure 4.2 present the result of particle size distribution analysis of all the studied shales. The analysis was done by combining the results of sieving analysis (for

particles size larger than 75 µm) and hydrometer analysis (for particle size finer than 75 µm). Particle size distribution analysis allows the determination of the proportion of particles distributed over particle-size ranges. Samples from the Tukau and Lambir formations fall in the field of silty clay while samples from the Miri and Sibuti formations fall in the field of sandy silt. Samples from the Setap Shale Formation fall in the silty sand and sandy silt fields. Based on the results, shales from the Tukau and Lambir formations are clayey shales (clay dominant: 50 – 55%), shale from the Miri and Sibuti formations are silty shales (silt dominant: 59 – 62 %), and shale from the Setap Shale Formation is sandy shale (sand dominant: 46 %).
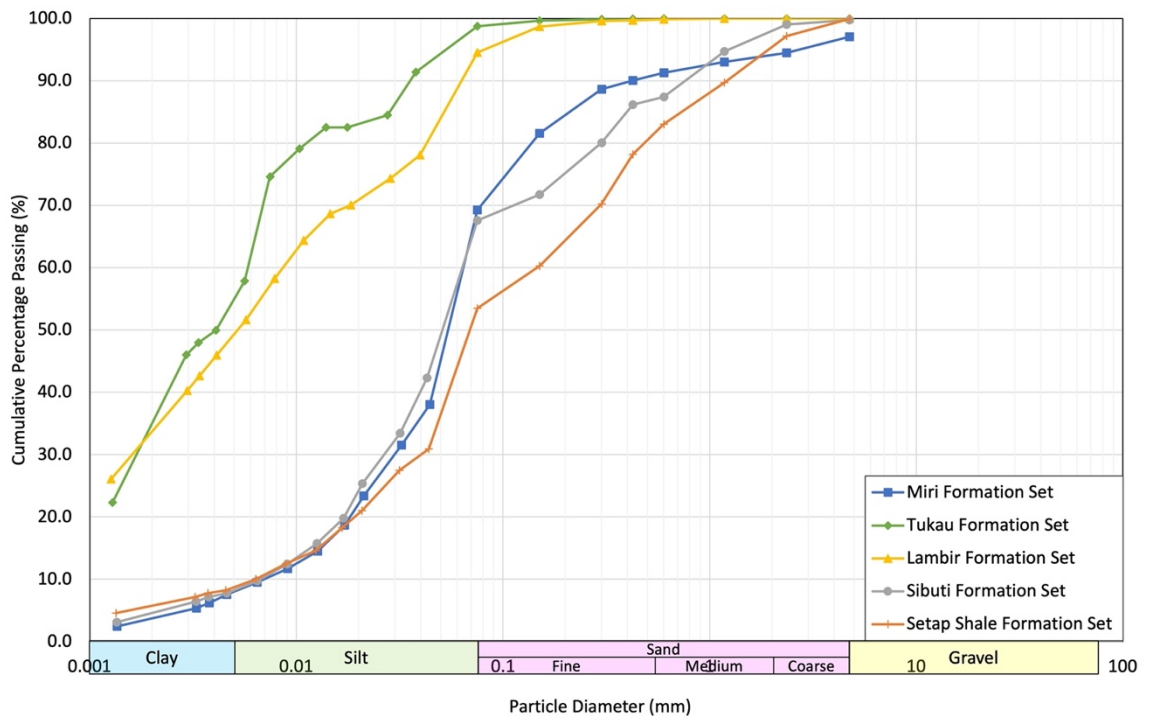
Figure 4.2: Particle size distribution analysis graph with ASTM particle classification scale for all the studied shales based on average values. The average values were taken from two sample sets per formation.
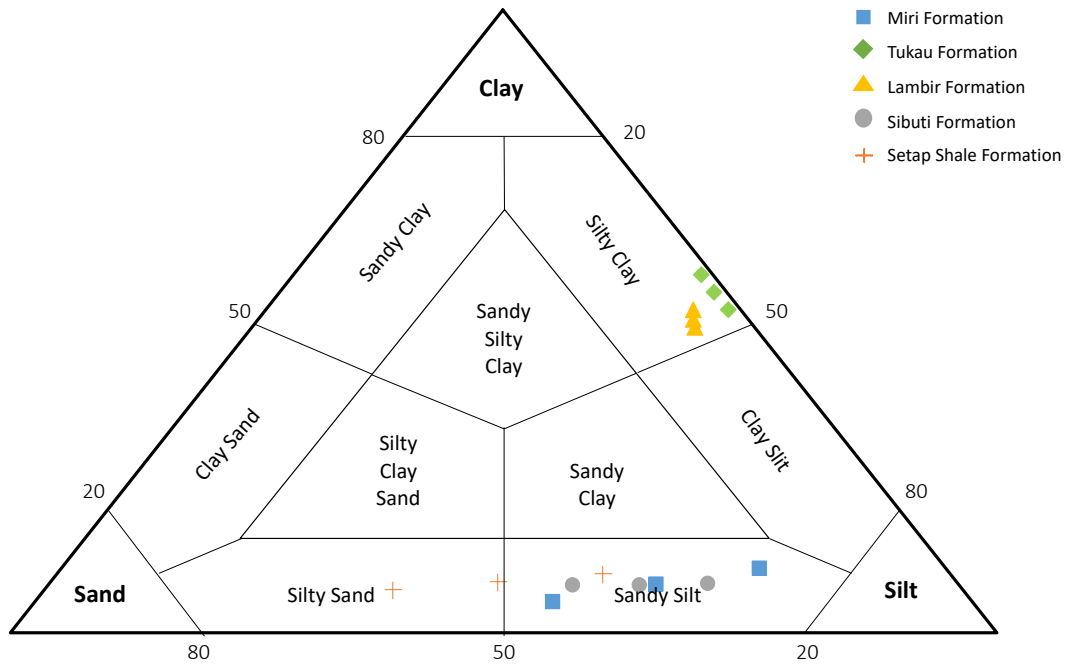
Figure 4.3: Sediment nomenclature plot, after Trefethen (1950).

Table 4.2: Particle-size analysis results and classification for all the studied shales.

Geological formation	Particle-size analysis based on ASTM scale (% by weight)			Textural Classification	Sediment Classification – Trefethen, 1950
	Clay (<0.005 mm)	Silt (0.005 - 0.075 mm)	Sand (0.075 - 4.75 mm		
Miri					
Set 1	4.9	52.5	40.2	Silty Shale	Sandy Silt
Set 2	10.2	70.9	15.5	Silty Shale	Sandy Silt
Average	7.6	61.7	27.8	Silty Shale	Sandy Silt
Tukau					
Set 1	57.5	41.3	1.2	Clayey Shale	Silty Clay
Set 2	52.0	46.7	1.3	Clayey Shale	Silty Clay
Average	54.8	43.9	1.3	Clayey Shale	Silty Clay
Lambir					
Set 1	52.0	43.2	4.8	Clayey Shale	Silty Clay
Set 2	49.0	44.9	6.1	Clayey Shale	Silty Clay

Geological formation	Particle-size analysis based on ASTM scale (% by weight)			Textural Classification	Sediment Classification – Trefethen, 1950
	Clay (<0.005 mm)	Silt (0.005 - 0.075 mm)	Sand (0.075 - 4.75 mm		
Average	50.5	44.0	5.5	Clayey Shale	Silty Clay
Sibuti					
Set 1	7.6	53.1	38.9	Silty Shale	Sandy Silt
Set 2	7.9	66.7	25.4	Silty Shale	Sandy Silt
Average	7.8	59.8	32.2	Silty Shale	Sandy Silt
Setap Shale					
Set 1	7.0	35.2	57.8	Sandy Shale	Silty Sand
Set 2	9.4	55.3	35.1	Silty Shale	Sandy Silt
Average	8.2	45.3	46.4	Sandy Shale	Silty Sand

*Some percentage of sediment loss (0.1 – 3 %) during sieving for shale samples from the Miri, Sibuti, and Setap Shale Formation.

4.4. Moisture Content

Table 4.3 presents the results of initial moisture content for all the shale samples. The measurements were determined before slake durability test. The Setap Shale Formation has the lowest initial moisture content of 4.2 %, followed by the Sibuti Formation with 4.9 %, the Miri Formation with 9.5 %, the Lambir Formation with 11.9 %, and the Tukau Formation with 19.1 %.

Table 4.3: Results of the initial moisture content for all shale samples before slake durability test.

Initial moisture content before slake durability test (%)					
Sample Set	**Miri**	**Tukau**	**Lambir**	**Sibuti**	**Setap Shale**
Set 1	10.0	21.0	11.4	4.7	4.3
Set 2	9.0	17.2	10.5	5.0	4.0

Initial moisture content before slake durability test (%)					
Sample Set	Miri	Tukau	Lambir	Sibuti	Setap Shale
Average	9.5	19.1	11.9	4.9	4.2

4.5. Specific Gravity Test

The specific gravity (Gs) is the mass of a unit volume of soil solids divided by the mass of an equivalent volume of gas-free distilled water of the same temperature. Table 4.4 presents the specific gravity test results of the studied shale sample. Typically, a higher value in Gs indicates the materials have higher finer materials (such as clay) and consist of more heavy minerals (such as iron, rutile, and zircon).

Table 4.4: Results of the specific gravity tests for all the studied shales.

Specific gravity (gcm^3)					
Sample Set	Miri	Tukau	Lambir	Sibuti	Setap Shale
Set 1	2.61	2.10	3.50	3.37	3.19
Set 2	2.52	2.35	3.64	3.32	2.14
Average	2.56	2.22	3.57	3.34	2.66

4.6. Atterberg's Limit

Atterberg's limits are valuable parameters that accurately define the boundaries at which physical changes in the soil occur. Water content in cohesive soil has a significant impact on its behaviour. As the amount of water added to soil increases, its physical behaviour changes from solid phase to semi-solid to plastic and liquid. The liquid limit is the lowest moisture content at which the soil changes from the plastic state to a liquid state. Meanwhile, the plastic limit is the moisture content at which the soil changes from a semi-solid state to a plastic state. The difference in water content between liquid limit (LL) and plastic limit (PL) is the plasticity index (PI). Soils with a higher PI value typically have a higher clay content. In addition, the Activity of a sample soil is the ratio of the PI to the clay fraction content. Activity

indicates the type of clay mineral in the sample. Activity values of more than 1.25 are considered active and are prone to swell and shrink with the changes of moisture content. In contrast, Activity values of less than 0.75 are considered inactive and are less sensitive to the changes in moisture content. Activity values in the range of 0.75 and 1.25 are classified as normal.

Table 4.5 presents the Atterberg's limits of the studied shale, which include the liquid limit, plastic limit, and plasticity index. Among the formations, shale from the Sibuti Formation has the lowest LL and PI values, followed by the Setap Shale, Miri, Lambir and Tukau Formation. Shale from the Miri, Tukau, Lambir, and Sibuti Formation has the same PL value of 20. On the contrary, shale from the Setap Shale Formation has a PL value of 17. Based on the Activity result, the clay in shales from the Miri, Sibuti, and Setap Shale is active, while the clay in shales from the Tukau and Lambir shale is inactive. The results show that, despite the high LL of the clayey shale from the Tukau and Lambir shale, their clays are inactive and are not prone to high swelling potential. The clays can adsorb more water without losing their physical behaviour. However, the clays in shale from Miri, Sibuti, and Setap Shale Formation are active with low plasticity. The clays from all formations have low to medium plasticity.

Table 4.5: Summary results of Atterberg's Limit.

Formation	Type of Shale	Liquid Limit (LL)	Plastic Limit (PL)	Plastic Index (PI)	% of Clay	Activity	
Miri	Silty	34	20	14	7.6	1.75	Active
Tukau	Clayey	44	20	23	54.8	0.46	Inactive
Lambir	Clayey	41	20	21	50.5	0.46	Inactive
Sibuti	Silty	32	20	12	7.8	1.50	Active
Setap Shale	Sandy	33	17	16	8.2	2.00	Active

4.7. Porosity and Permeability

Porosity is the percentage of the volume of void space within the rock. On the other hand, permeability is the measure of the ease of a fluid flowing through the rock and is typically associated with the presence of cracks and fractures. Since coring was done at 0° to the bedding/lamination, the porosity and permeability of the core sample are essentially the horizontal porosity and permeability of the rock. Horizontal permeability usually yields a higher value than vertical permeability, sometimes by order of magnitude or more (Satter & Iqbal, 2016). This is because laminations usually act as a barrier to vertical permeability. However, it should also be noted that the shale permeability results may be liable to be overestimated since the fissility of shale and additional cracks due to drilling may grossly inflate the actual permeability value.

Table 4.6 presents the shale samples' porosity and permeability results. Shale from the Lambir Formation has higher porosity and permeability than shale from the Sibuti Formation. Based on the average value, the Lambir shale has porosity of 21.24 % and permeability of 21.27 mD while the Sibuti shale has porosity of 9.07 % and permeability of 5.44 mD. High porosity and permeability values suggest more void spaces, larger void sizes, and a network of interconnected pores within the sample.

Table 4.6: The porosity (by grain volume) and the permeability of the representative shale sample from the Lambir and Sibuti formations.

Geological Formation	Porosity by grain volume (%)	Permeability (mD)
Lambir		
Set 1	24.22	51.13
Set 2	15.26	0.38
Set 3	24.24	12.31
Average	*21.24*	*21.27*
N (No. of sample)	*3*	*3*
Standard Deviation	*5.18*	*26.54*

Geological Formation	Porosity by grain volume (%)	Permeability (mD)
Sibuti		
Set 1	8.85	0.92
Set 2	10.85	4.93
Set 3	7.50	10.48
Average	*9.07*	*5.44*
N (No. of sample)	*3*	*3*
Standard Deviation	*1.69*	*4.80*

4.8. Slake Durability Test

Slake durability test is a laboratory test designed by Franklin et al. (1972), to measure the durability of weak rocks by mimicking the effect of weathering through cycles of wetting and drying. The index values were calculated as the percentage ratio of final to initial weights of the sample in the drum after each disintegration cycle. The classification systems used in this study were based on Franklin et al. (1972) and Gamble (1971). Franklin et al. (1972) categorised the durability of weak rocks based on the first cycle index values (I_{d1}) while Gamble (1971) suggested using the second cycle index values (I_{d2}) for rocks of higher durability.

Table 4.7 presents the results of slake durability tests and durability classification on the studied shale samples. In general, the tests were repeated two times to yield average values. However, the tests were repeated three times for Tukau, Lambir, and Setap Shale formations as the discrepancy values between the first and second test results were more than 5%. From the lowest to the highest, the durability variation of the shales from all five formations based on average I_{d1} results is as follows: Lambir (9.5 %), Miri (23.0 %), Tukau (32.1 %), Setap Shale (34.8 %), Sibuti (38.7 %). Meanwhile, the durability variation based on average I_{d2} is Lambir (0.0 %), Tukau (0.3 %), Sibuti (2.8 %), Miri (6.3 %), Setap Shale (6.4 %).

Based on Franklin et al. (1972) classification, the sampled shales of Lambir and Miri formations have very low durability while those from Tukau, Setap Shale, and Sibuti formations are categorised as having low durability. All index results were

classified as very low durability according to Gamble (1971) classification. Since the results were more significant during the first cycle, Franklin et al. (1972) classification is used to categorise the shales in this study. It is noted that the Tukau Formation yields inconsistent I_{d1} results for all three tests. This could be due to the nature and composition of the rocks. Some fragments of amber were retained in the drum after the first cycle (Figure 4.6b). The amount of amber clasts might affect the durability if they were affected by the temperature during oven drying.

In addition to the index values, descriptions of the fragments retained in the drum (Figure 4.5) during the cycle were also noted. According to ASTM D4644-16, fragments retained in the drum are classified into Type I, Type II, or Type III (Figure 4.5) based on visual observation. Type I represents the materials retained to have remained virtually unchanged. Type II represents the materials retained to have consisted of large and small fragments. Lastly, Type III represents the materials retained to be exclusive of small fragments. Figure 4.6 shows closed-up photos of some of the grains fragment.

Figure 4.4 shows the photographs taken at the initial sample state, sample state after the first cycle and the second cycle during the slake durability test. The initial sample state photos display the original condition of the 10 cylindrical core samples. The cores were uniform in weight, height, and size. The total weight of the samples per set test was 450 - 550 g. After the first cycle, the samples degraded into large and small fragments (Type II). Type II observations were noted in the Miri, Sibuti and Setap Shale formations. A new observation was added, representing materials that are retained in the drum as consolidated and lumpy. This observation was noted for the Tukau and Lambir formations in the first disintegration cycle. After the second cycle, most samples were further broken down into elusively small fragments, Type III. For the lowest durability shale (Lambir Formation), the drum was empty after the second cycle.

Figure 4.7 displays the photographs of particle settlement and colour of slaking fluid taken after the durability cycle. The changes in pH of the slaking fluid

before and after durability cycles were noted. Only slaking fluid from the Miri Formation changed to slightly alkaline. The rest of the formations become slightly acidic after the durability cycle.

Table 4.7: Slake durability test results of the studied shales.

Geological Formation	First Cycle – Index Values & Classification			Second Cycle – Index Values & Classification	
	I_{d1} (%)	Franklin & Chandra, 1972	Gamble, 1971	I_{d2} (%)	Gamble, 1971
Miri					
Set 1	23.2	Very Low	Very Low	6.7	Very Low
Set 2	22.7	Very Low	Very Low	5.9	Very Low
Average	*23.0*	*Very Low*	*Very Low*	*6.3*	*Very Low*
Tukau					
Set 1	15.6	Very Low	Very Low	0.1	Very Low
Set 2	30.0	Low	Very Low	0.0	Very Low
Set 3	50.9	Medium	Very Low	0.9	Very Low
Average	*32.1*	*Low*	*Very Low*	*0.3*	*Very Low*
Lambir					
Set 1	11.5	Very Low	Very Low	0.0	Very Low
Set 2	15.8	Very Low	Very Low	0.0	Very Low
Set 3	1.2	Very Low	Very Low	0.1	Very Low
Average	*9.5*	*Very Low*	*Very Low*	*0.0*	*Very Low*
Sibuti					
Set 1	38.1	Low	Very Low	2.7	Very Low
Set 2	39.3	Low	Very Low	2.8	Very Low
Average	*38.7*	*Low*	*Very Low*	*2.8*	*Very Low*
Setap Shale					
Set 1	31.3	Low	Very Low	4.1	Very Low
Set 2	35.5	Low	Very Low	8.2	Very Low
Set 3	37.6	Low	Very Low	6.9	Very Low

Geological Formation	First Cycle – Index Values & Classification			Second Cycle – Index Values & Classification	
	I_{d1} (%)	Franklin & Chandra, 1972	Gamble, 1971	I_{d2} (%)	Gamble, 1971
Average	*34.8*	*Low*	*Very Low*	*6.4*	*Very Low*

Initial sample state	Materials retained in the drum	
10 pieces of core samples before oven drying	**First Cycle**	**Second Cycle**
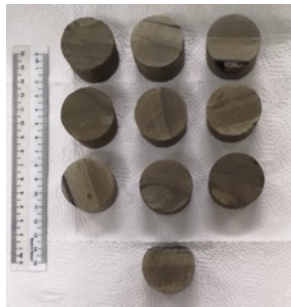
(a) Miri Formation

Average I_{d1}: 23.0%

Type II: Consist of large and small pieces

Average I_{d2}: 6.3%

Type II: Consist of large and small pieces

(b) Tukau Formation

Average I_{d1}: 32.1%

Consolidated and Lumpy

Average I_{d2}: 0.3%

Initial sample state	Materials retained in the drum	
10 pieces of core samples before oven drying	**First Cycle**	**Second Cycle**
		Almost empty with exclusively small fragments and amber

(c) Lambir Formation

	Average I_{d1}: 13.6%	*Average I_{d2}: 0.0%*
	Consolidated and Lumpy	*Empty*

(d) Sibuti Formation

	Average I_{d1}: 38.7%	*Average I_{d2}: 2.8%*
	Type II: Consist of large and small pieces	*Type III: Exclusively small fragments*

(e) Setap Shale Formation

Initial sample state	Materials retained in the drum	
10 pieces of core samples before oven drying	**First Cycle**	**Second Cycle**
	Average I_{d1}: 34.8%	*Average I_{d2}: 6.4%*
	Type II: Consist of large and small pieces	*Type III: Exclusively small fragments*

Figure 4.4 Photographs of sample state during slake durability test
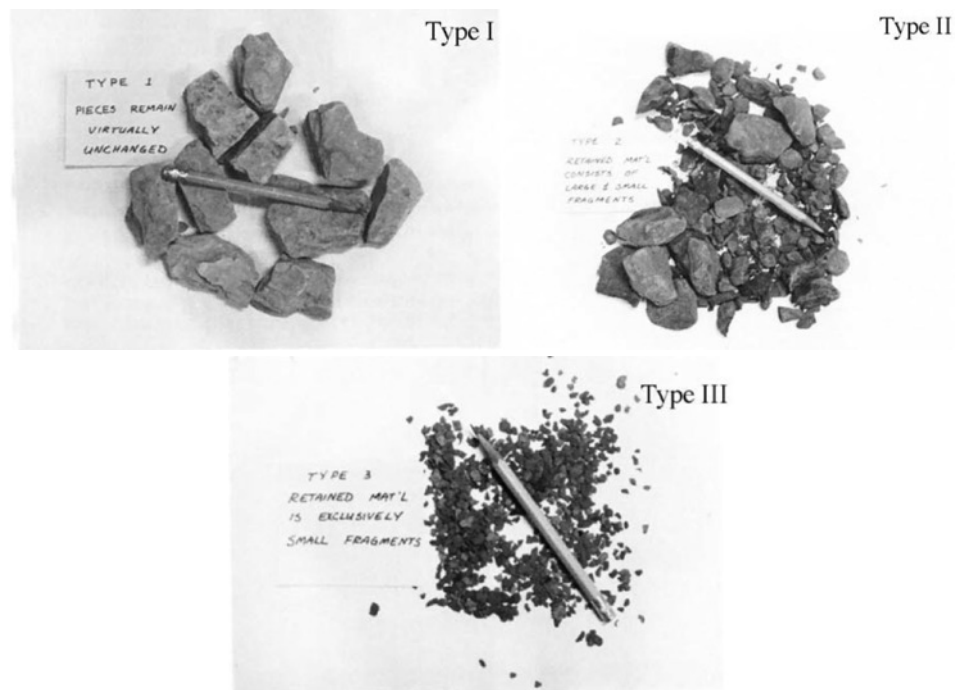
Figure 4.5: (Type I) Retained materials remain virtually unchanged; (Type II) Retained materials consist of large and small fragments; (Type III) Retained materials are exclusively small fragments.

Figure 4.6: Closed-up photographs of some of the fragments retained in the drum (a) Miri Formation; (b) Tukau Formation; (c) Lambir Formation (d) Sibuti Formation; (e) Setap Shale Formation.

Slaking fluid with particles settlement after slake cycle	Changes in the pH of slaking fluid	
	First Cycle	**Second Cycle**
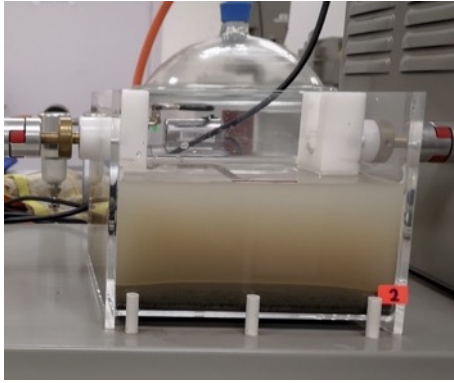
(a) Miri Formation

| | **Before:** pH 8.0 *Slightly alkaline* **After:** pH 7.6 *Slightly alkaline* | **Before:** pH 8.4 *Slightly alkaline* **After:** pH 7.1 *Slightly alkaline* |

(b) Tukau Formation
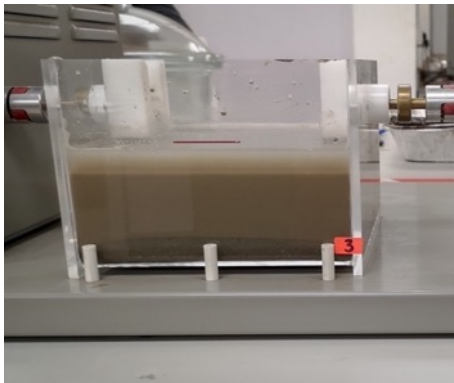
| | **Before:** pH 8.0 *Slightly alkaline* **After:** pH 7.0 *Neutral* | **Before:** pH 7.3 *Slightly alkaline* **After:** pH 5.9 *Slightly acidic* |

(c) Lambir Formation
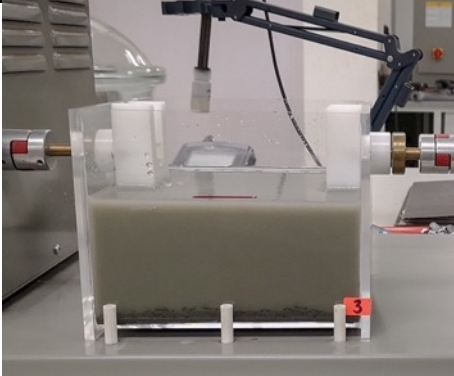
| | **Before:** pH 8.3 *Slightly alkaline* **After:** pH 5.0 *Slightly acidic* | **Before:** pH 7.4 *Slightly alkaline* **After:** pH 6.5 *Slightly acidic* |

(d) Sibuti Formation

Slaking fluid with particles settlement after slake cycle	Changes in the pH of slaking fluid	
	First Cycle	**Second Cycle**
	Before: pH 7.7 *Slightly alkaline* **After:** pH 5.5 *Slightly acidic*	**Before:** pH 7.2 *Slightly alkaline* **After:** pH 5.4 *Slightly acidic*

(e) Setap Shale Formation
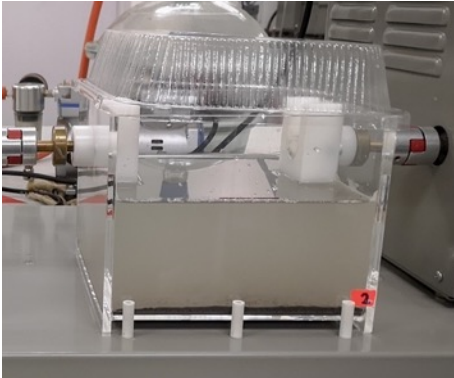
	Before: pH 7.8 *Slightly alkaline* **After:** pH 6.1 *Slightly acidic*	**Before:** pH 8.0 *Slightly alkaline* **After:** pH 7.5 *Slightly alkaline*

Figure 4.7 Photographs of slaking fluid and particle settlement and changes in the average pH values during the durability cycle.

4.9. Shale Physical Properties and Its Durability

Based on the particle size distribution analysis, shale in the Lambir Formation can be categorised as clayey shale with a clay percentage of 50.5% while shale of the Sibuti Formation is categorised as silty shale with a silt percentage of 59.8%. This shows that there is a correlation between clay content and durability. The Lambir shale has 50.5 % clay content while the Sibuti shale has 7.8%. A similar finding has been reported by several researchers such as Dick et al. (1992), Dhakal et al. (2002), Sadisun et al. (2005), Nandi et al. (2009a), and Selen et al. (2020). Figure 4.8 shows that shale with a clay content of less than 10% typically has higher durability and the durability decreases when the clay content is more than 45%. Shale with higher clay content

has higher water absorption and adsorption values that subsequently weakens the inter-granular bonds and promote slaking (Gautam et al., 2013). However, it is noted that shale from the Tukau Formation created an inconsistency in its durability test results. This may be due to the nature of the rocks such as the type of clay minerals present, type of grains cementation, and its porosity.
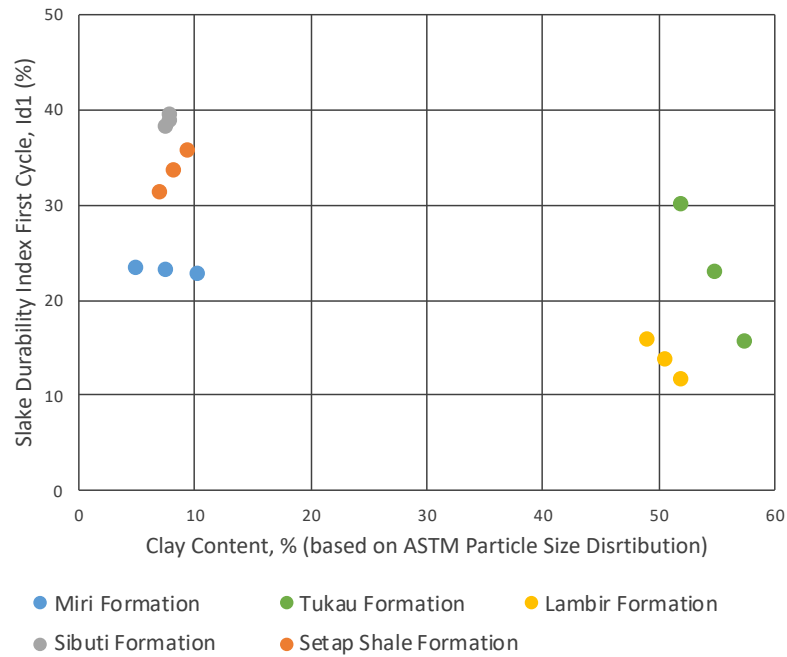
Figure 4.8: Correlation graph of durability index (I_{d1}) and clay content.

Figure 4.9 shows that omitting the inconsistent values of the Tukau Formation, there is a linear correlation between durability and initial moisture content. The low durability shale of the Lambir Formation has a higher initial moisture content of 11.9 % compared to the more durable shale of the Sibuti Formation with the initial moisture content of 4.9 %. When exposed to moisture, moisture-sensitive rocks slake rapidly, and the strength loss is proportional to the saturation degree of the rock material (Selen et al., 2020).
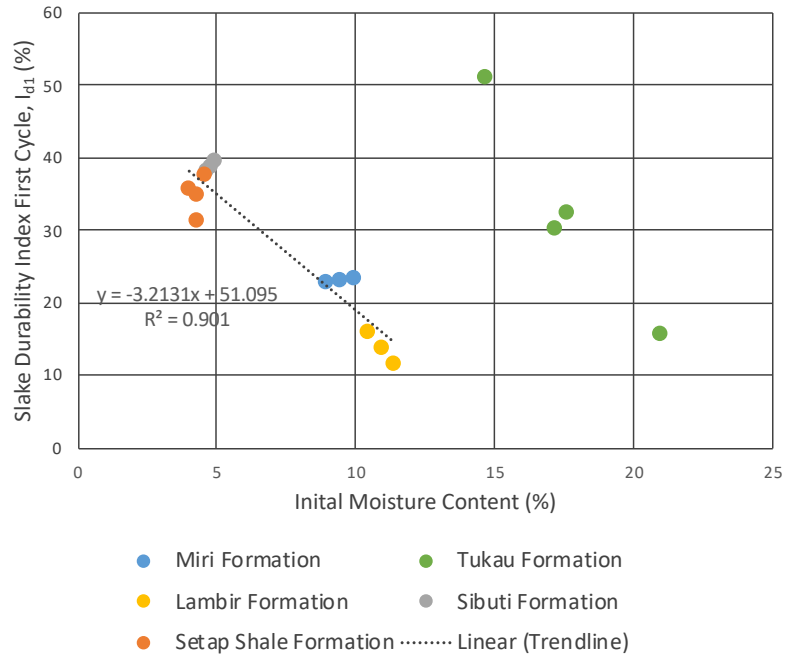
Figure 4.9: Correlation graph of durability index (I_{d1}) and initial moisture content.

The summary of the physical properties of all the studied shales are presented in Table 4.8. The current study shows that the durability classification by Franklin et al. (1972) is more significant and useful in classifying durability. Based on the results of the first cycle durability index (I_{d1}), the increasing order of durability among the formations is Lambir (9.5 %) < Miri (23.0 %) < Tukau (32.1 %) < Setap Shale (34.8 %) < Sibuti (38.7 %). Thus, concluded that the lowest durability shale is from Lambir Formation and the highest durability shale is from Sibuti Formation. Further analyses also have been carried out on shale from these two formations to determine the mineralogy, geochemistry, and microtexture analysis. The results are discussed in Section 4.10 onwards.

Table 4.8: Summary of the physical properties for all the studied shales.

Physical Properties	Formation				
	Miri	Tukau	Lambir	Sibuti	Setap Shale
Age	Middle Miocene	Middle Miocene – Pliocene	Middle – Late Miocene	Miocene	Oligocene – Early Miocene
Particle Size Distribution (%)					
Clay	7.6	54.8	50.5	7.8	8.2
Silt	61.7	43.9	44.0	59.8	45.3
Sand	27.8	1.3	5.5	32.2	46.4
Textural Classification	Silty Shale	Clayey Shale	Clayey Shale	Silty Shale	Sandy Shale
Initial Moisture Content (%)	9.5	19.1	11.9	4.9	4.2
Specific Gravity	2.56	2.22	3.57	3.34	2.66
Atterberg's Limit					
Liquid Limit	34	44	41	32	33
Plastic Limit	20	20	20	20	17
Plasticity Index	14	23	21	12	16
Clay Activity	1.75 Active	0.46 Inactive	0.46 Inactive	1.50 Active	2.00 Active
Porosity (%)	ND	ND	21.24	9.07	ND
Permeability (mD)	ND	ND	21.27	5.44	ND
Slake durability Index					
I_{d1} *(%)*	23.0 Very Low	32.1 Low	9.5 Very Low	38.7 Low	34.8 Low

*ND: Not determined

Chapter 5: Mineralogical, Geochemistry, and Microtextural Analysis

5.1. Introduction

This chapter presents the mineralogy, chemical composition, and microtextural analysis of the highest and durable shale in the study area. The correlation between the results is discussed at the end of the chapter. Discussion on mineral composition, geochemistry, microtexture heterogeneities and voids to the rock durability are discussed in Section 5.5.

5.2. X-Ray Diffraction (XRD)

5.2.1. Bulk Mineralogy

Table 5.1 presents the bulk mineralogy of shales with the lowest and the highest durability. Both shales were composed of mainly of quartz (48 – 52 %), muscovite/illite (16 – 22 %) and amorphous minerals (10 – 16 %). Albite and smectite minerals are not present in the shales of Lambir Formation, while K-feldspar is only found as a trace mineral. Figure 5.1 illustrates percentage difference in mineralogy between the two shales. The difference in relative mineralogy percentage between Lambir and Sibuti Formation are pyrite by 148 %, kaolinite by 41 %, illite by 29 %, chlorite by 6 %, and quartz by 5 %. The percentage difference in amorphous materials between the two shales is 45%. Both shales contain the same amount of anatase minerals.

Table 5.1: Results of XRD analysis for shales of lowest (Lambir) and highest (Sibuti) durability

Mineral abundance (wt. %)	Geological formation	
	Lambir Formation	Sibuti Formation
Quartz	51.3	48.7
Muscovite/Illite	22.0	16.5

Mineral abundance (wt. %)	Geological formation	
	Lambir Formation	**Sibuti Formation**
Amorphous	10.0	15.8
Albite	not detected	5.6
Kaolinite	7.9	5.2
Chlorite	5.4	5.1
K feldspar	trace	1.0
Smectite	not detected	1.0
Anatase	0.7	0.7
Pyrite	2.7	0.4
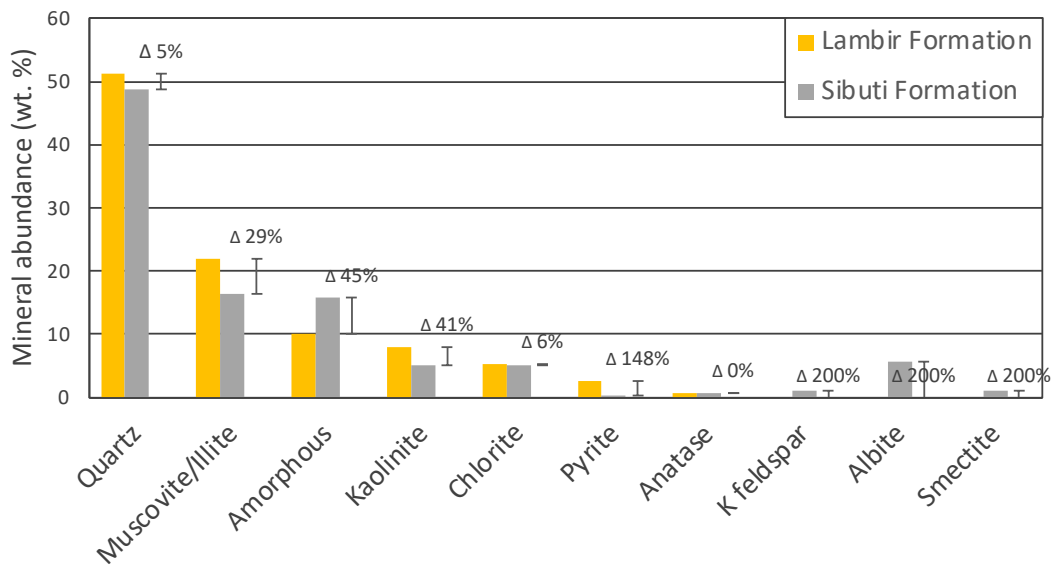
Figure 5.1: Comparison of relative minerals abundance in shales from Lambir and Sibuti Formation. Percentage difference (Δ %) refers to the ratio of absolute difference to average of the two numbers.

5.2.2. Clay Speciation

Clay minerals are generally separated into five groups: kaolinite, mica, smectite, vermiculite, and chlorite. Precise identification of clay minerals is necessary as most clay minerals contain defects or disorders, which are hard to be modelled using untreated XRD patterns. The changes in X-ray diffraction patterns of clay minerals for air dried and glycolated treatment can be referred in Figure 5.2. Table 5.2 presents

94

results of XRD clay speciation analysis of clay fraction <4 µm, treated with ethylene glycol for Lambir and Sibuti formations. Illite is the most abundant clay minerals followed by kaolinite, chlorite and smectite. Figure 5.3 compares the percentage difference in clay minerals abundance between the two formations. The percentage differences in relative clay minerals abundance between the two shales are smectite by 200% , chlorite by 25 %, illite by 17 %, and kaolinite by 5 %. Smectite is not detected in the Lambir Formation.
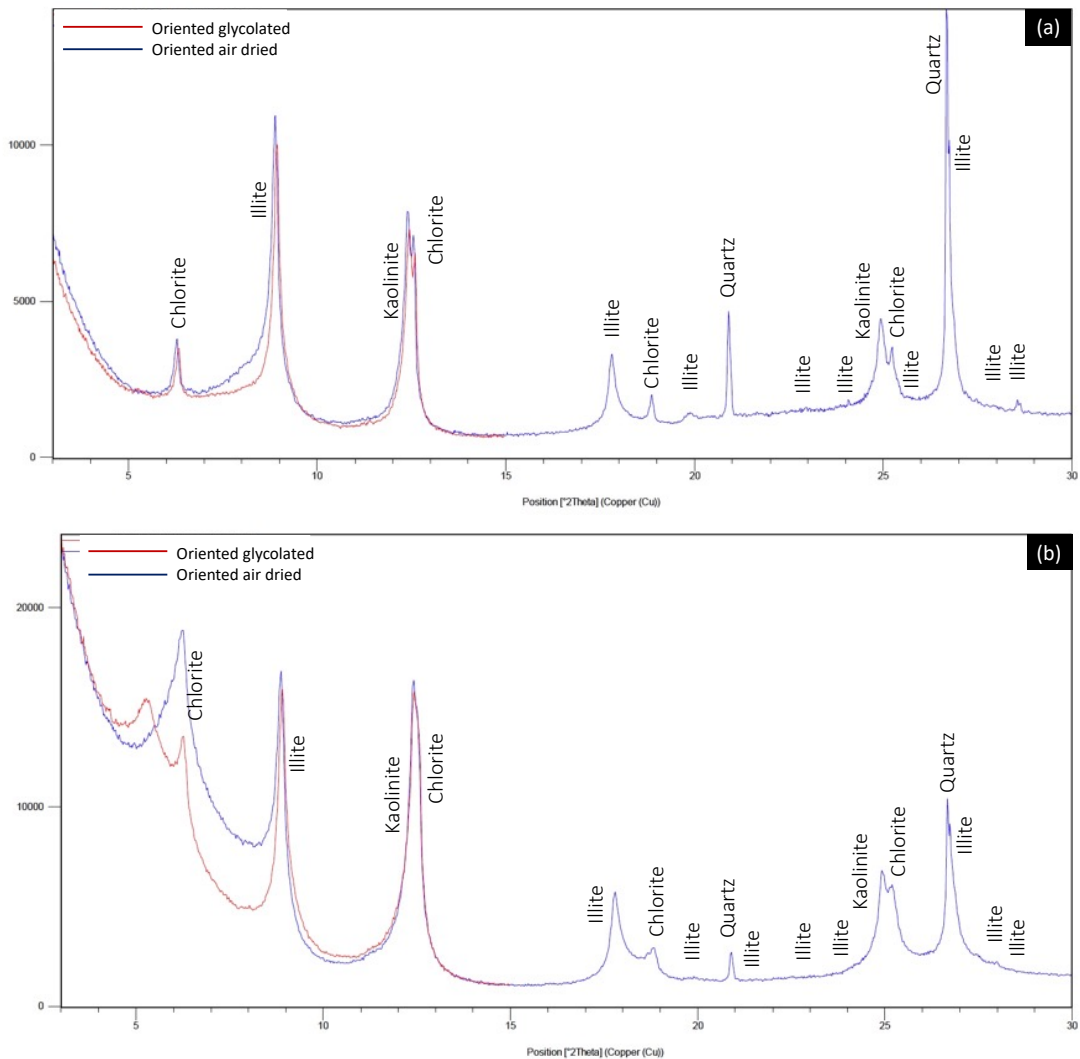
Figure 5.2: X-ray diffraction patterns of clay minerals during clay speciation analysis (a) Shale in Lambir Formation; (b) Shale in Sibuti Formation.

Table 5.2: Results of clay speciation analysis for shales of lowest (Lambir) and highest (Sibuti) durability.

Relative abundance of clay minerals (wt. %)	Geological formation	
	Lambir Formation	Sibuti Formation
Illite	65	55
Kaolinite	21	22
Chlorite	14	18
Smectite	not detected	5
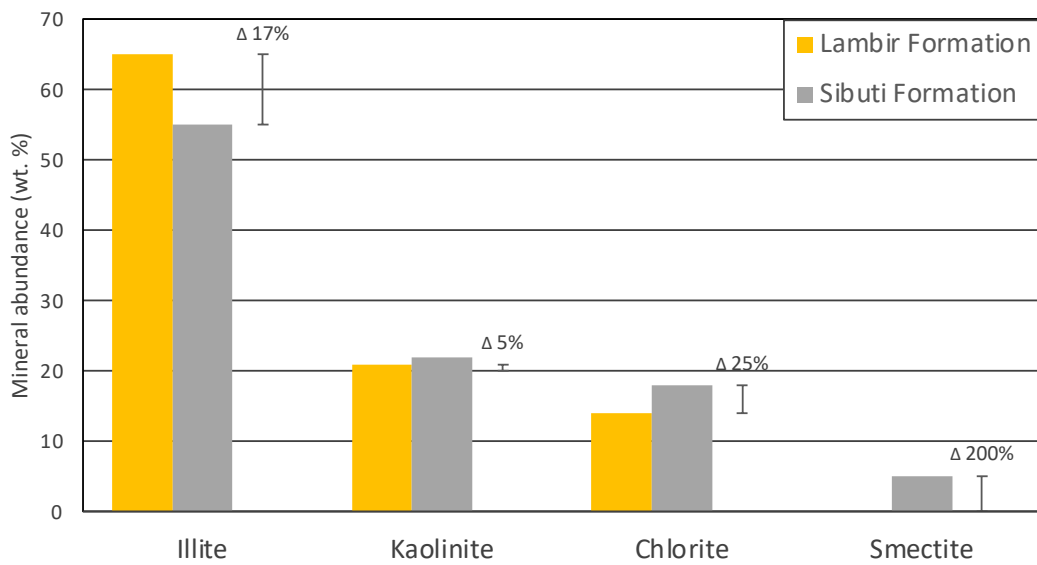
Figure 5.3: Comparison of relative clay minerals abundance in shales of Lambir and Sibuti Formation. Percentage difference (Δ %) refers to the ratio of absolute difference to average of the two numbers.

5.3. X-Ray Fluorescence (XRF)

5.3.1. Element Oxides/Bulk Rock Composition

Table 5.3 presents the results of the XRF analysis of shales in the Lambir and Sibuti formations. The major element oxides in the shale samples are SiO_2 (60 – 62 %), Al_2O_3 (16 – 18 %), Fe_2O_3 (4 – 6 %), K_2O (4 – 6 %), and MgO (1 – 2 %). The proportions of other chemical components, including TiO_2, Na_2O, P_2O_5, MnO, CaO, and Cr_2O_3 are relatively lower and within 0.01 - 0.80 %. Co_3O_4, CuO, and NiO exist in less than 0.005 %. Loss of Ignition (LOI) values for the shales are in the ranges of 10.60 – 11.27 Wt. %

and 8.00 – 8.47 Wt. % for Lambir and Sibuti Formation respectively. The higher LOI values for the Lambir Formation could be due to higher organic matter, carbonates, or clay materials (Heiri et al., 2001). In this case, mainly may be controlled by organic matter and/or clay minerals. Figure 5.4 shows elemental oxides distribution by percentage in each shale samples. Lambir Formation has a higher percentage of Al_2O_3 compared to the Sibuti Formation. The percentage of Fe_2O_3, MgO, CaO, and Na_2O is higher in the Sibuti Formation compared to the Lambir Formation.

Table 5.3: Geochemical composition of shales from Lambir (Lowest durability) and Sibuti formations (highest durability)

Element oxides (in wt. %)	Geological formation			
	Lambir Formation		Sibuti Formation	
	Set 1	Set 2	Set 1	Set 2
SiO_2	60.71	60.26	61.88	60.45
Al_2O_3	18.34	18.00	16.14	17.17
Fe_2O_3(T)	4.03	4.16	5.76	6.05
K_2O	3.05	2.98	2.60	2.74
MgO	1.04	1.05	1.83	1.97
TiO_2	0.80	0.77	0.79	0.81
Na_2O	0.13	0.13	0.66	0.60
P_2O_5	0.06	0.06	0.07	0.07
V_2O_5	0.025	0.025	0.020	0.021
MnO	0.018	0.016	0.048	0.050
CaO	0.01	0.01	0.70	0.68
Cr_2O_3	0.01	0.01	< 0.01	< 0.01
Co_3O_4	< 0.005	< 0.005	< 0.005	< 0.005
CuO	< 0.005	< 0.005	< 0.005	< 0.005
NiO	< 0.003	< 0.003	< 0.003	< 0.003
LOI	10.60	11.27	8.00	8.47
Total	98.83	98.75	98.51	99.09
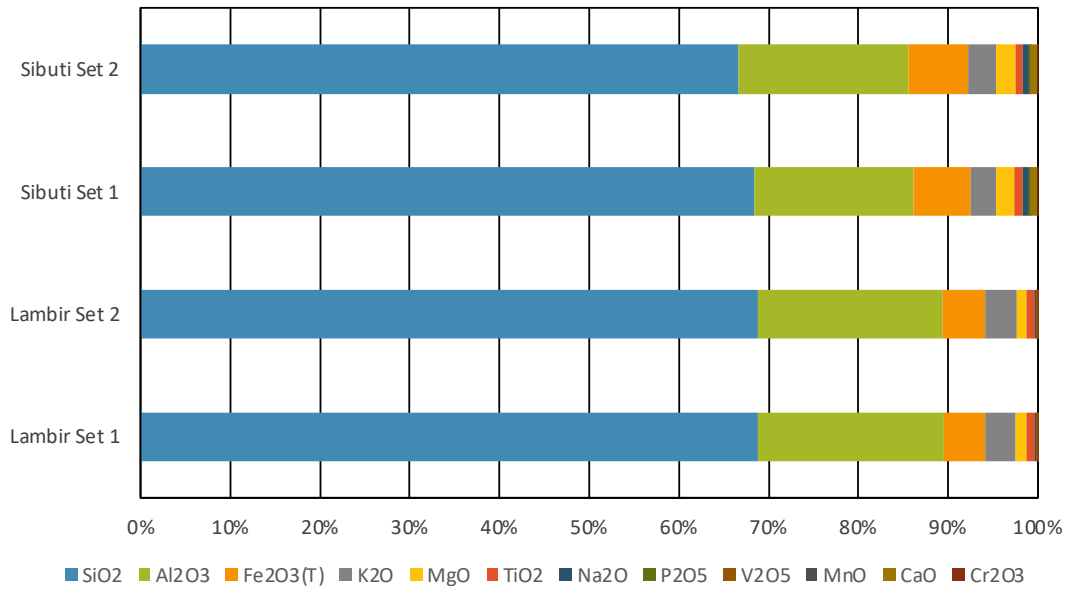
Figure 5.4: Distribution of elemental oxides composition of shales by percentage in Lambir and Sibuti formations.

5.3.2. Geochemical Classification

On the field, shales are distinguished from other fine-grained sedimentary rocks by their fissility and lamination. Meanwhile, geochemical classification is used to classify sedimentary rocks based on their chemical composition. Herron (1988) geochemical classification is the most widely used scheme to classify terrigenous sands and shales. The concentration ratios used are log Fe_2O_3/K_2O and log SiO_2/Al_2O_3 ratios, which indicate mineralogical stability and mineralogical maturity respectively. The plot of log ratios of Fe_2O_3/K_2O against SiO_2/Al_2O_3 shows that samples from the Lambir and Sibuti Formation falls within the shale field (Figure 5.5).
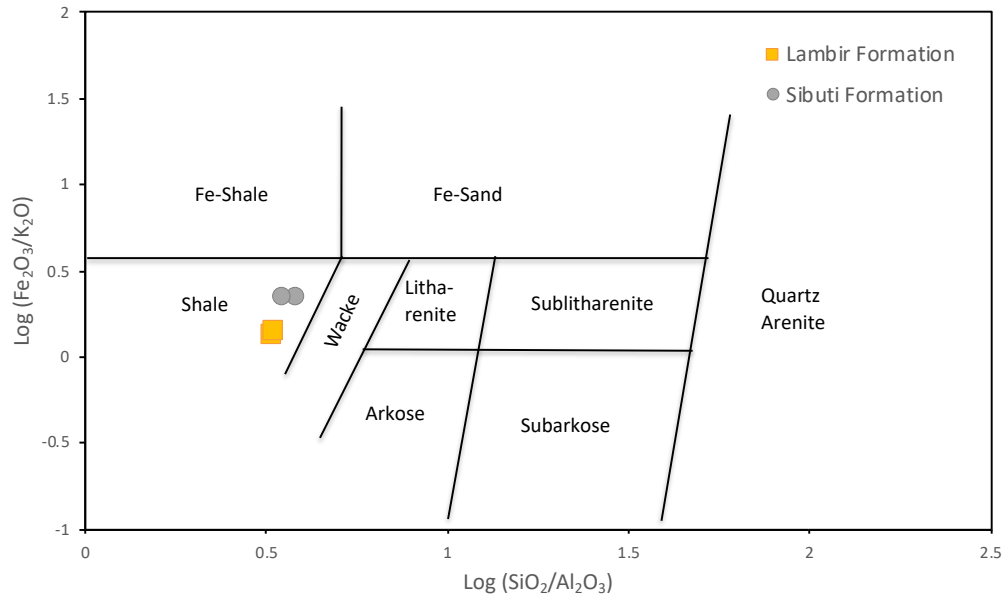
Figure 5.5: Geochemical classification of terrigenous sands and shales, after Herron (1988)

5.3.3. Chemical Weathering Indices

Chemical weathering indicators are used to characterise weathering profiles by calculating the molecular proportions of major oxide that is relatively stable, with one that is readily removed by weathering. Weathering Index of Parker (WIP) is based on the proportions of mobile alkali and alkaline earth metals such as sodium, potassium, magnesium, and calcium. Vogt's Residual Index (V) is used in assessing the maturity of clays as residual sediment while the Chemical Index of Alteration (CIA) used the extent of feldspars to clays conversion. The Chemical Index of Weathering (CIW) is similar to CIA, except that K_2O is eliminated from the equation to remove the effect of diagenesis. Table 5.4 presents the calculated chemical weathering indices for shales of the Lambir and Sibuti formations. These indices are used by geochemists to study the weathering that happened in geological times and gave rise to the sediments that formed the rocks (i.e., the weathering of the source rocks of the grains in the shales). Accordingly, the source area of the Sibuti and Lambir formations was undergone moderate and intensive weathering respectively during their deposition. However, it is not a reflection of the present-day weathering. The individual element mobility will give a clear picture in comparison to the bulk rocks after natural slake durability test is conducted.

Table 5.4: Chemical indices values of shales from Lambir and Sibuti Formation

Chemical weathering indices	Optimum fresh value	Optimum weathered value	Geological formation			
			Lambir Formation		Sibuti Formation	
			Set 1	Set 2	Set 1	Set 2
Weathering Index of Parker (WIP) - Parker (1970)	> 100	0	33.78	33.43	38.42	39.44
Vogt's Residual Index (V) - Vogt (1927)	< 1	Infinite	7.96	7.73	2.78	2.86
Chemical Index of Alteration (CIA) - Nesbitt et al. (1982)	≤ 50	100	83.85	83.89	76.33	77.37
Chemical Index of Weathering (CIW) - Harnois (1988)	≤ 50	100	99.52	99.51	88.05	89.31

5.4. Microtextural Analysis

Microtextural analysis of shales is studied through hand specimen and thin section photomicrographs and scanning electron microscope (SEM) images. Visual descriptions of the rock features are characterised into the following: (i) grain size and matrix, (ii) lamination and particle orientation, (iii) fossil content, and (iv) porosity. Hand specimen photomicrographs are used to assess the overall texture of the rock up to 1 mm scale while thin section photomicrographs are used to study microfeatures up to 50 μm scale. Since the porosity of shales is generally very low, SEM images are used to study the pore distribution up to 1 μm scale.

5.4.1. Lambir Formation

5.4.1.1. Texture and fabric: parallel laminated shale – skeletal microfabric

Figure 5.6a shows the heterogeneity unit of the representative shale sample from the Lambir Formation. The laminations between silty layers (0.3 – 0.5 mm thickness) and

clay-rich matrix layer (1.6 – 3.3 mm thickness) are continuous, planar, and parallel. Silty layers have larger grains and appear lighter than finer and darker clay-rich matrix layers. Quartz laminae in the sample appear in patches. The sedimentary facies of the Lambir Formation is associated with tidal dominated environment (Abdul Rahman et al., 2019)).

Figure 5.6d shows the difference in grain sizes between the two laminations observed in the thin section. The top layer is the fine-grained clay-rich matrix layer, and the bottom layer is the coarse-grained silty layer. Calcite skeletal particles or fossils that can be distinguished due to their structures and high birefringence in cross polarised appear to be more abundant in the silty layer. Some clay-rich matrix layers are slightly calcareous (Figure 5.6e). Figure 5.6f shows lamination between the more abundant coal laminae, thin silty, and clay-rich layers. These gradational variations are due to the changes in the tidal energy variations during deposition.

In some layers, there is a more abundant black and flaky coal laminae with an orientation parallel to the lamination (Figure 5.6b, f). The preferred orientation of the coal laminae is disrupted or changed due to biogenic activity, post-depositional environment, or the presence of post-depositional sedimentary structures (Figure 5.6c). The types of coal laminae vary from organic matter (peat) to lignite depending on their maturity. The organic matter in the Neogene sediments of northern Borneo is immature to very early-mature in nature (Togunwa et al., 2015). Organic coal laminae are opaque in thin sections whereas lignite coal laminae are light to dark brown in thin sections (Figure 5.6f). Figure 5.6a, b shows microphotographs of the Lambir shale showing coal laminae appears as flaky black laminae in hand specimen.

The parallel orientation of the particles characterised the oriented fabric. The terms used in the fabric description of the sample are adopted from Olphen (1964), Edil (1988), Huppert (1988), Moon et al. (1995), and Jeremias (2000). The orientation of the particles shows a well-developed microlamination (Figure 5.6f). The grain-to-grain relations between the clay fabric are predominantly floating grains in a discontinuous matrix. Huppert (1988) characterised such fabric as skeletal

microfabric, where the clay is organised into aggregates, grain coatings, and connectors between silt size grains. The intergranular pores between the particles are irregular.
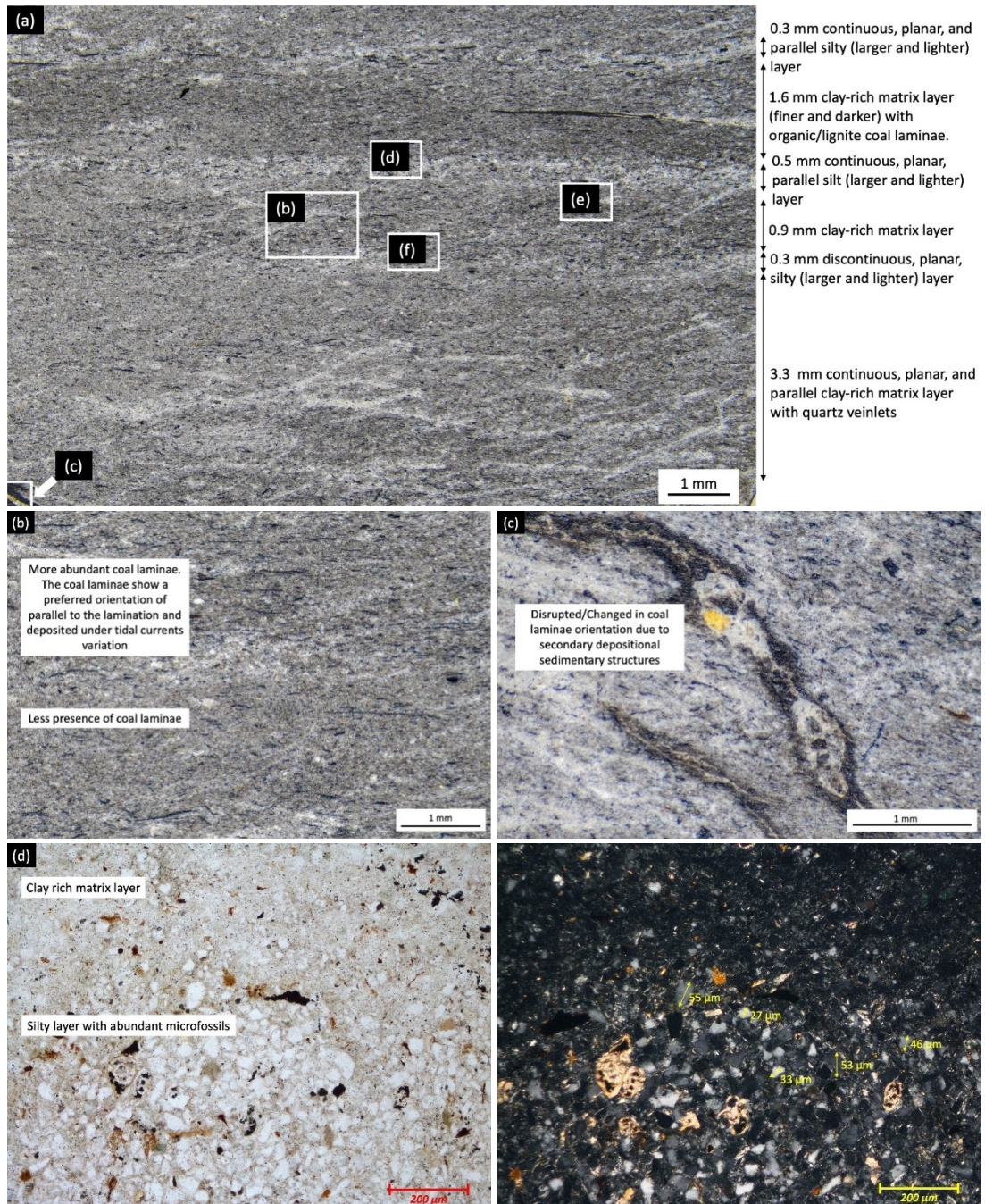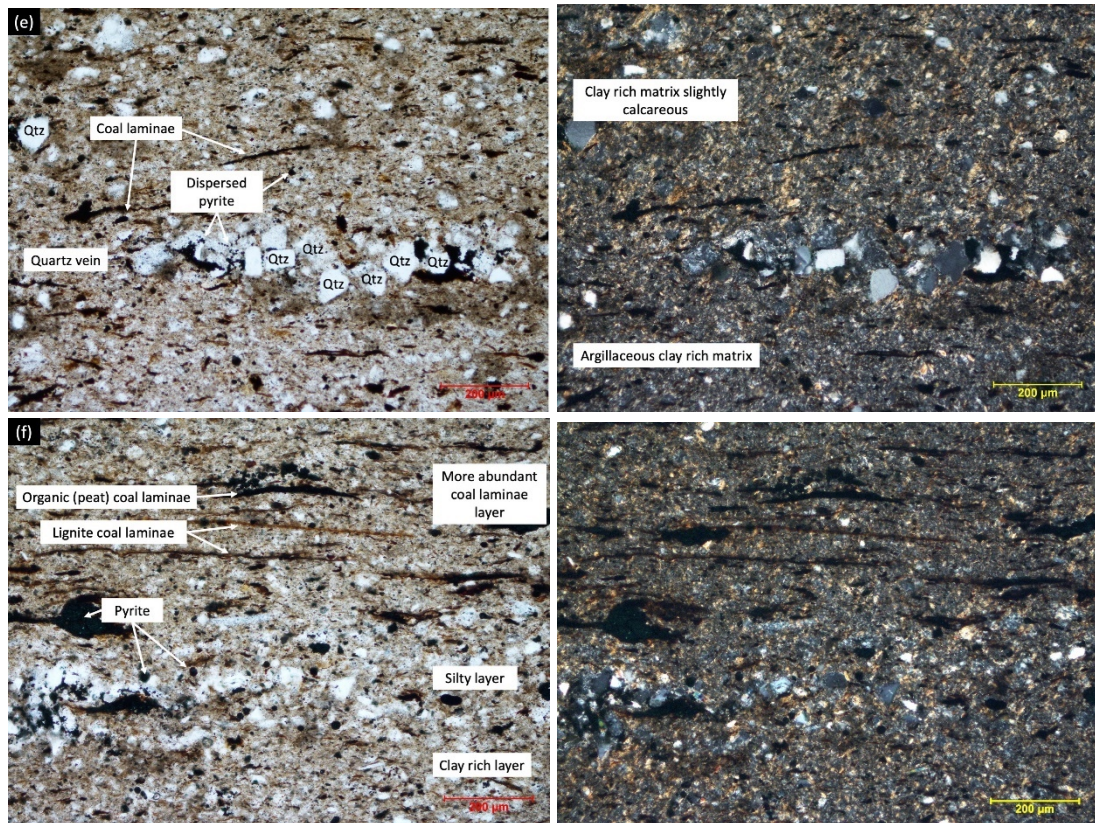
Figure 5.6: Side view microphotographs of the selected Lambir Shale sample, (a-c) in polished hand specimen and (e-f) in thin section [right: plane polarised (ppl); left: cross polarised (XPL)]. (**a**) Continuous, planar, and parallel lamination of silty and clay-rich layer. Quartz veinlets are observed at the bottom. (**b,f**) More abundant coal laminae shows a preferred parallel orientation to the lamination. (**c**) Disrupted/Changed orientation of coal laminae due to the presence of secondary sedimentary structures. (**d**) Difference in grains size between clay-rich and silty layers. Fossils are abundant in the larger silty layer. (**e**) Quartz vein formed in a patch. Pyrite and coal laminae are dispersed within the sample. (**f**) Lamination between more abundant coal laminae layer, thin silty layer, and clay-rich layer. These gradational variations are due to the changes in the tidal current during deposition.
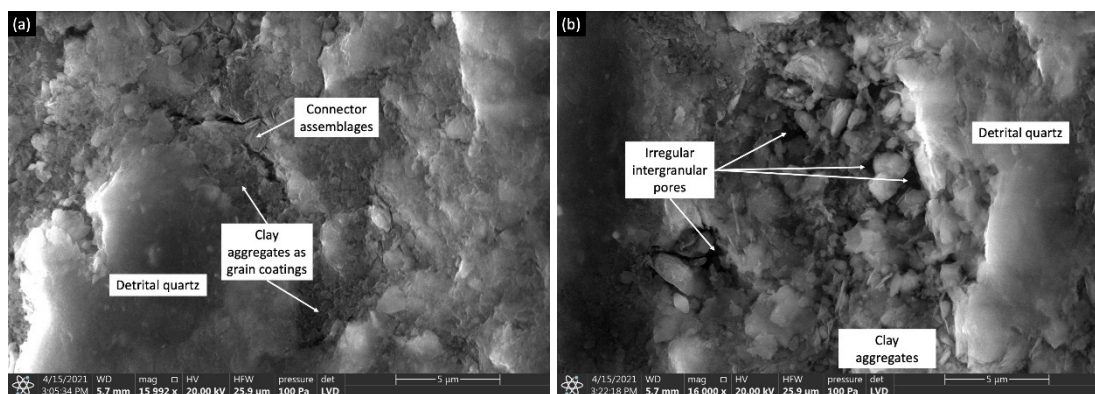
Figure 5.7: SEM photographs of the Lambir Shale showing skeletal microfabric. A.The matrix is discontinuous with clay minerals organised into aggregates, grain coatings, and connector assemblages between the particles. B. Intergranular pores between the particles are irregular.

5.4.1.2. Grain size, matrix, and composition – subrounded, low sphericity grains in the potassic clay (illite) matrix

The grain size of fine-grained rock such as shale can be challenging to study under the optical microscope. Larger grains of minerals such as quartz are typically used to note the roundness and size of the grains. Quartz grains in the Lambir shale sample are subrounded and have low sphericity. The sizes range from 1.6 to 50 μm. The grains are also poorly sorted. Some of the quartz crystals show inclusions of finer minerals, possibly chlorite, calcite, and biotite. Therefore, infer that the grains are detrital. Sedimentary rocks in this region are derived from recycled sedimentary/metasedimentary sources (Nagarajan et al., 2017a; Nagarajan et al., 2017b; Nagarajan et al., 2020).

The matrix surrounding the quartz grains is composed of very fine amorphous, colourless clay minerals (illite, kaolinite, and chlorite), and iron oxy-hydroxides. EDS mapping is carried out to identify the composition of the selected area of the sample. EDS map in Figure 5.9 shows that the clay matrix has a high composition of aluminium (Al) and potassium (K). Fine quartz grains can be seen in the silica (Si) and oxygen (O) elemental map. A localised pyrite framboids [iron (Fe) and sulphur (S) elemental map] can be seen distributed within the coal lamina [carbon (C) elemental map]. Other features that can be seen from the EDS map are the presence of magnesium (Mg) rich minerals and heavy minerals rutile/anatase [titanium (Ti) elemental map]. The Mg may be associated with the fossil fragments, which are made up of Mg-Calcite/dolomite. The presence of these heavy minerals in sedimentary rock of these regions has also been reported by Nagarajan et al. (2017b) as transported and reworked sources.
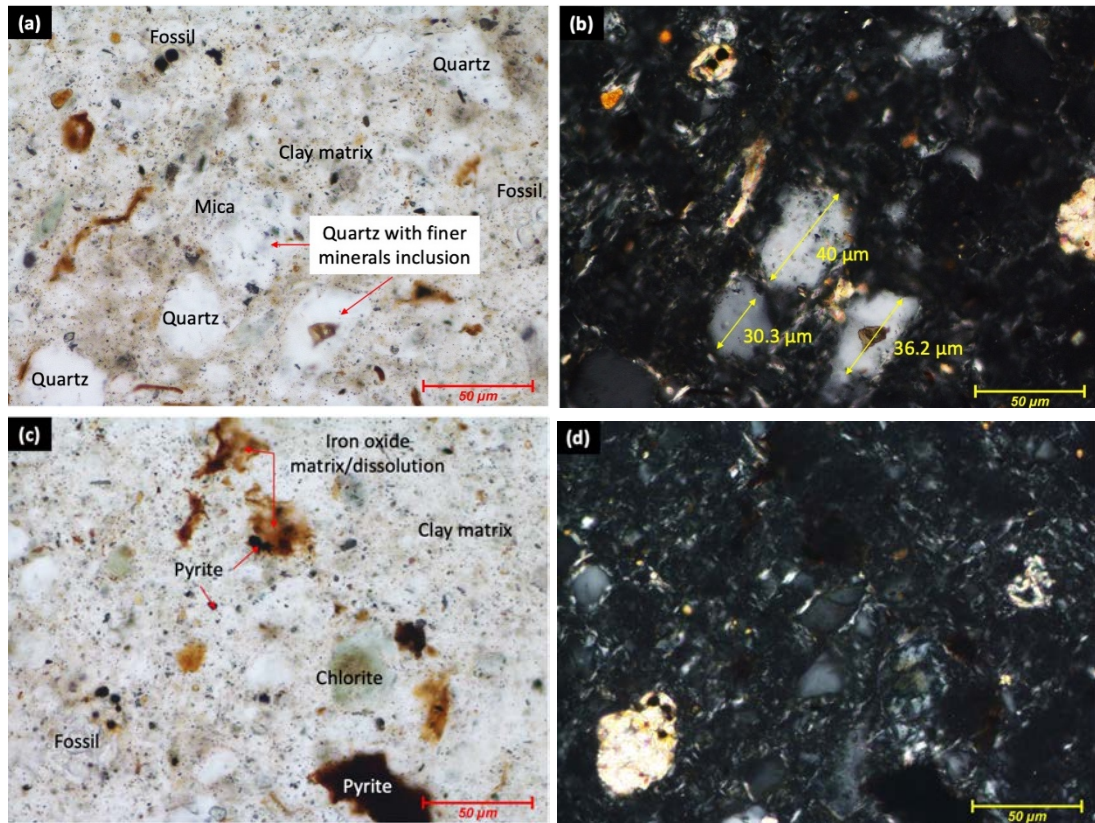
Figure 5.8: Thin section microphotographs of the representative Lambir Shale. (a,c) under plane polarised light, ppl. (b,d) under cross polarised light, xpl. Quartz grains are subrounded and have low sphericity. (a,b) Quartz grains in a colourless amorphous and clay minerals matrix. Some of the quartz grains show the inclusion of finer grain minerals. (c,d) Foraminifera and mineral grains in clay-rich matrix.
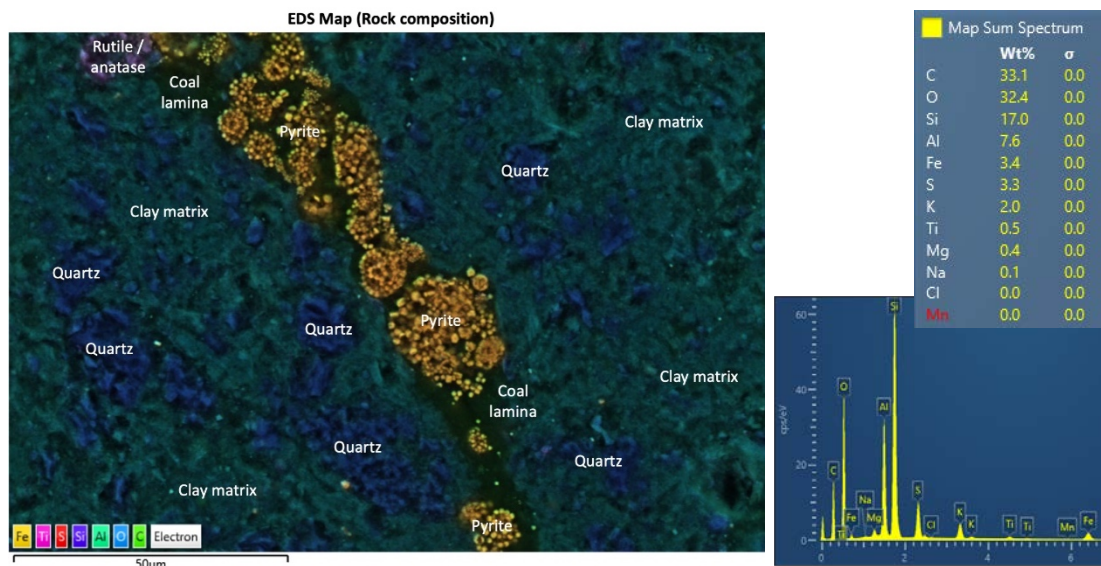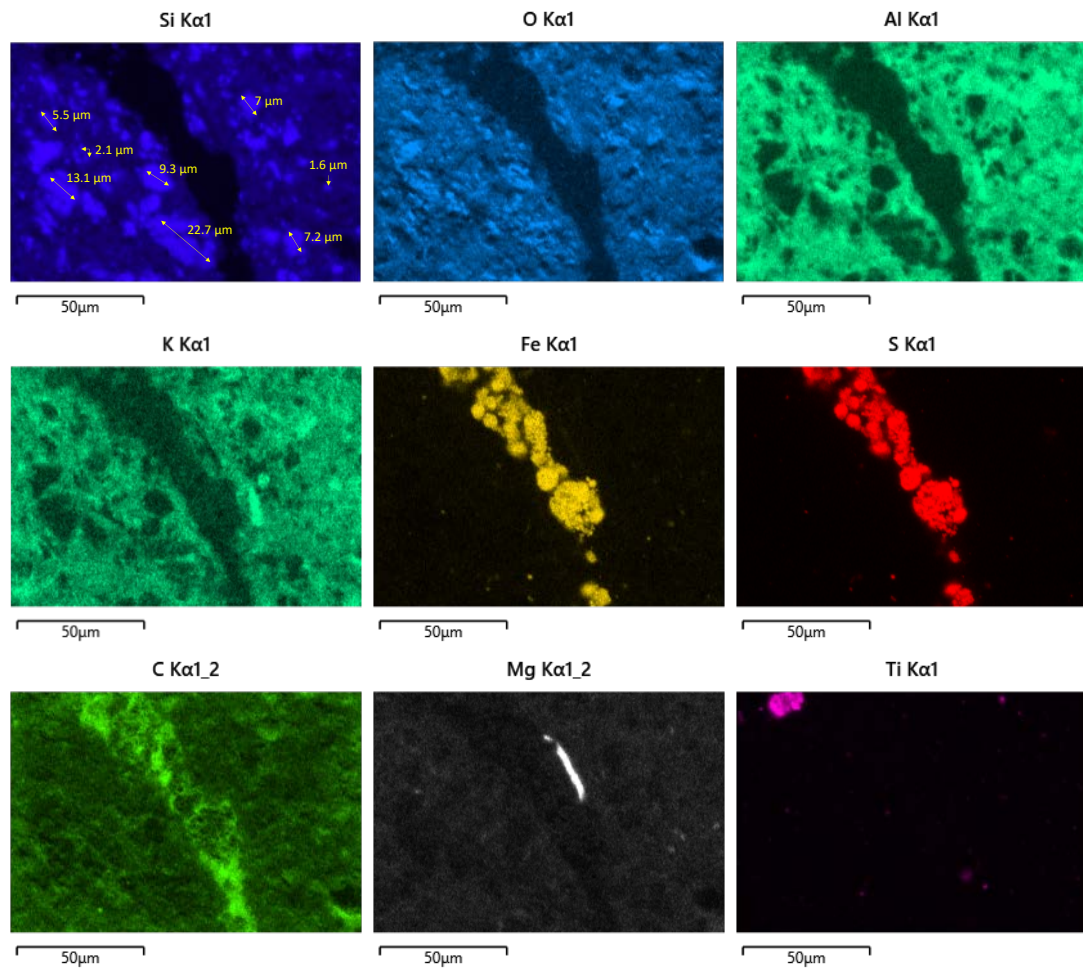
Figure 5.9: EDS layered map and its elemental maps. Quartz (corresponding to Si, O) are coloured blue; potassic clay matrix (corresponding to Al, K) are coloured minty green; pyrite framboids (corresponding to Fe, S) are coloured yellow and red; organic coal lamina (corresponding to C) are coloured bright green; K – illite, Na – kaolinite & smectite. Ti can be associated with residual clay minerals or controlled by heavy minerals. i.e. Rutile or anatase (Ti) are detrital minerals during sediment recycling.

A large amount of framboidal and equant pyrites (syngenetic and diagenetic; Liu et al. (2019) are found dispersed within the sample. Some are found localised within the fossils and coal laminae. Pyrites are typically less than 2 mm in size and deposited in a reducing/suboxic-anoxic deposition environment (Liu et al., 2019). They are opaque in a thin section and show high reflectance (bright yellowish spots) under refractive light (Figure 5.10). Pyrites can be identified from their metallic brassy yellow colour in microphotographs of hand specimens (Figure 5.11).
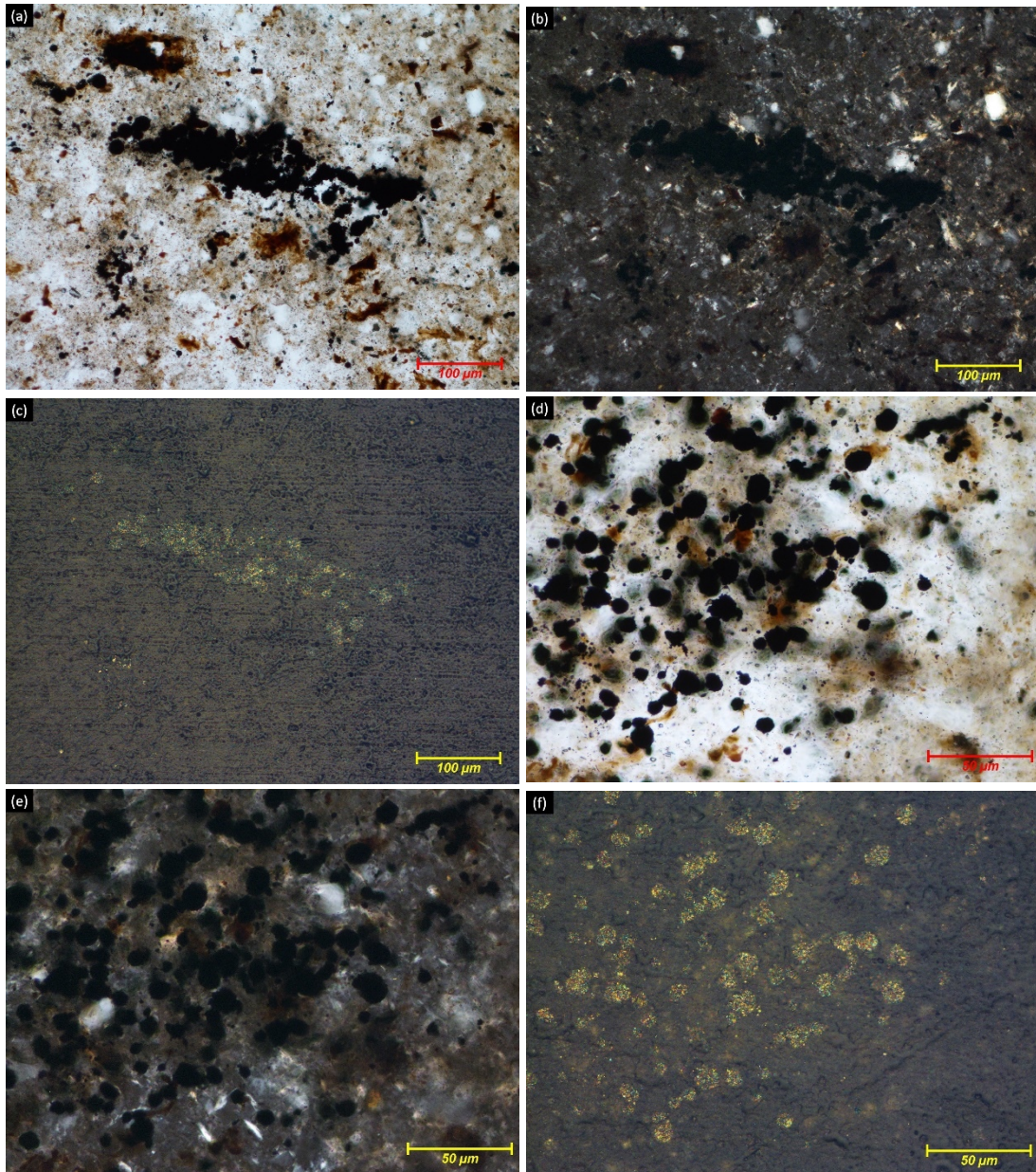
Figure 5.10: Thin section microphotographs of pyrites found in the Lambir Shale sample. (a, d) plane polarised (ppl); (b, e) cross polarised (xpl); (c,f) reflecting light. Pyrites are opaque minerals under polarised microscope view and have high reflectance of bright yellow under refracting light. (a,b,c) Aggregates and clusters of pyrites. (d,e,f) Discrete pyrites.
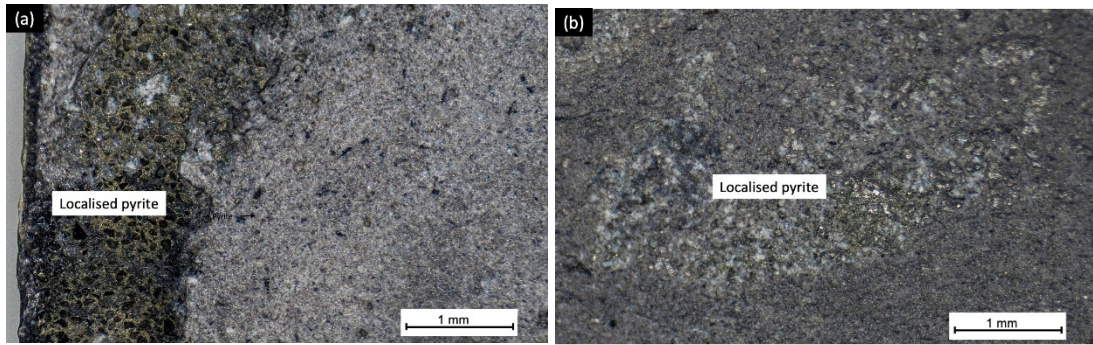
Figure 5.11: Polished hand specimen microphotographs of the localised pyrite found in the Lambir shale sample. The pyrites are metallic brassy yellow in colour. (a) From the plan view of the representative sample. (b) From the section view of the representative sample.

5.4.1.3. Fossils: benthic foraminifers

There is an abundant number of microfossils found within the sample. The well-preserved chambers of the foraminifera suggest rapid sedimentation during the deposition of the sediments. When the organism decomposes, its chambers are infilled with diagenetic calcite, pyrites and micro quartz. These minerals commonly occur as infill, typically within foraminifera chambers associated with organic materials (Buckman et al., 2020). Honza (1996) and Banda (1999) in their foraminiferal analysis, reported that the Lambir Formation belongs to Middle Miocene *Globorotalia (T.) peripheronda* Zone. Reported fossils found include *Orbulina suturalis, Orbulina universa, Sphaeroidinellopsis seminula seminula,* and *Sphaeroidinellopsis disjuncta*. The forams are more benthic than planktic corresponding to their deposition environment.
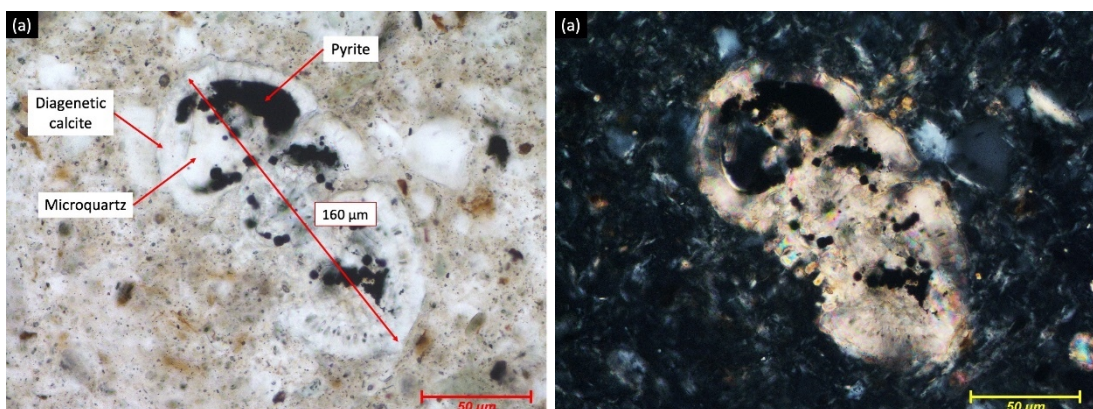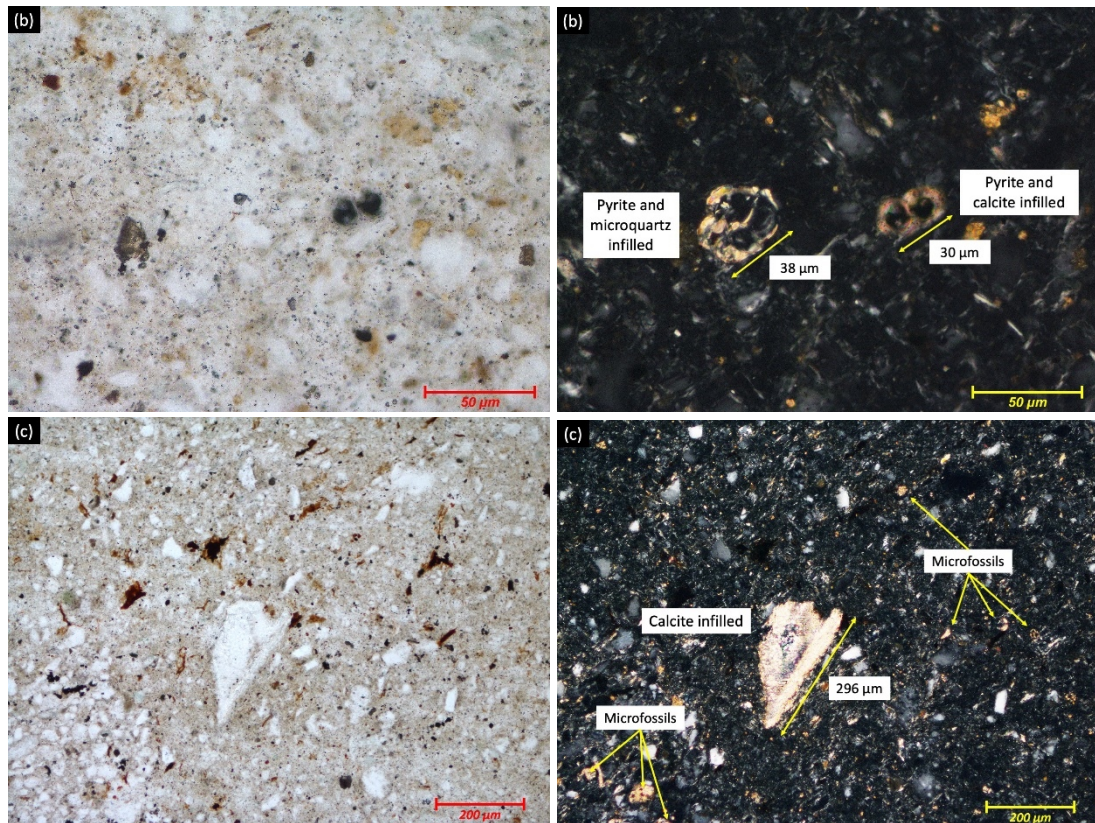
Figure 5.12: Thin section microphotographs of the Lambir Shale showing the presence of foraminifers. The fossils are infilled with calcite, pyrite and microquartz. Left: plane polarised (ppl), Right: cross polarised (xpl).

5.4.1.4. Porosity

The overall observations from SEM images of the shale from the Lambir Formation show that the porosity is mainly comprised of an abundant number of micro-pores. The pore sizes range from 0.2 µm up to 2.3 µm. Some of these pores have been filled by pore-filling clay minerals. Figure 5.13(h, i) shows the pore distributions between the grains. Wang et al. (2019) found that positive correlations between clay content and organic matter to porosity are partly due to the organic and clay-associated pores. A similar observation is seen in the Lambir shale (Figure 5.13). This is due to the nature of the particles that created macro-pores within its sheets and along with the grain-to-grain contact. In addition, since permeability depends upon how well the pore network is interconnected, the presence of microfractures in the sample increases its permeability (Figure 5.13f, g). Some of the microfractures have also have been infilled by pore-filling clay minerals.
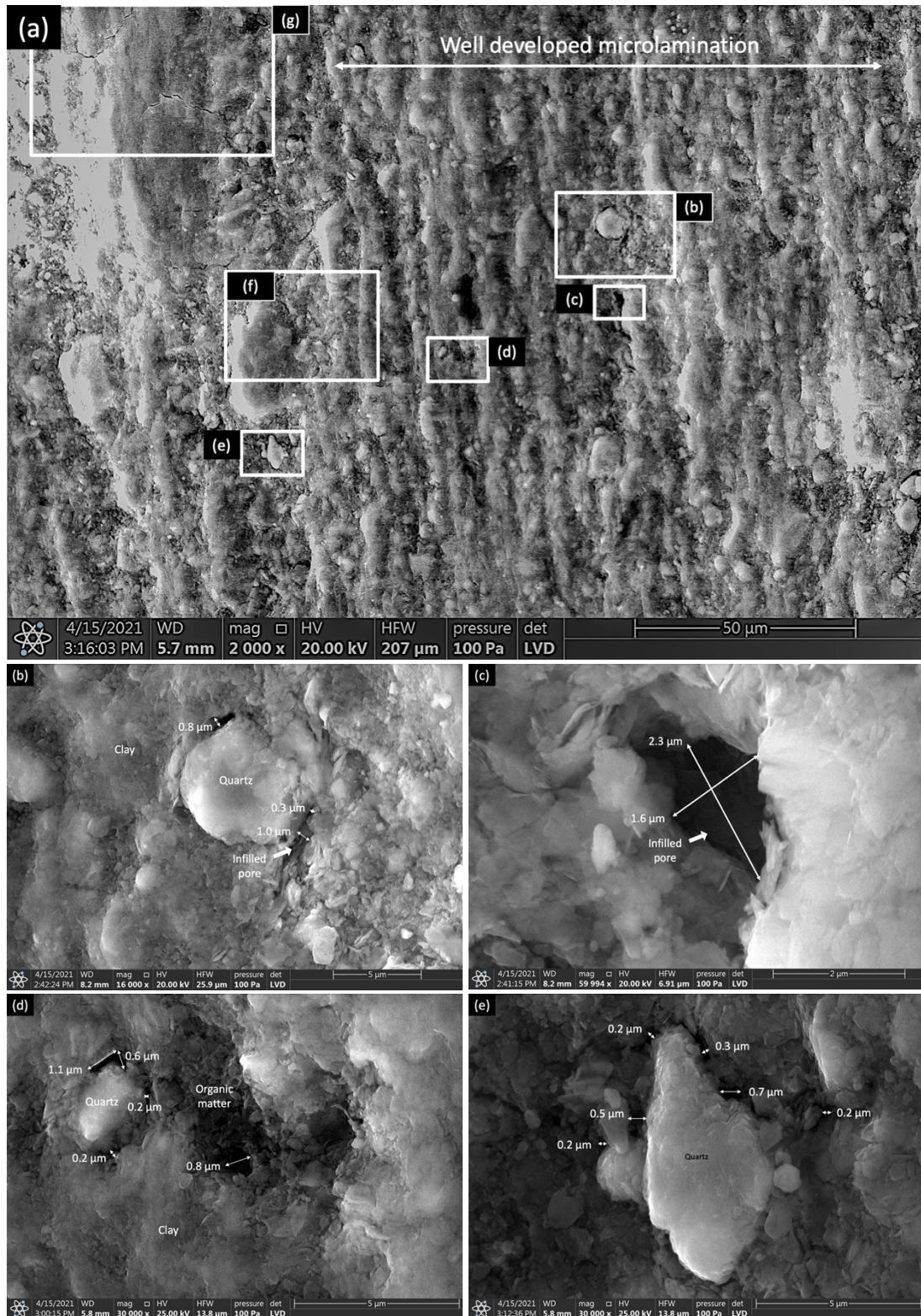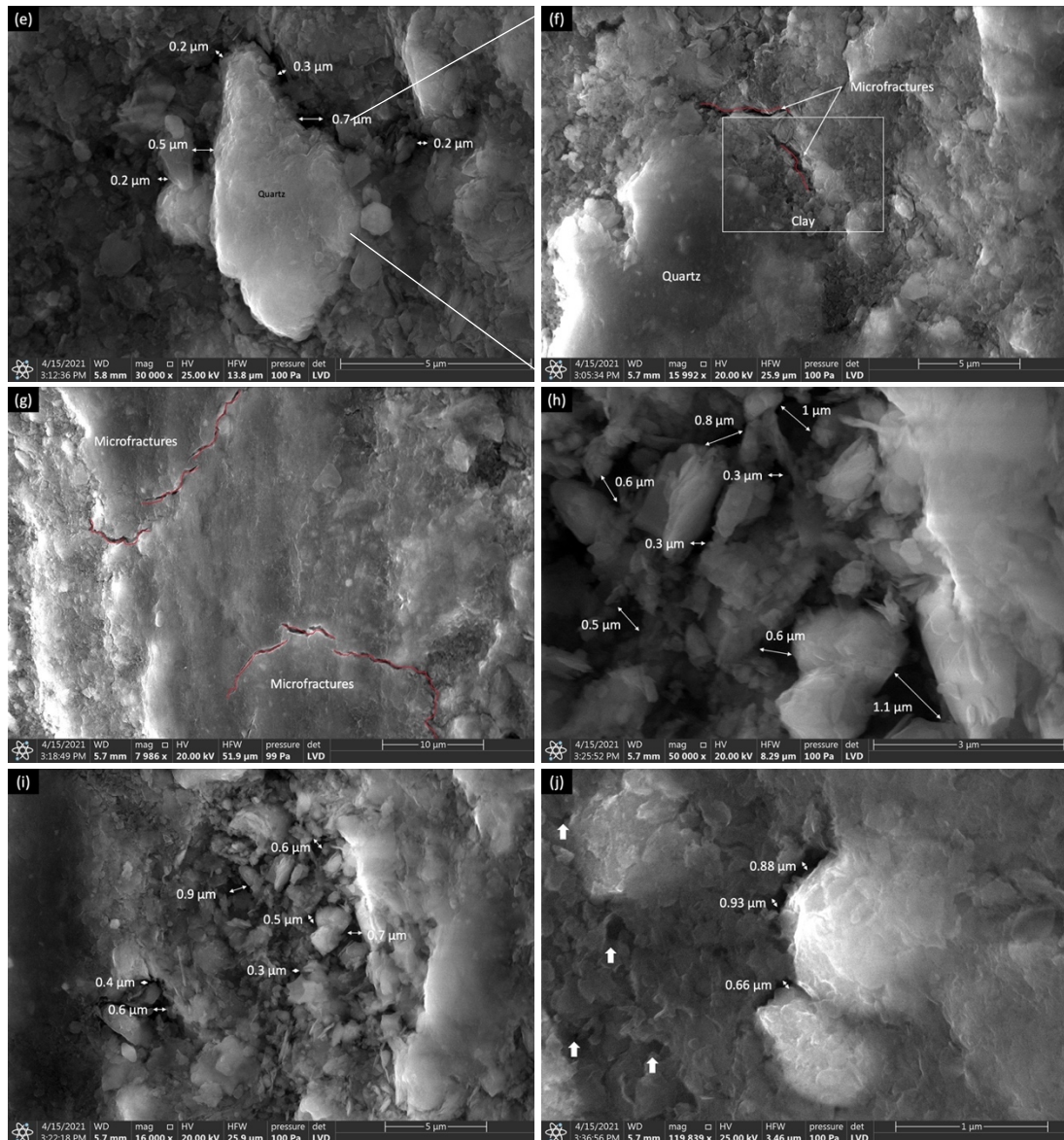
Figure 5.13: SEM images of the representative shale sample from the Lambir Formation. **(a)** Image showing the overall image of an area in the shale sample under 2000 x magnification. **(b-e)** Images showing the visible micro-pores between the grains. **(f-g)** Images showing the presence of microfractures in the sample. **(h-i)** Images showing the distributions of the micropores within the matrix in shale. **(j)** Image shows the nanopores within then organic matter and clay aggregates (in arrow).

5.4.2. The Sibuti Formation

5.4.2.1. Texture and fabric: parallel laminated shale – turbostratic microfabric

Figure 5.14 shows the heterogeneity unit of the representative shale sample from the Sibuti Formation. There are more gradational variations within the sample

between mid-grey to dark grey layers. Thin section microphotographs reveal that the layers are fine-grained with a slightly calcareous and argillaceous clay matrix. There is also a thin layer of slightly denser opaque minerals. Continuous and discontinuous quartz veinlets are observed within the sample. The depositional environment of the Sibuti Formation is associated with shallow marine shelves (Khor et al., 2014).

Figure 5.15 shows the continuous, planar, and parallel lamination within the sample. The particles appear in an oriented fabric instead of random. From the microphotographs of the thin section, the layers that made up the unit are a slightly calcareous layer, argillaceous clay-rich matrix, and a larger silt-sized grain layer with more abundant opaque minerals. Some opaque minerals are pore filled in nature and are oriented relatively parallel to lamination.

The microlaminations are well developed in the sample. The clay particles occur in both grain-to-grain contacts and floating grains. The clay matrix is continuous in which the clastic grains are completely immersed. The clay particles are forced into a tight face-to-face contact, moulding around the grain (Figure 5.16). Huppert (1988) suggested the term turbostratic microfabric for such fabric arrangement. Elongated micropores dominate the pore space.
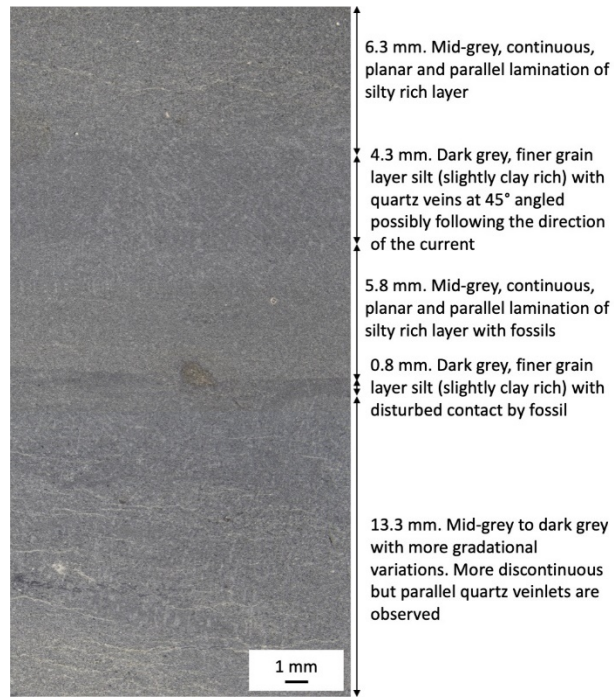
Figure 5.14: Microphotograph of the polished slab shale samples of the Sibuti Formation. The sample is polished to reveal subtle sedimentary features of the rock. Parallel lamination between dark-grey (fine-grained) and mid-grey (slightly larger grained than dark-grey laminae) are observed. Quartz veinlets and specks of microfossils can also be seen.
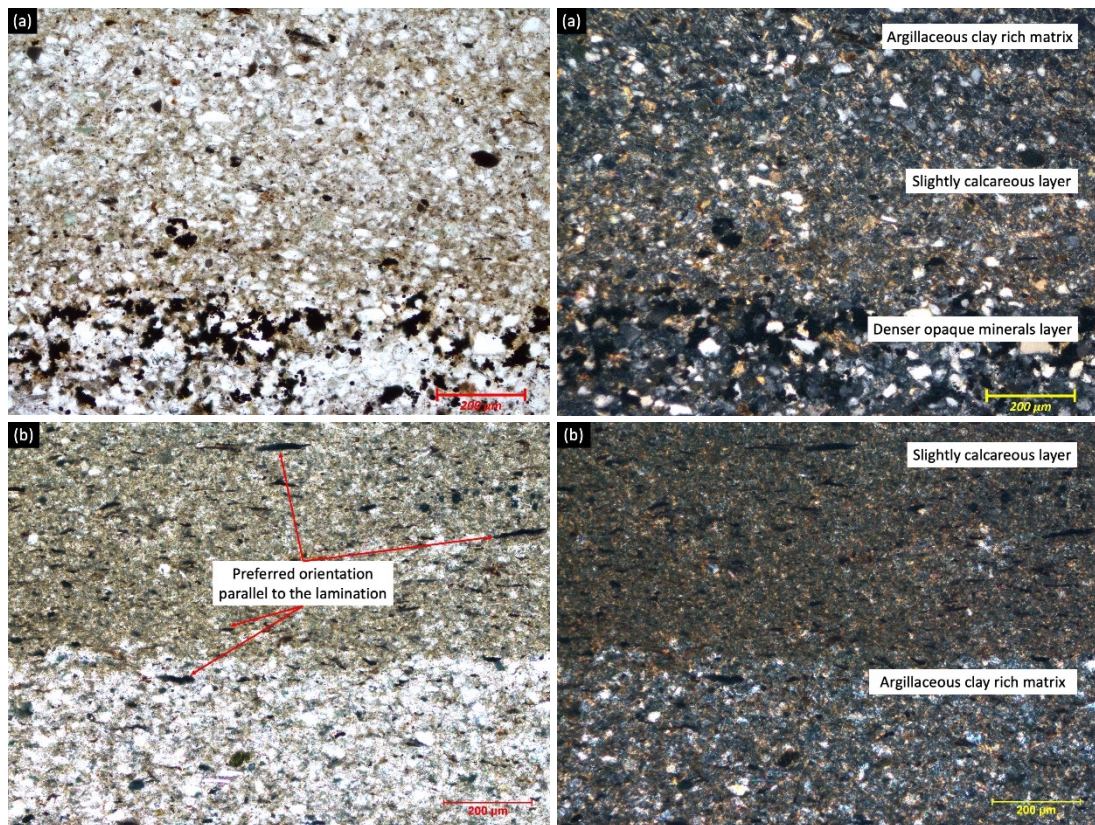
Figure 5.15: Thin section microphotographs of the representative shale sample of the Sibuti Formation. Left: plane polarised (ppl); Right: cross polarised (xpl). (**a**) Parallel lamination

between argillaceous clay-rich matrix, slightly calcareous, and denser opaque minerals layer. (**b**) Mineral particles show a preferred orientation parallel to the lamination of slightly calcareous and argillaceous clay-rich matrix layers.
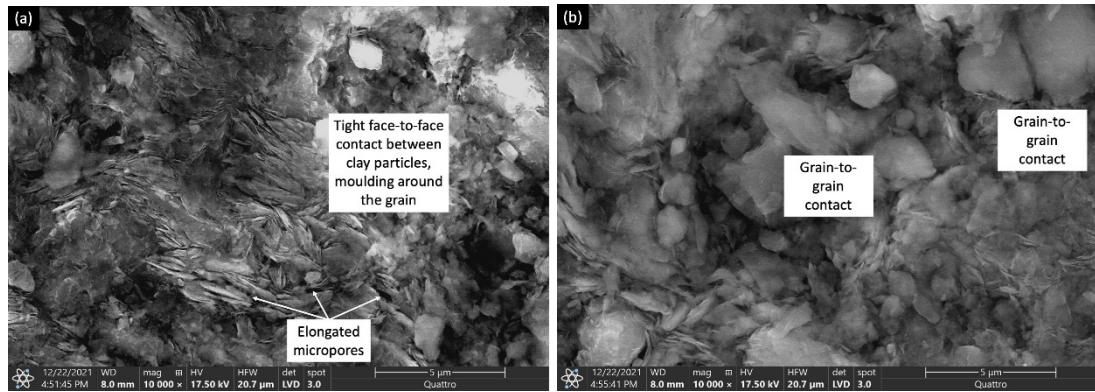
Figure 5.16: SEM photographs of the representative shale sample of the Sibuti Formation showing turbostratic microfabric. (**a**) The clay matrix is continuous with the clay particles arranged tightly face-to-face, moulding around the grain. Pore spaces are dominated by elongated micropores. (**b**) There are grain-to-grain contacts between the particles.

5.4.2.2. *Grain size, matrix, and composition: angular, low sphericity in potassium, magnesium, and calcite rich clay matrix*

Fine-grained rocks like shale can be difficult to investigate under an optical microscope because of their grain size. Larger grains, such as quartz, are commonly used to describe the roundness and size of the grains. Quartz grains in the representative Sibuti shale sample are angular and have low sphericity. The size of the quartz grains is between 4.5 and 50 µm (Figure 5.17). The particles are moderately sorted. More quartz can be seen in the Sibuti Shale sample compared to the Lambir shale sample. The Neogene sedimentary rocks are formed from recycled sedimentary/metasedimentary sources (Ramasamy Nagarajan et al., 2017a; Ramasamy Nagarajan et al., 2017b; Nagarajan et al., 2020) and thus show angular grains.
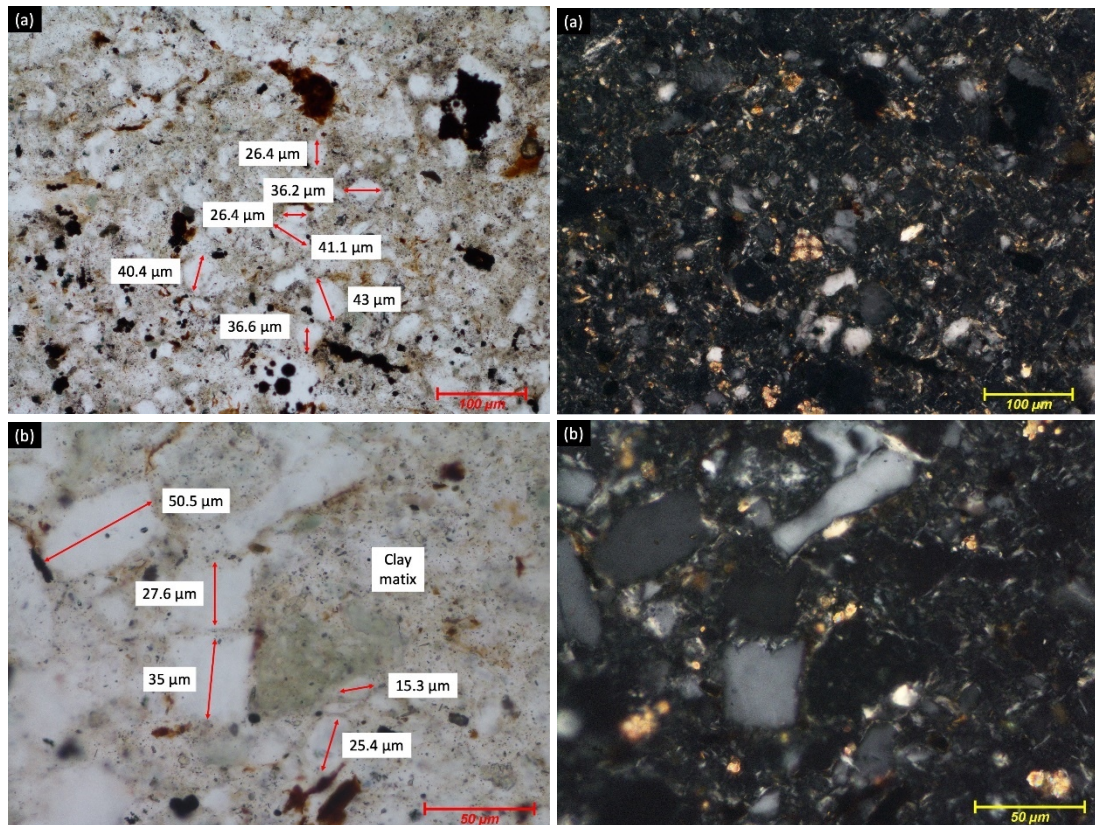
Figure 5.17: Thin section microphotographs of the grain sizes of the representative of the Sibuti Shale. The particles are angular with low sphericity and are moderately sorted in clay matrix. Left: plane polarised (ppl), Right: cross polarised (xpl).

The matrix surrounding the quartz grains is composed of very fine amorphous and colourless clay minerals (illite, chlorite and kaolinite,). EDS mapping is carried out to determine the elemental composition of the matrix. The clay minerals from XRD analysis reveal the presence of illite, kaolinite, chlorite, and smectite. The clay matrix from EDS mapping shows a higher percentage of potassium (K), magnesium (Mg), calcium (Ca), and sodium (Na). Potassium-rich clays are commonly represented by illite while sodium and magnesium rich clays are commonly represented by kaolinite and smectite. Pyrites occurrence in the sample is concentrated within the organic-rich layer and are formed by syngenetic and digenetic processes (Liu et al., 2019). Organic matter plays an important role in fambroid formation (Sawlowicz, 2000). There is also the presence of scattered heavy minerals rutile/anatase [titanium (Ti) elemental map] within the sample.

EDS Map (Rock composition)
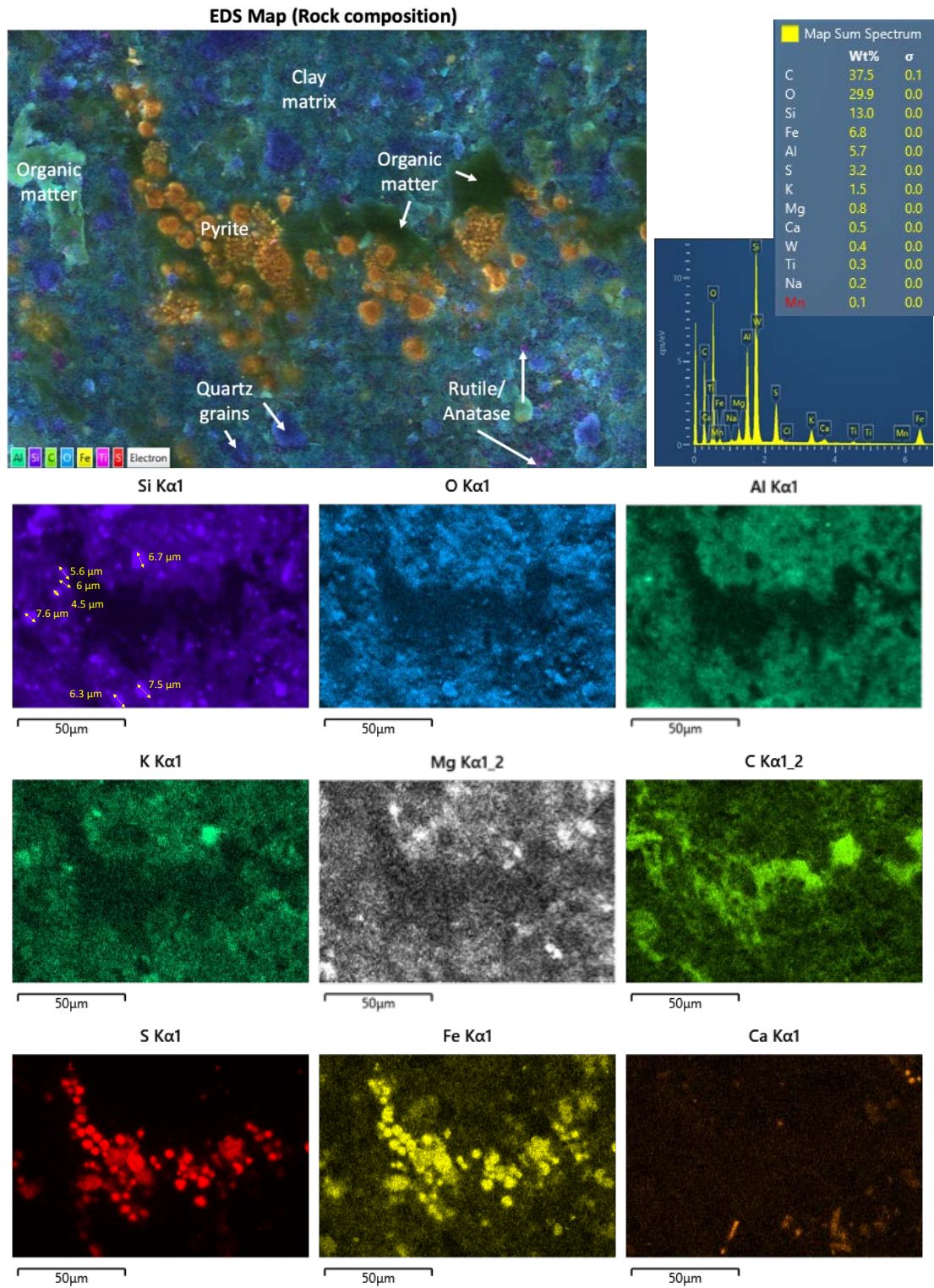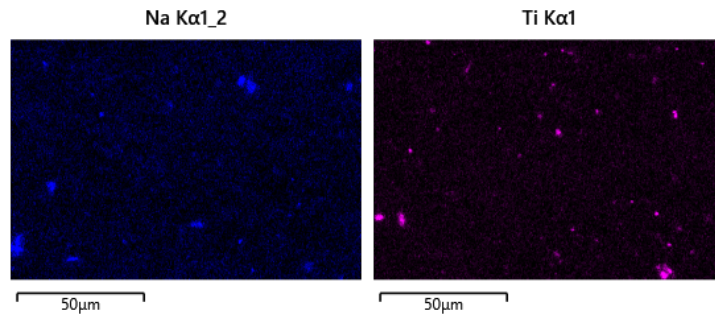
Figure 5.18: EDS layered map and its elemental maps. Quartz grains (corresponding to Si, O) are coloured blue; K-Mg rich clay matrix (corresponding to Al, O, K) are coloured minty green and white; pyrites (corresponding to Fe, S) are coloured yellow and red; organic matter (corresponding to C) are coloured bright green; calcite (corresponding to Ca) are coloured orange; K – illite, Na – kaolinite & smectite. Ti can be associated with residual clay minerals or controlled by heavy minerals. Rutile or anatase (Ti) are detrital minerals during sediment recycling.
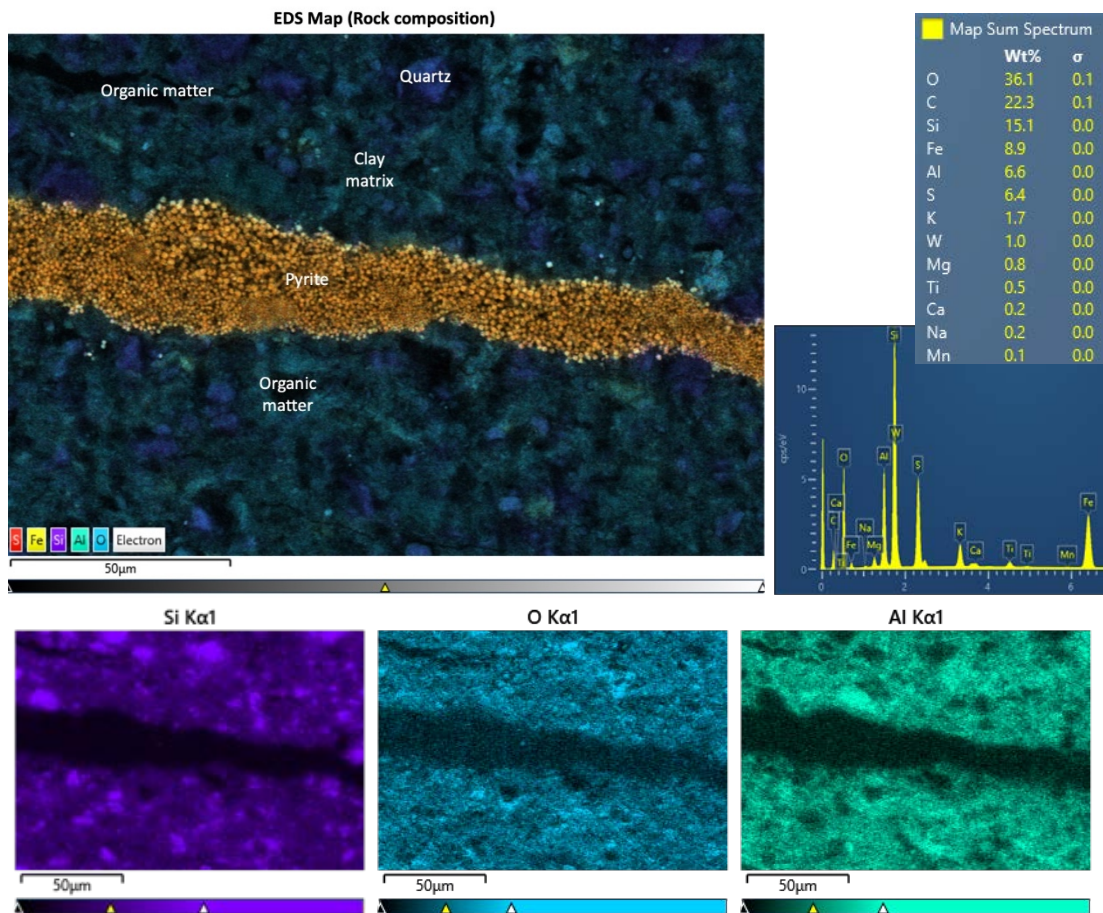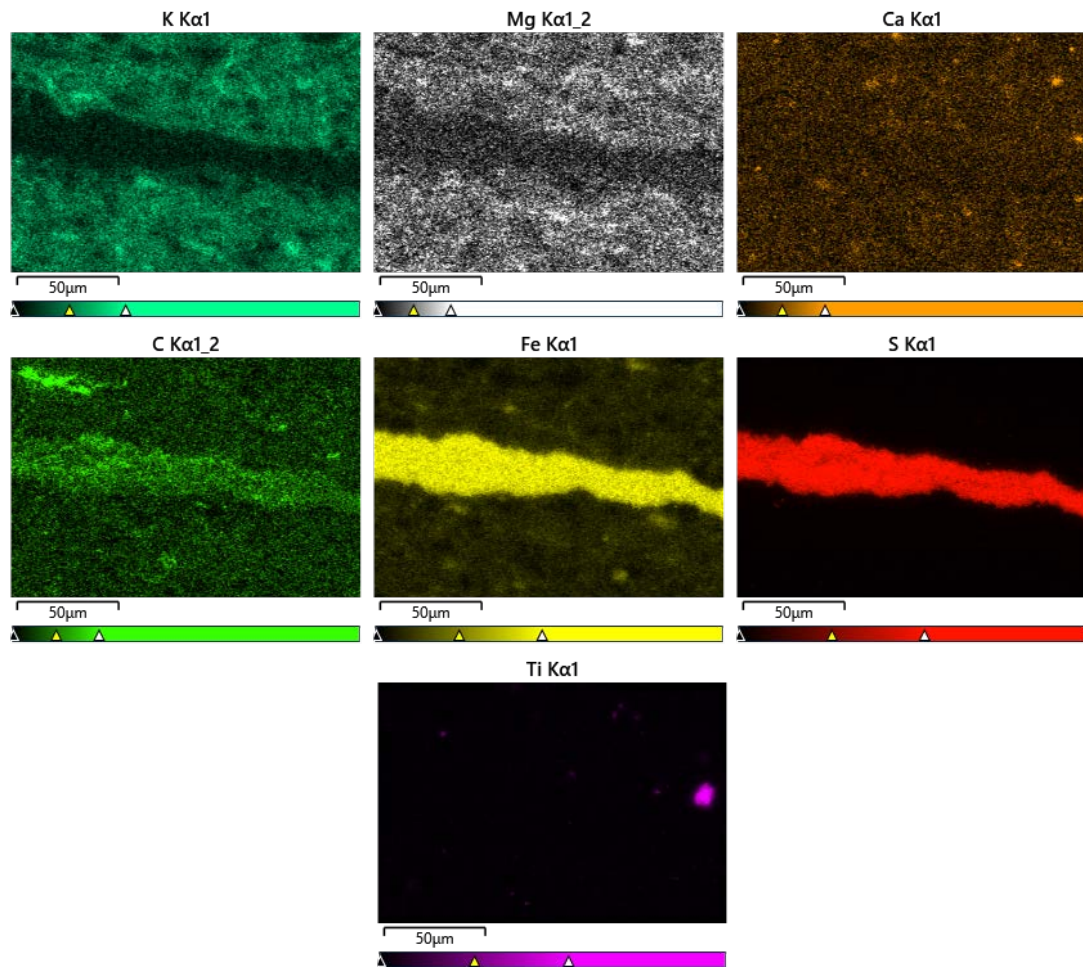
Figure 5.19: EDS layered map and its elemental maps. Quartz (corresponding to Si, O) are coloured purple and blue; K-Mg rich clay matrix (corresponding to Al, O, K) are coloured minty green and white; pyrites (corresponding to Fe, S) are coloured yellow and red; organic matter (corresponding to C) are coloured bright green; calcite (corresponding to Ca) are coloured orange; K – illite, Na – kaolinite & smectite. Ti can be associated with residual clay minerals or controlled by heavy minerals. Rutile or anatase (Ti) are detrital minerals derived from the source area by sediment recycling.

5.4.2.3. *Fossils: planktic foraminifers*

A large number of microfossils have been identified in the sample (Figure 5.20). The foraminifera's well-preserved chambers show fast sedimentation deposition. The organism's chambers are filled with diagenetic calcite, pyrites, and microquartz as it decomposes. Honza (1996) and Banda (1999) documented 40 marine, planktic foraminifers specifies from the Sibuti Formation. The most common is *Globigeriniodes sicanus, which is confined to* the Early Miocene *Globigerinoides sicanus* Zone. Other species reported in the zone are *Globigerina cf. ciperoensis,*

Globigerina praebulloides occlusa, Globigerinoides diminutus, Globigerinoides obliquus obliquus, Globorotalia (T) cf. obesa, Globorotalia (T.) obesa, Globorotalia (T.) opima opima-opima nana transistion, Praeorbulina glomerosa glomerosa, Praeorbulina transitoria, Globigerinita unicava unicava, and Globigerinatella insueta. In addition, possible fossils of Robulus (Lenticulina) and Bolivina can also be found in this thin section.
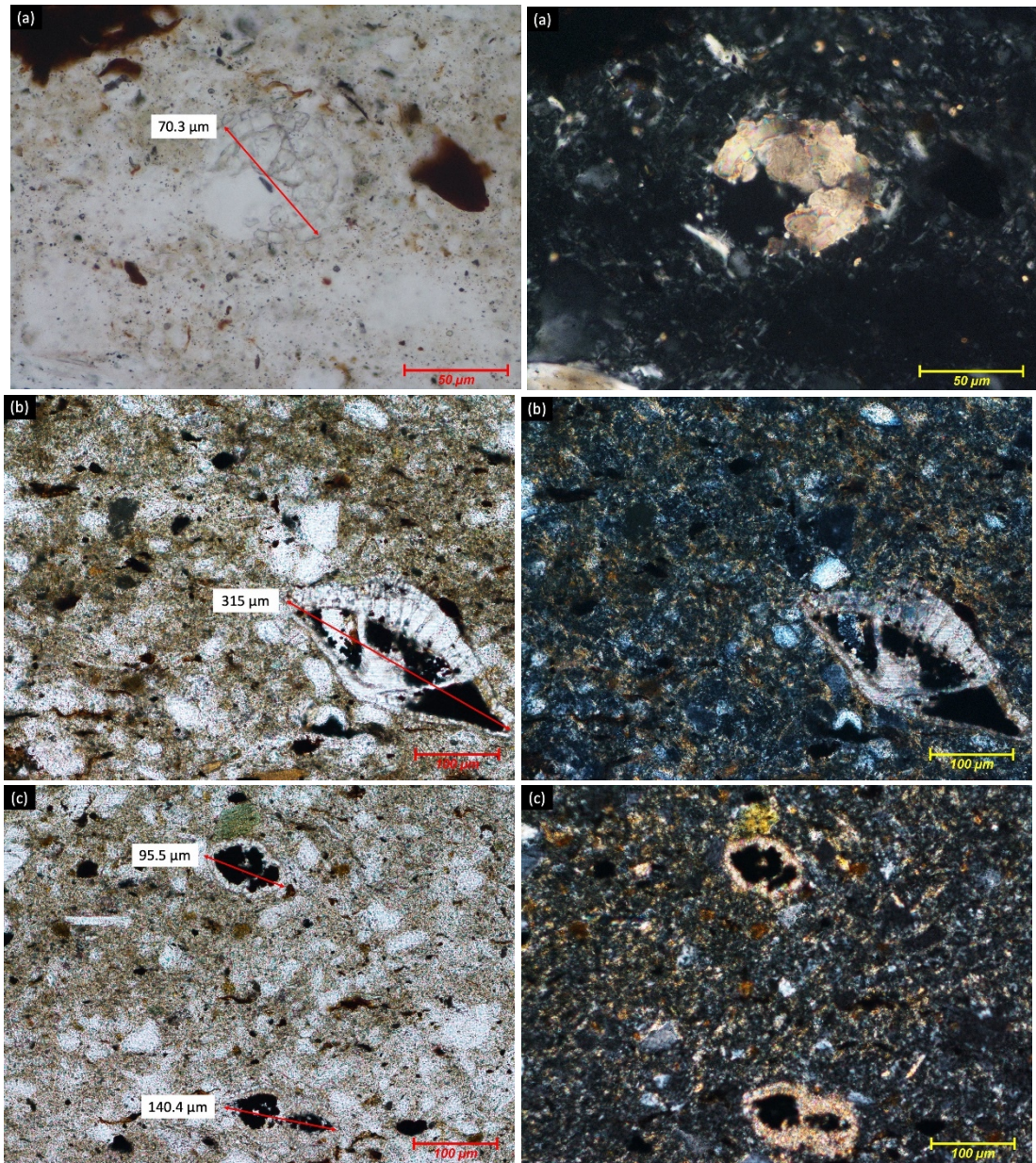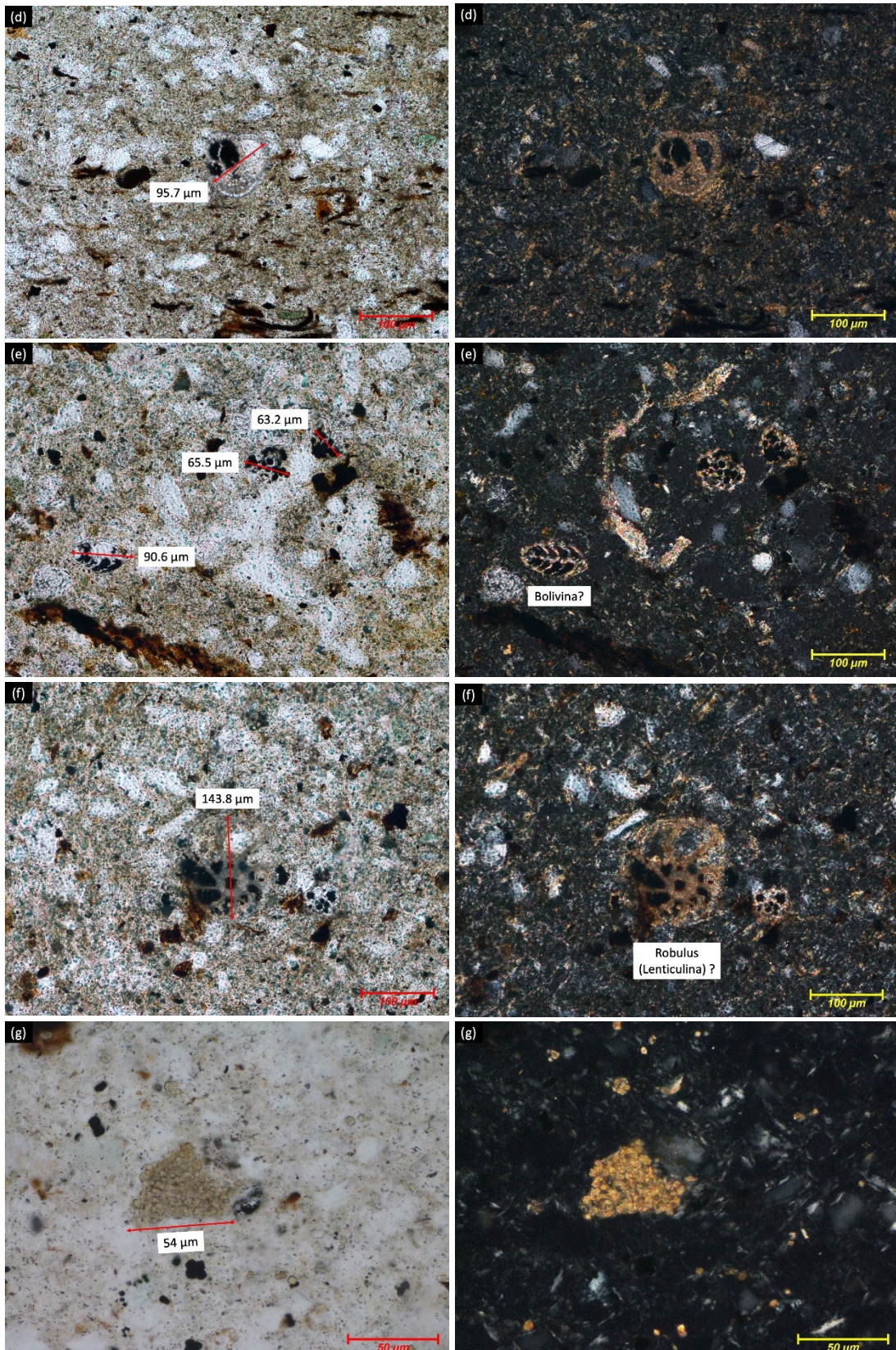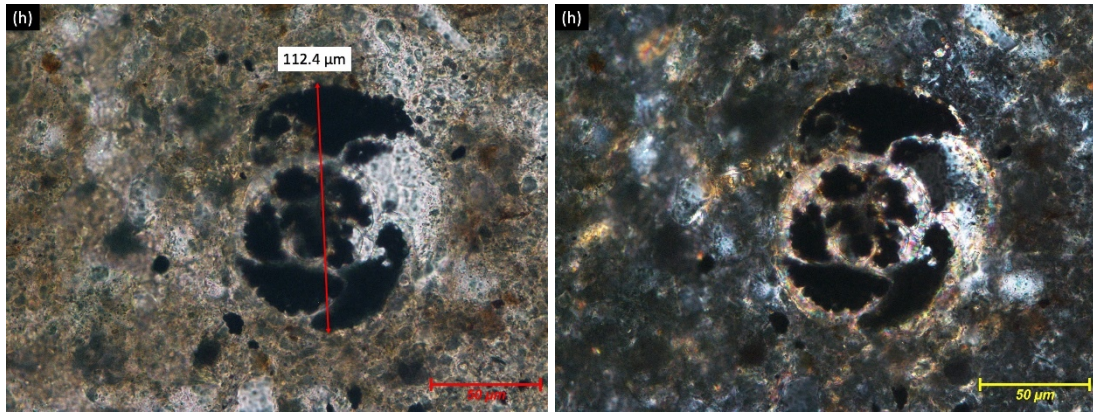
Figure 5.20: Thin section microphotographs of the Sibuti Shale showing the presence of foraminifers. The fossils are infilled with calcite, pyrite and microquartz. Left: plane polarised (ppl), Right: cross polarised (xpl).

EDS mapping is carried out on the white specks of mm fossil that can be seen on the hand specimen. Figure 5.20 shows the thin section microphotographs of the foraminifera in-plane polarised and cross polarised lights. The fossils are made up of calcites, whereas most of the foraminifera chambers are filled pyrites (opaque in both ppl and xpl-view; Figure 5.20). From EDS mapping, the foraminera's chamber is infilled with carbon (organic matter, C elemental map) and iron sulphides (Fe and S elemental map). The marginal chamber is infilled with sodium clay (kaolinite, smectite) and calcite. Pollastro (1981) has highlighted that simultaneous precipitation of kaolinite and pyrite is common which is from the gels in the bacteria-rich micro-environment of the test or otherwise, the fine clay minerals may be introduced between the pyrites in framboids during the late diagenesis (Sawlowicz, 2000).

From the SEM-EDS mapping (Figure 5.21), it is clear that the chambers are filled with organic matter and pyrite framboids. Some of the chambers are partially filled and others are filled completely. The clay matrix surrounding the fossil is iron, potassium, magnesium, and carbon-rich possibly present as a mixture in the cementation. Some micro quartz grains are also observed within the chambers which represents the clay fraction (<4 μm). Thus, it can be inferred that the micro quartz exists as pore-filling cement and overgrowths to detrital silt grains (Buckman et al. 2020).

The variance in the mineral composition between the matrix and foraminifera chambers suggests a different geochemical microenvironment at a small sediment layer scale during fluid migration and localised dissolution. EDS spot analysis revealed a small percentage of zinc-rich mineral (potentially sphalerite) associated with the iron sulphides. The occurrence of sphalerite is rare due to its tendency to form in low hydrogen sulphide levels and precipitated after preferential formation. The Zn bearing minerals may be associated with sulphur or carbonates as either sphalerite or smithsonite as traces of first cycle provenance and may be recycled from the source region. However, the oxidised framboids may contain Fe and Zn as the chemical constituents which have been registered by Luther et al. (1982).
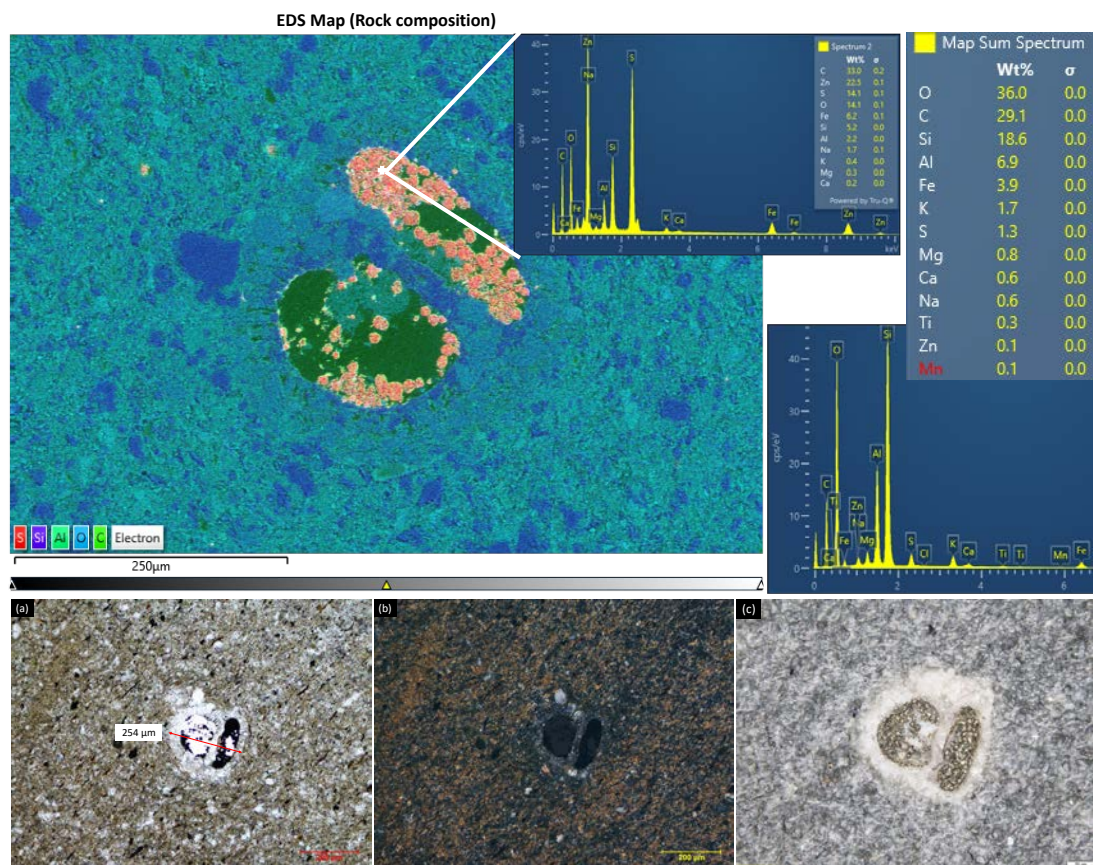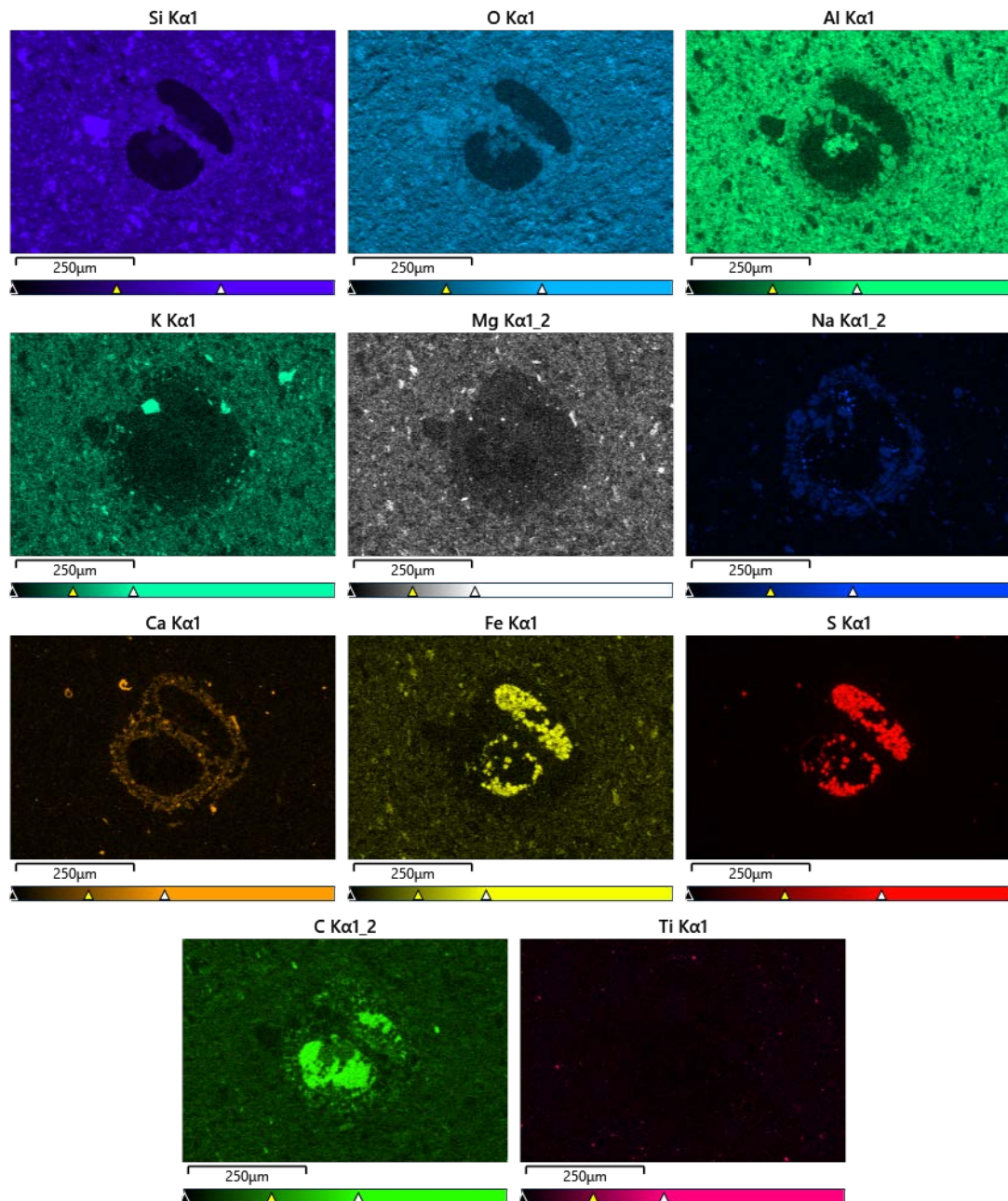
Figure 5.21: EDS map of foraminifera fossil showing the infilled minerals composition and the clay matrix. The fossils are infilled with organic matter, pyrite, calcite, kaolinite, smectite, and micro quartz. The composition of elements such as K, Fe, Mg is mainly controlled by the clay minerals. Heavy minerals rutile/anatase (TiO_2) are scattered within the sample.

5.4.2.4. Porosity

The overall observations from SEM images of the shale from the Sibuti Formation show that the porosity is mainly comprised of nano to micro-pores (Figure 5.22). The pore sizes range from less than 0.1 µm and up to 0.85 µm. Most of these pores have been filled by consolidated and well stacked pore-filling clay minerals, which

subsequently formed the nanopores. Hence, this contributes to the lower porosity of the rock. Microfractures are not observed within the sample.
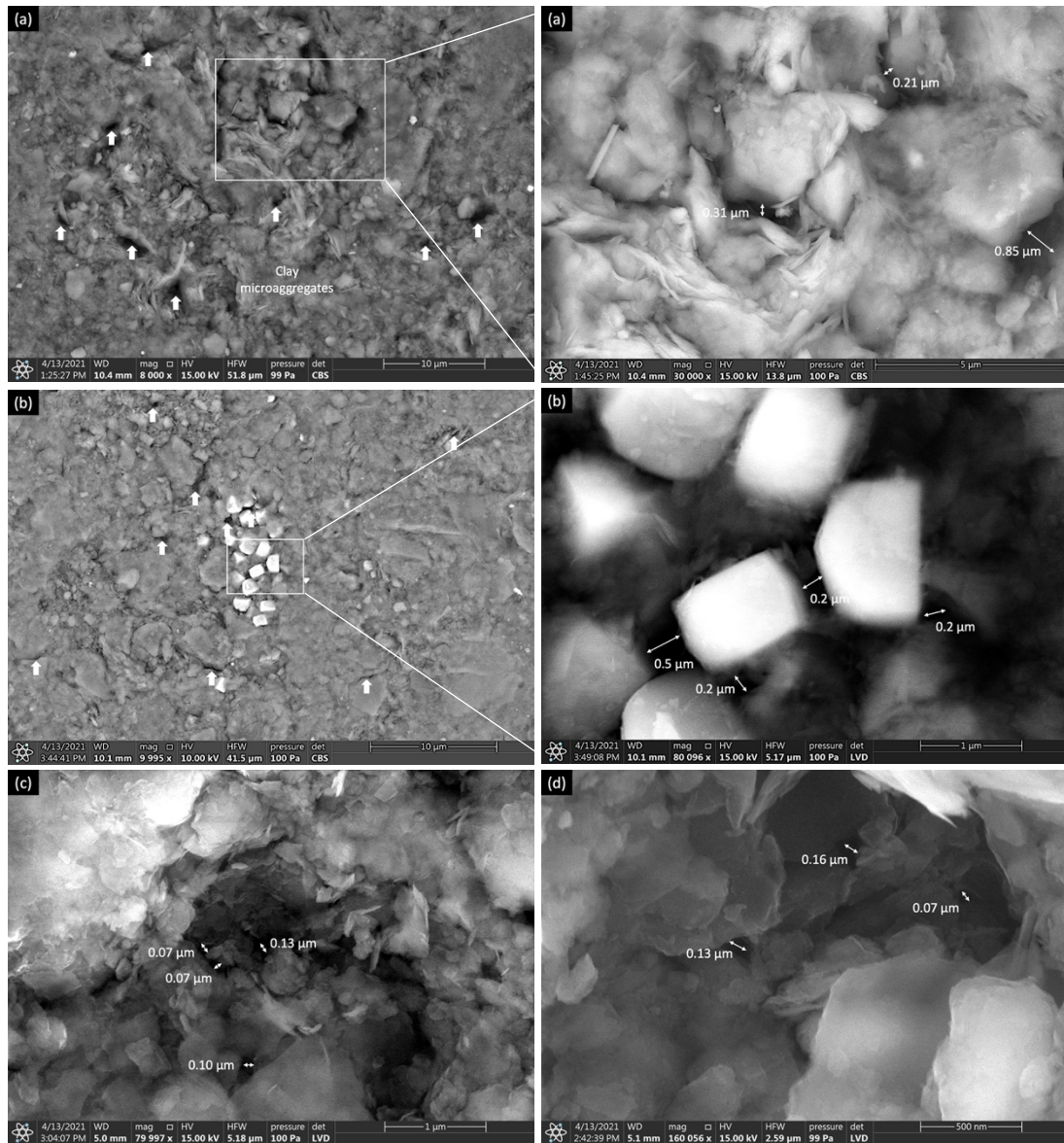
Figure 5.22: SEM images of the representative shale sample from the Sibuti Formation. (**a-b**) Images showing the visual pores in higher magnification between the grain-to-grain contact. (**c-d**) Images showing the distributions of the nanopores within the sample.

5.5. Properties of Highest and Lowest Durability Index (I_{d1}) Shale

Table 5.5 summarises the field characteristic, physical properties, mineralogy, geochemistry, and microtexture of the lowest and highest durable shale in the current study. The physical properties and durability have been discussed in Section

4.9. The main differences in mineralogy between shale of the Lambir and Sibuti formations are the higher percentage of pyrite, kaolinite, and illite, and the absence of smectite and albite (plagioclase) in the Lambir Formation. The presence of pyrite is a good indicator of potential chemical weathering (Belgeri et al., 1998; Soga et al., 2005). The high percentage of pyrite leads to lower shale durability due to its high reactivity with oxygen. The products of its oxidation include sulfate minerals, iron oxides, and sulphuric acid. The release of sulphuric acid promotes rock cracking and alters the diagenetic bonds between the particles.

Researchers such as Taylor et al. (1970), Sadisun et al. (2005), and Nandi et al. (2009a) suggested that smectite has a pronounced effect on durability due the osmotic swelling on the structure of the mixed layer clay. However, in the current study, the effect of shrinking and swelling of expandable mineral smectite does not contribute to the low durability of the Lambir shale. The low clay activity from Atterberg's limit test also supports the finding. On the other hand, a high percentage of illite shows a significant relationship to the durability of shale. Illite is non-expandable mixed layer clay that has a high capability in water adsorption due to its cation exchange capacity (CEC). The common CEC values related to the clay minerals can be referred to Table 2.3.

Although kaolinite has low CEC, it is found to have an influence on the durability. According to Moriwaki (1974), for shales with kaolinite as the primary clay mineral, the pore air compression mechanism is the primary force in influencing the slaking behaviour. The result is supported by Vallejo et al. (1993) who confirmed that shales with predominant kaolinite clay have a macropores system in their structure. When water is drawn into the shale due to capillary suction, the entrapped air in the macropores exerts stress on the solid skeleton causing the material to collapse in tension.

In addition to the clay minerals, the composition of clays is also important in studying their durability. Franklin et al. (1972) found that durability can be studied from the dispersion of clay minerals during rock-water interaction. Sodium clays are

the easiest to disperse followed by potassium, magnesium, and barium clays. Mixed layer clay such as illite and smectite contain inter layer of potassium ions that favour hydration and ion adsorption. From the chemical composition results of the studied clay, sodium and magnesium are higher in the Sibuti shale whereas potassium is more in the Lambir shale. Hence, it can be deduced that, the potassium-illite influence the low durability of the Lambir shale while for the Sibuti shale, sodium and magnesium clay play a role in its durability.

The Lambir and Sibuti shales for shows two types of fabric in their structure as per the microtextural analysis. The Lambir shale has parallel microlamination with skeletal microfabric while the Sibuti shales has parallel microlamination with turbostratic microfabric. Fabric contributed to durability of the rock due to the void ratio and permeability difference created by the different types of fabrics (Koralegedara et al., 2017). Higher porosity and permeability increase the water-rock interaction contact and thus promote slaking. As measured in the lab, the Lambir shale has a higher porosity and permeability than the Sibuti shale. Under SEM images, an abundant amount of micropores and microfractures exists in the particle arrangement of the Lambir shale. The clays are organised into aggregates, grain coating, and connector between the grains, thus creating irregular intergranular pores between the particles. The pores observed are between 0.2 µm up to 2.3 µm. Meanwhile, in the Sibuti shale, only nano and micro-pores of sizes less than 0.1 µm and up to 0.85 µm can be observed under SEM images. The clays are condensed into a tight face-to-face contact, moulding around the grains. The pores were found to be slightly elongated.

Table 5.5: Summary of the field characteristic, physical properties, mineralogy, geochemistry, and microtextural of the representative unit of the lowest and highest durable shale in the studied area.

Properties	Parameters	Unit	Lowest Durable Shale	Highest Durable Shale
	Formation		Lambir Formation	Sibuti Formation
	Age		Middle – Late Miocene	Miocene

Properties	Parameters	Unit	Lowest Durable Shale	Highest Durable Shale
Field			Brownish grey, firm, fissile, laminated with very thin sandstone layer	Light to dark grey, very hard, stiff, brittle, fissile, non-laminated
Physical	**Particle Size Distribution**			
	Clay	%	50.5	7.8
	Silt	%	44.0	59.8
	Sand	%	5.5	32.2
	Classification		Clayey Shale	Silty Shale
	Initial Moisture Content	%	11.9	4.9
	Specific Gravity		3.57	3.34
	Atterberg's Limit			
	Liquid Limit	%	41	32
	Plastic Limit	%	20	20
	Plasticity	%	21	12
	Clay Activity		0.46 (Inactive)	1.50 (Active)
	Porosity	%	34.8	9.07
	Permeability	mD	21.27	5.44
	Slake durability Index			
	Index, I_{d1}	%	13.6 (Very Low)	38.7 (Low)
	Index, I_{d2}	%	0.0 (Very Low)	2.8 (Low)
Mineralogy	**Quartz**	wt. %	13.6	38.7
	Illite	wt. %	22.0	16.5
	Kaolinite	wt. %	7.9	5.2
	Chlorite	wt. %	5.4	5.1
	Smectite	wt. %	Not detected	1.0
	Amorphous	wt. %	10.0	15.8
	Albite	wt. %	not detected	5.6
	Pyrite/Sulfides	wt. %	2.7	0.4
	Clay Speciation			
	Illite	wt. %	65	55
	Kaolinite	wt. %	21	22
	Chlorite	wt. %	14	18
	Smectite	wt. %	Not detected	5
	SiO_2	wt. %	60.49	61.17

Properties	Parameters	Unit	Lowest Durable Shale	Highest Durable Shale
Geo-chemistry		wt. %		
	Al_2O_3		18.17	16.66
	$Fe_2O_3(T)$	wt. %	4.10	5.91
	K_2O	wt. %	3.02	2.67
	MgO	wt. %	1.05	1.90
	TiO_2	wt. %	0.79	0.80
	Na_2O	wt. %	0.13	0.63
	MnO	wt. %	0.017	0.049
	CaO	wt. %	0.01	0.69
	LOI	%	10.94	8.24
Micro-textural	**Fabric**		Parallel laminated shale – skeletal microfabric	Parallel laminated shale – turbostratic microfabric
	Grain size, matrix, and composition		Quartz grain sizes range from 1.6 to 50 µm. Poorly sorted, subrounded, and low sphericity in K clay matrix (Illite)	Quartz grain sizes range from 4.5 to 50 µm. Moderately sorted, angular, low sphericity in K, Mg (Smectite), and Ca rich matrix
	Fossils		Abundant in benthic foraminifers	Abundant in planktic foraminifers
	Porosity		Presence of microfractures and micro-pores	Nano and micro-pores. Microfractures are not observed

Chapter 6: Natural Slake Test and Weathering Mechanisms

6.1. Introduction

This chapter presents the results of natural slake durability tests and the discussion on weathering mechanisms, that took place during the short-term weathering.

6.2. Natural Slake Weathering Test

6.2.1. Weather Data

The total duration of the natural slake weathering test was 66 days, from 19th November 2021 to 4th February 2022. The experiment was put on hiatus from 8th to 19th January 2022 when the tests set up were taken indoors for further analysis. Table 6.1 summarises the weather data recorded by the Vantage Pro 2 Weather Station, throughout the duration of the experiment. The humidity data were shared by the Malaysian Meteorological Department (MET). The mean and standard deviation of the temperature, humidity, rain, and rain rate in the area were 27.6 ± 2.4 °C, 88.5 ± 3.4 %, 0.4 ± 2.3 mm, and 2.6 ± 16.0 mm/h respectively.

Variability of the weather data can be determined by calculating the coefficient variation, CV (CV = standard deviation / mean) (Lovie, 2005). As a rule of thumb, a CV of less than 1 can be considered low variability and a CV of equal and more than 1 can be considered high variability. The CV of the temperature and humidity data were 0.09 and 0.14, suggesting low variability. Figure 6.1 shows the tabulation data of the temperature and humidity during the 66 days. The CV of the rain and rain rate were 5.75 and 6.23, suggesting high variability. Hence, it can be concluded that the effect of rock weathering in the study area is significantly influenced by the wetting (rainfall) and drying (duration of intense sunlight exposure) events.

Table 6.1: Summary of the weather data recorded by the Vantage Pro 2 Weather Station throughout the experiment duration.

n= 66 days of hourly weather data	Weather Parameters			
	Temperature (°C)	Humidity (%)	Rain (mm)	Rain rate (mm/h)
Max. value	34.8	100.0	36.83	276.1
Min. value	22.8	51.0	0.00	0.00
Sum	-	-	600.61	-
Mean, μ	27.6	88.5	0.4	2.6
Standard Deviation, σ	2.4	3.4	2.3	16.0
Coefficient Variation, CV ($\frac{\sigma}{\mu}$)	0.09	0.04	5.75	6.23
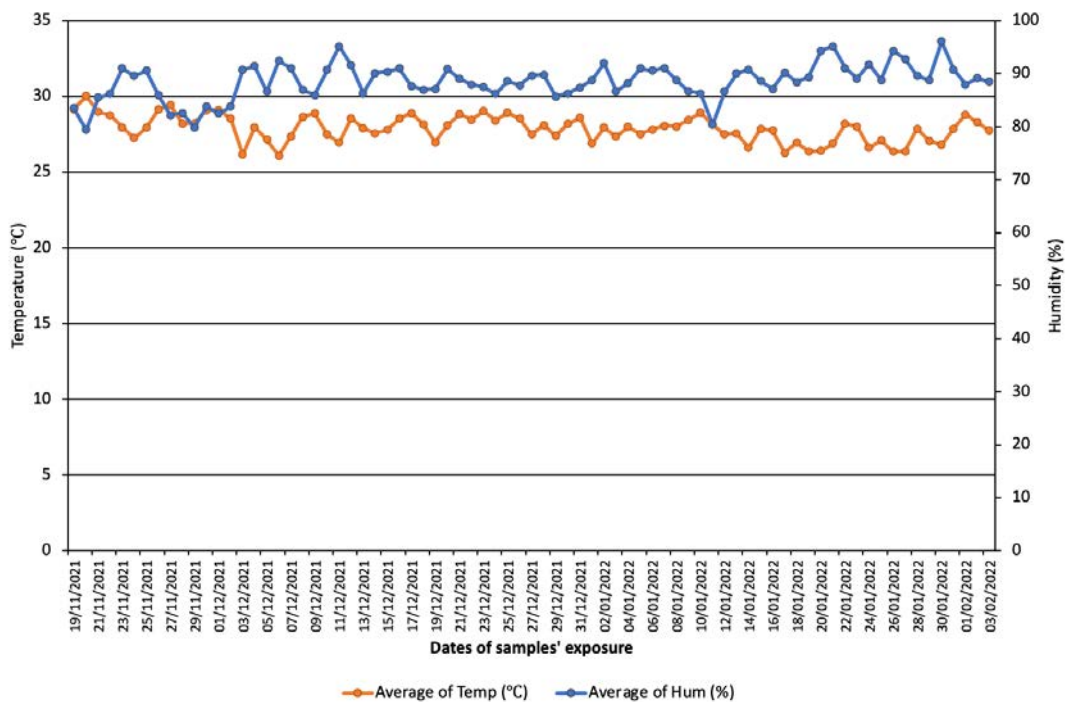
Figure 6.1: Variability of the temperature and humidity data during the testing period.

A total of 157 rain hours were recorded with a rainfall accumulation of 600.61 mm. Figure 6.2 shows the total duration and amount of rain throughout the experiment duration. The most amount of rain was recorded in week 4 with

cumulative rainfall of 136.11 mm and a total rain duration of 26 hours. The least amount of rain was recorded in Week 2 with cumulative rainfall of 12.96 mm and a total rain duration of 6 hours.
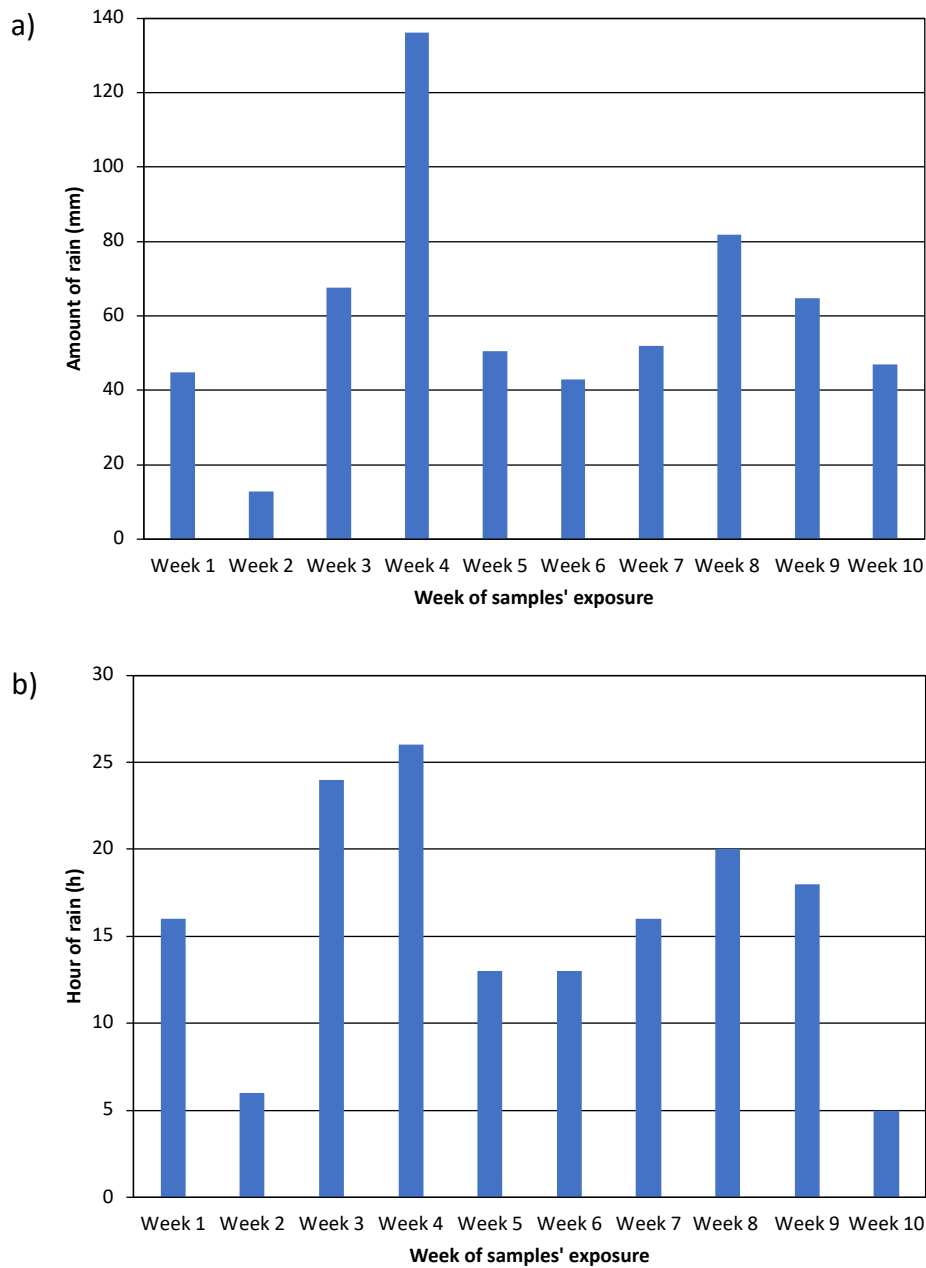
Figure 6.2: (a) The total amount of rain and (b) the total duration of rain during the testing period.

The definition of a rain event as proposed by Chen et. al (2013) is a continuous rain that took place in consecutive rainy hours. *Department of Irrigation and Drainage Malaysia* 2022) classified rain events into 4 categories: light rain (1-10

mm/h), moderate rain (11-30 mm/h), heavy rain (31-60 mm/h), and very heavy rain (> 60 mm/h). A total of 64 rain events were observed. Figure 6.3 shows the histogram of the rain duration and rain intensity of each rain events recorded during the experiment. Forty-two percent (42%) of the rain events had a rain duration of less than 1 hour and 9% of the rain events had duration of more than 5 hours. There were 34 light rain events, 16 moderate rain events, 8 heavy rain events, and 6 very heavy rain events. The mean rain rate and standard deviation for each rainfall category were 2.76 ± 3.26 mm/h, 20.45 ± 5.73 mm/h, 49.48 ± 8.34 mm/h, and 83.78 ± 8.76 mm/h respectively.

a)

b)
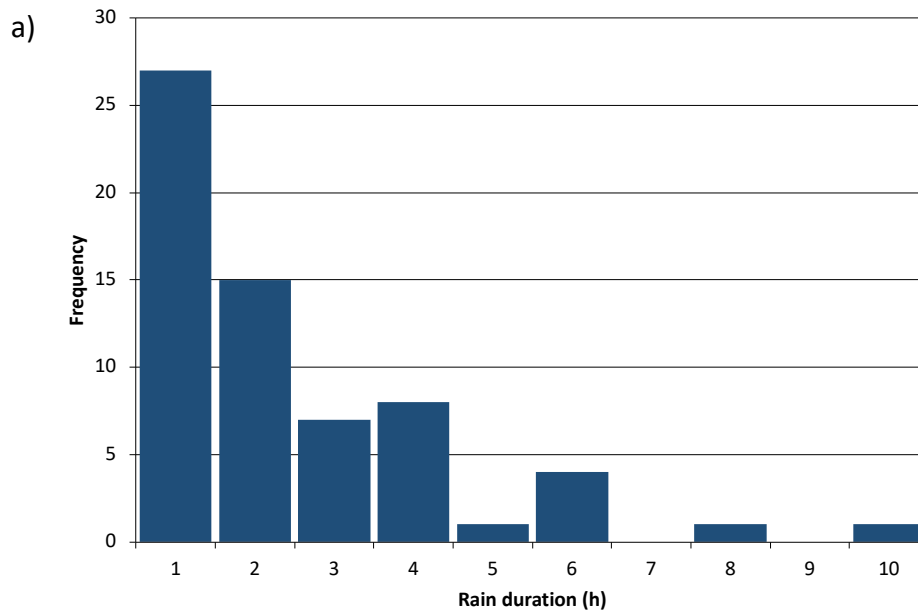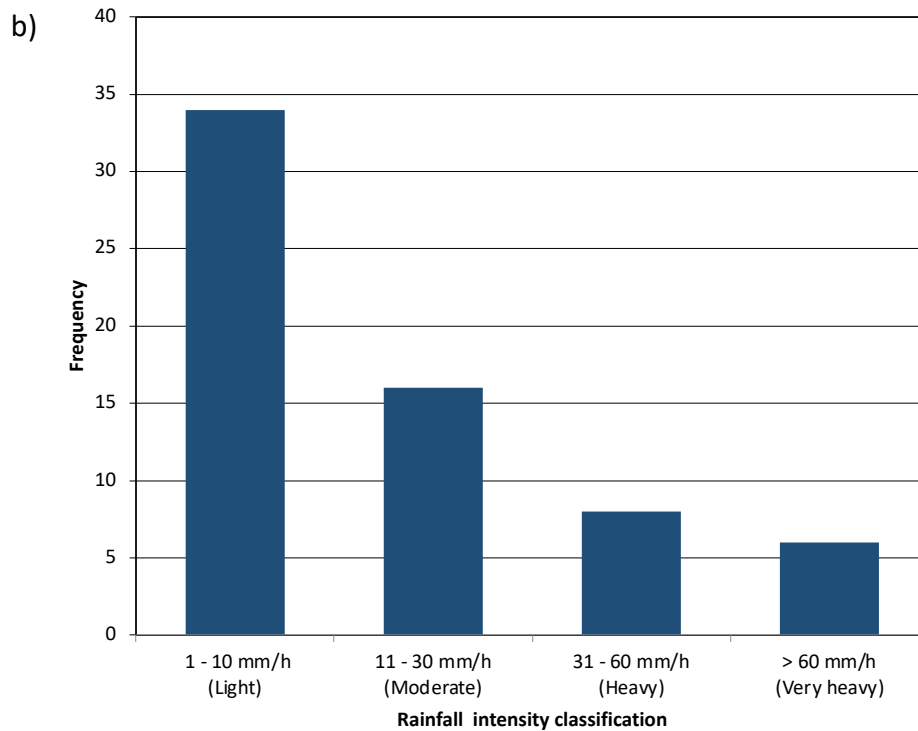
Figure 6.3: Histograms of (a) the rain duration and (b) the rain intensity of the rainy events during the testing period.

6.2.2. Weathering Phases

The middle and final weathering phases of the sample sets were determined based on the percentage of weight loss during the weathering exposure (Figure 6.5). The middle phase was determined when the sample set on the 2 mm sieve of the natural slake test set-up had lost 50% of the original weight. The final phase was when the material had entirely disintegrated and lost 100% of its original weight. Rainfall is regarded as the wetting event, and the Temperature-Humidity-Wind (THW) Index refers to the intensity of drying after the rain events. THW Index is used as the indicator of drying in this study. The index considered the heating effects of the sunlight and the cooling effects of the wind to reflect the apparent temperature outside the shade.

It can be observed that the shale lost significant weight after an intense rainfall event. Lai et al. (2022) reported a strong correlation between rainfall intensity on the disintegration of clay-bearing rocks from the Sibuti Formation. By comparing

the values of the D_R of the rocks after each rain event, they found that rainfall intensity higher than 2 mm/h contributes significantly to the slaking behaviour.

Table 6.2 shows the number of wetting and drying events throughout the exposure. Shale from the Lambir Formation reached its middle weathering phase during week 4 of the weathering exposure, after 26 rain events. The sample reached its final weathering phase after another 18 rain events in week 7. Concurrently, the more durable shale from the Sibuti Formation took seven weeks to reach its middle phase and fully disintegrate after 20 rain events later, in week 10.

Figure 6.4 shows the weight loss percentage of the sample sets placed under a shed during the natural slake test. The heat index is used to reflect the combined air temperature and the relative humidity of the shaded area. There is no apparent correlation between the weight loss percentage and the heat index. However, shale from the Sibuti Formation shows a positive increment of about 4% to its original weight during the exposure, while the Lambir shale fluctuates between -1 to 1%. This observation strongly indicates the active and high swelling potential of clays in the Sibuti shale and the inactive clays in the Lambir shale. Hence support the Atterberg Limit results of the rock properties.

Table 6.2: Wetting and drying events during the natural slake weathering test.

| Week of Exposure | No. of Rain Events | Rainfall Intensity | | | | Average THW Index (°C) | Weathering Phase | |
		Light	Moderate	Heavy	Very Heavy		Lambir Shale	Sibuti Shale
Week 1	7	5	1	1	-	31.24	*Initial*	*Initial*
Week 2	3	1	1	-	1	30.82		
Week 3	8	4	4	-	-	29.09		
Week 4	8	3	2	1	2	29.46	*Middle*	
Week 5	2	1	-	-	1	30.63		
Week 6	6	4	1	-	1	30.29		
Week 7	10	6	3	1	-	29.37	*Final*	*Middle*
Week 8	9	5	2	1	1	28.74		
Week 9	9	5	1	3	-	28.82		
Week 10	2	1	-	1	-	29.89		*Final*
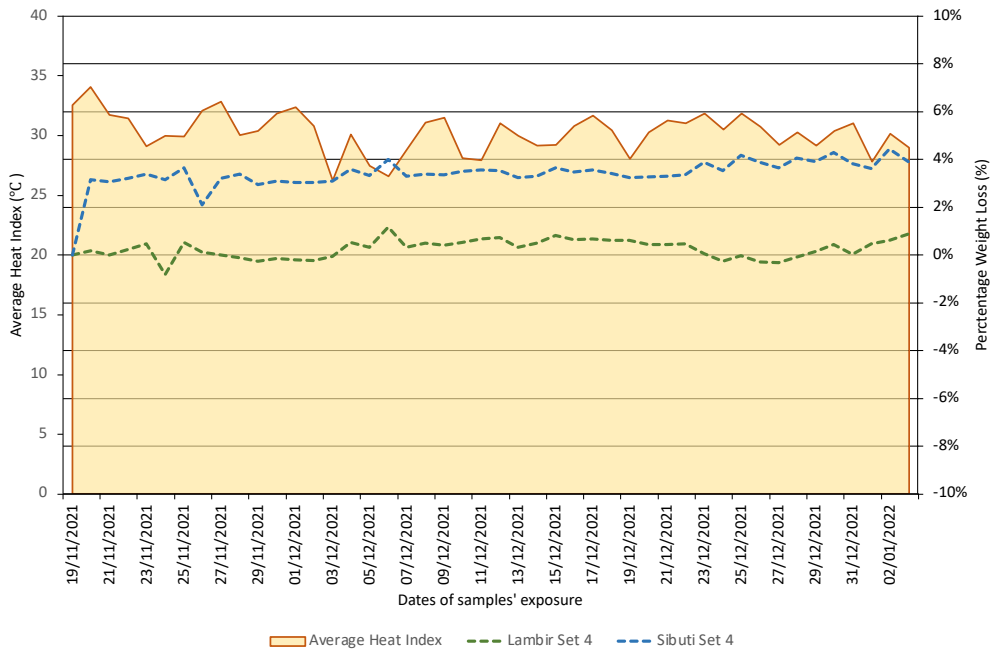
Figure 6.4: Changes in the weight of the sample sets placed under the shed during the natural slake weathering test.
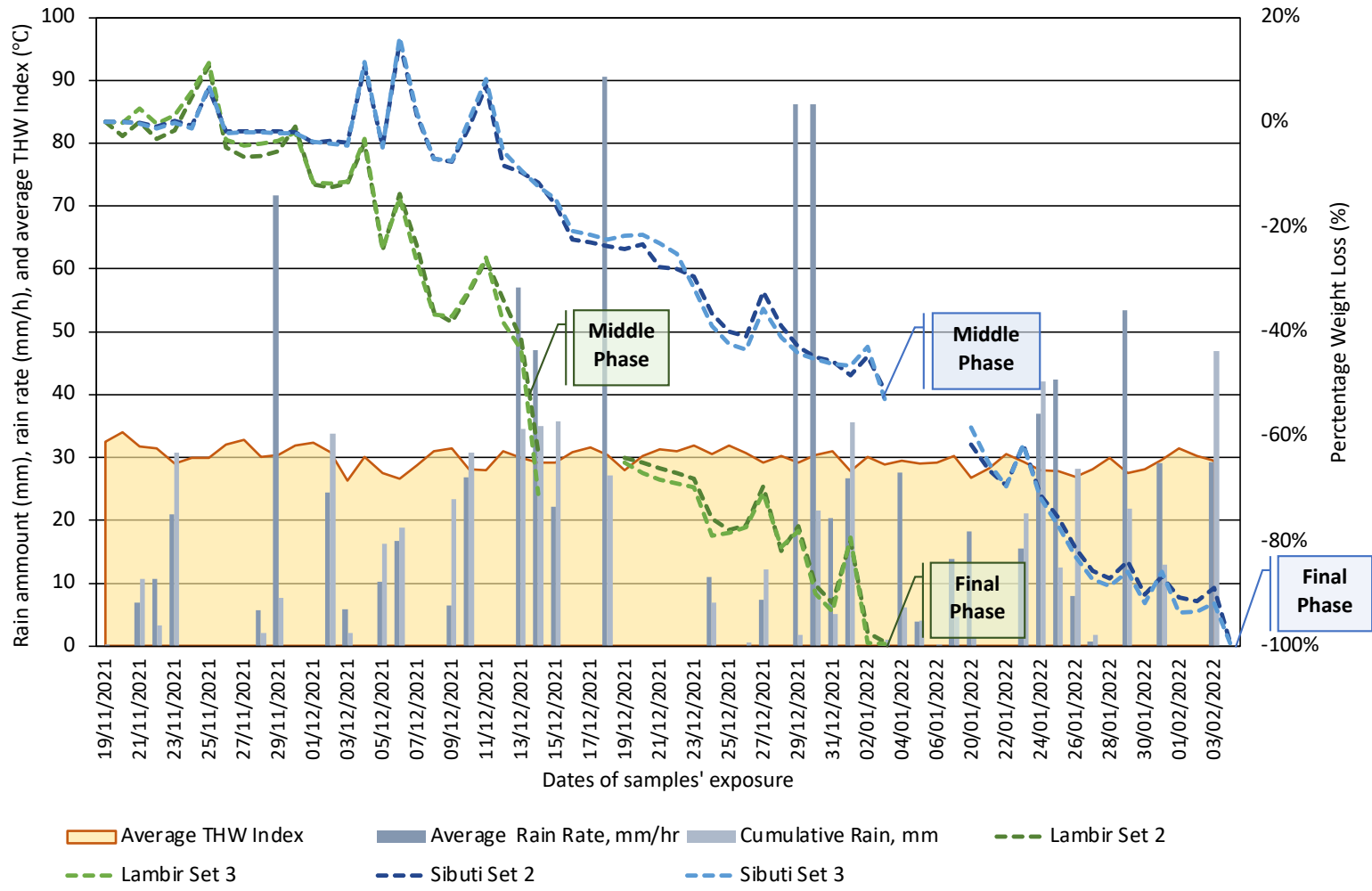
Figure 6.5:The changes in weight (%) of the sample set during the natural weathering exposure.
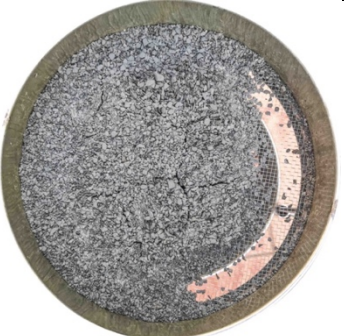
6.2.3. Physical Weathering

Physical weathering refers to the weathering process that contributes to in situ fracturing and disintegrating rock without altering its chemical content. For tropical climates such as in this studied region, the primary mechanism responsible for the physical weathering is the wetting and drying cycle. Figure 6.6 compares the slaking behaviour of the Lambir and Sibuti Shale during the 66 days of natural climatic exposure. Higher rainfall rates that occurred in a short period (less than one hour up to 10 hours) contributed to the wet period whereas a high evaporation rate of 29°C to 30°C contributed to the dry period. Description of the materials retained on the 2mm sieve was based on subjective observations with a referral from Santi et al. (1998) jar slake classification.

Figure 6.7 shows the grain size analysis of the studied samples in their middle phase of weathering, respectively. The disintegration ratio, D_R of the Lambir shale, is higher than the Sibuti shale. The D_R values could be misleading as D_R values closer to 1 are deemed durable (Erguler et al., 2009; Gautam et al., 2013). For the studied shale, the slaking behaviour and brittleness of the shales do not reflect their durability. The classification method is inadequate in classifying the shale with high clay content. The nature of the rock will affect the D_R values. It was observed that the clayey shale from the Lambir Formation and the silty shale from the Sibuti Formation exhibited different slaking behaviour as they weathered. Figure 6.11 and Figure 6.12 show the significant changes in slaking behaviour of shales after consequential wetting and drying events. The initial slake on both samples starts with cracks along the planar surface of its lamination. As weathering continues, clayey shale from the Lambir Formation degrades into mud-like consistency while silty shale from the Sibuti Formation disintegrates into chip slaking. The initial crack propagation rate in the Sibuti shale is faster than the Lambir shale under the same weather conditions.

No. of Week	Formation	
	Lambir Shale	Sibuti Shale
Initial		
	Observation 10 pieces of intact core samples.	***Observation*** 10 pieces of intact core samples.
Week 1		
	Observation Cracks formed and grew along the lamination.	***Observation*** Cracks formed and grew along the lamination.
Week 2		
	Observation Crack lines disappeared and filled with clay particles.	***Observation*** Crackings propagate into coalescence and shales start to degrade to small fragments.
Week 3		

No. of Week	Formation	
	Lambir Shale	Sibuti Shale
	Observation Muddy surface gradually decreases with continous rain.	***Observation*** Shale continues degrade into smaller fragmens.
Week 4		
	Observation The muddy surface significantly decreases with continuous rain.	***Observation*** Shale continues to degrade into smaller fragments.
Week 5		
	Observation The muddy surface significantly decreases with continuous rain.	***Observation*** Shale continues to degrade into smaller fragments.
Week 6		

No. of Week	Formation	
	Lambir Shale	Sibuti Shale
	Observation The muddy surface significantly decreases with continuous rain.	***Observation*** Shale continues to degrade into smaller fragments.
Week 7		
	Observation Shale has completely disintegrated.	***Observation*** Shale continues to degrade into smaller fragments.
Week 8	Test Completed	
		Observation Shale continues to degrade into smaller fragments.
Week 9	Test Completed	
		Observation Shale continues to degrade into smaller fragments.

No. of	Formation	
Week	Lambir Shale	Sibuti Shale
Week 10	Test Completed	
		Observation Shale has completely disintegrated.

Figure 6.6: Weekly natural slake test photos of the Lambir and Sibuti during the 66 days testing period.

Disintegration Ratio, DR during the middle phase of weathering		
	Lambir Shale	Sibuti Shale
Set 1	0.8551	0.1440
Set 2	0.7660	0.1626
Set 3	0.8159	0.1486
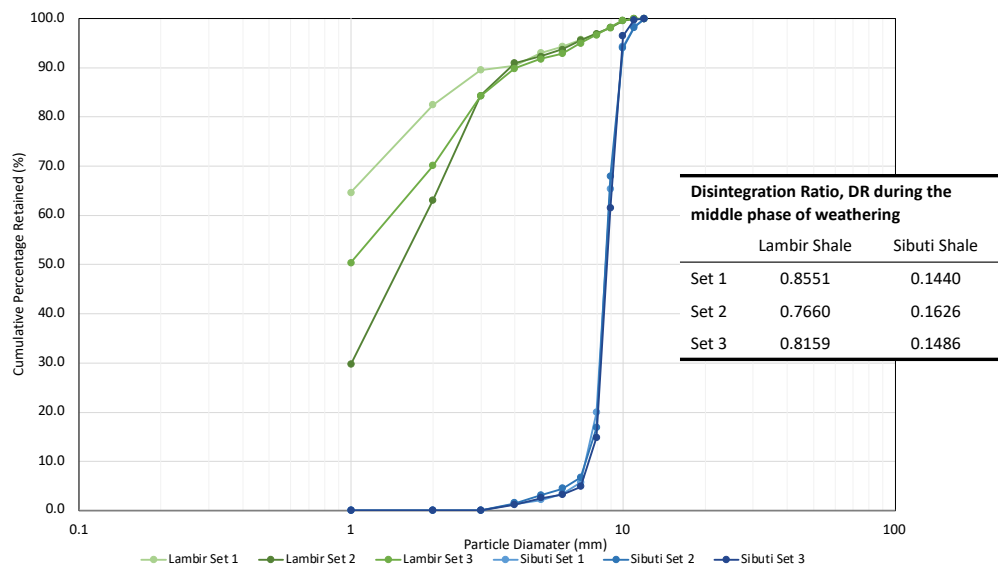
Figure 6.7: Grain size analysis of the Lambir and Sibuti shale during the middle phase of weathering. The disintegration ratio, D_R of the samples is the ratio of area under the curve to the total encompassing area.

Silty shale chips into smaller fragments after 7 rain events, while clayey shale loses its mud consistency shape after 18 rain events. However, the Lambir shale took a shorter time (46 days) to fully disintegrated compared to the Sibuti shale (66 days). Perry et al. (1982) reported that chip slaking is relatively stable and resists further degradation. The rate of deterioration of large coarse fragments can occur promptly,

141

but the rate substantially decreases with smaller particle sizes. It is believed that an equilibrium point may exist between the range of particle sizes. Smaller fragments have a larger surface area, thus larger amount of cumulative force is required to further breakdown the fragments into smaller pieces. Zhang et al. (2021) have reported that while the slake durability index of rock sample gradually decreases during the drying and wetting cycle, its porosity and water absorption gradually increases. The damage caused by the water-rock interaction decreases and tends to be stable when the number of cycles increases.

The mode of slaking between the two shale types is summarised in Figure 6.8 and Figure 6.9 for the Lambir and Sibuti formations respectively. Slaking refers to the physical breakdown of a rock due to the wetting and drying process (Pinho et al., 2017). Slaking can only occur provided that the dry rock is rapidly wetted at high rainfall intensity to allow for the pressure build-up of the internally entrapped air (Zaher et al., 2005; Zaher et al., 2008; Rosa et al., 2012; Le Bissonnais, 2016). The mechanisms responsible for the slaking of the studied shale samples are believed to be from a combination of the following: (i) mechanical breakdown from raindrops, (ii) differential stress after drying, (iii) internal entrapped air compression, (iv) differential swelling/expansion of clays, (v) water adsorption, and (vi) physio-chemical dispersion. Figure 6.10 shows the sample state after the first and second rain events. Slaking was not observed after the first rain event, which lasted less than one hour with 0.25 mm of rain. Raindrops were visible on the rock surface, but the wetting intensity was insufficient to induce slaking. After the second rain event, the sample began to slake and cracks along the lamination plane.
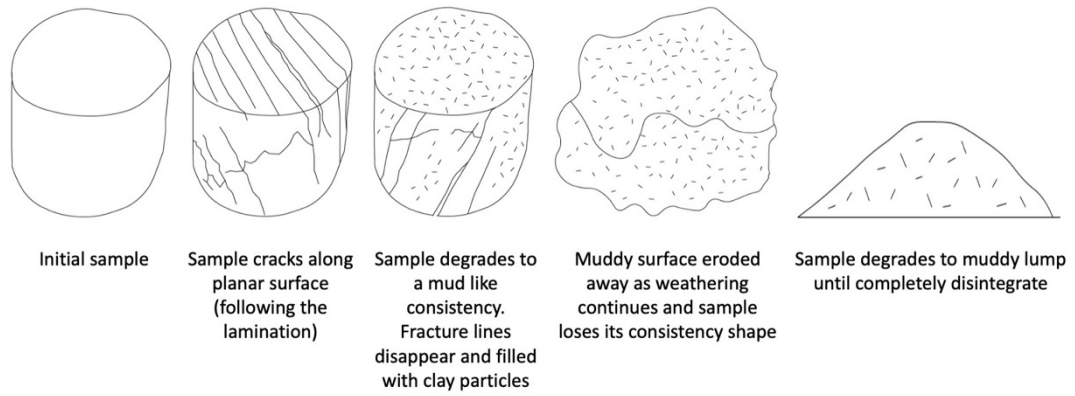
Figure 6.8: Illustration showing the mode of slaking of the clayey shale from the Lambir Formation.
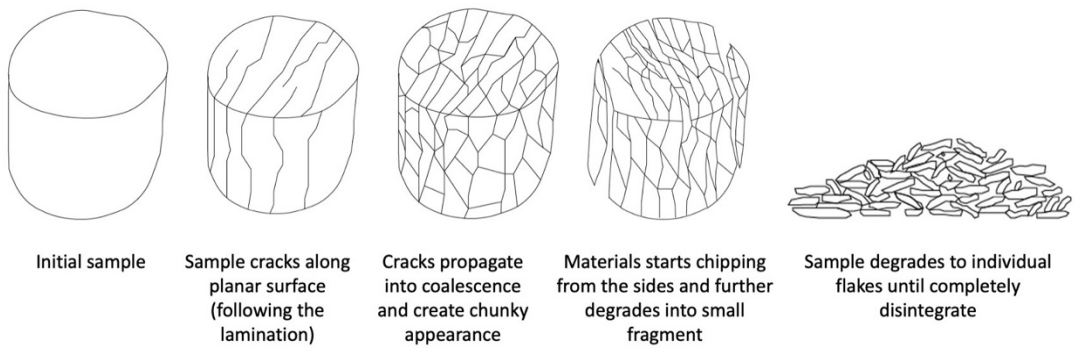
Figure 6.9: Illustration showing the mode of slaking of the silty shale from the Sibuti Formation.

Rain event 1	Rain event 2
Rain amount: 0.25 mm	Rain rate: 8.72 mm/h
Duration: < 1 hour	Rain amount: 9.65 mm
	Duration: 5 hours
Rain imprints can be seen on the exposed surface. The amount of rainwater was not sufficient to induce slaking.	Cracks occur along the lamination plane due to the mechanical breakdown from the raindrop impact followed by differential stress after drying.
Lambir Formation (Clayey Shale)	

Rain event 1	Rain event 2
Rain amount: 0.25 mm	Rain rate: 8.72 mm/h
Duration: < 1 hour	Rain amount: 9.65 mm
	Duration: 5 hours
Rain imprints can be seen on the exposed surface. The amount of rainwater was not sufficient to induce slaking.	Cracks occur along the lamination plane due to the mechanical breakdown from the raindrop impact followed by differential stress after drying.

Sibuti Formation (Silty Shale)

Figure 6.10: Photos were taken after a relatively air-dried period (within hours) of the first and second rain events during the natural slake test.

Rosa et al. (2012), in their study of slaking occurrence under rainfall, found that initial disaggregation occurred due to cumulative kinetic energy and mechanical impact caused by the raindrops. The compressive stress of raindrop impact is converted into lateral shear stress in undrained situations, causing the rock to crack and split apart (Le Bissonnais, 2016). As the rapid wetting continues, slaking advances thenceforth due to the increased pressure and compression of the internal entrapped air (Vallejo et al., 2001; Abd-Alrahman et al., 2020). Water penetrated the

rock by capillary suction during hydration and trapped the air that initially filled in the macropores (Moriwaki, 1974; Perry et al., 1982). According to Means et al. (1963), at equilibrium, the model of air and water in the macropore can be expressed following Equation 6.1. Accordingly, the relationship between the pore air pressure and the macropore diameter can be obtained following Equation 6.2.

$$\pi d T_s - p(\pi d^2)/4 + u(\pi d^2)/4 = 0 \qquad\qquad 6.1$$

$$p = u + (4T_s)/d \qquad\qquad 6.2$$

where:

d	=	Diameter of macropore (assume to be cylindrical)
T_s	=	Surface tension of water acting on the meniscus
p	=	Air pressure
u	=	Pore water pressure

Equation 4.2 demonstrated that the pore air pressure of entrapped air in a macropore increases as the diameter of the macropore decreases. Slaking is suggested to be more pronounced in shales containing small diameter pores. Compared to their slaking behaviour, the rate of crack propagation in the Sibuti shale happened more rapidly, and become more brittle compared to the Lambir shale. The Sibuti shale has nano- to micro-pores with size ranges from less than 0.1 μm and up to 0.85 μm. On the contrary, the Lambir shale has micro-pores of 0.2 μm up to 2.3 μm. As the shales weathered, the existing pores enlarged, up to 57.4 μm (Figure 6.13 and Figure 6.14). The distribution of macro-pores was also increased as the rock slakes to smaller grain materials. Hence, it increases the pore spaces between the individual grains. During weathering, the grains' size degraded, and the microtextural of the shale changed from a well-developed dense structure to a porous fabric (Figure 6.13 and Figure 6.14).

The entrapped air in the macropore exerts tension on the shale skeleton, causing local expansion along the weakest planes of lamination. Additionally, when drying occurred, the intense evaporation rate caused an increase in the negative pore pressure and left the rock severely desiccated (Abd-Alrahman et al., 2020). The

condition exists in a state of tension and stresses the structure thus resulting in subsequent tensile failure within the intracrystalline bonds of the rock particles. Hence, the cracks propagated and coalescence.

The Lambir shale consists of predominantly non-expandable clays of illite and kaolinite. The expandable mineral smectite is not detected in the Lambir shale but is present in the Sibuti shale. Previous researchers such as Taylor et al. (1970), Dick Dick et al. (1992), Sadisun et al. (2005), Nandi et al. (2009a), and Koralegedara et al. (2017) reported that the presence of swelling and expandable clays such as smectite and montmorillonite decrease the rock's durability. However, the results in this study demonstrate that the presence of smectite affects the slaking behaviour and brittleness of the shale sample but has no influence on its durability. Smectite has the ability to adsorb water externally on the surface, within the interlamellar space, and interparticular space between the clay aggregates. Thus, as it expands, not only does the pore air pressure increase and finally rupture to form cracks, but the cementation between the particles is also weakened (Zhang et al., 2014).

On the other hand, illite and kaolinite adsorb water gradually, with illite adsorbed a significantly more water content than kaolinite (Hatch et al., 2011). Unlike smectite, water adsorption for illite and kaolinite occurs only externally on the surface through van der walls interaction between the particle surface and the water molecules. Based on the results of the Atterberg Limit, the Lambir shale has a higher plasticity index than the Sibuti shale. In other words, the Lambir shale behaves plastically (easily to be molded) at a higher water content compared to the Sibuti shale. Additionally, the higher initial moisture content of the Lambir shale suggests a longer drying time compared to the Sibuti shale. The strength of shale reduced while it was in a water-absorbing state (Liu et al., 2017; Du et al., 2018; Zhang et al., 2021). Hence, the durability and rate of disintegration of the Lambir shale are lower than the Sibuti shale.

Mode of Slaking				
1	2	3	4	5

Lambir Formation (Clayey Shale)

Initial state of the sample. Day 1 (19/11/2021)	Sample cracks along the laminations after the second rain event. Day 3 (21/11/2021) Rain event 2 (light) Rain rate: 8.72 mm/h Rain amount: 9.65 mm Duration: 5 hours	Crack lines disappear and fill with clays. Sample turns to mud like consistency after 7 rain events. Day 6 (24/11/2021) Rain event 7 (heavy) Rain rate: 48 mm/h Rain amount: 29.46 mm Duration: 4 hours	Muddy surface eroded away following progressive rainfall. The sample loses its consistency after 18 rain events. Day 19 (7/12/2021) Rain event 18 (light) Rain rate: 8.65 mm/h Rain amount: 1.77 mm Duration: 2 hours	Sample degrades to muddy lump until completely disintegrate. Photo was taken after 35 rain events. Day 43 (31/12/2021) Rain event 35 (Moderate) Rain rate: 20.30 mm/h Rain amount: 5.08 mm Duration: 1 hour

Figure 6.11: Slaking mode of clayey shale from the Lambir Formation. Photos were taken after a relatively air-dried period (within hours) of the rain event.

Mode of Slaking				
1	2	3	4	5

Sibuti Formation (Silty Shale)

Initial state of the sample.	Sample cracks along the laminations after the second rain event.	Crack lines propagate and coalescence into a chunky appearance after 5 rain events.	Slake fragments began to chip from the sample and degrade into smaller pieces.	Sample degrades to individual flakes until completely disintegrate. Photo was taken after 54 rain events.
Day 1 (19/11/2021)	Day 3 (21/11/2021)	Day 5 (23/11/2021)	Day 6 (24/11/2021)	Day 56 (25/01/2022)
	Rain event 2 (light)	Rain event 5 (moderate)	Rain event 7 (heavy)	Rain event 54 (Heavy)
	Rain rate: 8.72 mm/h	Rain rate: 15 mm/h	Rain rate: 48 mm/h	Rain rate: 42.35 mm/h
	Rain amount: 9.65 mm	Rain amount: 1.02 mm	Rain amount: 29.46 mm	Rain amount: 12.44 mm
	Duration: 5 hours	Duration: 1 hour	Duration: 4 hours	Duration: 4 hours

Figure 6.12: Slaking mode of silty shale from the Sibuti Formation. Photos were taken after a relatively air-dried period (within hours) of the rain event.

Lambir Formation (Clayey Shale)

Initial Macropores	Middle Phase Weathering	Final Phase Weathering
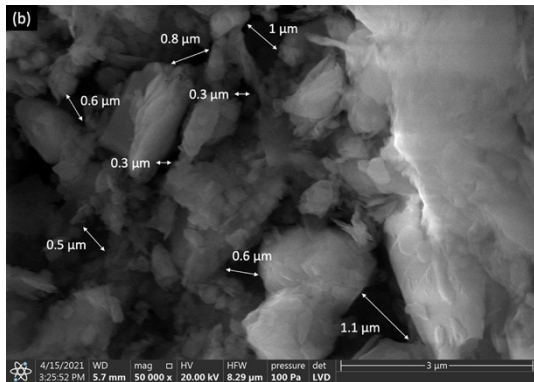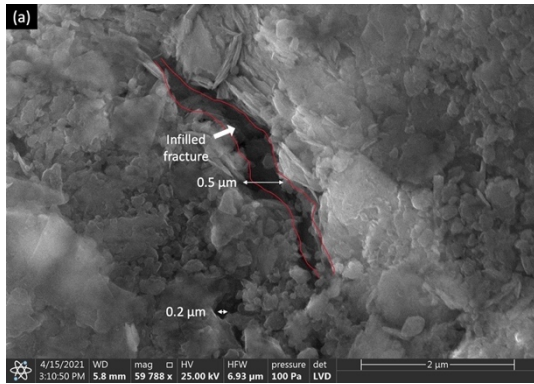
Presence of microfractures and micro-pores of size 0.2 μm, up to 2.3 μm.
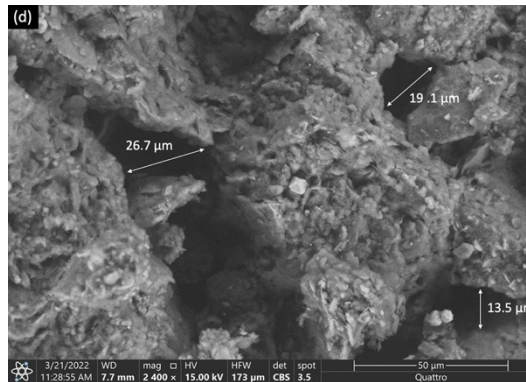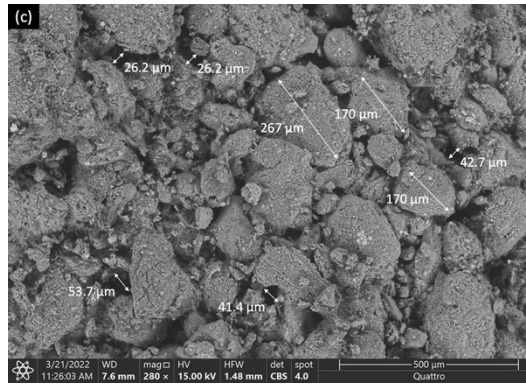
Shale slaked to small fragments with sizes up to 267 μm. Micro-pores enlarged to up to 53.7 μm.
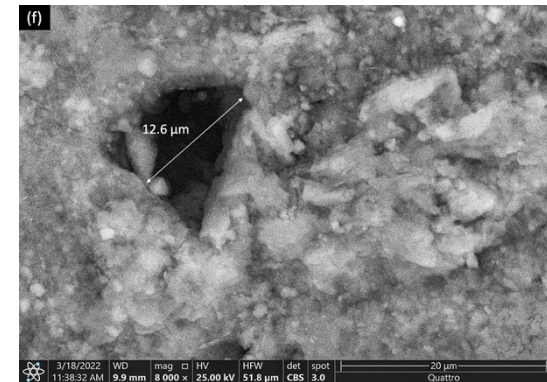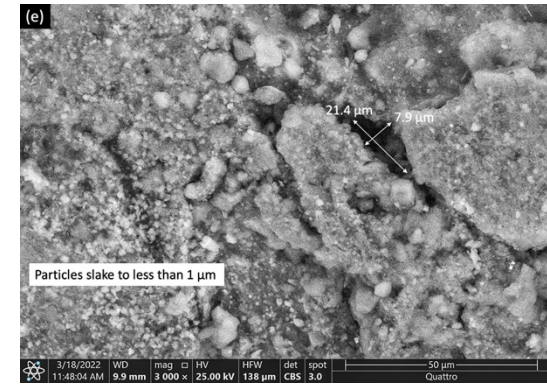
Fragments further degraded to less than 1 μm. More distribution of micro-pores is observed surrounding the smaller grains.

Figure 6.13: Changes in the Lambir shale micropores and grain sizes throughout the weathering process.

Sibuti Formation (Silty Shale)

Initial Macropores	Middle Phase Weathering	Final Phase Weathering
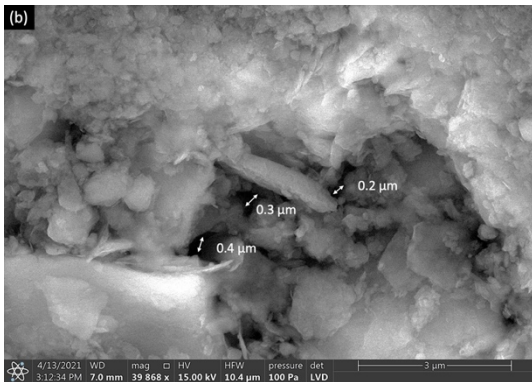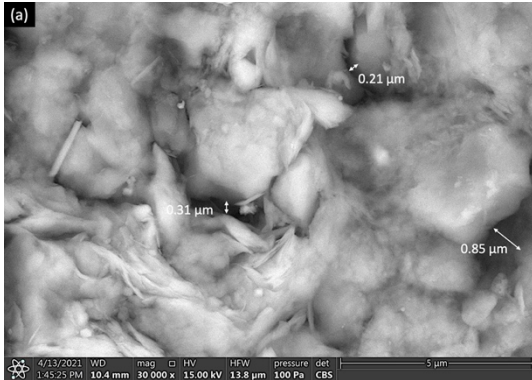
Nano and micro-pores of size 0.1 µm, up to 0.85 µm. Microfractures are not observed
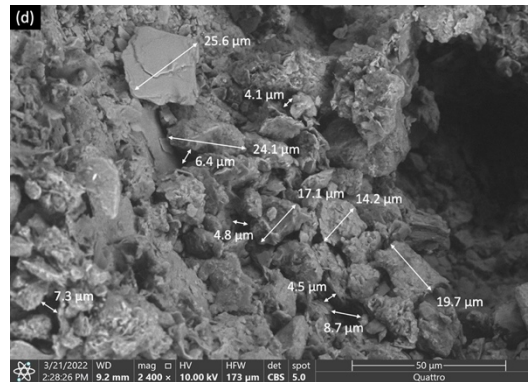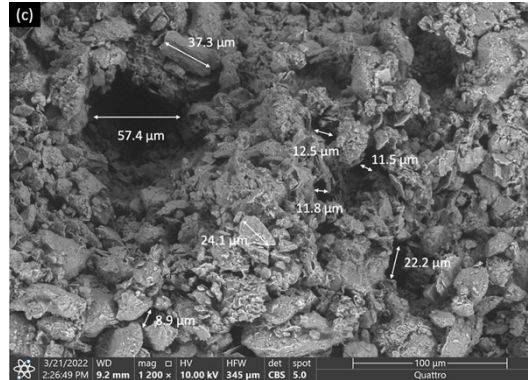
Shale slaked to small fragments with sizes up to 37.3 µm. Micro-pores enlarged to up to 57.4 µm.
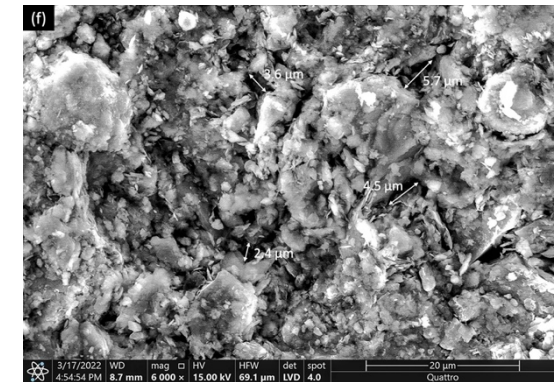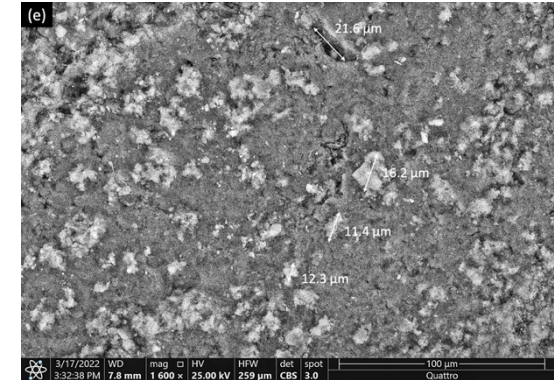
Minerals growth can be observed in (e). More distribution of micro-pores is observed surrounding the smaller grains.

Figure 6.14: Changes in the Sibuti shale micropores and grain sizes throughout the weathering process

6.2.4. Chemical Weathering

It is found that weathering of shales in the studied region involves both physical and chemical weathering. After the physical breakdown of the rock, chemical weathering occurred due to the interaction between the chemical composition and minerals of the rock with air and water. The reaction takes place mostly on the exposed surface of the rock and is further facilitated due to the high surface temperature (Dixon, 2013). Major reactions involved in chemical weathering associated with the studied shales include hydrolysis and oxidation.

Mineralogy and geochemistry of the studied shales were determined during the initial, middle, and final phase of the weathering, slaking test, control set up (no rain exposure), complete weathered materials, and weathered surface on the field. Table 6.2 and Table 6.3 presents the results of the bulk mineralogy and chemical composition. To justify the correlation between the parameters, the data were assessed for their suitability in Factor Analysis using SPSS software.

Table 6.3: Bulk mineralogy of the studied shale at initial, middle, and final weathering phase, slake, control (no rain), complete weathering, and field condition.

Shale Sample	Quartz	Albite/ Plagioclase	K-Feldspar	Muscovite/ Illite	Kaolinite	Chlorite	Smectite	Anatase	Pyrite	Gypsum	Jarosite	Amorphous
Lambir Initial	51.30	n.d.	trace	22.00	7.90	5.40	n.d.	0.70	2.70	n.d.	n.d.	10.00
Lambir Middle 1	39.10	n.d.	n.d.	24.20	7.20	2.40	n.d.	0.40	0.90	n.d.	n.d.	25.80
Lambir Middle 2	39.70	n.d.	n.d.	25.10	8.50	3.40	n.d.	0.60	0.90	n.d.	n.d.	21.80
Lambir Final 1	44.90	n.d.	n.d.	21.30	8.10	3.70	n.d.	0.70	1.10	n.d.	n.d.	20.20
Lambir Final 2	46.60	n.d.	n.d.	20.30	7.10	3.30	n.d.	0.40	1.80	n.d.	n.d.	20.50
Lambir Jar Slake	50.40	n.d.	n.d.	20.00	7.10	4.90	n.d.	0.60	2.40	n.d.	n.d.	14.60
Lambir Control Set	47.30	n.d.	n.d.	19.90	7.20	3.90	n.d.	0.50	1.90	n.d.	n.d.	19.30
Lambir Field	59.00	n.d.	n.d.	19.70	9.70	1.80	n.d.	0.30	2.10	n.d.	n.d.	7.40
Lambir Weathered	48.00	n.d.	n.d.	20.10	6.70	2.80	n.d.	0.40	0.60	n.d.	1.40	20.00
Sibuti Initial	48.70	5.60	1.00	16.50	5.20	5.10	1.00	0.70	0.40	n.d.	n.d.	15.80
Sibuti Middle 1	50.40	4.10	0.50	13.20	3.90	4.80	n.d.	0.30	0.30	n.d.	n.d.	22.50
Sibuti Middle 2	43.80	5.20	0.50	15.70	5.30	5.40	n.d.	0.50	0.40	0.30	n.d.	22.90
Sibuti Final 1	48.60	4.60	0.90	16.30	5.10	7.00	n.d.	0.60	0.20	n.d.	n.d.	16.70
Sibuti Final 2	48.50	4.10	1.20	15.60	5.30	6.10	n.d.	0.50	0.30	n.d.	n.d.	18.40
Sibuti Jar Slake	39.00	2.50	0.70	15.10	4.20	4.90	n.d.	0.50	0.30	n.d.	n.d.	32.80
Sibuti Control Set	46.70	3.90	0.60	14.80	3.90	5.30	trace	0.50	0.20	0.30	n.d.	23.80
Sibuti Field	46.10	4.70	0.50	17.70	4.80	5.10	n.d.	0.40	0.20	n.d.	n.d.	20.50
Sibuti Weathered	39.30	2.30	0.70	12.70	4.10	4.60	n.d.	0.30	0.60	4.40	n.d.	31.00

Table 6.4: Geochemistry of the studied shale at initial, middle, and final weathering phase, jar slake, control (no rain), complete weathering, and field condition.

Shale Sample	SiO_2	Al_2O_3	$Fe_2O_3(T)$	MnO	MgO	CaO	Na_2O	K_2O	TiO_2	P_2O_5	Cr_2O_3	V_2O_5	LOI
Detection Limit	*0.01*	*0.01*	*0.01*	*0.001*	*0.01*	*0.01*	*0.01*	*0.01*	*0.01*	*0.01*	*0.01*	*0.003*	
Lambir Initial 1	60.71	18.34	4.03	0.018	1.04	0.01	0.13	3.05	0.80	0.06	0.01	0.025	10.60
Lambir Initial 2	60.26	18.00	4.16	0.016	1.05	0.01	0.13	2.98	0.77	0.06	0.01	0.025	11.27
Lambir Middle 1	52.12	21.93	3.12	0.027	1.09	0.04	0.14	2.97	0.72	0.06	0.02	0.020	17.35
Lambir Middle 2	55.26	22.59	2.94	0.024	1.21	0.03	0.15	3.37	0.79	0.07	0.02	0.024	13.90
Lambir Final 1	58.27	20.39	3.78	0.014	0.94	0.02	0.16	3.17	0.79	0.06	0.02	0.024	12.45
Lambir Final 2	60.60	19.16	3.79	0.017	0.94	0.02	0.17	3.19	0.81	0.06	0.02	0.021	10.82
Lambir Jar Slake	60.34	18.26	3.96	0.025	1.16	0.02	0.14	3.07	0.78	0.06	0.01	0.020	10.98
Lambir Control	59.43	18.95	3.74	0.021	1.08	0.04	0.15	3.10	0.79	0.07	0.01	0.023	11.53
Lambir Field	64.83	17.37	3.09	0.018	0.74	0.03	0.14	2.85	0.82	0.04	0.02	0.019	9.97
Lambir Weathered	59.01	17.67	4.86	0.018	1.02	0.08	0.15	2.93	0.75	0.07	0.01	0.023	12.27
Sibuti Initial 1	61.88	16.14	5.76	0.048	1.83	0.70	0.66	2.60	0.79	0.07	0.01	0.020	8.00
Sibuti Initial 2	60.45	17.17	6.05	0.050	1.97	0.68	0.60	2.74	0.81	0.07	0.01	0.021	8.47
Sibuti Middle 1	62.08	17.46	5.57	0.063	1.73	0.72	0.65	2.54	0.74	0.08	0.01	0.020	8.38
Sibuti Middle 2	62.30	16.05	5.67	0.060	1.71	0.82	0.66	2.57	0.73	0.09	0.01	0.019	7.85
Sibuti Final 1	60.68	17.64	5.78	0.060	1.80	0.51	0.67	2.59	0.77	0.09	0.01	0.017	8.25
Sibuti Final 2	59.87	18.45	5.88	0.062	1.88	0.47	0.64	2.65	0.78	0.09	0.01	0.019	8.63
Sibuti Jar Slake	60.35	17.36	6.09	0.059	1.97	0.69	0.60	2.75	0.80	0.09	0.01	0.020	8.40
Sibuti Control	61.16	16.65	5.95	0.057	1.90	0.85	0.63	2.68	0.80	0.09	0.02	0.021	8.32
Sibuti Field	61.91	16.75	5.99	0.060	1.86	0.57	0.62	2.70	0.80	0.08	0.01	0.021	7.87
Sibuti Weathered	56.05	15.59	7.46	0.083	1.78	1.91	0.55	2.50	0.74	0.10	0.01	0.018	10.77

6.2.4.1. Factor Analysis

Factor Analysis is a useful statistical tool to ascertain the number of factors necessary to generate a set of variables, indicate the degree of correlation between the variables and the factors, and research and evaluate the common factors (Zarei et al., 2013). Table 6.5 shows the KMO and Bartlett's Test for the chemical composition datasets. The chemical composition dataset yields a KMO adequacy of 0.658 and Bartlett's significance level of 0.000. The KMO measure yield value greater than 0.5, suggesting that the sample dataset is adequate for Factor Analysis (Shrestha, 2021). The small significant level (<0.05) from Bartlett's Test of sphericity indicates that the dataset is factorable and significant for Factor Analysis. Principal Component Analysis (PCA) was carried out to extract the various factors and Varimax Rotation was performed to secure the relationship among the factors. An Eigenvalue indicates the measure of the factor's significance whereas loading values of > 0.75, 0.75 – 0.50, and 0.50 – 0.30 suggest strong, moderate, and weak associations respectively (Liu et al., 2003). Coupled with the loading values of greater than 0.3, Eigenvalues > 1 (strong significance) were taken as the criterion of the variable extractions. The component loading (Varimax rotated) and total variance explained are tabulated in Table 6.6.

Table 6.5: KMO and Bartlett's Test evaluation of chemical composition datasets for factor analysis.

Kaiser-Meyer-Olkin (KMO) Measure of Sampling Adequacy		0.658
Bartlett's Test of Sphericity	Approximate Chi-Square	374.072
	Degrees of freedom (df)	78
	Significance level	0.000

Table 6.6: Variables and factor loading of the sediment chemical composition dataset after Varimax rotation.

Chemical Composition	Component Factor	
	1	2
MnO	0.977	
Fe_2O_3 (T)	0.941	

Chemical Composition	Component Factor	
	1	2
Na$_2$O	0.914	
K$_2$O	-0.907	
CaO	0.906	
MgO	0.901	
P$_2$O$_5$	0.889	
V$_2$O$_5$	-0.681	
Al$_2$O$_3$	-0.670	-0.590
Cr$_2$O$_3$	-0.517	
SiO$_2$		0.947
LOI	-0.606	-0.773
TiO2	-0.369	0.686
Eigenvalue	7.988	2.195
% of total variance	61.444	16.885
Cumulative %	61.444	78.329

Extraction Method: Principal Component Analysis. Rotation Method: Varimax with Kaiser Normalization. a. Rotation converged in 4 iterations.

Results of the analysis indicated that there are two factors responsible for the short-term chemical weathering of the Lambir and Sibuti shale. These two factors accounted for 78.33 % of the cumulative total variance. Factor 1 has the highest significance in chemical weathering of the studied shale with an eigenvalue of 8.0. The factor explained 61.44 % of the total variance. MnO, Fe$_2$O$_3$, Na$_2$O, CaO, MgO, and P$_2$O$_5$, are strongly loaded with Factor 1. These elements attribute to the chemical weathering due to their mobility in association with the clay minerals. Additionally, the strong loading of Fe$_2$O$_3$ corresponds to the rapid oxidation of pyrite in the samples. Further discussion on elements mobility and pyrite oxidation during the short-term weathering can be referred in Section 6.2.4.2 and Section 6.2.4.3.

K$_2$O, V$_2$O$_5$, Al$_2$O$_3$, Cr$_2$O$_3$, and LOI show a negative loading in Factor 1 and correlate to the instability of feldspar, illite clay, and organic matter. The intense

leaching of the mobile elements prevents the accumulation of organic matter in the sediment (Garzanti et al., 2013). Since the study of carbonate/organic matter content in the studied sample is out of scope for the current research, an assumption is made based on the Loss of Ignition (LOI) values. LOI has been used to estimate the amount of organic matter and carbonates (Dean, 1974; Heiri et al., 2001; Santisteban et al., 2004). On the other hand, Vanadium is also closely associated with organic matter. Vanadium can exist in four oxidation states, +2, +3, +4, and +5. Hence, vanadium can easily substitute in iron-rich minerals or aluminium in the clay octahedral structures, forming a new clay mineral (Kelley, 2017).

The significance of Factor 2 based on the eigenvalue is 2.20 and explained 16.89 % of the total variance. SiO_2 is strongly loaded and TiO_2 is moderately loaded with factor 2. SiO_2 and TiO_2 are chemical elements that remained inert to the chemical weathering. SiO_2 is associated with the mineral quartz, ergo the higher amount of SiO_2 and quartz in a rock, the more durable against chemical weathering.

6.2.4.2. Elements mobility

Factor 1 shows a highly significance of the oxides Mg, P, Fe, Mn, Na, and Ca during the short-term weathering. These elements are the most mobile elements due to their ionic potential (Millot et al., 2013). The fine-grained Illite in particular is frequently disturb due to the disproportionate of the aluminium ion in its arrangement. The Al ion is typically partially replaced by Mg, Ca, Na, Fe^{2+}, Fe^{3+}, and K ions (Millot et al., 2013). The association of these elements can be observed evidently from the hydrochemistry results of the water collected during the natural slake weathering test (Table 6.7). The mobile elements were efficiently flushed from the sample shale by the rainfall. Water collected during the middle phase of weathering represents the dissolution of the minerals in the Lambir shale after 26 days and 46 days for the Sibuti shale. The remaining dissolution of the fully disintegrated samples was collected during the final phase of weathering. The results show that a high concentration of aluminium (average of 139.41 mg/L) in the Lambir shale at the

middle phase of weathering. This supports the displacement of the Al ions in the illite structure.

The Lambir shale shows similar order of ions concentration during the middle and final phase of weathering. The order of ions concentration is SO^{4-} > Al^{3+} > Mg^{2+} > Cl^- > Ca^{2+} > $Fe^{2+/3+}$ > K^- > Na^+ > Rb^+. A different trend of ions concentration is observed in the Sibuti shale during the middle and final phase of weathering. During the middle phase, the order of ions concentration follows the order of ions concentration in the Lambir shale. However, during the final phase, the ions concentration is Ca^{2+} > Cl^- > K^- > Mg^{2+} > Na^+ > Al^{3+} > $Fe^{2+/3+}$ > Rb^+ > SO^{4-}. The changes in ions concentration suggest a mineral/chemical precipitation occurred during the short-term weathering in the Sibuti shale. In contrast, the short-term chemical weathering in Lambir shale is mainly due to the hydrolysis process in the favour of elements mobility.

Single element mobility, defined as α can be calculated with reference to a non-mobile element during weathering. Most chemical weathering indices such as CIA, WIP are based on the principal assumption that certain major oxides such as Al_2O_3, Fe_2O_3, and TiO_2 are immobile and remain constant during weathering while the mobile element such as SiO_2, Na_2O, K_2O, CaO, and MgO decrease (Duzgoren-Aydin et al., 2002). From the chemical composition results of the studied shales, TiO_2 is an immobile element and remains constant throughout the weathering process. Hence the calculation of single element mobility with reference to Gaillardet et al. (1999) and Garzanti et al. (2013) can be calculated based on equation 6.3. In the study of element mobility and transport, the concentration ratio in the sample is typically normalised to the concentration ratio in the parent Upper Continental Crust (UCC) of McLennan (2001). The calculated α for the elements in the studied shale composition are tabulated in Table 6.8.

$$\alpha_E^{Ti} = [Ti/E]_{sample}/[Ti/E]_{UCC} \qquad 6.3$$

where:

α_E^{Ti} $\qquad$ = $\qquad$ Single element mobility of element E, relative to immobile Ti

$[Ti/E]_{sample}$ =   Concentration ratio of mobile Ti to element E in the sample

$[Ti/E]_{UCC}$ =   Concentration ratio of mobile Ti to element E based on UCC

      The mobility of the elements during the short-term natural weathering shows a slightly different trend between the Lambir and the Sibuti shale. The sequences are outlined in equations 6.4 and 6.5 for the Lambir and the Sibuti shale respectively. Both shale samples indicate strong leaching for Ca and Na. The small cations (Na, Ca, and Sr) are in fact known to be selectively removed from weathering. Larger cations, on the other hand, are kept by preferential exchange and adsorption on secondary minerals (Nesbitt et al., 1980; Garzanti et al., 2013). However, the magnitude of the mobility for Ca and Na in the Lambir shale is substantially more compared to the Sibuti shale. The α^{Ti}_{Ca} in the Lambir shale ranges between 110 and 410 and the same for $\alpha^{Ti}Na$ in the range of 27 $-$ 35. In contrast, the α^{Ti}_{Ca} in the Sibuti shale ranges between 5 and 9 and between 6 to 8 for $\alpha^{Ti}Na$. Dispersion of the elements can been in Figure 6.15. The elemental maps provide some insight into the ion's substitutions on the clay minerals. It is believed that the mobility of the elements in Lambir shale is intensified by the acidic condition produced during pyrite oxidation, which corresponds to the strong loading of Fe_2O_3 in Factor 1.

$$\alpha^{Ti}_{Ca} > \alpha^{Ti}_{Na} > \alpha^{Ti}_{Mn} > \alpha^{Ti}_{P} > \alpha^{Ti}_{Mg} > \alpha^{Ti}_{Fe} > \alpha^{Ti}_{K} > \alpha^{Ti}_{Cr} > \alpha^{Ti}_{V} > \alpha^{Ti}_{Al} \qquad 6.4$$

$$\alpha^{Ti}_{Ca} > \alpha^{Ti}_{Na} > \alpha^{Ti}_{P} > \alpha^{Ti}_{Mn} > \alpha^{Ti}_{K} > \alpha^{Ti}_{Mg} > \alpha^{Ti}_{Cr} > \alpha^{Ti}_{V} > \alpha^{Ti}_{Al} > \alpha^{Ti}_{Fe} \qquad 6.5$$
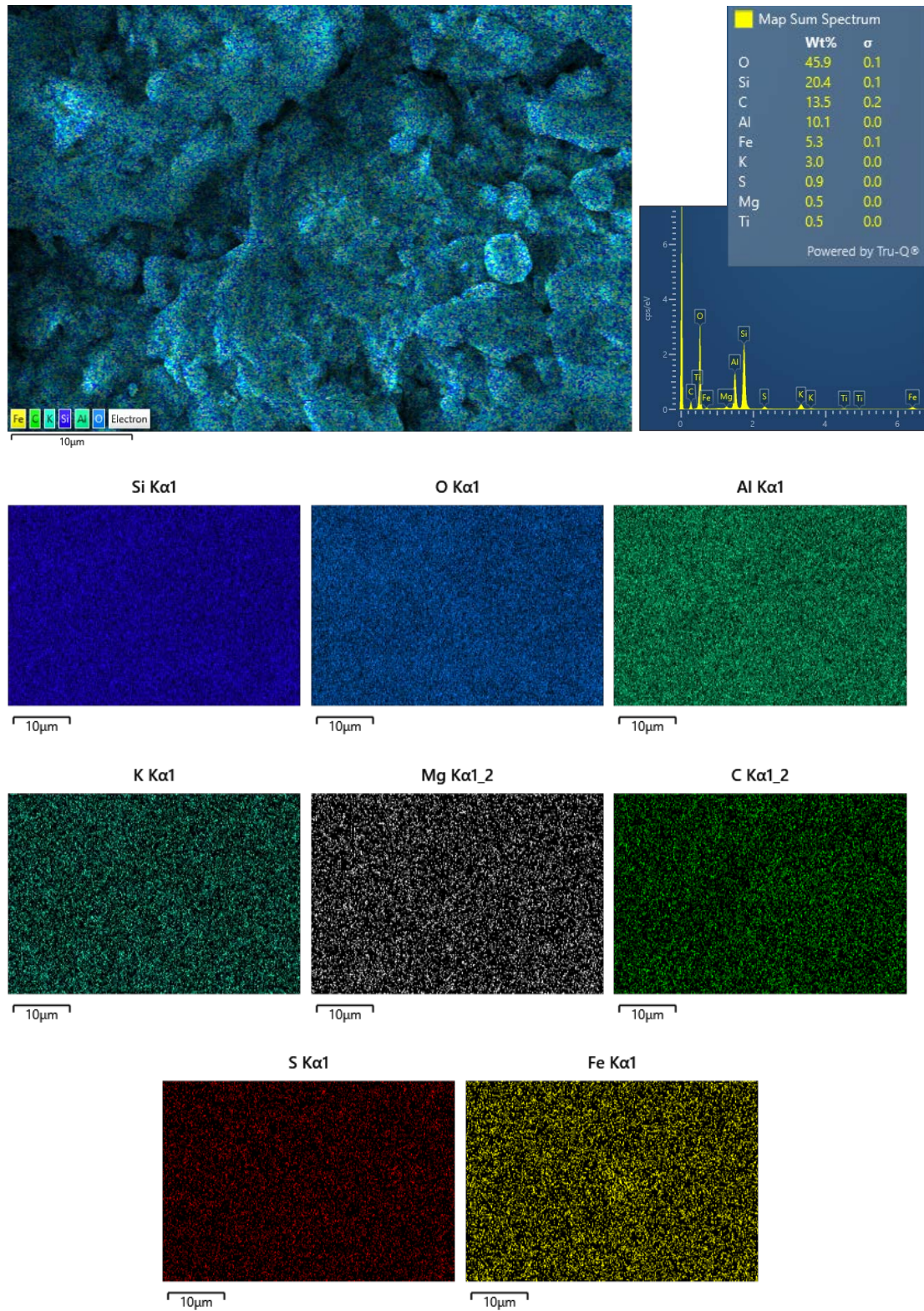
Figure 6.15: EDS layered map and its elemental maps of the Lambir shale during middle phase of weathering. The compositions of the elements can be seen scattered across the sample as dispersed elements.

6.2.4.3.   Pyrite Oxidation

Pyrite (FeS$_2$) is a common type of sulfide mineral typically associated with coal, organic matter, and metal ores (Blowes et al., 2003; Giblin, 2009). It may exist in framboidal, individual equant, or both depending on the stage of diagenesis and the environment during their formation. Oxidation of pyrite occurs when the mineral is exposed to air and water. Pyrite oxides to iron and other metals, sulfate, and sulphuric acid. The oxidation process could take place 10 to 100 days for a complete depletion of O$_2$ into the water phase and can be validated through an increase of sulfate (SO$_4$) (van der Jagt, 2005).

In the Lambir hydrochemistry results (Table 6.7), the pyrite can be seen oxidised rapidly even in the middle phase of weathering. The SO$_4$ concentration at the middle stage of weathering is 1245 mg/L (average) and the pyrite is still oxidising even at the final stage of weathering with the SO$_4$ concentration of 645 mg/L (average). However, in the Sibuti shale, the pyrite oxidation took place only up to the middle stage of weathering as no concentration of SO$_4$ is detected at the final stage of weathering. At a constant relative humidity, the oxidation of pyrite was found to decrease with time due to the production of an aqueous film of FeSO$_4$ and H$_2$SO$_4$ that limits the O$_2$ diffusion (Jerz et al., 2004).

The initial mineralogical analysis of shale shows that the Lambir shale contains more pyrite than the Sibuti shale. The percentage difference is by 148 % (Figure 5.1). The oxidation of pyrite in the Lambir shale produced an acidic condition of pH 3.9 and a circumneutral pH of 6.9 in the Sibuti shale. The difference in the pH conditions depends on the hydrolysis process and the precipitation of ferrous/ferric ions (King, 2013). The initial oxidation of pyrite produces one mole of Fe^{2+}, two moles of SO$_4{}^2$ and two moles of H$^+$ for every mole of pyrite oxidized (Equation 6.6). The most important oxidant is the O$_2$ and Fe^{3+}. Following acidic conditions, the Fe (II) may be oxidised to Fe (III) (Equation 6.7). Meanwhile, in basic conditions, Fe (III) oxyhydroxides (ferrihydrite) may be precipitated. Equation 4.9 summarises the overall stoichiometry of the oxidation.

Table 6.7: Hydrochemistry results of the collected water during the natural slake weathering test.

Sample	Unit	pH	Cl	SO$_4$	Ca	Mg	K	Na	Fe	Rb	Cs	V	Al
Lambir Middle 1	mg/L	3.9	53	1550	12.7	78	1.4	0.7	3.336	0.054	0.001	0.001	180.99
Lambir Middle 2	mg/L	3.9	43	940	11.7	58.7	1.8	2.1	0.37	0.059	0.001	0.001	97.83
Lambir Final 1	mg/L	3.9	48	867	13.5	53	7.5	1.8	4.84	0.096	0.001	0.001	90.74
Lambir Final 2	mg/L	3.9	21	423	10.8	20.7	2.7	1.6	5.369	0.088	0.001	0.001	45.04
Sibuti Middle 1	mg/L	7.1	17	206	61.6	11.2	15.3	6.9	0.666	0.007	0.001	0.001	0.419
Sibuti Middle 2	mg/L	7.0	14	182	58.7	9.4	7.2	4.9	0.314	0.005	0.001	0.001	0.204
Sibuti Final 1	mg/L	7.0	6	0	24.4	2.4	2.9	0.4	0.142	0.005	0.001	0.001	0.145
Sibuti Final 2	mg/L	6.9	4	0	24.2	2.7	3.2	2.7	0.206	0.004	0.001	0.001	0.254

Table 6.8: Calculated α^{Ti}_E values of the elements in the chemical composition.

Sample Set	Single Element Mobility Index relative to mobile Ti, α^{Ti}_E									
	α^{Ti}_{Al}	α^{Ti}_{Fe}	α^{Ti}_{Mn}	α^{Ti}_{Mg}	α^{Ti}_{Ca}	α^{Ti}_{Na}	α^{Ti}_K	α^{Ti}_P	α^{Ti}_{Cr}	α^{Ti}_V
Lambir Initial 1	0.97	1.45	5.03	2.48	491.02	35.05	1.29	3.13	1.42	0.89
Lambir Initial 2	0.95	1.35	5.45	2.36	472.61	33.74	1.27	3.01	1.37	0.86
Lambir Middle 1	0.73	1.69	3.02	2.13	110.48	29.29	1.20	2.81	0.64	1.01

Sample Set	Single Element Mobility Index relative to mobile Ti, α^{Ti}_E									
	α^{Ti}_{Al}	α^{Ti}_{Fe}	α^{Ti}_{Mn}	α^{Ti}_{Mg}	α^{Ti}_{Ca}	α^{Ti}_{Na}	α^{Ti}_{K}	α^{Ti}_{P}	α^{Ti}_{Cr}	α^{Ti}_{V}
Lambir Middle 2	0.78	1.97	3.73	2.11	161.63	30.00	1.16	2.65	0.70	0.92
Lambir Final 1	0.86	1.53	6.39	2.71	242.44	28.13	1.23	3.09	0.70	0.92
Lambir Final 2	0.94	1.56	5.40	2.78	248.58	27.14	1.25	3.17	0.72	1.08
Lambir Slake	0.95	1.44	3.53	2.17	239.37	31.74	1.25	3.05	1.38	1.09
Lambir Control	0.93	1.55	4.26	2.36	121.22	30.00	1.26	2.65	1.40	0.96
Lambir Field	1.05	1.94	5.16	3.57	167.77	33.36	1.42	4.81	0.73	1.21
Sibuti Initial 1	1.09	1.00	1.86	1.39	6.93	6.82	1.50	2.65	1.40	1.10
Sibuti Initial 2	1.05	0.98	1.84	1.33	7.31	7.69	1.46	2.71	1.44	1.08
Sibuti Middle 1	0.94	0.97	1.33	1.38	6.31	6.48	1.44	2.17	1.31	1.03
Sibuti Middle 2	1.01	0.94	1.38	1.38	5.46	6.30	1.40	1.90	1.29	1.07
Sibuti Slake	1.02	0.96	1.54	1.31	7.12	7.59	1.43	2.08	1.42	1.12
Sibuti Control	1.07	0.98	1.59	1.36	5.78	7.23	1.47	2.08	0.71	1.06
Sibuti Field	1.06	0.98	1.51	1.39	8.61	7.35	1.46	2.35	1.42	1.06

process. In the presence of calcite minerals impurities, the pH of the aqueous solution is expected to be slightly alkaline or circumneutral due to the action of buffering (King, 2013). The precipitation of alteration products of pyrite is often reported in circumneutral conditions, which may attribute to the low mobility of Fe in the Sibuti shale compared to the Lambir shale.

$$FeS_2 + \frac{7}{2}O_2 + H_2O \rightarrow Fe^{2+} + 2SO_4^{2-} + 2H^+ \qquad 6.6$$

$$Fe^{2+} + \frac{1}{4}O_2 + H^+ \rightleftharpoons Fe^{3+} + \frac{1}{2}H_2O \qquad 6.7$$

$$Fe^{3+} + 3H_2O \rightleftharpoons Fe(OH)_3 + 3H^+ \qquad 6.8$$

$$FeS_2(s) + \frac{15}{4}O_2(aq) + \frac{7}{2}H_2O(aq) \rightarrow 2SO_4^{2-} + Fe(OH)_3(s) + +4H^+(aq) \quad 6.9$$
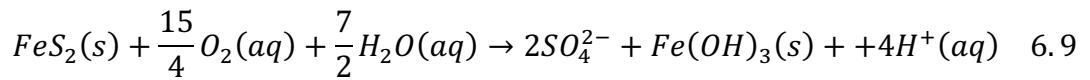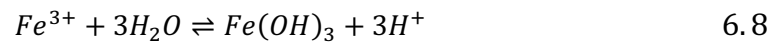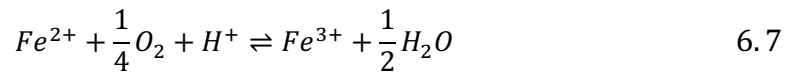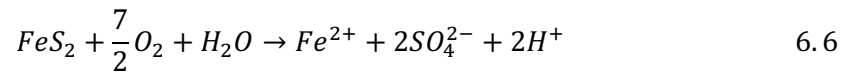
The oxidation of pyrite in the Lambir shale can be observed through the leaching of the Fe from the matrix of the rock (Figure 6.16, Figure 6.17). In addition, due to the high porosity and presence of microcracks in the fabric of the Lambir shale, small-scale oxidation of the pyritic grains is suspected to have taken place much earlier on the outcrop. The leaching of Fe in the Sibuti shale during the middle phase of weathering is restricted and moderate compared to the Lambir shale (Figure 6.18). At the final phase of weathering, new minerals can be seen precipitated in the Sibuti shale (Figure 6.19). Mineralogy analysis confirmed the formation of a small amount of gypsum in the weathered Sibuti shale. The formation of gypsum validates the interaction of calcium carbonate (calcite) and sulfuric acid (Sadisun et al., 2005). Equations $6.10 - 6.13$ outline the stoichiometry of the pyrite alteration to the gypsum process (Ritsema et al., 1993). The presence of calcite in the studied shale does not decrease the durability as reported by (Russell 1982) but play a role in the chemical weathering process.

$$4FeS_2(s) + 15O_2(g) + 14H_2O \rightarrow 4Fe(OH)_3(s) + 8SO_4^{2-}(aq) + 16H^+(aq) \qquad 6.10$$

$$CaCO_3(s) + 2H^+(aq) \rightarrow Ca^{2-}(aq) + H_2O + CO_2(g) \qquad 6.11$$

$$CaMg(CO_3)_2(s) + 4H^+(aq) \rightarrow Ca^{2+}(aq) + Mg^{2+}(aq) + 2H_2O + 2CO_2(g) \qquad 6.12$$

$$CaCO_3(s) + 2H^+(aq) + SO_4^{2-}(aq) + H_2O \rightarrow CaSO_4 \cdot 2H_2O(s) + CO_2(g) \qquad 6.13$$
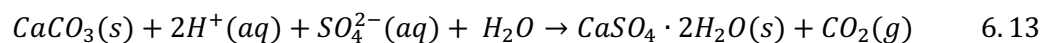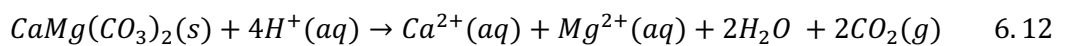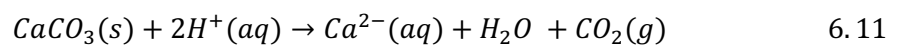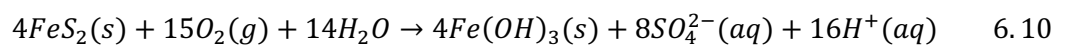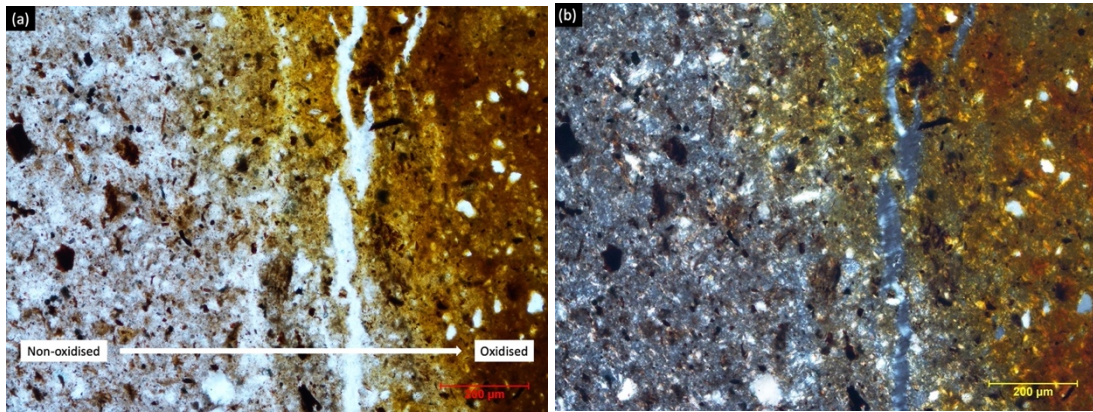
Figure 6.16: Thin section microphotographs of pyrite oxidation process observed in the Lambir shale. (a) plane polarised, ppl; (b) cross polarised, xpl.
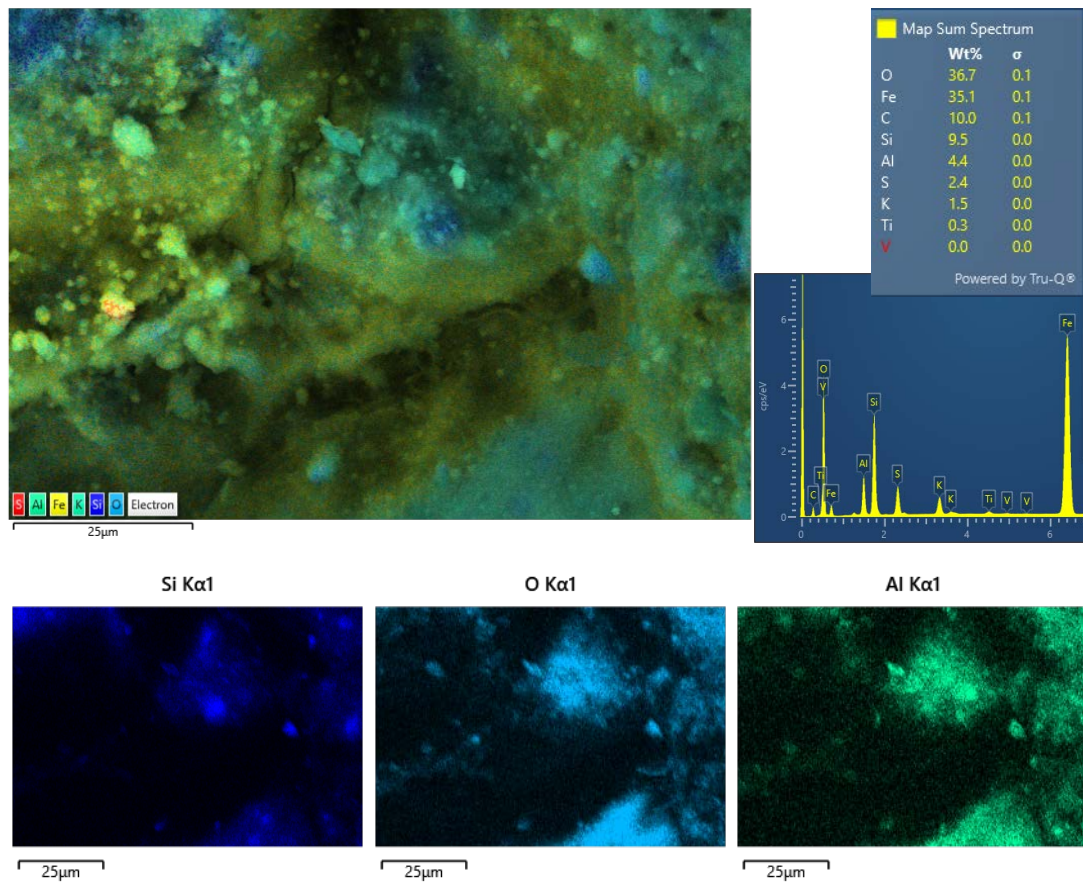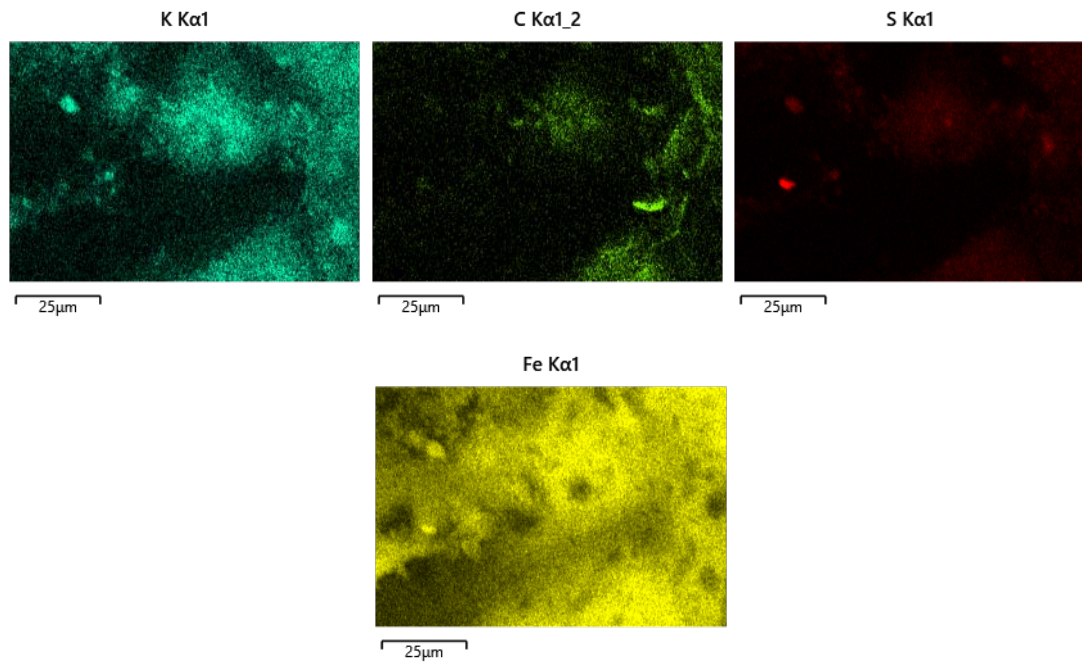
Figure 6.17: EDS layered map and its elemental maps of the Lambir shale showing the pyrite oxidation process in the final phase of weathering. The Fe is found occupying the matrix of the rock.
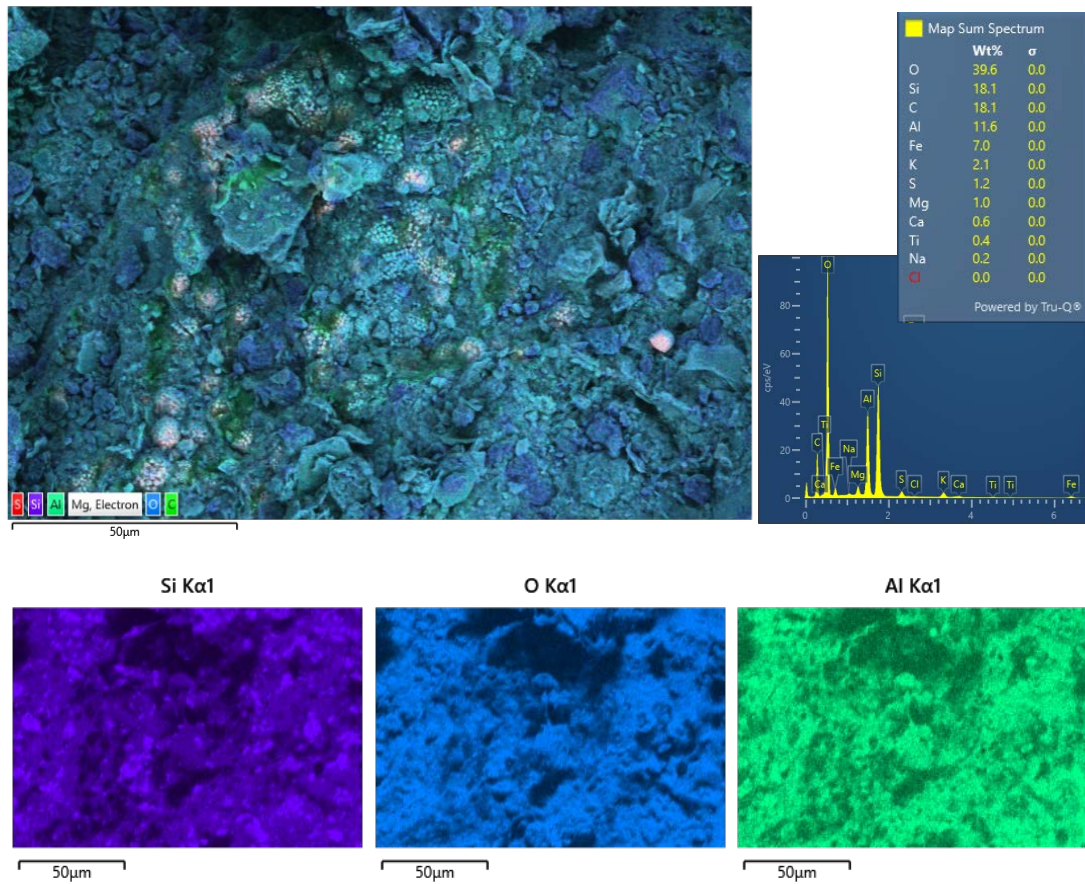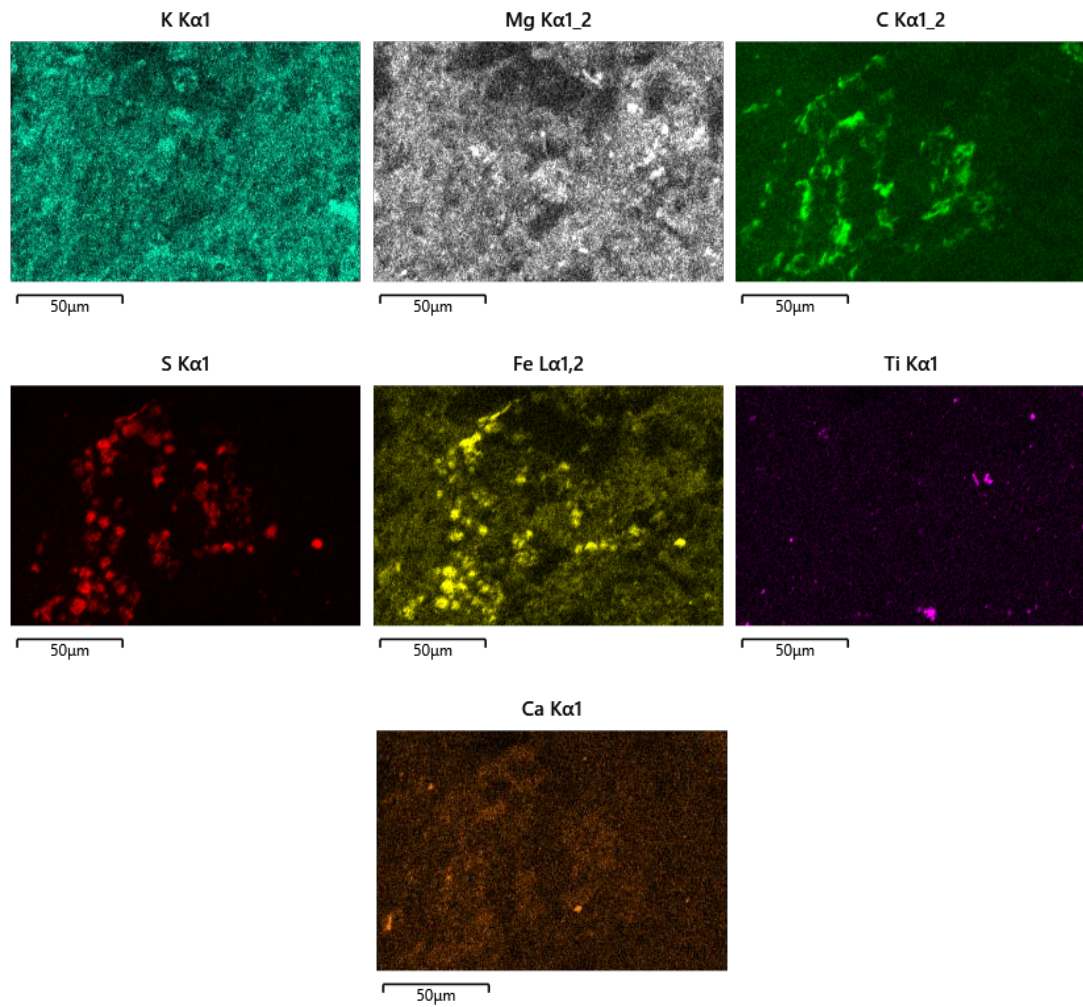
Figure 6.18: EDS layered map and its elemental maps of the Sibuti shale showing the moderate pyrite oxidation process during the middle phase of weathering.
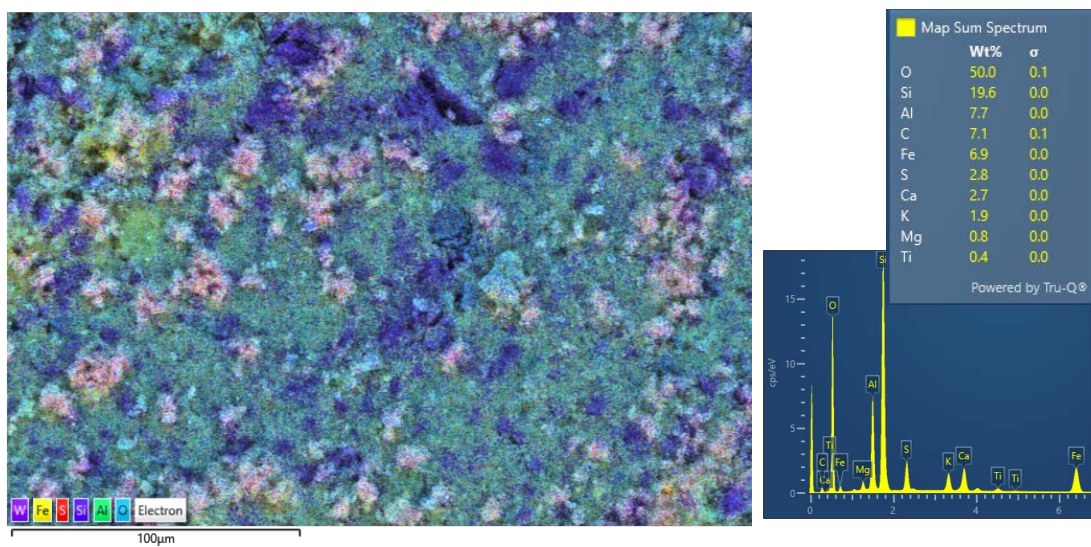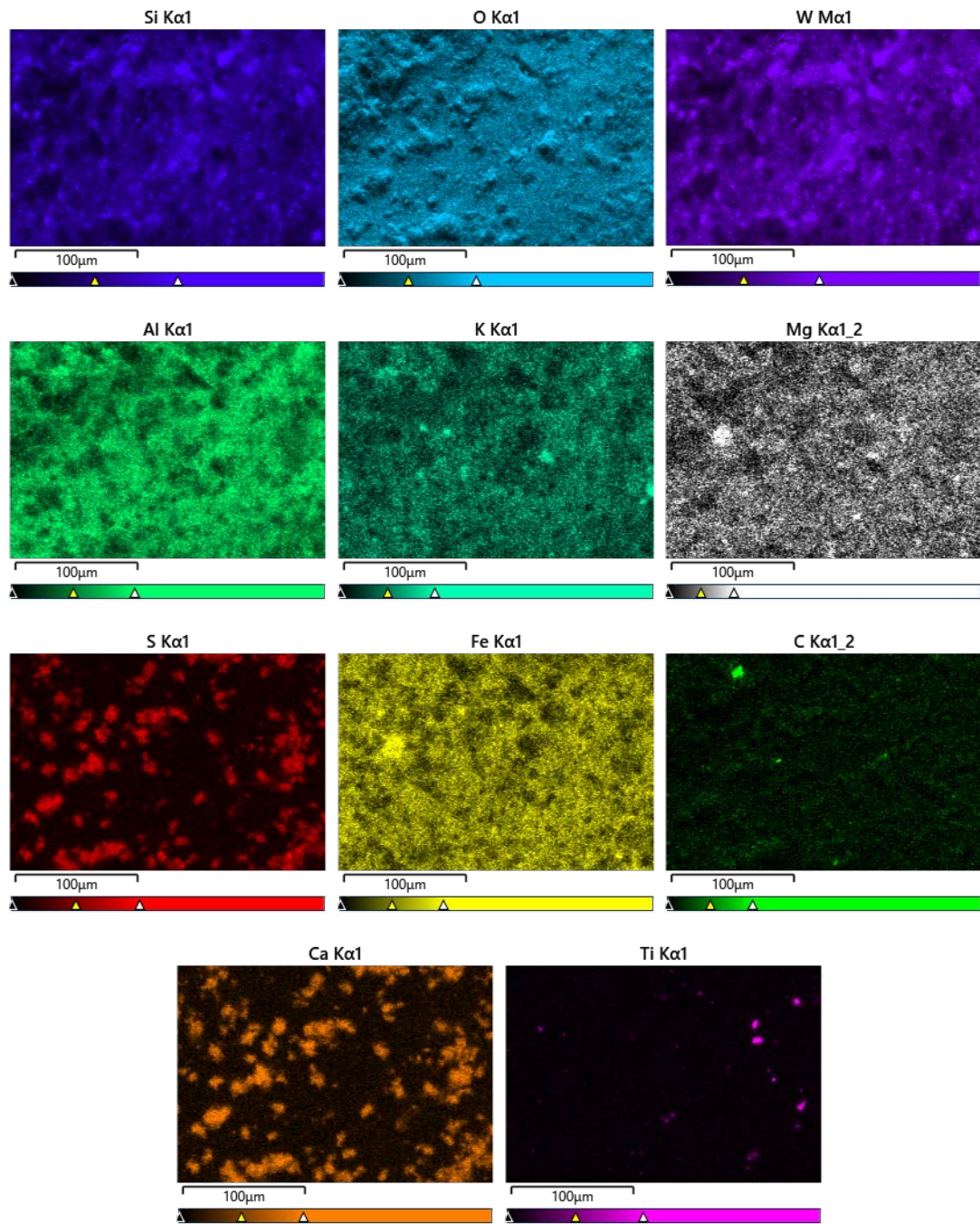
Figure 6.19: EDS layered map and its elemental maps of the Sibuti shale showing new minerals precipitated at the final phase of weathering.

Chapter 7: Conclusions and Future Recommendations

7.1. Conclusions

The theme of the research was to study the durability and short-term weathering of the Northern Sarawak shale. Several reports of landslides and road damages have been reported in the studied area over the years. In particular, the recent construction of the Pan Borneo Highway has been facing several issues with the erratic behaviour of shale and clay-bearing rocks. Inadequate understanding of the transitional nature from rock to the soil-like materials, both physical and chemically, during weathering limits the remediation approaches. Hence, this work aims to contribute to the shale durability assessment, its properties (physical, mineralogy, geochemistry, and textural), and behaviour during physical and chemical weathering.

The first objective of the research was to identify the most and least durable shale in the Northern Sarawak. Five fresh and unweathered shale samples were cored from the exposed outcrops within the region between Miri and Batu Niah. Due to the limitation of exposure and accessibility, the shale samples collected were essentially representative shale units of the five geological formations. The formations from younger to older include the Miri, Tukau, Lambir, Sibuti and Setap Shale Formations. The assessment of the durability was carried out following ASTM D4644-16 standard procedure. Based on the results of Id1, the increasing order of durability among the formations was Lambir (11.5%) < Tukau (15.6%) < Miri (23.2%) < Setap Shale (31.3%) < Sibuti (38.1%). According to the durability classification, all five formations has low to very low durability. The Lambir shale has the lowest durability while the Sibuti shale has the highest durability.

The second objective aimed to determine shale's physical, mineralogical, and chemical composition. In short, the amount and types of clay, moisture content, porosity, permeability, and the presence of reactive iron oxyhydroxides (pyrite) contributed to the low durability of the Lambir shale. The Lambir shale was

categorised as clayey shale with a clay composition of 50.5 % and initial moisture content of 11.9 %. The results suggested that the clay has high absorption and adsorption values, weakening the inter-granular bonds and promoting rock disintegration.

Interestingly, Atterberg's limit test results showed that the Lambir shale clays were inactive, indicating the absence of expandable clay. The plasticity index yields a higher value than the Sibuti shale. This was confirmed by the absence of expandable mineral smectite in its mineralogy through XRD analysis. Microtextural and chemical composition analysis revealed that the clay in the Lambir shale was predominantly potassium illite. Potassium ions in the interlayer of the mixed clay structure favoured hydration and ions adsorption.

The fabric and texture of the Lambir shale influenced the porosity and permeability of the rock unit. The clays were found to be arranged in skeletal microfabric, with abundant irregular micropores of sizes between 0.2 µm to 2.3 µm. Microfractures were also observed under SEM. The distribution of micropores and microfractures increased the surface area for water-rock interaction. In contrast, the more durable Sibuti shale was categorised as silty shale with 7.8 % clay content. Although it has a lower initial moisture content and had less plasticity, the clays were active. It can be inferred from the results that the slaking behaviour of the Sibuti shale was due to the swelling clay potential. Mineralogy analysis confirmed the presence of expandable smectite. Nano and micropores of sizes ranging from less than 0.1 µm and up to 0.85 µm were found in the Sibuti shale. The clays were condensed in a turbostratic microfabric, which resulted in the low porosity and permeability of the rock. Therefore, the findings show a clear correlation between shale properties and durability.

Further, the third objective of the research was to investigate the relationship between durability against short-term weathering. A natural slake test was carried out where the shale samples from the Lambir and the Sibuti shale were exposed to the natural climatic conditions until complete disintegration. Initial, middle, and final

phases were determined based on the weight loss percentage. Mineralogy, geochemistry, and water analysis were carried out at each phase to study the changes during weathering. Their slaking behaviour in regard to rain events was also recorded. The study found that, under natural weathering, the studied shale breakdown by both physical and chemical weathering mechanisms. The initial disintegration occurred due to the mechanical breakdown from the rainfall intensity. Differential stress during drying caused further cracks along the lamination plane. Following that, the Lambir and Sibuti shale showed two different modes of slaking depending on their rock properties. The Lambir shale gradually degrades to muddy lump while the Sibuti shale degrades to individual slakes until completely disintegrated.

The high clay content and high porosity in the Lambir shale during continuous hydration caused the rock to transition into a muddy lump. Due to the high moisture content, the rock took longer time to dry. The strength of the rock reduced while it was in a water-absorbing state, and the surface material was gradually removed as the rain continued. On the other hand, the effect of swelling and shrinking of the expandable smectite may contribute to the slaking behaviour of the Sibuti shale. As the clay expanded, the volume of the rocks increased and caused subsequent tensile failure due to internal pore air compression. It was observed that the rate of slaking occurred rapidly at the beginning of weathering and substantially decreased as the shale degraded to smaller fragments. The micropores in both shales enlarged, and the distribution of micropores increased as the particles degraded. The Lambir shale took 46 days, while the Sibuti shale took 66 days to fully disintegrated.

Results obtained from factor analysis indicated that the main processes involved in the chemical weathering of the studied shale under natural climatic conditions were the dissolution of clay due to elements' mobility and pyrite oxidation. Both shale samples showed strong leaching for Ca and Na. The preferential removal of these ions was due to their differential sized and ionic charges. The order of elements' mobility calculated during chemical weathering in the Lambir shale was $\alpha_{Ca}^{Ti} > \alpha_{Na}^{Ti} > \alpha_{Mn}^{Ti} > \alpha_{P}^{Ti} > \alpha_{Mg}^{Ti} > \alpha_{Fe}^{Ti} > \alpha_{K}^{Ti} > \alpha_{Cr}^{Ti} > \alpha_{V}^{Ti} > \alpha_{Al}^{Ti}$. Meanwhile, the

mobility in the Sibuti shale was $\alpha_{Ca}^{Ti} > \alpha_{Na}^{Ti} > \alpha_{P}^{Ti} > \alpha_{Mn}^{Ti} > \alpha_{K}^{Ti} > \alpha_{Mg}^{Ti} > \alpha_{Cr}^{Ti} > \alpha_{V}^{Ti} > \alpha_{Al}^{Ti} > \alpha_{Fe}^{Ti}$. The magnitude of elements leaching in the Lambir shale is higher than in the Sibuti shale due to the strong effect of pyrite oxidation. Pyrite oxidation released iron and other metals, sulfate, and sulphuric acid. The acidic condition promotes further oxidation of Fe (II) to Fe (III). In the Sibuti shale, however, the presence of carbonates (calcite) neutralised the acidic condition and supported the precipitation of Fe (III) oxyhydroxides. Mineralogy analysis confirmed the presence of gypsum during the chemical weathering.

Finally, the last objective was to establish which properties would be useful in differentiating a high and low durable shale. The findings show that clay content is the primary indicator of differentiating the durability of the Lambir and Sibuti shale. The high clay content will associate with higher moisture content and subsequently contribute to the low durability. In addition, the shale's fabric and microtexture influence the porosity and permeability. A high porosity and permeability values increase the rock-water interaction and promote slaking. The presence of pyrite is also the main indicator contributing to low durability due to its rapid oxidation. The selection of the most useful shale properties could be made on a case-by-case basis, depending on the feasibility.

On the field, the first visible sign would be the inspection of any acid drainage caused by the pyrite oxidation. The Lambir shale excreted reddish-brown discharge during coring, and some rusty discolouration can be seen on the heavily weathered surface. Results from the laboratory characterisation demonstrated the use of determining shale's physical properties in predicting its durability. Since particle size distribution analysis mainly was time-consuming, specific gravity can provide a helpful estimation of the content of clay and heavy minerals. Specific gravity reflects the overall density of the rock composition. The typical specific gravity value of shale was $2.06 - 2.67$ gcm^{-3}. A specific gravity value of more than 3 gcm^{-3} indicated a higher clay and heavy minerals content such as pyrite. Next, porosity and permeability would be also helpful in predicting durability. Moreover, Atterberg's limit would be an advantageous parameter in postulating the slaking behaviour.

Although mineralogy, chemical composition, and microtextural analysis were often costly and required complex laboratory resources, an initial rock analysis would help foresee the possible complications and hazard issues in the area. Oxidation of pyrite took place rapidly upon contact with water. It is concluded from the study that the shale from the Lambir Formation is more susceptible to weathering and is less durable compared to the Sibuti Formation. The type and amount of clay, microfabric, porosity, and presence of pyrite contributed the most to the low durability. It is recognised that the erosion of shale due to weathering is severe in this region. This research revealed the cause of shale erosion and is hoped to give insights for future remediation and prevention techniques. The common practice of protection of erosion after the exposure of slope is by shotcreting/guniting. The finding of this research paths the way of alternative solution to prevent the soil erosion. First and second months after the construction exposure were predicted to be crucial due to the rapid pyrite oxidation. The remedial technique may be considered control on the sulfide oxidation by limiting water contact, acid neutralisation treatment, and/or utilising biotechnology techniques in the use of bactericides. More research needs to be carried out for a successful and cost-effective remedial method.

7.2. Future Recommendations

Lastly, for a successful research continuation, it should be emphasised that future studies must be linked to the development and monitoring of engineering practice. The following is a list of research suggestions:

a) Laboratory studies on a bigger sample size of shale and other clay-bearing rocks from multiple layers of the geological formations, to validate the characterisation.

b) Investigate the carbonate content and related chemical weathering process involved during the natural slake weathering test.

c) Studies on the cost-effective techniques in remedial and prevention methods in stabilising and prevent rock degradation such as controlling sulfide

oxidation by limiting water contact, acid neutralisation treatment, and/or utilising biotechnology techniques in the use of bactericides.

d) The elemental leaching approach can be adapted to figure out the intensity of leaching at various stages of the durability test.

e) The kinetic process during chemical reactions may be studied to estimate how quick the chemical changes.

References

Abd-Alrahman, E., Ayman, A. H., & Medhat, R. (2020). Impact of Slaking Shale Behaviour on Damage of Engineering Structures, Saudi Arabia. *Geotechnical Research*, *7*(2), 117-131. https://doi.org/10.1680/jgere.20.00011

Abdul Rahman, M. N., & Tahir, S. (2019). Middle Miocene Wave Influenced Tidal Dominated Lambir Formation, Miri, Sarawak: Case Study in Tusan Beach and Lambir Hill. *Geological Behavior*, *3*, 20-27. https://doi.org/10.26480/gbr.01.2019.20.27

Alatas, I. M., Kamaruddin, S., Nazir, R., Irsyam, M., & Himawan, A. (2015). Shear Strength Degradation of Semarang Bawen Clay Shale Due to Weathering Process. *Jurnal Teknologi*, *77*(11), 109-118. https://doi.org/10.11113/jt.v77.6429

Alling, H. L. (1945). Use of Microlithologies as Illustrated by Some New York Sedimentary Rocks. *Geological Society of America Bulletin*, *56*(7), 737-756. https://doi.org/10.1130/0016-7606(1945)56[737:UOMAIB]2.0.CO;2

Alonso, E., & Pineda, J. (2006). *Weathering and Degradation of Shales: Experimental Observations and Models of Degradation* VI South American Rock Mechanics Conference, Cartagena de Indias, Colombia. https://www.researchgate.net/publication/266618329_Weathering_and_degradation_of_shales_experimental_observations_and_models_of_degradation

ASTM. (2006). *D2487-17e1 Standard Practice for Classification of Soils for Engineering Purposes (Unified Soil Classification System)*. ASTM International. https://doi.org/10.1520/D2487-17E01

ASTM. (2016). *D4644-16 Standard Test Method for Slake Durability of Shales and Other Similar Weak Rocks*. ASTM International. https://doi.org/10.1520/D4644-16

ASTM. (2017a). *C117-17 Standard Test Method for Materials Finer Than 75-Mm (No. 200) Sieve in Mineral Aggregates by Washing*. ASTM International. https://doi.org/10.1520/C0117-17

ASTM. (2017b). *D7928-17 Standard Test Method for Particle-Size Distribution (Gradation) of Fine-Grained Soils Using the Sedimentation (Hydrometer) Analysis*. ASTM International. https://doi.org/10.1520/D7928-17

ASTM. (2019a). *2216-19 Standard Test Methods for Laboratory Determination of Water (Moisture) Content of Soil and Rock by Mass*. ASTM International. https://doi.org/10.1520/D2216-19

ASTM. (2019b). *C136/C136m-19 Standard Test Method for Sieve Analysis of Fine and Coarse Aggregates*. ASTM International. https://doi.org/10.1520/C0136_C0136M-19

Atterberg, A. (1905). Die Rationelle Klassifikation Der Sande Und Kiese. *Chemiker Zeitung*, *29*, 195-198.

Bailey, S. W. (1980). Summary of Recommendations of Aipea Nomenclature Committee. *Clay minerals*, *15*, 85. https://doi.org/10.1180/claymin.1980.015.1.07

References

Banda, R. M. (1999). *The Geology and Planktic Foraminiferal Biostratigraphy of the Northwest Borneo Basin, Sarawak, Malaysia* [PhD, University of Tsukuba]. Japan.

Belgeri, J. J., & Siegel, T. C. (1998). Design and Performance of Foundations in Expansive Shale. Proceedings of the Ohio River Valley Soils Seminar, Louisville, KY.

Bell, F. G. (1978). The Physical and Mechanical Properties of the Fell Sandstones, Northumberland, England. *Engineering Geology*, *12*, 1-29. https://doi.org/https://doi.org/10.1016/0013-7952(78)90002-9

Bell, F. G. (2005). Engineering Geology | Problematic Rocks. In R. C. Selley, L. R. M. Cocks, & I. R. Plimer (Eds.), *Encyclopedia of Geology* (pp. 543-554). Elsevier. https://doi.org/https://doi.org/10.1016/B0-12-369396-9/00220-3

Bellanger, M., Homand, F., & Remy, J. (1993). Water Behaviour in Limestones as a Function of Pores Structure: Application to Frost Resistance of Some Lorraine Limestones. *Engineering Geology*, *36*(1-2), 99-108. https://doi.org/10.1016/0013-7952(93)90022-5

Berisavljevic, Z., Berisavljevic, D., Rakic, D., & Radić, Z. (2018). Application of Geological Strength Index for Characterization of Weathering-Induced Failures. *Journal of the Croatian Association of Civil Engineers*, *70*(10), 891-903. https://doi.org/10.14256/JCE.1876.2016

Bhatia, M. R. (1985). Rare Earth Element Geochemistry of Australian Paleozoic Graywackes and Mudrocks: Provenance and Tectonic Control. *Sedimentary Geology*, *45*(1), 97-113. https://doi.org/10.1016/0037-0738(85)90025-9

Blatt, H. (1983). Sedimentary Petrology. *Geological Magazine*, *120*(5), 516-517. https://doi.org/10.1017/S0016756800027576

Blatt, H., Middleton, G.V., Murray, R.C. (1980). *Origin of Sedimentary Rocks*. Prentice-Hall.

Blatt, H., & Totten, M. W. (1981). Detrital Quartz as an Indicator of Distance from Shore in Marine Mudrocks. *SEPM Journal of Sedimentary Research*, *51*(4), 1259-1266. https://doi.org/10.1306/212f7e7d-2b24-11d7-8648000102c1865d

Blowes, D. W., Ptacek, C. J., Jambor, J. L., & Weisener, C. G. (2003). 9.05 - the Geochemistry of Acid Mine Drainage. In H. D. Holland & K. K. Turekian (Eds.), *Treatise on Geochemistry* (pp. 149-204). Pergamon. https://doi.org/https://doi.org/10.1016/B0-08-043751-6/09137-4

Boggs, S. J. (2009). Mudstones and Shales. In J. S. Boggs (Ed.), *Petrology of Sedimentary Rocks* (2 ed., pp. 194-219). Cambridge University Press. https://doi.org/10.1017/CBO9780511626487.007

Brinkman, R. (1985). *Mineralogy and Surface Properties of the Clay Fraction Affecting Soil Behavior and Management.* Soil Physics and Rice, Laguna, Philippines. https://edepot.wur.nl/317389

Bryson, L. S., Gomez-Gutierrez, I. C., & Hopkins, T. C. (2011). Correlations between Durability and Geotechnical Properties of Compacted Shales. In *Geo-Frontiers 2011* (pp. 4109-4118). https://doi.org/10.1061/41165(397)420

Bryson, L. S., Gomez-Gutierrez, I. C., & Hopkins, T. C. (2012). Development of a New Durability Index for Compacted Shale. *Engineering Geology*, *139-140*, 66-75. https://doi.org/10.1016/j.enggeo.2012.04.011

References

BS. (1990). *Bs-1377 Methods of Test for Soils for Civil Engineering Purposes*. British Standards Institution.

Buckman, J., Mahoney, C., März, C., & Wagner, T. (2020). The Secret 'after Life' of Foraminifera: Big Things out of Small. *Minerals*, *10*, 550. https://doi.org/10.3390/min10060550

Chigira, M. (1990). A Mechanism of Chemical Weathering of Mudstone in a Mountainous Area. *Engineering Geology*, *29*(2), 119-138. https://doi.org/10.1016/0013-7952(90)90002-I

Crook, K. A. W., Dott, R. H., Jr., & Shaver, R. H. (1974). Lithogenesis and Geotectonics: The Significance of Compositional Variation in Flysch Arenites (Graywackes). In *Modern and Ancient Geosynclinal Sedimentation* (Vol. 19, pp. 0). SEPM Society for Sedimentary Geology. https://doi.org/10.2110/pec.74.19.0304

Czerewko, M. A., & Cripps, J. C. (2012). Mudrocks, Clays and Pyrite. In J. Burland, T. Chapman, H. Skinner, & M. Brown (Eds.), *Ice Manual of Geotechnical Engineering: Volume I Geotechnical Engineering Principles, Problematic Soils and Site Investigation* (pp. 481-516). https://doi.org/10.1680/moge.57074.0481

Dean, W. (1974). Determination of Carbonate and Organic Matter in Calcareous Sediments and Sedimentary Rocks by Loss on Ignition: Comparison with Other Methods. *Journal of Sedimentary Petrology*, *44*, 242-248. https://doi.org/10.1306/74D729D2-2B21-11D7-8648000102C1865D

Department of Irrigation and Drainage Malaysia. (2022). Department of Irrigation and Drainage Malaysia. Retrieved 5/3/2022 from https://publicinfobanjir.water.gov.my/hujan/?lang=en

Dhakal, G., Yoneda, T., Kato, M., & Kaneko, K. (2002). Slake Durability and Mineralogical Properties of Some Pyroclastic and Sedimentary Rocks. *Engineering Geology*, *65*(1), 31-45. https://doi.org/https://doi.org/10.1016/S0013-7952(01)00101-6

Dìaz-Pèrez, A., Cortès-Monroy, I., & Roegiers, J. (2007). The Role of Water/Clay Interaction in the Shale Characterization. *Journal of Petroleum Science and Engineering*, *58*(1-2), 83-98. https://doi.org/10.1016/j.petrol.2006.11.011

Dick, J. C., & Shakoor, A. (1992). Lithological Controls of Mudrock Durability. *Quarterly Journal of Engineering Geology and Hydrogeology*, *25*(1), 31-46. https://doi.org/10.1144/gsl.Qjeg.1992.025.01.03

Dick, J. C., Shakoor, A., & Wells, N. (1994). A Geological Approach toward Developing a Mudrock-Durability Classification System. *Canadian Geotechnical Journal*, *31*(1), 17-27. https://doi.org/10.1139/t94-003

Du, J., Hu, L., Meegoda, J. N., & Zhang, G. (2018). Shale Softening: Observations, Phenomenological Behavior, and Mechanisms. *Applied Clay Science*, *161*, 290-300. https://doi.org/https://doi.org/10.1016/j.clay.2018.04.033

Duzgoren-Aydin, N., Aydin, A., & Malpas, J. (2002). Re-Assessment of Chemical Weathering Indices: Case Study on Pyroclastic Rocks of Hong Kong. *Engineering Geology*, *63*, 99-119. https://doi.org/10.1016/S0013-7952(01)00073-4

Edil, T. B. (1988). Soil Fabric. In *General Geology. Encyclopedia of Earth Science* (pp. 778-788). Springer US. https://doi.org/10.1007/0-387-30844-X_105

References

Erguler, Z. A., & Shakoor, A. (2009). Relative Contribution of Various Climatic Processes in Disintegration of Clay-Bearing Rocks. *Engineering Geology*, *108*(1), 36-42. https://doi.org/10.1016/j.enggeo.2009.06.002

Farrokhrouz, M., & Asef, M. (2013). *Shale Engineering: Mechanics and Mechanisms*. CRC Press.

Franklin, J. A., & Chandra, R. (1972). The Slake-Durability Test. *International Journal of Rock Mechanics and Mining Sciences & Geomechanics Abstracts*, *9*(3), 325-328. https://doi.org/https://doi.org/10.1016/0148-9062(72)90001-0

Franklin, J. A., & Dusseault, M. B. (1989). *Rock Engineering*. McGraw-Hill. https://books.google.com.my/books?id=WNJRAAAAMAAJ

Franklin, J. A., Gruspier, J. E., Ontario, Ministry of, T., Communications, Research, & Development, B. (1983). *Evaluation of Shales for Construction Projects: An Ontario Shale Rating System*. Ministry of Transportation and Communications, Research and Development Branch.

Gaillardet, J., Dupré, B., & Allègre, C. J. (1999). Geochemistry of Large River Suspended Sediments: Silicate Weathering or Recycling Tracer? *Geochimica et Cosmochimica Acta*, *63*(23), 4037-4051. https://doi.org/https://doi.org/10.1016/S0016-7037(99)00307-5

Gamble, J. C. (1971). *Durability-Plasticity Classification of Shales and Other Argillaceous Rocks* (Publication Number 7212171) [Doctoral Thesis, University of Illinois at Urbana-Champaign]. ProQuest One Academic. https://search-proquest-com.dbgw.lis.curtin.edu.au/docview/302466643?pq-origsite=summon

Garzanti, E., Padoan, M., Setti, M., Najman, Y., Peruta, L., & Villa, I. (2013). Weathering Geochemistry and Sr-Nd Fingerprints of Equatorial Upper Nile and Congo Muds. *Geochemistry, Geophysics, Geosystems*, *14*, 292-316. https://doi.org/10.1002/ggge.20060

Gautam, T. P., & Shakoor, A. (2013). Slaking Behavior of Clay-Bearing Rocks During a One-Year Exposure to Natural Climatic Conditions. *Engineering Geology*, *166*, 17-25. https://doi.org/10.1016/j.enggeo.2013.08.003

Gemici, Ü. (2001). Durability of Shales in Narlıdere, İzmi, Turkey, with an Emphasis on the Impact of Water on Slaking Behavior. *Environmental Geology*, *41*(3), 430-439. https://doi.org/10.1007/s002540100409

Giblin, A. E. (2009). Iron and Manganese. In G. E. Likens (Ed.), *Encyclopedia of Inland Waters* (pp. 35-44). Academic Press. https://doi.org/https://doi.org/10.1016/B978-012370626-3.00096-X

Gokceoglu, C., Ulusay, R., & Sonmez, H. (2000). Factors Affecting the Durability of Selected Weak and Clay-Bearing Rocks from Turkey, with Particular Emphasis on the Influence of the Number of Drying and Wetting Cycles. *Engineering Geology*, *57*(3-4), 215.

Goldich, S. S. (1938). A Study in Rock-Weathering. *Journal of Geology*, *46*, 17. https://doi.org/10.1086/624619

Grim, R. E., Bradley, W. F., & White, W. A. (1957). Petrology of the Paleozoic Shales of Illinois. https://core.ac.uk/download/pdf/17355387.pdf (Illinois State Geological Survey)

Gu, X., Rempe, D. M., Dietrich, W. E., West, A. J., Lin, T.-C., Jin, L., & Brantley, S. L. (2020). Chemical Reactions, Porosity, and Microfracturing in Shale During

References

Weathering: The Effect of Erosion Rate. *Geochimica et Cosmochimica Acta*, *269*, 63-100. https://doi.org/10.1016/j.gca.2019.09.044

Gupta, V., & Ahmed, I. (2007). The Effect of Ph of Water and Mineralogical Properties on the Slake Durability (Degradability) of Different Rocks from the Lesser Himalaya, India. *Engineering Geology*, *95*(3), 79-87. https://doi.org/10.1016/j.enggeo.2007.09.004

Hack, H. R. G. K. (2020). Weathering, Erosion, and Susceptibility to Weathering. In M. Kanji, M. He, & L. Ribeiro e Sousa (Eds.), *Soft Rock Mechanics and Engineering* (pp. 291-333). Springer International Publishing. https://doi.org/10.1007/978-3-030-29477-9_11

Harnois, L. (1988). The Ciw Index: A New Chemical Index of Weathering. *Sedimentary Geology*, *55*, 319-322. https://doi.org/10.1016/0037-0738(88)90137-6

Hatch, C., Wiese, J., Crane, C., Harris, K., Kloss, H., & Baltrusaitis, J. (2011). Water Adsorption on Clay Minerals as a Function of Relative Humidity: Application of Bet and Freundlich Adsorption Models. *Langmuir : the ACS journal of surfaces and colloids*, *28*, 1790-1803. https://doi.org/10.1021/la2042873

Heidari, M., Momeni, A., & Mohebbi, Y. (2018a). Durability Assessment of Clay-Bearing Soft Rocks by Using New Decay Index. *Periodica polytechnica. Periodica polytechnica.*, *62*(3). https://doi.org/10.3311/PPci.11284

Heidari, M., Momeni, A., & Mohebbi, Y. (2018b). Durability Assessment of Clay-Bearing Soft Rocks by Using New Decay Index. *Periodica Polytechnica*, *62*(3). https://doi.org/10.3311/PPci.11284

Heidari, M., Rafiei, B., Mohebbi, Y., & Torabi-Kaveh, M. (2015). Assessing the Behavior of Clay-Bearing Rocks Using Static and Dynamic Slaking Indices. *Geotechnical and Geological Engineering*, *33*(4), 1017-1030. https://doi.org/10.1007/s10706-015-9884-6

Heiri, O., Lotter, A. F., & Lemcke, G. (2001). Loss on Ignition as a Method for Estimating Organic and Carbonate Content in Sediments: Reproducibility and Comparability of Results. *Journal of Paleolimnology*, *25*(1), 101-110. https://doi.org/10.1023/A:1008119611481

Herron, M. M. (1988). Geochemical Classification of Terrigenous Sands and Shales from Core or Log Data. *Journal of Sedimentary Research*, *58*(5), 820-829. https://doi.org/10.1306/212f8e77-2b24-11d7-8648000102c1865d

Hirsch, D. M. (2012). *How to Make a Thin Section*. https://davehirsch.com/other/thinsections/

Honza, R. M. B. E. (1996). Miocene Stratigraphy of Northwest Borneo Basin. Annual Geological Conference '96, Kota Kinabalu, Sabah.

Hopkins, T. C., & Deen, R. C. (1984). Identification of Shales. *Geotechnical testing journal*, *7*(1), 10-18. https://doi.org/10.1520/GTJ10479J

Huang, P. M., & Wang, M. K. (2005). Minerals, Primary. In D. Hillel (Ed.), *Encyclopedia of Soils in the Environment* (pp. 500-510). Elsevier. https://doi.org/10.1016/B0-12-348530-4/00464-1

Hudec, P. P. (1998). Rock Properties and Physical Processes of Rapid Weathering and Deterioration. *Proceedings of 8th International Congress of IAEG*, *1*, 335-341. http://web2.uwindsor.ca/courses/earth_science/hudec/publications/rockpropweather.pdf

References

Huppert, F. (1988). Influence of Microfabric on Geomechanical Behaviour of Tertiary Finegrained Sedimentary Rocks from Central North Island, New Zealand. *Bulletin of the International Association of Engineering Geology - Bulletin de l'Association Internationale de GÈologie de l'IngÈnieur*, *38*, 83-93.

Hutchison, C. S. (2005). Chapter Vi - Miri Zone. In C. S. Hutchison (Ed.), *Geology of North-West Borneo* (pp. 77-134). Elsevier. https://doi.org/10.1016/B978-044451998-6/50008-9

Ingram, R. L. (1953). Fissility of Mudrocks. *Geological Society of America Bulletin*, *64*(8), 869-878. https://doi.org/10.1130/0016-7606(1953)64[869:FOM]2.0.CO;2

Ingram, R. L. (1954). Terminology for the Thickness of Stratification and Parting Units in Sedimentary Rocks. *Geological Society of America Bulletin*, *65*, 937. https://doi.org/10.1130/0016-7606(1954)65[937:Tfttos]2.0.Co;2

ISRM. (1981). Suggested Method: Rock Characterization, Testing and Monitoring. In E. T. Brown (Ed.). International Society for Rock Mechanics (ISRM).

ISRM. (2007). The Complete Isrm Suggested Methods for Rock Characterization, Testing and Monitoring: 1974–2006. In U. J. A. H. R. (Ed.), *Suggested Methods Prepared by the Commission on Testing Methods*. International Society for Rock Mechanics (ISRM).

Jakaitė, L. (2019). *Feldspars*. https://strike-dip.com/feldspars/

Jeremias, F. T. (2000). *Geological Controls on the Engineering Properties of Mudrocks of the North Lisbon Area* [PhD thesis, University of Sheffield].

Jeremias, J. M. O., António B. Pinho,, & Isabel M. R. Duarte, H. S., and Mario Camilo Torres Suárez. (2020). Mudrocks as Soft Rocks: Properties and Characteristics. In M. H. Milton Kanji, Luís Ribeiro e Sousa (Ed.), *Soft Rock Mechanics and Engineering*. Springer Nature Switzerland.

Jerz, J., & Rimstidt, J. D. (2004). Pyrite Oxidation in Moist Air. *Geochimica et Cosmochimica Acta*, *68*, 701-714. https://doi.org/10.1016/S0016-7037(03)00499-X

Jin, L., Mathur, R., Rother, G., Cole, D., Bazilevskaya, E., Williams, J., Carone, A., & Brantley, S. (2013). Evolution of Porosity and Geochemistry in Marcellus Formation Black Shale During Weathering. *Chemical Geology*, *356*, 50-63. https://doi.org/10.1016/j.chemgeo.2013.07.012

Jin, L., Ravella, R., Ketchum, B., Bierman, P. R., Heaney, P., White, T., & Brantley, S. L. (2010). Mineral Weathering and Elemental Transport During Hillslope Evolution at the Susquehanna/Shale Hills Critical Zone Observatory. *Geochimica et Cosmochimica Acta*, *74*(13), 3669-3691. https://doi.org/10.1016/j.gca.2010.03.036

Kelley, K. D., Scott, C.T., Polyak, D.E., and Kimball, B.E. (2017). *Critical Mineral Resources of the United States—Economic and Environmental Geology and Prospects for Future Supply: U.S. Geological Survey Professional Paper 1802* (K. J. Schulz, DeYoung, J.H., Jr., Seal, R.R., II, and Bradley, D.C, Ed.). https://doi.org/ https://doi.org/ 10.3133/pp1802U

Kessler, F.-L., & Jong, J. (2015). Northwest Sarawak: A Complete Geologic Profile from the Lower Miocene to the Pliocene Covering the Upper Setap Shale, Lambir and Tukau Formations. *Warta Geologi*, *41*(3-4), 45-51. https://www.researchgate.net/publication/311614817_Northwest_Sarawak

_A_Complete_Geologic_Profile_from_the_Lower_Miocene_to_the_Pliocene_Covering_the_Upper_Setap_Shale_Lambir_and_Tukau_Formations

Kessler, F.-L., & Jong, J. (2017). The Roles and Implications of Several Prominent Unconformities in Neogene Sediments of the Greater Miri Area, Nw Sarawak. *Warta Geologi*, *43*(4), 1-8. https://www.researchgate.net/publication/320620042_The_roles_and_implications_of_several_prominent_unconformities_in_Neogene_sediments_of_the_greater_Miri_area_NW_Sarawak

Kessler, F.-L., Jong, J., & Madon, M. (2019). Two New Important Outcrops Along the Pan-Borneo Highway in the Lambir Hills, Miri Area, Northern Sarawak. *Warta Geologi*, *45*, 387-393. https://doi.org/10.7186/wg454201901

Khor, S., Hassan, M. H., & Barbeito, M. (2014). Sedimentology and Stratigraphy of the Miocene Kampung Opak Limestone (Sibuti Formation), Bekenu, Sarawak. *Bulletin of the Geological Society of Malaysia*, *60*, 45-53. https://doi.org/10.7186/bgsm60201405

King, F. (2013). *A Review of the Properties of Pyrite and the Implications for Corrosion of the Copper Canister*. Svensk Kärnbränslehantering AB, Swedish Nuclear Fuel and Waste Management Company. https://books.google.com.my/books?id=wt3izQEACAAJ

Koralegedara, N. H., & Maynard, J. B. (2017). Chemical, Mineralogical and Textural Properties of the Kope Formation Mudstones: How They Affect Its Durability. *Engineering Geology*, *228*, 312-322. https://doi.org/10.1016/j.enggeo.2017.08.025

Kuenen, P. H. (1959). Turbidity Currents a Major Factor in Flysch Deposition. *Eclogae Geol. Helvetiae*, *51*(3), 1009-1021.

Kuenen, P. H. (1960). Sand - Its Origin, Transportation, Abrasion and Accumulation. *Geological Society of South Africa*, *62*, 1-33.

Lai, T. Y., Loo, V. H., Wong, V. K., & Wong, K. S. (2022). Modification of the Natural Slake Test and Assessment of Slaking Behavior of a Shale from Malaysia under Rainfall. *Geotechnical and Geological Engineering*. https://doi.org/10.1007/s10706-022-02085-x

Lashkaripour, G. R., & Boomeri, M. (2002). The Role of Mineralogy on Durability of Weak Rocks. *Journal of Applied Sciences*, *2*(6), 698-701. https://doi.org/10.3923/jas.2002.698.701

Le Bissonnais, Y., Y. (2016). Aggregate Stability and Assessment of Soil Crustability and Erodibility: I. Theory and Methodology. *European Journal of Soil Science*, *67*(1), 11-21. https://doi.org/10.1111/ejss.4_12311

Lerouge, C., Robinet, J.-C., Debure, M., Tournassat, C., Bouchet, A., Fernández, A. M., Flehoc, C., Guerrot, C., Kars, M., Lagroix, F., Landrein, P., Madé, B., Negrel, P., Wille, G., & Claret, F. (2018). A Deep Alteration and Oxidation Profile in a Shallow Clay Aquitard: Example of the Tégulines Clay, East Paris Basin, France. *Geofluids*, *2018*, 1606753. https://doi.org/10.1155/2018/1606753

Li, J., Liao, X., Wang, K., Wu, X., Chen, J., & Xi, Y. (2019). Study on the Geochemical Characteristics and Weathering Behavior of Black Shale. In *Geo-Congress 2019* (pp. 514-521). https://doi.org/10.1061/9780784482124.052

References

Liao, X., Wang, K., Wu, X., Ling, S., Guo, D., & Xi, Y. (2019). Characteristics of Interactions between Black Shale and Water. *E3S Web Conf.*, *98*, 01033. https://doi.org/10.1051/e3sconf/20199801033

Ling, S., Wu, X., Zhao, S., & Liao, X. (2018). Evolution of Porosity and Clay Mineralogy Associated with Chemical Weathering of Black Shale: A Case Study of Lower Cambrian Black Shale in Chongqing, China. *Journal of Geochemical Exploration*, *188*, 326-339. https://doi.org/10.1016/j.gexplo.2018.02.002

Liu, C.-W., Lin, K.-H., & Kuo, Y.-M. (2003). Application of Factor Analysis in the Assessment of Groundwater Quality in a Blackfoot Disease Area in Taiwan. *Science of The Total Environment*, *313*(1), 77-89. https://doi.org/https://doi.org/10.1016/S0048-9697(02)00683-6

Liu, D., Wang, Z., Zhang, X., Wang, Y., Zhang, X., & Li, D. (2017). Experimental Investigation on the Mechanical and Acoustic Emission Characteristics of Shale Softened by Water Absorption. *Journal of Natural Gas Science and Engineering*, *50*. https://doi.org/10.1016/j.jngse.2017.11.020

Liu, X., Song, Y., Xia, Z., & Chen, R. (2020). Assessing the Slake Durability of Red Stratum Sandstone in Different Solution Environments by a Novel Dual Rotation Test. *Engineering Geology*, *267*, 105503. https://doi.org/10.1016/j.enggeo.2020.105503

Liu, Z., Dongxia, C., Zhang, J., Lü, X., Wang, Z., Liao, W., Shi, X., Tang, J., & Xie, G. (2019). Pyrite Morphology as an Indicator of Paleoredox Conditions and Shale Gas Content of the Longmaxi and Wufeng Shales in the Middle Yangtze Area, South China. *Minerals*, *9*, 428. https://doi.org/10.3390/min9070428

Lovie, P. (2005). Encyclopedia of Statistics in Behavioral Science. In. https://doi.org/10.1002/0470013192.bsa107

Lundegard, P. D., & Samuels, N. D. (1980). Field Classification of Fine-Grained Sedimentary Rocks. *Journal of Sedimentary Petrology*, *50*(3), 0781-0786.

Luther, G. W., III, Giblin, A., Howarth, R. W., & Ryans, R. A. (1982). Pyrite and Oxidized Iron Mineral Phases Formed from Pyrite Oxidation in Salt Marsh and Estuarine Sediments. *Geochimica et Cosmochimica Acta*, *46*, 2665-2669. https://doi.org/10.1016/0016-7037(82)90385-4

Marques, E. A. G., Vargas, E. D. A., & Antunes, F. S. (2005). A Study of the Durability of Some Shales, Mudrocks and Siltstones from Brazil. *Geotechnical & Geological Engineering*, *23*(3), 321-348. https://doi.org/10.1007/s10706-004-1605-5

Masada T., H. X. (2013). Rock Mass Classification System: Transition from Rmr to Gsi. *Ohio Department of Transportation.*

McKee, E. D., & Weir, G. W. (1953). Terminology for Stratification and Cross-Stratification in Sedimentary Rocks. *Geological Society of America Bulletin*, *64*, 381. https://doi.org/10.1130/0016-7606(1953)64[381:Tfsaci]2.0.Co;2

McLennan, S. (2001). Relationships between the Trace Element Composition of Sedimentary Rocks and Upper Continental Crust. *Geochemistry Geophysics Geosystems - GEOCHEM GEOPHYS GEOSYST*, *2*. https://doi.org/10.1029/2000GC000109

Means, R. E., & Parcher, J. V. (1963). *Physical Properties of Soils [by] R.E. Means [and] J.V. Parcher*.

References

Millot, G., Farrand, W. R., & Paquet, H. (2013). *Geology of Clays: Weathering · Sedimentology · Geochemistry*. Springer Berlin Heidelberg. https://books.google.com.my/books?id=1UD8CAAAQBAJ

Miscevic, P. R.-B., T. (2001). Weathering Process in Eocene Flysch in Region of Split (Croatia). *Rudarsko Geolosko Naftni Zbornik*, *13*(1), 47-55. https://hrcak.srce.hr/13415

Moon, V. G., & Beattie, A. (1995). Textural and Microstructural Influences on the Durability of Waikato Coal Measures Mudrocks. *Quarterly journal of engineering geology*, *28*, 303 - 312.

Moriwaki, Y. (1974). *Causes of Slaking in Argillaceous Materials* [PhD dissertation, University of California at Berkeley, CA]. USA.

Nagarajan, R., Armstrong-Altrin, J. S., Kessler, F.-L., & Jong, J. (2017a). Petrological and Geochemical Constraints on Provenance, Paleoweathering, and Tectonic Setting of Clastic Sediments from the Neogene Lambir and Sibuti Formations, Northwest Borneo. In (pp. 123-153). https://doi.org/10.1016/B978-0-12-803386-9.00007-1

Nagarajan, R., Armstrong-Altrin, J. S., Kessler, F. L., Hidalgo-Moral, E. L., Dodge-Wan, D., & Taib, N. I. (2015). Provenance and Tectonic Setting of Miocene Siliciclastic Sediments, Sibuti Formation, Northwestern Borneo. *Arabian Journal of Geosciences*, *8*(10), 8549-8565. https://doi.org/10.1007/s12517-015-1833-4

Nagarajan, R., Armstrong-Altrin, J. S., Kessler, F. L., & Jong, J. (2017). Chapter 7 - Petrological and Geochemical Constraints on Provenance, Paleoweathering, and Tectonic Setting of Clastic Sediments from the Neogene Lambir and Sibuti Formations, Northwest Borneo. In R. Mazumder (Ed.), *Sediment Provenance* (pp. 123-153). Elsevier. https://doi.org/10.1016/B978-0-12-803386-9.00007-1

Nagarajan, R., Kessler, F.-L., Jong, J., Ramkumar, M., Ali, A., Dayong, V., Shanmugarajah, L., Vusak, N., Sivanasvaran, K., & Kinanthi, D. (2020). Geochemistry of the Palaeocene-Eocene Upper Kelalan Formation, Nw Borneo: Implications on Palaeoweathering, Tectonic Setting, and Provenance. *Geological Journal*. https://doi.org/10.1002/gj.3950

Nagarajan, R., Roy, P. D., Jonathan, M. P., Lozano, R., Kessler, F. L., & Prasanna, M. V. (2014). Geochemistry of Neogene Sedimentary Rocks from Borneo Basin, East Malaysia: Paleo-Weathering, Provenance and Tectonic Setting. *Geochemistry*, *74*(1), 139-146. https://doi.org/10.1016/j.chemer.2013.04.003

Nagarajan, R., Roy, P. D., Kessler, F. L., Jong, J., Dayong, V., & Jonathan, M. P. (2017b). An Integrated Study of Geochemistry and Mineralogy of the Upper Tukau Formation, Borneo Island (East Malaysia): Sediment Provenance, Depositional Setting and Tectonic Implications. *Journal of Asian Earth Sciences*, *143*, 77-94. https://doi.org/https://doi.org/10.1016/j.jseaes.2017.04.002

Nandi, A., Liutkus, C., & J, W. (2009a). Geotechnical Characterization of Sevier and Rome Shale, East Tennessee. *43rd U.S. Rock Mechanics Symposium and 4th U.S.-Canada Rock Mechanics Symposium*. https://www.researchgate.net/publication/254542428_Geotechnical_Characterization_of_Sevier_And_Rome_Shale_East_Tennessee

References

Nandi, A., & Whitelaw, M. (2009b). Effect of Physico-Chemical Factors on the Disintegration Behavior of Calcareous Shale. *Environmental and Engineering Geoscience*, *15*(4), 273-285. https://doi.org/10.2113/gseegeosci.15.4.273

Nesbitt, H. W., Markovics, G., & price, R. C. (1980). Chemical Processes Affecting Alkalis and Alkaline Earths During Continental Weathering. *Geochimica et Cosmochimica Acta*, *44*(11), 1659-1666. https://doi.org/https://doi.org/10.1016/0016-7037(80)90218-5

Nesbitt, H. W., & Young, G. M. (1982). Early Proterozoic Climates and Plate Motions Inferred from Major Element Chemistry of Lutites. *Nature*, *299*(5885), 715-717. https://doi.org/10.1038/299715a0

Nesbitt, H. W., & Young, G. M. (1984). Prediction of Some Weathering Trends of Plutonic and Volcanic Rocks Based on Thermodynamic and Kinetic Considerations. *Geochimica et Cosmochimica Acta*, *48*(7), 1523-1534. https://doi.org/10.1016/0016-7037(84)90408-3

Nicholson, S. (2001). Climatic and Environmental Change in Africa During the Last Two Centuries. *Climate Research*, *17*, 123-144. https://doi.org/10.3354/CR017123

O'Brien, N. R., & Slatt, R. M. (1990). *Argillaceous Rock Atlas*. Springer-Verlag.

ODOT. (2011). Rock Slope Design Guide. *Ohio Department of Transportation*.

Olphen, H. V. (1964). An Introduction to Clay Colloid Chemistry. *Soil Science*, *97*(4). https://journals.lww.com/soilsci/Fulltext/1964/04000/An_Introduction_to_Clay_Colloid_Chemistry.13.aspx

Parker, A. (1970). An Index of Weathering for Silicate Rocks. *Geological Magazine*, *107*(6), 501-504. https://doi.org/10.1017/S0016756800058581

Peng, L. C., Hassan, K., Leman, M. S., Nasib, B. M., & Karim, R. A. (1997). Towards Producing a Stratigraphic Lexicon of Malaysia. https://gsm.org.my/products/702001-101655-PDF.pdf

Perry, E. F., & Andrews, D. E. (1982). *Slaking Modes of Geologic Materials and Their Impact on Embankment Stabilization* 61st Annual Meeting of the Transportation Research Board, Washington District of Columbia, United States.

Pettijohn, F. J. (1975). *Sedimentary Rocks* (Vol. 3). Harper & Row New York.

Pettijohn, F. J., Potter, P. E., & Siever, R. (1972). *Sand and Sandstone*. Springer New York. https://doi.org/10.1007/978-1-4615-9974-6

Picard, M. D. (1971). Classification of Fine-Grained Sedimentary Rocks. *Journal of Sedimentary Research*, *41*(1), 179-195. https://doi.org/10.1306/74d7221b-2b21-11d7-8648000102c1865d

Pinho, A. B., Andrade, P. S., & Duarte, I. M. R. (2017). Physical Weathering. In P. T. Bobrowsky & B. Marker (Eds.), *Encyclopedia of Engineering Geology* (pp. 1-5). Springer International Publishing. https://doi.org/10.1007/978-3-319-12127-7_219-1

Pollastro, R. M. (1981). Authigenic Kaolinite and Associated Pyrite in Chalk of the Cretaceous Niobrara Formation, Eastern Colorado. *Journal of Sedimentary Petrology*, *51*(2), 553-562. http://pubs.er.usgs.gov/publication/70012148

Potter, P. E., Maynard, J. B., & Depetris, P. J. (2005). *Mud and Mudstones: Introduction and Overview*. Springer Berlin Heidelberg. http://lib.ugent.be/catalog/rug01:000889161

References

Potter, P. E., Maynard, J. B., & Pryor, W. A. (1980). Sedimentology of Shale. https://doi.org/10.1007/978-1-4612-9981-3 (Springer, New York, NY)

Putera Agung, M. A., Pramusandi, S., & Damianto, B. (2017). Identification and Classification of Clayshale Characteristic and Some Considerations for Slope Stability. *African Journal of Environmental Science and Technology*, *11*(4), 163-197. https://doi.org/10.5897/AJEST2014.1792

Rahman, R. A., Kunjappan, M., & Ismail, N. F. A. b. (2019). Weather and Climate *Malaysia Meteorological Department (Annual Report 2019)*. https://www.met.gov.my/content/pdf/penerbitan/laporantahunan/laporantahunan2019.pdf

Revia Oktaviani, Paulus P Rahardjo, & Imam A Sadisun. (2018). The Clay Shale Durability Behavior of Jatiluhur Formation Based on Dynamic and Static Slaking Indices. *International Journal of Scientific & Engineering Research*, *9*(5). https://www.ijser.org/researchpaper/The-Clay-ShaleDurability-Behavior-of-Jatiluhur-Formation-Based-on-Dynamic-and-Static-Slaking-Indices.pdf

Rieder, M., Cavazzini, G., D'yakonov, Y. S., Frank-Kamenetskii, V. A., Gottardi, G., Guggenheim, S., Koval, P. V., Mueller, G., Neiva, A. M. R., Radoslovich, E. W., Robert, J. L., Sassi, F. P., Takeda, H., Weiss, Z., & Wones, D. R. (1999). Nomenclature of the Micas. *Mineralogical Magazine*, *63*(2), 267-279.

Ritsema, C., & Groenenberg, J. (1993). Pyrite Oxidation, Carbonate Weathering, and Gypsum Formation in a Drained Potential Acid Sulfate Soil. https://doi.org/10.2136/sssaj1993.03615995005700040015x

Rosa, J., Cooper, M., & Darboux, F. (2012). Conditions for the Occurrence of Slaking and Other Disaggregation Processes under Rainfall. *Hydrology*, *3*. https://doi.org/10.3390/hydrology3030027

Russell, D. J. (1982). Controls on Shale Durability: The Response of Two Ordovician Shales in the Slake Durability Test. *Canadian Geotechnical Journal*, *19*(1), 1-13. https://doi.org/10.1139/t82-001

Sadisun, I., Shimada, H., Ichinose, M., & Matsui, K. (2004). *Textural and Mineralogical Properties of Argillaceous Rocks in Relation to Their Propensity to Slaking*. https://doi.org/10.13140/2.1.2287.4248

Sadisun, I. A., Bandono, B., Shimada, H., Ichinose, M., & Matsui, K. (2010). *Physical Disintegration Characterization of Mudrocks Subjected to Slaking Exposure and Immersion Tests* (Vol. 5) [disintegration; mudrock; exposure; immersion; slaking test]. http://ijog.bgl.esdm.go.id/index.php/IJOG/article/view/105

Sadisun, I. A., Shimada, H., Ichinose, M., & Matsui, K. (2005). Study on the Physical Disintegration Characteristics of Subang Claystone Subjected to a Modified Slaking Index Test. *Geotechnical & Geological Engineering*, *23*(3), 199-218. https://doi.org/10.1007/s10706-003-6112-6

Santi, P. M., & Higgins, J. D. (1998). Methods for Predicting Shale Durability in the Field. *Geotechnical testing journal*, *21*(3), 195-202.

Santisteban, J., López, R., Pamo, E., Dabrio, C., Zapata, M., Gil-García, M., Castaño Castaño, S., & Alfaro, P. (2004). Loss on Ignition: A Qualitative or Quantitative Method for Organic Matter and Carbonate Mineral Content in Sediments? *Journal of Paleolimnology*, *32*. https://doi.org/10.1023/B:JOPL.0000042999.30131.5b

References

Sarawak Government. (2021). Retrieved 2/7/2021 from https://sarawak.gov.my/web/home/article_view/159/176/?id=159

Sawlowicz, Z. (2000). Framboids: From Their Origin to Application. *Pr. Mineral.*, *88*.

Schmitt, L., Forsans, T., & Santarelli, F. J. (1994). Shale Testing and Capillary Phenomena. *International Journal of Rock Mechanics and Mining Sciences & Geomechanics Abstracts*, *31*(5), 411-427. https://doi.org/10.1016/0148-9062(94)90145-7

Selen, L., Panthi, K. K., & Vistnes, G. (2020). An Analysis on the Slaking and Disintegration Extent of Weak Rock Mass of the Water Tunnels for Hydropower Project Using Modified Slake Durability Test. *Bulletin of Engineering Geology and the Environment*, *79*(4), 1919-1937. https://doi.org/10.1007/s10064-019-01656-2

Shakoor, A., & Brock, D. (1987). Relationship between Fissility, Composition, and Engineering Properties of Selected Shales from Northeast Ohio. *Environmental and Engineering Geoscience*, *xxiv*(3), 363-379. https://doi.org/10.2113/gseegeosci.xxiv.3.363

Shen, P., Tang, H., Wang, D., Su, X., & Huang, L. (2020). Weakening of Mudstone Fragments Due to Disintegration: An Experimental Investigation. *Bulletin of Engineering Geology and the Environment*, *79*(10), 5477-5497. https://doi.org/10.1007/s10064-020-01874-z

Shrestha, N. (2021). Factor Analysis as a Tool for Survey Analysis. *American Journal of Applied Mathematics and Statistics*, *9*, 4-11. https://doi.org/10.12691/ajams-9-1-2

Soga, K., & Mitchell, J. (2005). *Fundamentals of Soil Behavior, 3rd Edition*.

Spears, D. A. (1980). Towards a Classification of Shales. *Journal of the Geological Society*, *137*(2), 125-129. https://doi.org/10.1144/gsjgs.137.2.0125

Stow, D. A. V., & Piper, D. J. W. (1984). Deep-Water Fine-Grained Sediments: Facies Models. *Geological Society, London, Special Publications*, *15*(1), 611. https://doi.org/10.1144/GSL.SP.1984.015.01.38

Sudo, T., & Shimoda, S. (1978). *Clays and Clay Minerals of Japan (Developments in Sedimentology)*. Elsevier Science.

Tanner, W. F. (1969). The Particle Size Scale. *Journal of Sedimentary Research*, *39*(2), 809-812.

Taylor, R. K. (1988). Coal Measures Mudrocks Composition, Classification and Weathering Processes. *Quarterly journal of engineering geology*, *21*(1), 85-99. https://doi.org/10.1144/GSL.QJEG.1988.021.01.06

Taylor, R. K., & Cripps, J. C. (1987). Weathering Effects: Slopes in Mudrocks and over-Consolidated Clays. In Anderson MG & R. KS (Eds.), *Slope Stability* (pp. 405–445). Wiley.

Taylor, R. K., & Smith, T. J. (1986). The Engineering Geology of Clay Minerals: Swelling, Shrinking and Mudrock Breakdown. *Clay minerals*, *21*(3), 235-260. https://doi.org/10.1180/claymin.1986.021.3.01

Taylor, R. K., & Spears, D. A. (1970). The Breakdown of British Coal Measure Rocks. *International Journal of Rock Mechanics and Mining Sciences & Geomechanics Abstracts*, *7*(5), 481-501. https://doi.org/10.1016/0148-9062(70)90002-1

References

Taylor, R. K., & Spears, D. A. (1981). Laboratory Investigation of Mudrocks. *Quarterly journal of engineering geology*, *14*(4), 291-309. https://doi.org/10.1144/GSL.QJEG.1981.014.04.08

Togunwa, O., Abdullah, W., Hakimi, M., & Barbeito, P. (2015). Organic Geochemical and Petrographic Characteristics of Neogene Organic-Rich Sediments from the Onshore West Baram Delta Province, Sarawak Basin: Implications for Source Rocks and Hydrocarbon Generation Potential. *Marine and Petroleum Geology*, *63*. https://doi.org/10.1016/j.marpetgeo.2015.02.032

Tourtelot, H. A. (1960). Origin and Use of the Word "Shale". *American Journal of Science*, *258*, 335-343.

Trefethen, J. M. (1950). Classification of Sediments. *American Journal of Science*, *248*(1), 55. https://doi.org/10.2475/ajs.248.1.55

Tse, A. (2016). Tse A.C and Eyang F. Geotechnical Characteristics of Weak Shales in the Calabar Flank, Southeastern Nigeria. Journal of Earth Sciences and Geotechnical Engineering 2016; 6(1): 123-133. https://www.researchgate.net/publication/302906198_Tse_AC_and_Eyang_F_Geotechnical_Characteristics_of_weak_Shales_in_the_Calabar_Flank_Southeastern_Nigeria_Journal_of_Earth_Sciences_and_Geotechnical_Engineering_2016_61_123-133

Tucker, M. E. (1994). *Sedimentary Petrology* (2nd ed.). Blackwell.

Tuğrul, A., & Gürpinar, O. (1997). A Proposed Weathering Classification for Basalts and Their Engineering Properties (Turkey). *Bulletin of Engineering Geology and the Environment*, *55*(1), 139-149. https://doi.org/10.1007/BF02635416

Vallejo, L. E., & Stewart-Murphy, A. (2001). Influence of Pore Wall Roughness on the Slaking of Shales. DC Rocks 2001, The 38th U.S. Symposium on Rock Mechanics (USRMS),

Vallejo, L. E., Welsh, R. A., Lovell, C. W., & Robinson, M. K. (1993). The Influence of Fabric and Composition on the Durability of Appalachian Shales. In C. H. McElroy & D. A. Lienhart (Eds.), (pp. 15-28). ASTM International. https://doi.org/10.1520/STP15934S

van der Jagt, H. (2005). Geochemistry | Soil, Major Inorganic Components. In P. Worsfold, A. Townshend, & C. Poole (Eds.), *Encyclopedia of Analytical Science (Second Edition)* (pp. 188-195). Elsevier. https://doi.org/https://doi.org/10.1016/B0-12-369397-7/00243-0

Velde, B., & Meunier, A. (2008). *The Origin of Clay Minerals in Soils and Weathered Rocks* (Vol. 418). https://doi.org/10.1007/978-3-540-75634-7

Vogt, T. (1927). Sulitjelmafeltets Geologi Og Petrografi. *Norges Geologiske Undersokelse*, *121*, 1-560.

Wang, Q., Wang, T., Liu, W., Zhang, J., Feng, Q., Lu, H., & Peng, P. a. (2019). Relationships among Composition, Porosity and Permeability of Longmaxi Shale Reservoir in the Weiyuan Block, Sichuan Basin, China. *Marine and Petroleum Geology*, *102*, 33-47. https://doi.org/https://doi.org/10.1016/j.marpetgeo.2018.12.026

Wentworth, C. K. (1922). A Scale of Grade and Class Terms for Clastic Sediments. *The Journal of geology*, *30*(5), 377-392. https://doi.org/10.1086/622910

References

Winslow, D. N., & Lovell, C. W. (1981). Measurements of Pore Size Distributions in Cements, Aggregates and Soils. *Powder Technology*, *29*(1), 151-165. https://doi.org/10.1016/0032-5910(81)85013-9

Wood, L. E. (1984). Shale Materials, Engineering Classificationshale Materials, Engineering Classification. In C. W. Finkl (Ed.), *Applied Geology* (pp. 517-523). Springer US. https://doi.org/10.1007/0-387-30842-3_63

World Weather & Climate Information. (2021). Retrieved 2/7/2021 from https://weather-and-climate.com/average-monthly-precipitation-Rainfall,miri-sarawak-my,Malaysia

World Weather Online. (2021). Retrieved 14/07/2021 from

Yagiz, S. (2001). Overview of Classification and Engineering Properties of Shales for Design Considerations. *Construction and Materials Issues 2001*, 156-165.

Young, D. A. (1983). Alkali Feldspars. In *Mineralogy* (pp. 2-7). Springer US. https://doi.org/10.1007/0-387-30720-6_2

Zaher, H., & Caron, J. (2008). Aggregate Slaking During Rapid Wetting: Hydrophobicity and Pore Occlusion. *Canadian Journal of Soil Science*, *88*, 85-97. https://doi.org/10.4141/CJSS07021

Zaher, H., Caron, J., & Ouaki, B. (2005). Modeling Aggregate Internal Pressure Evolution Following Immersion to Quantify Mechanisms of Structural Stability. *Soil Science Society of America Journal - SSSAJ*, *69*. https://doi.org/10.2136/sssaj2005.0001

Zarei, H., & Bilondi, M. (2013). Factor Analysis of Chemical Composition in the Karoon River Basin, Southwest of Iran. *Applied Water Science*, *3*. https://doi.org/10.1007/s13201-013-0123-0

Zhang, Z., Jiang, Q., Zhou, C., & Liu, X. (2014). Strength and Failure Characteristics of Jurassic Red-Bed Sandstone under Cyclic Wetting–Drying Conditions. *Geophysical Journal International*, *198*(2), 1034-1044. https://doi.org/10.1093/gji/ggu181

Zhang, Z., Niu, Y., Shang, X., Ye, P., Zhou, R., & Gao, F. (2021). Deterioration of Physical and Mechanical Properties of Rocks by Cyclic Drying and Wetting. *Geofluids*, *2021*, 6661107. https://doi.org/10.1155/2021/6661107